Assessing the Sources and Chemistry of Nitrogen Oxides in the Remote Oceanic Atmosphere

Simone Thirstrup Andersen

Doctor of Philosophy

University of York

Chemistry

March 2022

Abstract

Atmospheric nitrogen oxides ($NO_x = NO + NO_2$) play a key part in controlling the abundance of OH and O_3 in the atmosphere.

Long-term measurements of NO_x at the Cape Verde Atmospheric Observatory have been used to investigate fundamental processes in the remote marine boundary layer (MBL). The measurements were conducted using a chemiluminescence detector with two different photolytic converters for NO_2 conversion, which give comparable results when correcting for artefacts.

The photostationary state (PSS) of NO-NO_2-O_3 was used to evaluate our current understanding of the oxidation processes occurring in the MBL. Good agreement was observed between measured and PSS-derived NO_2 calculated from measurements of NO, O_3, and jNO_2, modelled values of peroxy radicals ($RO_2 + HO_2$), and annually averaged halogen monoxides (IO + BrO) for air masses with [CO] $<$ 90 ppbV. However, in air masses with [CO] $>$ 100 ppbV, a missing oxidant converting NO into NO_2 on the order of 18.5-104 pptV (assuming the same rate coefficient as CH_3O_2 with NO) was needed for the measured and PSS-derived NO_2 to agree.

Formation of nitric acid (HNO_3) has traditionally been seen as a sink of NO_x, however, it has recently been suggested that photolysis of particulate nitrate (pNO_3^-) is up to orders of magnitude faster than photolysis of gas-phase HNO_3, which could make it an important source of nitrous acid (HONO) and NO_x in the MBL. Here, it is shown that the enhancement factor of particulate nitrate photolysis compared to gas-phase HNO_3 decreases with increasing pNO_3^- concentration. This largely reconciles previous studies and can potentially be explained by a surface-enhanced mechanism described by the Langmuir isotherm.

Both the missing oxidants and the recycling of NO_x through pNO_3^- can have important implications for atmospheric oxidants such as OH and O_3 and their trends in both polluted and clean environments.

Contents

List of Abbreviations

ACD apparent column denisty

ACS absorbtion cross section

APN acyl peroxy nitrates

AQD Air Quality Design Inc.

ARNA Atmospheric Reactive Nitrogen over the remote Atlantic

BB Biomass burning

BLC blue light converter

BOC British Oxygen Company

CAPS Cavity Attenuated Phase Shift

CCD charge-coupled device

CDP Cloud Droplet Probe

CE conversion efficiency

CES Cavity Enhanced Spectroscopy

CIMS Chemical Ionization Mass Spectrometry

CLD chemiluminescence detector

CRDS Cavity Ring-Down Spectroscopy

CVAO Cape Verde Atmospheric Observatory

DMT Droplet Measurement Technologies

DOAS Differential Optical Absorption Spectroscopy

ESR Electron Spin Resonance

FAGE fluorescence assay by gas extension

FTIR Fourier-Transform Infrared spectroscopy

GAW Global Atmosphere Watch

GC-FID gas chromatograph coupled with a Flame Ionization Detector

GFS Global Forecast System

GPT gas phase titration

HIRAC Highly Instrumented Reactor for Atmospheric Chemistry

HYSPLIT Hybrid Single-Particle Langrangian Integrated Trajectory

IC ion chromatography

LED light emitting diode

LIF Laser Induced Fluorescence

LOD limit of detection

LOPAP Long Path Absorption Photometer

MBL marine boundary layer

MCM Master Chemical Mechanism

MIESR Matrix Isolation with Electron Spin Resonance Detection

MPAN peroxymethacryloyl nitrate

NDIR Non-Dispersive Infrared spectroscopy

NIR near infrared

NOPR net ozone production rate

NPL National Physical Laboratory

NSS non-sea-salt

PAG pure air generator

PAN peroxyacetyl nitrate

PBL planetary boundary layer

PC photolysis/chemiluminescence

PCASP Passive Cavity Aerosol Spectrometer Probe

PLC photolytic converter

PM10 particulate matter with an aerodynamical diameter below 10 μm

PMT photomultiplier tube

pNO_3^- particulate nitrate

ppbV parts per billion by volume

ppmV parts per million by volume

pptV parts per trillion by volume

PSS photostationary state

PTFE polytetrafluoroethylene

RH relative humidity

sccm standard cubic centimeter per minute

SLRs straight-and-level-runs

SOA secondary organic aerosols

stL standard litre

STT stratosphere-troposphere transport

TILDAS Tunable Infrared Laser Differential Absorption Spectroscopy

UV ultraviolet

UV-CEAS UV-vis Cavity Enhanced Absorption Spectroscopy

VOCs volatile organic compounds

WCC World Calibration Centre

List of Figures

List of Tables

Acknowledgements

First and foremost, I want to thank my supervisors, James Lee and Lucy Carpenter, for their guidance and support over the past 3.5 years. It has been a true privilege to work alongside such knowledgeable, ambitious and inspirational people.

Secondly I want to thank the SPHERES Natural Environment Research Council (NERC) Doctoral Training Partnership for funding this PhD.

Thirdly, a big thank you to all the people who have helped me with my research over the years; Luis for technical support at the CVAO, Katie and Shalini for running the other instruments at the CVAO and helping me settle in with running the NO_x instrument, Martyn for helping me learn to use Python, Beth for doing box modelling for me, Tomás for getting me GEOS-Chem outputs, Matt for doing FLEXPART back trajectories for the CVAO, Rosie and Adam for helping me with the filter samples during the ARNA campaigns, and the rest of the ARNA team for supplying data and being great company during the ARNA campaigns!

Next I want thank the incredible group of people at WACL I've been able to call my friends and colleagues for the last 3.5 years. Thank you for welcoming me with open arms, being a social group of people who always invite new people to social gatherings, and for always being up for a discussion about scientific and programming problems!

A huge thank you is also owed to my previous supervisors; Ole John Nielsen, Mads P. Sulbaek Andersen, and Barbara J. Finlayson-Pitts, and their research groups for introducing me to research, showing me how incredible it can be to work in atmospheric science, and for encouraging me to pursue a PhD! You are a huge part of why I have made it this far.

Last but definitely not least, I want to thank my friends and family here and back home for supporting me and encouraging me to pursue a PhD abroad! It would not have been possible without all of you.

Author's declaration

I declare that this thesis is a presentation of original work and I am the sole author. This work has not previously been presented for an award at this, or any other, University. All sources are acknowledged as references.

Chapter 2 has been adapted from the following paper, where Luis Neves ran the instrument on a day-to-day basis. Martyn Ward and I wrote the script processing the data. Matthew Rowlinson ran the back-trajectory analysis. Beth Nelson developed the photolytic converter setup. Chris Reed and Katie Read have both been in charge of running the instrument prior to me starting my PhD. I performed the data analysis while discussing the results with the coauthors.

Andersen, S. T., Carpenter, L. J., Nelson, B. S., Neves, L., Read, K. A., Reed, C., Ward, M., Rowlinson, M. J., and Lee, J. D.: Long-term NO_x measurements in the remote marine tropical troposphere, *Atmos. Meas. Tech.*, 14, 3071–3085, https://doi.org/10.5194/amt-14-3071-2021, 2021.

Chapters 3 and 4 have been written as manuscript drafts, where multiple co-authors have contributed with measurements and model output, which I have used in the data analysis presented here.

Chapter 1

Introduction

1.1 Motivation

Atmospheric nitrogen oxides play a key role in tropospheric chemistry. They help to control the abundance of the two most important oxidants in the atmosphere, ozone (O_3) and the hydroxyl radical (OH) as well as causing acid rain through wet deposition. O_3 is most commonly known to the general public for its role in the stratosphere, where it protects all living creatures on Earth from ultraviolet radiation, however, the role of O_3 in the troposphere, which is the air we breathe, is less well known. Tropospheric O_3 is the main precursor for OH radicals, which are also known as the 'detergent of the atmosphere', and at high concentrations can also be a competitive direct oxidant of some volatile organic compounds (VOCs). Ozone is also an important air pollutant, causing a variety of respiratory diseases [1] and damage to plants in the form of reduced photosynthesis, visible injury and lowered quality [2]. The global burden of disease project estimated that long-term ground level O_3 exposure accounted for 365,000 premature deaths in 2019, which is approximately 5.5% of all premature deaths due to air pollution [3]. The relative yield loss of wheat, rice, maize, and soybean due to exposure to O_3 levels above 40 parts per billion by volume (ppbV) during the growing season has been estimated to

be 11.45–19.74%, 7.59–9.29%, 0.07–3.35%, and 6.51–9.92%, respectively, from 2010 to 2017 in China alone [4].

It has been shown by model studies that intercontinental transport of air pollution contributes to the O_3 concentration observed in other countries and continents, making it a global problem [5]. While O_3 production depends on emissions in urban and rural regions, approximately 80% of Earth's surface is either covered by oceans ($\sim$70%), glaciers ($\sim$3%), or barren land ($\sim$5.5%, e.g. desert, rocks, and beaches) [6] making it necessary to understand all the reaction mechanisms in the remote atmosphere leading to O_3 production and depletion to be able to evaluate O_3 policy goals in the future. The tropical marine boundary layer (MBL) is particularly important due to the high photochemical activity in the region, which has a high impact on the atmospheric lifetime and concentration of compounds such as methane (CH_4) [7] and O_3 [8]. However, due to a limited amount of measurements in the remote tropical MBL there is still significant uncertainty in the sources, sinks and cycling of nitrogen oxides, which are crucial for modelling O_3.

1.2 The Atmosphere

The atmosphere is divided into 5 layers based on the temperature gradient; the troposphere ($\sim$0-12 km), stratosphere ($\sim$12-50 km), mesosphere ($\sim$50-85 km), thermosphere ($\sim$85-600 km), and exosphere ($\sim$600-10,000 km). In the troposphere the temperature decreases with increasing altitude due to most of the heat being generated close to the surface of the Earth. As an air parcel heats up close to the surface it rises and as the pressure drops, the parcel expands and cools down. Increasing temperature with increasing altitude is observed in the stratosphere due to the ozone layer absorbing ultraviolet radiation. Where the troposphere and the stratosphere meet is called the tropopause. Approximately 99% of the atmospheric mass is located in the troposphere (85-90%) [9, 10] and the stratosphere ($\sim$10%) [9]. The tro-

posphere can be divided into two subcategories; the planetary boundary layer (PBL) and the free troposphere, where the PBL is defined as the layer directly affected by Earth's surface [11]. Local meteorology determines the height of the PBL ($\sim$0.8-3.0 km during the day) through turbulence caused by wind crossing land and the heating and cooling of the Earth's surface [11, 12]. As the temperature of water is not affected as quickly as the temperature of the ground, the height of the MBL varies a lot less over water [13].

Around 78% of the atmosphere consists of nitrogen molecules (N_2), 21% are oxygen molecules (O_2), and the last approximately 1% is a mixture of noble gases, trace gases (e.g. VOCs, O_3, CO_2), and particles. The concentration of trace gases and the composition of particles vary depending on where they are sampled due to the proximity to direct emission sources, and on transport and chemical processes occurring in the atmosphere. From the point a trace gas is emitted, it takes approximately a day to be well-mixed within the PBL above the emission source, a week to cross into the free troposphere, 2 weeks to be well-mixed along the same latitude, 1-2 months to be well-mixed within the hemisphere, months to reach the tropopause, roughly a year to cross equator, and around 10 years to cross the tropopause (see Figure 1.1 for summary) [9]. The different mixing times are caused by a combination of air moving from high to low pressure, the Coriolis force, convection, and gravity. Trace gases with short atmospheric lifetimes (hours-weeks) such as nitrogen oxides and many alkenes will therefore be removed from the atmosphere through oxidation processes and deposition before being well-mixed in the atmosphere. Gases with longer lifetimes (years) such as CO_2 and CH_4 will be mixed through transport, however, the concentrations observed in the southern hemisphere will be lower than the simultaneous measurements in the northern hemisphere due to higher emissions in the northern hemisphere.

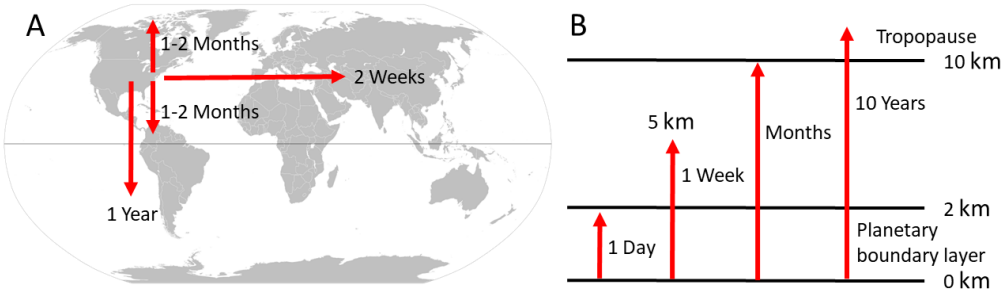

Figure 1.1: Panel A and B show the time scales of horizontal and vertical mixing in the troposphere, respectively. Based on figures in Jacob (1999).

1.3 Background Chemistry

1.3.1 Chemical Families

Chemical families describe a group of compounds, which have similar properties. In the atmosphere families can be used to describe a group of compounds which rapidly interconverts between each other. An example could be nitrogen oxides (NO_x) which is a combination of NO, NO_2, NO_3, NO_4, N_2O_4, and N_2O_5, however, NO_x is usually only defined as NO+NO_2 due to the very low ambient concentrations of the other nitrogen oxides. From here on NO_x is used to describe NO+NO_2. All other reactive nitrogen species than NO_x, which can also be called NO_x reservoir species are defined as NO_z (NO_3, NO_4, N_2O_4, N_2O_5, HONO, peroxy acetyl nitrate (PAN), particulate nitrate, organic nitrates etc.). The combination of NO_x and NO_z is defined as NO_y.

Other examples of chemical families in the atmosphere are O_x (O + O_3) and HO_x (H + OH + HO_2).

1.3.2 Ozone

Reactions (R1.1-R1.5) describe the dominant production and destruction mechanisms of O_3 occurring in the stratosphere also known as the Chapman cycle [14]. It has later been shown that O_3 is also destroyed by catalytic nitrogen

oxide and halogen cycles [15,16] leading to the formation of the ozone hole [17].

$$O_2 + h\nu(<242\,\text{nm}) \longrightarrow 2\,O(^3P) \tag{R1.1}$$

$$O(^3P) + O_2 + M \longrightarrow O_3 + M \tag{R1.2}$$

$$O_3 + h\nu(<310\,\text{nm}) \longrightarrow O(^1D) + O_2 \tag{R1.3}$$

$$O(^1D) + M \longrightarrow O(^3P) \tag{R1.4}$$

$$O(^3P) + O_3 \longrightarrow 2\,O_2 \tag{R1.5}$$

Stratospheric ozone is transported to the troposphere through stratosphere-troposphere transport (STT) events. STT has been estimated to account for $\sim 4.6\%$ of the boundary layer (0-1 km) O_3, $\sim 15\%$ of the lower tropospheric O_3 (1-3 km), and $\sim 26\%$ of upper tropospheric O_3 (3-8 km) in America [18]. In the troposphere, photolysis of molecular oxygen is not possible since all solar radiation below 290 nm is absorbed in the stratosphere by oxygen and ozone. Tropospheric ozone is instead produced through photolysis of NO_2. Photolysis of NO_2 produces NO and $O(^3P)$, which rapidly reacts with O_2 to return O_3, however, O_3 oxidises NO into NO_2 creating a null-cycle as shown in reactions (R1.6-R1.8).

$$NO + O_3 \longrightarrow NO_2 + O_2 \tag{R1.6}$$

$$NO_2 + h\nu(\leq 410\,\text{nm}) \longrightarrow NO + O(^3P) \tag{R1.7}$$

$$O(^3P) + O_2 + M \longrightarrow O_3 + M \tag{R1.8}$$

A photostationary state between NO, NO_2, and O_3 is reached within minutes if it is not perturbed by other processes. To have a net production of O_3 other oxidants are necessary to convert NO into NO_2 such as peroxy radicals (RO_2, HO_2) as described in reactions (R1.9-R1.10) as described in details in

Chapter 3.

$$RO_2 + NO \longrightarrow RO + NO_2 \quad \text{(R1.9)}$$

$$HO_2 + NO \longrightarrow OH + NO_2 \quad \text{(R1.10)}$$

Reaction (R1.10) also offers a route to the OH radical, above its primary production via O_3 photolysis (reactions R1.3 and R1.11). Even though 99% of the atmosphere consists of N_2 and O_2, up towards 20% of $O(^1D)$ in the MBL reacts with H_2O instead of relaxing to the ground state $O(^3P)$ (Reaction R1.12) due to the reaction coefficient for $O(^1D)$+H_2O being an order of magnitude higher than the quenching [19]. If the NO_x mixing ratio is sufficiently low, then peroxy radicals react with themselves instead of NO, and O_3 depleting reactions dominate over O_3 production [20].

$$O_3 + h\nu(\leq 335\,\text{nm}) \longrightarrow O(^1D) + O_2 \quad \text{(R1.3)}$$

$$O(^1D) + H_2O \longrightarrow 2\,OH \quad \text{(R1.11)}$$

$$O(^1D) + M \longrightarrow O(^3P) \quad \text{(R1.12)}$$

$$OH + O_3 \longrightarrow HO_2 + O_2 \quad \text{(R1.13)}$$

$$HO_2 + O_3 \longrightarrow OH + 2\,O_2 \quad \text{(R1.14)}$$

$$RO_2 + RO_2 \longrightarrow 2\,RO + O_2 \quad \text{(R1.15)}$$

From the reaction mechanisms of O_3 it is evident that whether net O_3 production or destruction occurs depend on the availability of NO_x and peroxy radicals. NO_x mixing ratios below 10-30 parts per trillion by volume (pptV) are generally sufficiently low for net O_3 loss [20–22]. These conditions have previously been reported to apply most of the year in the remote Atlantic Ocean [23]. The availability of peroxy radicals depend on their precursors and photochemical activity. In the remote MBL, the dominant precursors are carbon monoxide (CO) and CH_4, which are oxidised to hydroperoxy (HO_2) and methyl peroxy (CH_3O_2) radicals by OH radicals (reaction R1.16-R1.17),

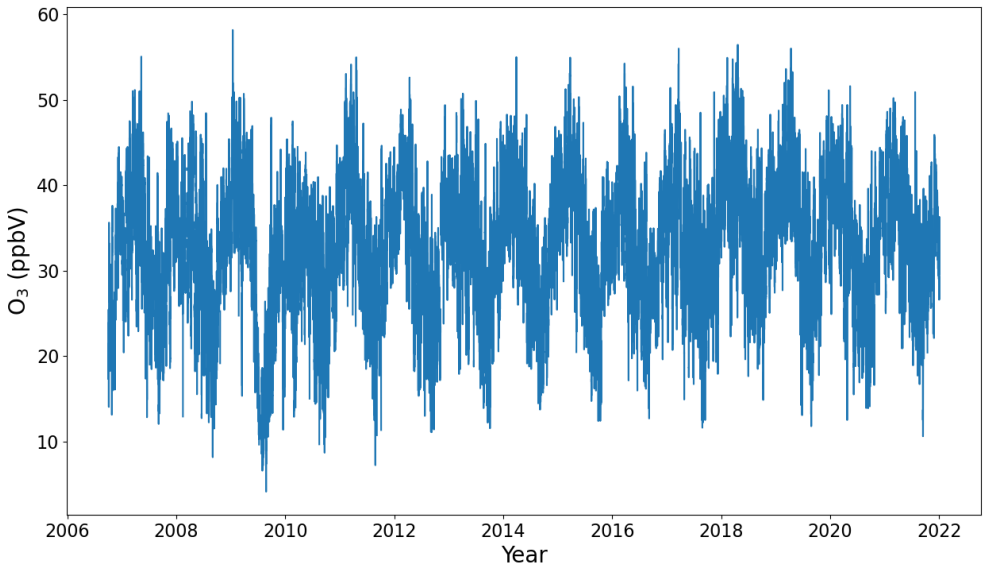

Figure 1.2: Ozone measured at the Cape Verde Atmospheric Observatory from 2006 to 2022.

respectively.

$$CO + OH \xrightarrow{O_2} HO_2 + CO_2 \tag{R1.16}$$

$$CH_4 + OH \xrightarrow{O_2} CH_3O_2 + H_2O \tag{R1.17}$$

Sicard (2021) [24] showed that on average the O_3 mixing ratio in urban and background environments have increased by 0.31 and 0.15 ppbV y^{-1} since 1990, respectively, where a decrease of 0.23 ppbV y^{-1} has been observed in rural areas. The increase/decrease observed is not evenly distributed over each year. This can be observed from the measured O_3 at the Cape Verde Atmospheric Observatory (CVAO) in Figure 1.2 where a clear increase in the yearly minimum O_3 mixing ratios is seen from 2011 to 2015 whereafter they stabilise.

1.3.3 Nitrogen Oxides

NO_x is naturally emitted from lightning [25], wild fires [26] and microbial activities in soil [27], but the dominant sources are anthropogenic in the form of combustion of fossil fuels and biomass burning [28] leading to mixing ratios of >100 ppbV in extremely polluted areas [29–32]. In a recent study, Miyazaki et al. (2017) [33] estimated NO_x produced from lightning to be 5.8 Tg N y^{-1} based on a 10-year mean from satellite observations. This is in good agreement with previous estimates of 5 ± 3 [25], 6.1 ± 0.46 [34], 3.3-5.9 [35], and 6.3 ± 1.4 Tg N y^{-1} [36]. Emissions from soil are associated with high uncertainties due to variable emissions depending on the microbes present and the fact that up to approximately half of the soil emissions are adsorbed onto the plants before reaching the canopy [27, 37]. Early studies estimated the global NO_x emissions from soil to vary from 5.5 Tg N y^{-1} [37] to 13 Tg N y^{-1} [27] above the canopy when attempting to take loss on the canopy into account. Some recent studies [33, 34, 38] derive approximately the same NO_x emissions from soils as Yienger and Levy II (1995) [37], however, they use the parameterization developed by Yienger and Levy II (1995) [37]. Recent studies using updated emission inventories for different types of soil or satellite measurements derive higher emissions of 8.9 [38], 7.9 [33], and 12.5 Tg N y^{-1} [39]. Estimates of NO_x emissions from biomass burning have been relatively constant over the past 25 years varying from 4.3-6.7 Tg N y^{-1} [28,33,34,38,40]. While estimates of biomass burning emissions have remained stable, emissions from fossil fuel combustion/anthropogenic sources have increased from 21.3 Tg N y^{-1} in the 1980's [41] to 25.5 Tg N y^{-1} in 2000 [38] and 28.7 Tg N y^{-1} averaged across 2005-2014 [33]. Minor contributions to the global NO_x budget come from aircrafts (0.5-0.6) [28, 33], ammonia oxidation (0.24-1.17) [42], and stratospheric injection (Total NO_y is 0.5 Tg N y^{-1}, however, only 0.1 Tg N y^{-1} as NO_x) [38, 40].

In remote regions where emission sources are limited, NO_x has been mea-

sured to be as low as a few pptV [23, 43, 44]. The sources of NO_x in remote oceanic regions have traditionally been attributed to long-range transport of peroxyacetyl nitrate (PAN) from polluted regions [45], oceanic emissions of alkyl nitrates [46] and shipping in marine environments [47].

NO_x is removed from the atmosphere through a combination of chemical and physical processes as described below. The most dominant removal processes are oxidation of NO_2 and NO by OH and HO_2 into nitric acid (HNO_3, reaction R1.18 and R1.19), respectively [35]. Assuming a temperature and pressure of 298 K and 1 hPa, respectively, and [OH] = 6×10^6 molecule cm^{-3} as previously observed in the remote MBL [48] gives a lifetime of NO_x of ~ 4.7 hours through this reaction [49], however, OH radicals are only present at that level at midday. At night time, when there is no photochemical production of NO and OH, NO_2 reacts with O_3 forming nitrate radicals (NO_3) (reaction R1.20). The reaction also occurs during the day, however, NO_3 radicals are rapidly photolysed back to NO_2. The NO_3 radical can react with NO_2 to form N_2O_5 (reaction R1.21), which is transformed into HNO_3 through hydrolysis on aerosols (reaction R1.22) [50].

$$NO_2 + OH \longrightarrow HNO_3 \quad \text{(R1.18)}$$

$$NO + HO_2 \longrightarrow HNO_3 \quad \text{(R1.19)}$$

$$NO_2 + O_3 \longrightarrow NO_3 + O_2 \quad \text{(R1.20)}$$

$$NO_2 + NO_3 \longrightarrow N_2O_5 \quad \text{(R1.21)}$$

$$N_2O_5 + H_2O \longrightarrow 2HNO_3 \quad \text{(R1.22)}$$

HNO_3 isconsidered a NO_x reservoir specie since it can be photolysed back to NO_2, however, the photolysis lifetime of HNO_3 is relatively long (~ 16.5 days using $jHNO_3(g) = 7 \times 10^{-7}$ s^{-1} (solar angle $\theta = 0°$) [51]) compared to the atmospheric removal through dry and wet deposition. Formation of nitric acid (HNO_3) has therefore traditionally been seen as a sink of NO_x, however,

recent studies suggest that photolysis of particulate nitrate (pNO_3^-) could be an important missing source of NO_x in the remote marine environment [44, 51, 52] as discussed in chapter 4.

The NO_3 radical is also a strong oxidant, and can react with a variety of different VOCs through primarily addition to alkenes forming organic nitrates [53], but also via hydrogen abstraction [54].

Organic nitrates can also be produced from acyl peroxy radicals reacting with NO_2. The formation of PAN is an example of this reaction (reaction R1.23-R1.25), where acetone is photolysed in the presence of O_2, followed by reaction with NO_2 instead of NO. PAN and other thermally labile peroxy nitrates are formed in polluted regions and transported at high altitudes to remote regions, where they thermally decompose back to peroxy radicals and NO_2 (reaction R1.26).

$$CH_3(O)CH_3 + h\nu \longrightarrow CH_3(O) + CH_3 \quad \text{(R1.23)}$$

$$CH_3(O) + O_2 \longrightarrow CH_3(O)O_2 \quad \text{(R1.24)}$$

$$CH_3(O)O_2 + NO_2 \longrightarrow CH_3(O)O_2NO_2\ \text{(PAN)} \quad \text{(R1.25)}$$

$$CH_3(O)O_2NO_2 \xrightarrow{\Delta} CH_3(O)O_2 + NO_2 \quad \text{(R1.26)}$$

Whether the formation of all organic nitrates serves as a permanent or a temporary NO_x sink is still uncertain [55]. While isoprene is readily oxidised by NO_3 at night to organic nitrates [56, 57], carbonyl nitrates have been found to be rapidly photolysed and thereby recycle NO_x in the morning [58, 59]. High yields of organic nitrates and secondary organic aerosols (SOA) have been observed from NO_3 oxidation of terpenes [60–63], however, recent studies have shown that organic nitrates in aerosols can behave as both a permanent sink or a reservoir of NO_x depending on the nature of the terpene and the relative humidity [60, 64].

Besides the removal of NO_x through oxidation to HNO_3, N_2O_5 hydrolysis on aerosols, and the formation of organic nitrates, NO_x is also lost through dry

deposition of NO_2 and NO_3 radicals reacting with aldehydes and dimethylsulphide ($(CH_3)_2S$) to form HNO_3 [35]. NO additionally react with OH to give nitrous acid (HONO), however, with a photolytic lifetime of approximately 12 minutes in the tropical MBL (see chapter 4), it is not considered a permanent sink for NO_x. Direct HONO emissions such as vehicle exhaust, wildfires and soils [65–67] are an important source of the hydroxyl radical (OH) [44,51,66–73] together with the photolysis of O_3 as described in reactions R1.3-R1.11.

1.4 Summary

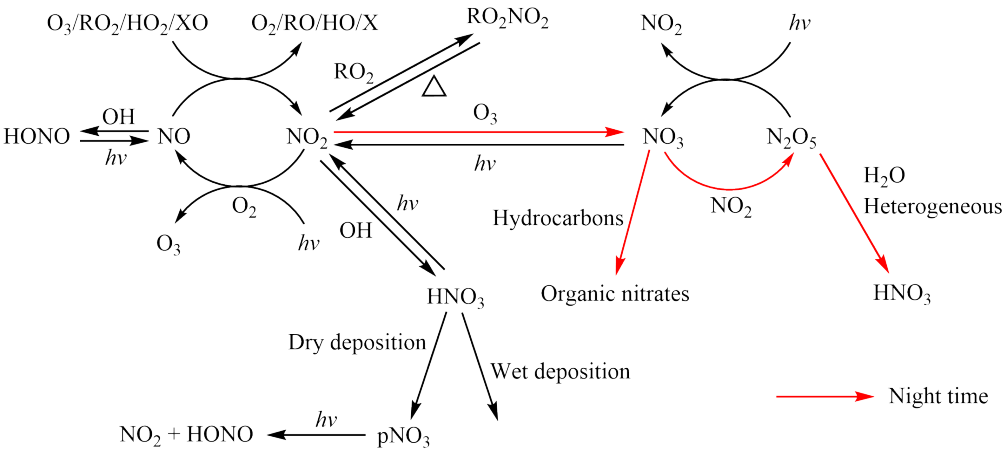

Figure 1.3: Reaction scheme of known NO_x chemistry.

O_3 production is controlled by the emissions of NO_x and VOCs, however, due to atmospheric transport the resulting O_3 pollution is not necessarily observed at the same place as the emissions. It is therefore crucial to understand all the chemistry related to O_3 production and destruction in different environments to be able to predict the outcome of reductions in NO_x and VOCs. Figure 1.3 summarises known NO_x chemistry. To be able to get a better understanding of the individual processes related to NO_x photochemical recycling and loss processes, and to investigate any unknown sources, it is necessary to investigate them away from direct emission sources. The remote MBL is an ideal location for such studies, as illustrated by Figure 1.4, which shows

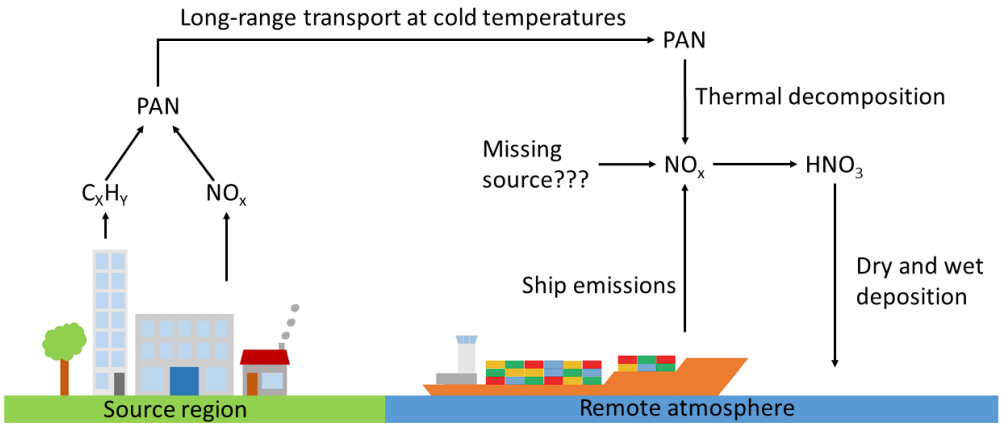

Figure 1.4: A simple summary of the known sources and sinks of NO_x in the remote MBL.

the known sources and sinks of NO_x in the remote MBL. Additionally, due to the relatively fast mixing within the boundary layer ($\sim$ 1 day), measurements made in the MBL are usually representative of a wide-ranging area.

1.5 Aims

It has been shown above that the availability of NO_x plays a key role in whether a region is O_3 producing or depleting. It is therefore crucial to understand the sources and sinks of NO_x as well as the chemical cycling of NO_x in the atmosphere. The aim of this thesis is, therefore, to improve our understanding of the atmospheric chemistry of NO_x in the remote MBL. This is achieved by:

- Evaluation of a new photolytic NO_2 converter for accurate NO_x measurements in the remote MBL at the Cape Verde Atmospheric Observatory (CVAO; 16° 51' N, 24° 52' W). Having reliable measurements is crucial to be able to investigate the chemical reactions occurring in the atmosphere, however, remote measurements of NO_x are subject to several challenges as described in chapter 2.

- Using NO_x, O_3, and VOC measurements at the Cape Verde Atmospheric Observatory to investigate fundamental oxidation chemistry using the

photostationary state of NO and NO_2. This can be used to evaluate our current understanding of NO_x cycling through oxidation by peroxy radicals and O_3 and thereby give an indication of the O_3 producing capacity of the MBL.

- Investigating new sources of NO_x using airborne and ground-based measurements of NO_x, HONO, aerosol surface area, and particulate nitrate (pNO_3^-). If models does not include all the significant sources and sinks of NO_x in the atmosphere, then they will be over-/underestimating NO_x, which could have an impact on other compounds such as O_3 and OH.

1.6 Thesis Outline

Chapter 2 briefly describes different techniques used to measure NO_x before describing the NO_x instrument deployed at the CVAO in detail. A year of NO_2 measurements conducted using two different photolytic converters, a traditional blue light converter (BLC) and a new photolytic converter (PLC), are compared to evaluate the reliability of the measurements. The measurements described have been published as a peer-reviewed article in *Atmospheric Measurement Techniques* (AMT).

Chapter 3 uses measurements of NO_x, O_3, VOCs, and photolysis rates from the CVAO to investigate the photostationary state equilibrium of NO and NO_2 in the remote MBL. Peroxy radicals are explored as a possible missing oxidant in air masses containing small amounts of aged pollution.

Chapter 4 uses airborne and ground-based measurements of HONO, NO_x, aerosol surface area, and particulate nitrate (pNO_3^-) to investigate missing sources of HONO in the tropical troposphere, in the CVAO region. NO_2 uptake on aerosols and photolysis of pNO_3^- on ambient aerosols are both explored.

Chapter 5 summarises the results and conclusions from the previous three chapters and discusses improvements to the measurements that could be useful

in the future.

Chapter 2

Long-term NO_x Measurements in the Remote Marine Tropical Troposphere

This chapter has been adapted from the following published article:

Andersen, S. T., Carpenter, L. J., Nelson, B. S., Neves, L., Read, K. A., Reed, C., Ward, M., Rowlinson, M. J., and Lee, J. D.: Long-term NO_x measurements in the remote marine tropical troposphere, *Atmos. Meas. Tech.*, 14, 3071–3085, https://doi.org/10.5194/amt-14-3071-2021, 2021.

Luis Neves runs the instrument on a day-to-day basis. Martyn Ward (University of York) and I wrote the script processing the data. Matthew Rowlinson (University of York) ran the back-trajectory analysis. Beth Nelson (University of York) developed the photolytic converter setup. Chris Reed (FAAM) and Katie Read (University of York) have both been in charge of the instrument prior to me starting my PhD. I performed the data analysis while discussing the results with the co-authors. All data analysis involving the new photolytic converter was developed by me.

2.1 Introduction

Long-term remote atmospheric nitrogen oxides, NO_x (NO + NO_2), measurements are rare due to the difficulty measuring very low (parts per trillion by volume (pptV)) mixing ratios. This is caused by low sensitivities of the instruments meaning higher mixing ratios of NO_x are needed to create a response significantly above the background. Low sensitivities usually result in a high limit of detection (LOD), which is the lowest mixing ratio that can be detected by the instrument. A variety of remote and *in-situ* techniques for measuring NO_x are available and summarised in Table 2.1, however, very few have the LOD and sensitivity needed to measure NO_x in remote regions and are suitable to run at remote sites. Some of the available techniques for measuring atmospheric NO_x are briefly described below.

Differential Optical Absorption Spectroscopy (DOAS) utilises the Beer-Lambert law where an absorption spectrum of the sample is compared to a reference spectrum over a specific range of wavelengths [75]. When measuring atmospheric trace gases, either direct sunlight or a light source with a known path length is used to estimate the apparent column denisty (ACD) of a given compound. Nitrogen monoxide, NO, can be observed in the deep UV at 186-227 nm [90, 91] and nitrogen dioxide, NO_2, using visible light at 435-470 nm [92, 93].

Both Fourier-Transform Infrared spectroscopy (FTIR) and Non-Dispersive Infrared spectroscopy (NDIR) are designed based on molecules absorbing infrared electro-magnetic radiation at specific absorption energies. Each molecule that absorbs infrared radiation has a specific absorption pattern like a fingerprint, however, when in the atmosphere multiple molecules can absorb in the same region causing spectral interferences [94]. Both methods can be used to measure NO at 1876 cm^{-1}, however, the absorption energy of water vapour (1595 cm^{-1}) interferes with the absorption energy of NO_2 (1617 cm^{-1}) and NO_2 can therefore not be measured quantitatively by FTIR and NDIR.

Table 2.1 Summary of remote and *in situ* measurement techniques for NO and NO_2.

	Compound Measured (NO/NO_2)	Limit of Detection (Averaging time)	Known challenges with the technique for remote measurements	Reference for the technique
Remote Techniques				
Differential Optical Absorption Spectroscopy (DOAS)	NO NO_2	1-2 ppbV[a] [74] <200 pptV[b] [76]	Measuring reference spectra	[75]
Fourier-Transform Infrared spectroscopy (FTIR)	NO			
Non-Dispersive Infrared spectroscopy (NDIR)	NO			
***In-situ* Techniques**				
Cavity Ring-Down Spectroscopy (CRDS)	NO NO_2	0.7 ppbV (8 sec) [77] 40 pptV (1 sec) [79]		[78]
Cavity Attenuated Phase Shift (CAPS)	NO_2	<60 pptV [80]		[81]
Laser-Induced Fluorescence (LIF)	NO NO_2	1.0 pptV (1 sec) [82] <4 pptV (1 min) [84]	Alignment of laser	[83]
NO Chemiluminescence	NO NO_2	1.0 ± 0.9 pptV (10 min)[c] 2.2 ± 2.7 pptV (10 min)[c]	Artefacts	[85]
Fast gas chromatography luminol chemiluminescence detection	NO_2	15 pptV (1 min) [86]		[86]
Tunable Infrared Laser Differential Absorption Spectroscopy (TILDAS)	NO_2	30 pptV (1 min) [87]	Cooling of detectors and lasers using liquid nitrogen Interferences	[88]
Matrix Isolation with Electron Spin Resonance Detection (MIESR)	NO_2	20 pptV (16 scans) [89]	Cryogenic trapping of the sample in a cold finger	[89]

[a]With a path length of 200 m. [b]With a path length of 5 km. [c]Determined in this study for hourly averaged data (2σ), however, the zero data used is only 10 minutes of measurements of the hour.

In Cavity Ring-Down Spectroscopy (CRDS) a laser is used to illuminate an optical cavity with a reflective mirror in each end and a detector in the opposite end of the laser [78]. Light slowly "leaks out" of the cavity and when the laser is turned off the decay in the light intensity can be detected. If there are light absorbing molecules in the cavity the light intensity drops faster than without them, which can be used to determine the concentration of the given compound in the cavity. NO has been measured using a laser with an output at 5.26 µm [77,95], where NO_2 has been measured using lasers with output at 405 nm [96] and 532 nm [79]. Cavity Attenuated Phase Shift (CAPS) works similarly to CRDS with an optical cavity with reflective mirrors in each end, but instead of measuring an intensity decay a phase shift is measured [81]. This can be accomplished by using a modulated continuous light source (430 nm light emitting diode (LED)) creating a sine or square wave which when detected will shift depending on how much absorber is present in the cavity [81].

In Laser Induced Fluorescence (LIF) spectroscopy molecules are excited by a laser to an excited state which emits light when returning to ground state which can in turn be detected [83]. NO has been excited using a 215 nm laser [82], where NO_2 can either be excited at 532 nm [97,98] or 585 nm [84,99].

When aqueous luminol (5-amino-2,3-dihydro-1,4-phthalazinedione) reacts with gas-phase NO_2 it creates chemiluminescence with maximum output at 425 nm [100], which can be detected using a photomultiplier tube (PMT). This technique has been shown to have a limit of detection around 50 pptV [100], however, it also has an artefact due to luminol reacting with O_3 and different alkyl nitrates such as peroxyacetyl nitrate (PAN) [101]. To separate NO_2 from the artefact, a new technique was invented; Fast gas chromatography luminol chemiluminescence detection, where NO_2 and PAN are separated by gas chromatography before reacting with luminol [86], which lowered the LOD to $\sim$15 pptV.

In Tunable Infrared Laser Differential Absorption Spectroscopy (TILDAS) an infrared laser beam is split in two, where one passes through a reference

cell with a high concentration of the compound in question to lock the beam on the correct wavelength and to locate the absorption lines to use in the measurements [88]. The second beam passes through the sample cell, where it is reflected back and forth using mirrors before exiting the cell to the detector, where the measured spectrum can be compared to that of the reference cell [88]. To measure NO_2 the absorption lines at 1593.3 cm^{-1} have been used even though water vapour has an absorption line at 1593.13 cm^{-1} [87]. Li et al. (2004) also observed an unknown interfering absorption line when taking the instrument in the field [87]. It is possible to use the lines at 1593.3 cm^{-1} in TILDAS since the infrared laser used in the instrument has such a narrow beam compared to the light source in FTIR and NDIR.

Matrix Isolation with Electron Spin Resonance Detection (MIESR) consists of trapping NO_2 cryogenically in an ice matrix using liquid nitrogen followed by laboratory determination by Electron Spin Resonance (ESR) detection [89]. ESR spectra are measured for each ambient sample and compared to reference spectra with different concentrations of NO_2 to determine the concentration in the sample.

The most widely used method and the one currently used at the Cape Verde Atmospheric Observatory (CVAO) is NO chemiluminescence, where NO in the presence of excess ozone is oxidized into excited state NO_2, which emits photons that can be detected [102]. NO_2 is generally converted into NO either catalytically by a heated molybdenum converter or photolytically, followed by NO chemiluminescence [103]. The molybdenum converter has historically been preferred due to its high conversion efficiency of at least 95%, but it also converts other reactive nitrogen species (NO_z) such as PAN, peroxymethacryloyl nitrate (MPAN) and other acyl peroxy nitrates (APN), HNO_3, p-HNO_3, HO_2NO_2, and HONO, potentially giving an overestimation of NO_2 [104–106]. Two separate studies have shown that a photolytic converter (PLC) with a wavelength of 385-395 nm have the smallest spectral overlap with interfering compounds compared to other commercially available photolytic sources [107, 108]. Reed

et al. (2016) [108] showed that in some configurations the PLC can heat up the sampled air making it possible for reactive nitrogen compounds such as PAN to decompose thermally and cause an overestimation of NO_2. This, however, causes only a negligible interference in warm regions such as Cabo Verde where PAN levels are extremely low [108] (measured to be <6 pptV in February 2020).

Several intercomparison studies of NO_x instruments have been performed over the years. NO is primarily measured using chemiluminescence or LIF, which have been compared during ground-based and aircraft campaigns [109–111]. During aircraft campaigns LIF and chemiluminescence have been shown to give comparable results from 20 to more than 100 pptV [109], which is in line with measurements on the ground where the two methods have been shown to agree within 17% for NO between 10 and 180 pptV [110]. Fehsenfeld et al. (1990) [112] compared a photolysis/chemiluminescence (PC), a TILDAS and a traditional luminol chemiluminescence instrument without a gas chromatograph in front for NO_2 measurements on the ground. All three methods agreed above 2 parts per billion by volume (ppbV) of NO_2, but interferences from PAN and O_3 could be observed in the luminol instrument below 2 ppbV. Down to the detection limit of the TILDAS the PC instrument and the TILDAS generally agreed. Gregory et al. (1990) [113] compared airborne NO_2 measurements below 200 pptV from a TILDAS, a PC, and a LIF instrument. All three techniques agreed within 30-40% when NO_2 was between 100 and 200 pptV, however, no good correlation was found below 50 pptV. In a more recent intercomparison by Bourgeois et al. (2022) [111] two NO techniques and three NO_2 techniques were compared when measuring biomass burning plumes. NO measurements were compared using a LIF and a chemiluminescence instrument, where the slope between the two instruments was 0.98 for 1 Hz data up to approximately 150 ppbV. The three techniques used to measure NO_2 during the intercomparison were chemiluminescence, LIF, and Cavity Enhanced Spectroscopy (CES). The LIF and CES measurements of NO_2 give comparable

values for measurements up to roughly 150 ppbV with a slope of 1.03, however, chemiluminescence consistently measure approximately 10% higher than LIF and CES giving slopes of 0.88 and 0.90, respectively, for 1 Hz data. The typical artefacts in NO_2 chemiluminescence measurements (HONO and methyl peroxy nitrate) were investigated in the study as well as differences in flush time, but they were all eliminated as potential causes for the observed discrepancies.

In the remote marine boundary layer (MBL) NO_x is often measured to be a few pptV [23, 43, 44], making most of the techniques described above unsuitable except NO chemiluminescence and LIF. Other important factors when choosing a technique for long-term remote measurements are maintenance and stability of the instrument, which currently favours chemiluminescence instruments. In this chapter a NO_2 converter, similar to that presented by Pollack et al. (2010) [107], which has been implemented on a NO chemiluminescence instrument to measure NO_x at the CVAO is thoroughly described. The data analysis procedure is explained in detail and the first two years of results with the new converter are presented and compared to the data obtained using a different converter.

2.2 Experimental

2.2.1 Location

The CVAO (16° 51' N, 24° 52' W) is located on the north eastern coast of São Vicente, Cabo Verde. The air masses arriving at the CVAO predominately come from the northeast (>95% of all wind direction measurements, see Figure 2.1) and have travelled over the Atlantic Ocean for multiple days since their last exposure to anthropogenic emissions, with the potential exception of ship emissions [13, 114]. The UK Meteorological Office NAME dispersion model [115] has previously been used to investigate the origin of the air masses arriving at the CVAO, which have been shown to be very diverse; North Amer-

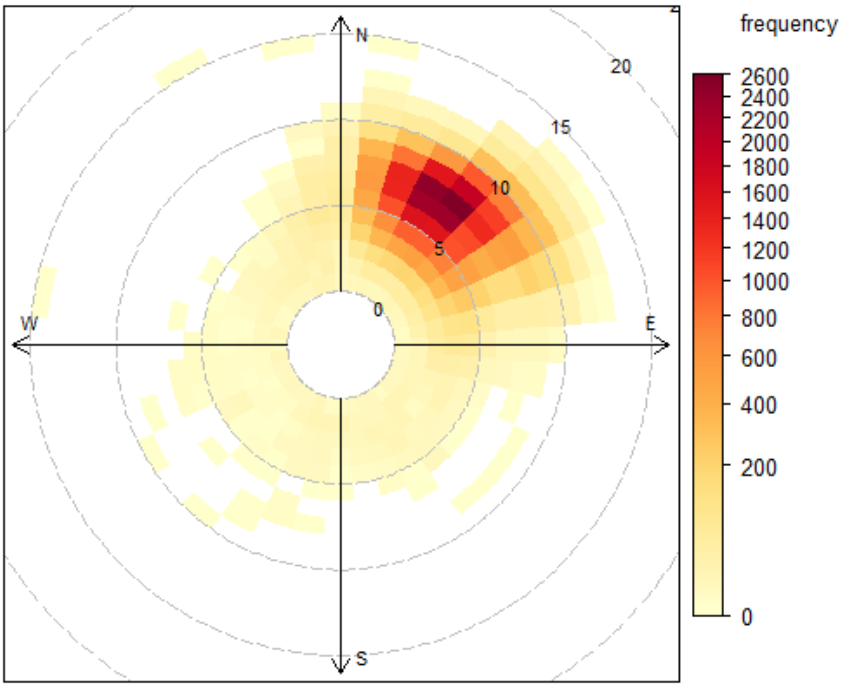

Figure 2.1: The frequency of hourly averaged wind speed and direction from January 2014 to August 2019. Each square symbolises 10 degrees of wind direction and 1 m s^{-1} wind speed. Each dashed circle shows an increase in wind speed of 5 m s^{-1}.

ica, the Atlantic, Europe, Arctic, and African regions [23]. During the spring and summer, the air masses predominantly originate from the Atlantic making it possible to investigate long-term remote marine tropospheric background measurements. During the winter, the CVAO receives air mainly from the Sahara, resulting in very high wintertime dust loadings [116–118]. The time zone of Cabo Verde is UTC-1. A full description of the CVAO site and associated measurements is given in Carpenter et al. (2010).

2.2.2 Measurement Technique

NO_x has been measured at the CVAO since 2006 using a NO_x chemiluminescence instrument manufactured by Air Quality Design Inc. (AQD), USA. The chemiluminescence technique involves the oxidation of NO by excess O_3 to excited NO_2 (R2.1) [102,119,120]. The excited NO_2 molecules can be deactivated

by emitting photons (R2.2) or by being quenched by other molecules (R2.3) such as N_2, O_2, and in particular H_2O. The emitted photons are detected by a PMT, which gives a signal linearly proportional to the mixing ratio of NO sampled. The measurement of NO_x and NO_2 requires photolytic conversion of NO_2 to NO (R2.4) followed by NO chemiluminescence detection [103].

$$NO + O_3 \longrightarrow NO_2^* + O_2 \tag{R2.1}$$

$$NO_2^* \longrightarrow NO_2 + h\nu\,(>600\,\mathrm{nm}) \tag{R2.2}$$

$$NO_2^* + M \longrightarrow NO_2 + M \tag{R2.3}$$

$$NO_2 + h\nu\,(\leq 410\,\mathrm{nm}) \longrightarrow NO + O(^3P) \tag{R2.4}$$

Further details of the technique are documented in [23,44,85,102,114,121,122].

2.2.3 Instrumental Set-up

Ambient air is sampled from a downward facing inlet placed into the prevailing wind with a fitted hood 10 m above the ground. A centrifugal pump at a flow rate of ~ 750 litres per minute pulls the air into a 40 mm glass manifold resulting in a linear sample flow of 10 m s^{-1}, giving a residence time to the inlet of the NO_x instrument of 2.3 s. To reduce the humidity and aerosol concentration in the sampled air, dead-end traps are placed at the lowest point of the manifold inside and outside the laboratory. A Nafion dryer (PD-50T-12-MKR, Permapure) is used to additionally dry the sampled air, using a constant sheath flow of zero air (PAG 003, Eco Physics AG) that has been filtered through a Sofnofil (Molecular Products) and activated charcoal (Sigma Aldrich) trap (dewpoint -15°C). The air is sampled perpendicular to the manifold through a 47 mm polytetrafluoroethylene (PTFE) filter with a pore size of 1.2 µm. Aerosol filters are recommended for NO_x instruments by Global Atmosphere Watch (GAW) to avoid heterogeneous reactions on aerosols giving an artefact. Another reason to use aerosol filters in front of NO_x instruments is their ability

to remove HNO_3 from the air, which could also cause an artefact. Instrument artefacts are described in detail in section 2.2.4.4. No loss of NO_x is expected on the filter.

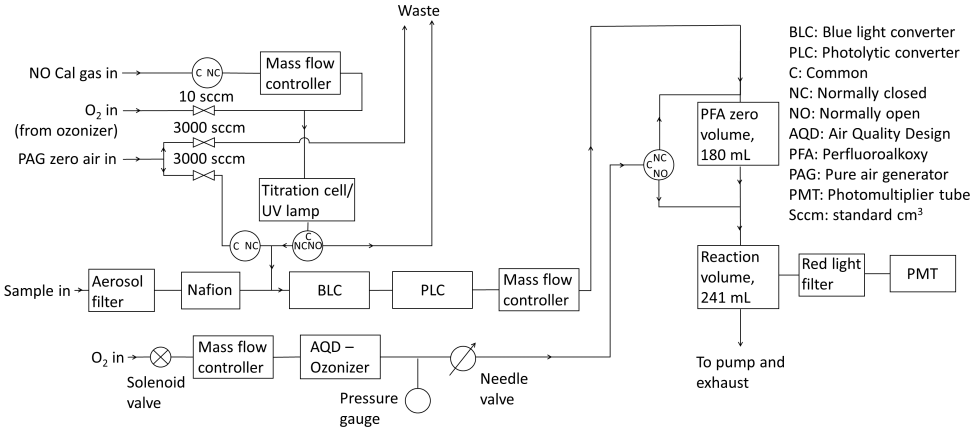

Figure 2.2: Flow diagram of the NO_x instrument at the CVAO.

A schematic diagram of the instrument is shown in Figure 2.2. Sampled air is passed through two different photolytic NO_2 converters, which are placed in series. The first is a commercial unit known as a blue light converter (BLC) supplied by AQD, as described in [123]. An ultra violet light emitting diode (UV-LED, 3 W, LED Engin, Inc.) array is placed in each end of a reaction chamber made of Teflon-like barium doped material (BLC, $\lambda = 385 \pm 10$ nm, volume = 16 cm^3). The entire block surrounding the reaction chamber is irradiated, giving the highest possible conversion efficiency of NO_2. Each array is cooled by a heat sink to maintain an approximately constant temperature inside of the converter when the diode arrays turn on. The second converter consists of two diodes (Hamamatsu Lightningcure L11921-500, $\lambda = 385 \pm 5$ nm) and a photolysis cell made of a quartz tube and two quartz windows glued to each end with a volume of 16 cm^3 (PLC) following the design of Pollack et al. (2010). Aluminium foil is wrapped around the quartz tube to increase the reflectivity to give the highest conversion efficiency of NO_2. The diodes are placed at each end of the quartz tube, as shown in Figure 2.3, without touching

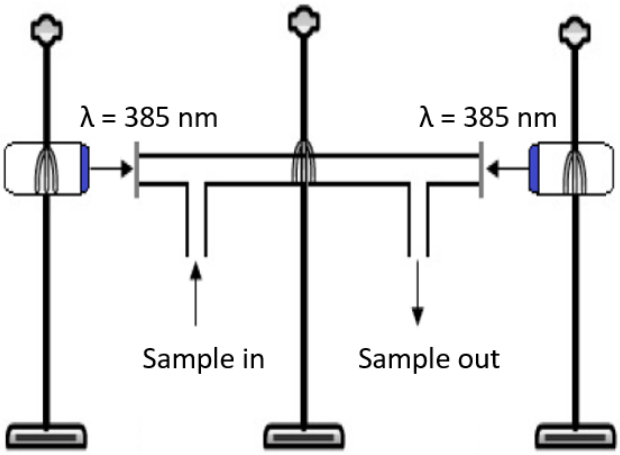

Figure 2.3: Diagram of the PLC (not to scale). The quartz tube (length = 20 cm, diameter = 1.0 cm, volume = 16 cm^3) is held in place by a clamp and clamp stand. Two Hamamatsu Lightningcure V3 diodes (λ = 385 nm) are positioned with the light source facing towards the tube, leaving approximately 2 mm distance between the diode and the glass window of the tube. Diodes are held in place with a clamp and clamp stand.

the windows to avoid increases in the temperature when the diodes turn on. BLCs have been used at the CVAO since the instrument was installed in 2006, with the most recent converter installed in April 2015 (a BLC2 model), where the wavelength was changed to 385 nm from 395 nm. The PLC was installed in March 2017. The air flow through the instrument is controlled at $\sim$1000 standard cubic centimeter per minute (sccm) by a mass flow controller (MKS, M100B) giving a residence time of 0.96 s through each of the converters.

To measure NO and NO_x (NO + NO_2 converted into NO) the air is introduced to the chemiluminescence detector (CLD), where NO is oxidized by excess O_3 into excited NO_2 in the reaction volume (241 mL, aluminium with gold coating [124]) shown in Figure 2.2. The reaction volume is kept at low pressure to minimize quenching of excited NO_2 and thereby maximize the NO chemiluminescence lifetime. The photons emitted from the excited NO_2 molecules when they relax to ground state are detected by the PMT (Hamamatsu R2257P) to give a signal for NO. NO_2 is converted into NO by turning on the BLC for 1 minute (irradiation time) followed by the PLC for 1 minute

(irradiation time), each period producing a signal due to NO + NO_2. The signal detected by the PMT (S_M) is caused by NO reacting with O_3 (S_{NO}), dark current from the thermionic emissions from the photocathode of the PMT (S_D), and an interference (S_I) which can be due to O_3-surface reactions that cause light emissions in the reaction cell, other reactions creating chemiluminescence, and from illumination of the chamber walls during NO_2 conversion [85, 108]:

$$S_M = S_{NO} + S_D + S_I \quad \text{(Eq. 2.1)}$$

The PMT is cooled to -30°C to reduce the dark current, giving the instrument a higher precision. Other molecules in the atmosphere such as alkenes also react with ozone and emit photons to reach their ground state, but at a different time-scale to that of NO_2 [125, 126]. This can give an interfering signal causing the NO and NO_x mixing ratios to be overestimated. Most of these reactions emit photons at 400-600 nm and are therefore filtered by a red transmission cut-off filter (Schott RG-610) placed in front of the PMT [125], however, ozonolysis of ethene produces hydrogen atoms, which can react with O_3 creating excited OH molecules that emit photons above 600 nm [127, 128]. The filter transmits photons with a wavelength higher than 600 nm [85]. A background measurement is therefore required to account for the dark current of the PMT, O_3-surface reactions, and for the remaining interfering reactions occurring at a different time-scale to that of NO_2. Background measurements are made by allowing ambient air to interact with O_3 in the zero volume (180 mL, PFA, Savillex, LLC) before reaching the reaction volume (Figure 2.2). Most excited NO_2 molecules will reach their ground state before the sample reaches the PMT, meaning the signal from NO will not be measured. The efficiency of the reaction between NO and O_3 in the zero volume is calculated from the calibration, as explained in section 2.2.4.3. Background measurements are performed every 5 minutes to take changing ambient conditions such as humidity into account, which affects both the signal from NO_2 and interference

reactions through quenching of excited molecules.

NO, NO_2 and the background signal are all detected on the same channel, and the instrument cycle is 1 min of background, 2 min of NO (when the NO_2 converters are off), 1 min of BLC NO_x (the BLC converter is on), and 1 min of PLC NO_x (the PLC is on).

2.2.4 Calibration

Prior to June 2019, calibrations were performed every 73 hours by standard addition in order to account for temperature and humidity changes in the ambient matrix. In June 2019 the calibration frequency was changed to every 61 hours to ensure that during any given month, calibrations are carried out for approximately equal periods during the night and the day. To calibrate the NO sensitivity, 8 sccm of 5 parts per million by volume (ppmV) NO calibration gas in nitrogen is added to the ambient air flow of $\sim$1000 sccm, giving an NO mixing ratio of approximately 40 ppbV. The mixing ratio used for calibrations are approximately 10,000 times that of the ambient measurements, however, due to reduced cylinder stability for lower NO mixing ratios it is difficult to calibrate at much lower mixing ratios and the chemiluminescence is expected to be linear across the range of expected mixing ratios [85]. The calibration gas is added between the PTFE filter and the NO_2 converter as shown in Figure 2.2. The conversion efficiency of the BLC and the PLC is calibrated by gas phase titration (GPT), where oxygen is added to the sampled NO calibration gas before entering the titration cell, which contains a UV lamp that converts oxygen to ozone. Between 60-80% of the NO calibration gas is oxidized into NO_2, giving a known mixing ratio of NO_2. A theoretical calibration sequence is shown in Figure 2.4. The first cycle is to calibrate the sensitivity and the second is to calibrate the NO_2 conversion efficiency. Each actual calibration includes three cycles of sensitivity calibration and two cycles of conversion efficiency calibration. The signal from NO_2 observed in the NO sensitivity

calibration is due to traces of NO_2 in the calibration gas. Figure C.1 shows the observed percentage of NO_2 in the calibration cylinders from January 2014 to August 2019 calculated from the measured sensitivity (sec. 2.2.4.1) and the conversion efficiency (CE) of the two converters (sec. 2.2.4.2):

$$\text{NO}_2 \text{ in cylinder (pptV)} = \frac{(\text{NO.c}_{(1)} - \text{NO}_{(1)})}{\text{Sensitivity} \times \text{CE}} \quad \text{(Eq. 2.2)}$$

$$\text{Percentage NO}_2 = \frac{\text{NO}_2 \text{ in cylinder}}{\text{NO}_2 \text{ in cylinder} + \text{NO cal conc.}} \quad \text{(Eq. 2.3)}$$

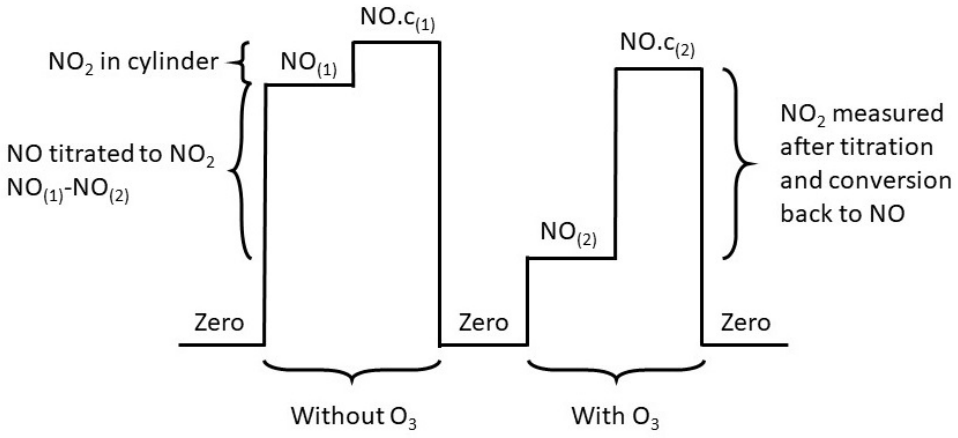

Figure 2.4: A theoretical calibration cycle. "NO" is the measurement of only NO i.e. when the converters are off, NO.c is when one of the converters are on therefore the measurement is NO + NO_2 and (1) and (2) represent untitrated and titrated NO, respectively.

The percentage is stable for both converters, however, the PLC shows approximately 3-4% NO_2 in the NO calibration gas compared to 5-10% for the BLC, which is caused by a BLC artefact (see section 2.2.4.4.2). The cylinders used were certified to $\leq$2% NO_2.

2.2.4.1 Sensitivity

The sensitivity of the instrument is calculated from the increase in counts per second caused by the calibration gas during NO calibration (untitrated, i.e. without O_3) and from the mixing ratio of the calibration gas as shown by

equation 2.4. The NO counts per second from the previous measurement cycle before the calibration is subtracted to give the increase due to the calibration gas. The previous cycle needs to be stable and low in NO to give an accurate sensitivity, which is the case at the CVAO.

$$\text{Sensitivity} = \frac{\text{Counts s}^{-1} \text{ during cal - Counts s}^{-1} \text{ in previous cycle}}{\text{NO cal conc.}} \tag{Eq. 2.4}$$

The sensitivity of the instrument depends on the pressure of the reaction chamber, the ozone mixing ratio in the reaction chamber, the flow of the sample through the reaction chamber, and the temperature of the reaction chamber. To maintain a stable sensitivity, all four parameters should be kept stable [129]. From January 2014 to August 2019 the sensitivity has varied between 2.7 and 7.4 counts s^{-1} $pptV^{-1}$ with changes of less than 5% between subsequent calibrations (see Figure C.2), unless the instrument has been turned off for a long period of time due to instrumental problems. As all the measured parameters that could affect the sensitivity has remained stable across the measurement period the most likely cause of the drop in sensitivity in 2016 is a drop in the ozone mixing ratio. The drop in sensitivity coincided with a power outage at the observatory, which could potentially have affected either the ozonizer or the power supply to the ozonizer. This theory is supported by an increase in sensitivity after the power supply was replaced in 2018.

2.2.4.2 Conversion Efficiencies

The conversion efficiency of the BLC and the PLC is calculated based on the titrated (with added O_3) and the untitrated (without added O_3) NO calibration gas as described in equation 2.5. The numerator gives how much of the NO is titrated into NO_2 and the denominator represents the NO_2 measured when taking the NO_2 content in the NO calibration gas into account. In equation 2.5, "NO" is the measurement of only NO i.e. when the converters are off,

"NO.c" is when one of the converters are on therefore the measurement is NO + NO_2 and (1) and (2) represent untitrated and titrated NO, respectively.

$$\mathrm{CE} = \frac{\text{Converted } NO_2 \text{ signal}}{\text{Amount of NO converted into } NO_2} = \frac{[(\mathrm{NO.c_{(2)}} - \mathrm{NO_{(2)}}) - (\mathrm{NO.c_{(1)}} - \mathrm{NO_{(1)}})]}{[\mathrm{NO_{(1)}} - \mathrm{NO_{(2)}}]} = 1 - \frac{\mathrm{NO.c_{(1)}} - \mathrm{NO.c_{(2)}}}{\mathrm{NO_{(1)}} - \mathrm{NO_{(2)}}} \quad \text{(Eq. 2.5)}$$

The CE of the BLC has varied from 82% to 91% between its installation in April 2015 and August 2019 ($jNO_2 \sim 3\ s^{-1}$). Prior to April 2015, an older generation BLC ($\lambda = 395$ nm) with a conversion efficiency of 30-35% was used ($jNO_2 \sim 0.5\ s^{-1}$). The conversion efficiency of the PLC has varied between 50% and 55% from its installation in March 2017 to August 2019 ($jNO_2 \sim 1\ s^{-1}$). See Figure C.3 for all the calculated conversion efficiencies.

2.2.4.3 Efficiency of the Zero Volume

Background measurements are made by reacting NO and interference compounds with O_3 in the zero volume (Figure 2.2). The system is set up so that NO_2 produced from NO will relax to the ground state before it is measured in the downstream reaction chamber, whereas it is assumed that any interfering compounds will emit photons when reaching the reaction chamber and be measured as a background signal [85, 129]. As mentioned above ozonolysis of ethene produces hydrogen atoms, which can react with O_3 in the sampling line to give excited OH radicals that fluoresce above 600 nm. With a fluorescence lifetime of ~ 2 ns [130] compared to ~ 55 µs [131] for NO_2, the produced OH radicals from ethene ozonolysis will not be measured in the background measurement. However, with ethene being <70 pptV 99% of the time and the ozonolysis reaction being slow compared to the residence time (lifetime of ethene at 60 ppbV of O_3 is ~ 5 days), the reaction is believed to give a negligible signal. If the zero volume is too small or the O_3 mixing ratio is too low, some untitrated NO may lead to NO_2 chemiluminescence within the reaction

chamber and the background will be overestimated. On the other hand, if the zero volume is too large, some of the interfering compounds may have relaxed to their ground state before the reaction chamber and the background signal will be underestimated. The residence time of the zero volume is 10.8 s compared to 14.5 s for the reaction volume. The efficiency of the zero volume can be calculated from the calibration cycle. The difference in background counts from before a calibration cycle to during the calibration cycle shows how much of the added NO from the calibration cylinder does not react with O_3 in the zero volume. By dividing this difference by the signal due to NO during the NO measurement of the calibration cycle, which is obtained by subtracting the NO measurement from the previous measurement cycle, the inefficiency of the zero volume is obtained. The efficiency is determined for each calibration cycle (Eq. 2.6) and plotted in Figure C.4. It is consistently above 98%.

$$\text{Efficiency}_{\text{ZV}} = 1 - \frac{\text{cal zero - measurement zero}}{\text{NO cal - previous NO cycle}} \qquad \text{(Eq. 2.6)}$$

2.2.4.4 Artefact Measurements

As described in section 2.2.3, NO_x measurements may have artefacts from chemiluminescence caused by interfering gas-phase reactions and/or from compounds produced by illumination of the reaction chamber walls as well as from pressure differences in the instrument [85, 108]. To estimate artefacts, it is necessary to measure the signal from NO_x-free air. The calibration sequence is followed by sampling NO_x-free air generated from a pure air generator (PAG 003, Eco Physics AG) for 30 minutes. According to the manufacturer, the PAG not only scrubs NO, NO_2 and NO_y from the ambient air but also SO_2, volatile organic compounds (VOCs), H_2O and O_3. Since the sensitivity of the instrument is dependent on the H_2O concentration due to enhanced NO_2^* quenching this could impact the artefact measurements. However, as the sampled ambient air is dried by a Nafion dryer the impact is expected to be small. An overflow of PAG air is introduced between the aerosol filter and the NO_2

converters as shown in Figure 2.2 and the cycle of background, NO, NO_x BLC, and NO_x PLC is used to estimate artefact NO and NO_2 measured by the instrument. The artefacts are estimated using the sensitivity and conversion efficiencies measured in ambient air, where humidity is expected to be higher. This could cause the artefacts to be either under- or overestimated.

2.2.4.4.1 NO Artefact

The NO artefact can be caused by two things; alkenes reacting with O_3 and giving chemiluminescence above 600 nm at approximately the same rate as NO_2 or a difference in pressure between the zero volume and the reaction volume. An artefact caused by alkenes will be positive and overestimate the NO mixing ratio, where an artefact due to a pressure difference can be either negative or positive. Interferences caused by alkenes have been evaluated by Alam et al. (2020) [125] to be negligible in urban environments (<1% of the NO measurement), where alkenes have been measured to be <2 ppbV. At the CVAO the 99^{th} percentile of the measured alkenes (ethene, propene, isoprene, and benzene) are all below 70 pptV and have slow rate coefficients with O_3 [125] suggesting it will also be negligible in the remote MBL. Fast reacting alkenes such as monoterpenes have not been measured and can therefore not be evaluated. The artefact can be estimated as the offset from 0 pptV when the mixing ratio sampled is 0 pptV. The NO mixing ratio is expected to be 0 pptV when sampling NO_x-free air or between 22.00 and 04.00 UTC at night. NO generated during the day is rapidly oxidized into NO_2 through reactions with O_3 and RO_2 after sunset. During the night, NO is not generated from photolysis of NO_2, and there are no significant local sources of NO at Cabo Verde when the air masses come from over the ocean (which is >95% of the time). The average NO mixing ratio between 22.00 and 04.00 UTC and the average NO mixing ratio from the PAG zero air tend to be very similar, with the PAG artefact (-3.7 ± 22.9 pptV (2σ), January 2014 – August 2019) generally lower than the night time artefact (0.4 ± 11.9 pptV (2σ), January 2014 –

August 2019). Time series of both NO artefact measurements can be found in Figure C.5. The night time NO artefact is used as it is measured more frequently, it contains the same ambient matrix with nothing scrubbed and to eliminate the possibility of residual NO influencing background measurements determined from the PAG. Additionally, none of the measured alkenes show a diurnal behaviour suggesting that if they were to cause a minor off-set in the NO measurements, it should be detected in the night time measurements. Since the PAG scrubs VOCs it will also not give an estimate of the artefacts caused by fast reacting alkenes.

2.2.4.4.2 NO_2 Artefact

NO_2 converters have previously been shown to have artefacts caused by thermal or photolytic conversion of reactive nitrogen compounds (NO_z) other than NO_2 as well as illumination of the chamber walls [85,108,132]. Fast reacting alkenes, which can cause overestimations of the NO mixing ratios, will not cause the NO_2 mixing ratio to be overestimated, since the raw NO signal is subtracted from the raw NO_x signal.

The spectral output of an NO_2 converter with a wavelength of 385 nm was compared to absorption cross sections of NO_2 and potential interfering species such as $BrONO_2$, HONO and NO_3 [108]. The photolytic converter was shown to have good spectral overlap with the NO_2 cross section with minimal spectral overlap with other NO_z species, except for a small overlap with the absorption cross section of HONO. The interference from $BrONO_2$, HONO and NO_3 have additionally been evaluated previously for a similar set-up using a Hg lamp [132]. At equal concentrations of NO_2 and NO_z species, $BrONO_2$ and NO_3 were estimated to maximum have an interference of 5% and 10%, respectively, using a lamp with a wider spectral overlap with the absorption cross sections of the interfering species than what is observed for the LEDs used at the CVAO [132] and therefore have a different flux of photons from the used lamps. At the CVAO, HONO levels have been measured to on average

peak at $\sim$5 pptV (at noon; see chapter 4). For the typical Gaussian output of a UV-LED this interference is calculated to be 2.0, 12.6, and 25.7% of the available HONO for UV-LEDs with principle outputs of 395, 385, and 365 nm respectively, resulting in a maximum interference of 0.63 pptV during peak daylight hours. Photolytic conversion of NO_z species is therefore not expected to be an important contributor to the NO_2 artefact at the CVAO due to the narrow spectral output of the LEDs (see sec. 3.2.1.1 for further discussion of photolytic artefacts).

Each converter is only on for 1 minute in a 5-minute cycle. For thermal conversion to be a major contributor to the artefact, the converter would have to increase in temperature during that one minute and not the rest of the cycle otherwise an increase in signal should be constant since the air continues to flow through the converters when they are turned off. Thermal decomposition of NO_z species is therefore not expected to have an effect in a climate like the one in Cabo Verde, where the sample temperatures are similar to the ambient temperatures (see sec. 3.2.1.1 for further discussion of thermal artefacts). The temperature increase of the sampled air has been measured for identical converters in the laboratory to be $\sim$1°C and $\sim$5°C for the PLC and the BLC, respectively.

It has been shown that the walls of a BLC made out of a porous Teflon-like doped block becomes contaminated from the ambient air over time, and when the walls are illuminated reactions take place on the surface causing an artefact [108, 132]. The BLC is similar to the one used by Reed et al. (2016) and it is therefore expected to have an artefact due to reactions taking place on the surface. The PLC is not expected to be contaminated in the same way as it does not have porous chamber walls. Ryerson et al. (2000) observed an increase in artefact over time when sampling ambient air for a similar PLC, however, this is not observed for the PLC in the very clean environment at the CVAO (0-10 pptV between August 2017 and August 2019, see below) and surface reactions are therefore expected to give a negligible artefact for the

PLC.

The total artefact can be determined by measuring the NO_2 signal when the NO_2 mixing ratio is 0 pptV, however, it is virtually impossible to scrub all NO_x from the ambient air and nothing else. To estimate the NO_2 artefact, PAG zero air is measured using both converters. The PLC measures between 0-10 pptV compared to 10-60 pptV using the BLC. Since, as discussed above, the NO_2 artefact of the PLC is assumed to be negligible (even though the photostationary state study in chapter 3 suggests an artefact of 0.7 pptV), the measurement of PAG zero air by the PLC is assumed to represent the remaining NO_2 in the zero air after scrubbing. If the PLC does have an artefact, then both NO_2 measurements will be overestimated by the amount of this artefact. The signal from the BLC when measuring PAG zero air is expected to be due to the illumination of the chamber walls in addition to the traces of NO_2 left in the zero air. The artefact due to wall reactions in the BLC can therefore be estimated by subtracting the signal measured by the PLC.

2.3 Data Analysis

Time periods with known problems such as maintenance on the manifold, ozone leaks, and periods when the PMT has not reached $< -28\,^{\circ}C$ are not included in the dataset. The mean and standard deviation of the zero (background), NO, NO_2 BLC and PLC are determined for each 5-minute measurement cycle. To avoid averaging over the time it takes the detector to change and stabilize between the different types of measurements, the last 50 seconds of the measurement cycle are used for the background and the NO counts, and the last 30 seconds for the BLC NO_x and the PLC NO_x counts. Each cycle is filtered based on the percentage standard deviations and differences in counts between subsequent cycles. If the standard deviation or the difference in counts are outside the mean $\pm$ 2σ (see Table 2.2) calculated from a 5-year period between 2014 and 2019, the cycle is not used for further analysis. This removes noisy

data as well as sharp spikes but keeps data with sustained increases lasting more than 5 minutes.

Table 2.2: Evaluation parameters of the measurements. When a measurement falls outside any of the intervals it will not be used for further data analysis. The mean ± xσ is calculated for 2014-2019 for the zero and NO measurements, and 2017-2019 for both NO_2 measurements.

Measurement	Standard deviation of a measurement cycle (mean ± 2σ, %)[a]	Difference in counts/s between subsequent cycles (mean ± 2σ)	Hourly mean ± 4σ (pptV)[b]	Difference between mean and median (mean ± 4σ, pptV)[c]
Zero	2.4 ± 1.7	-	-	-
NO	2.5 ± 10.6	0 ± 515	1.7 ± 47.9	0.2 ± 4.1
NO_2 BLC	2.5 ± 7.5	0 ± 1432	16.8 ± 175.2	1.5 ± 33.0
NO_2 PLC	2.1 ± 2.5	0 ± 738	17.3 ± 176.8	1.7 ± 33.0

[a]The percentage standard deviation for each measurement cycle is determined as the standard deviation of a cycle divided by the mean of the same cycle. [b]Extreme measurements are determined to be mixing ratios, which are outside the hourly mean ± 4 standard deviations of the hourly mixing ratio. [c]Extreme differences between the hourly mean and median of the mixing ratios are determined to be differences outside the hourly mean ± 4 standard deviations of the differences between the mean and median.

To obtain the signals due to NO and NO_2, the interpolated zero and NO measurements are subtracted from the NO and NO_x measurements, respectively. They are converted to a concentration by using the interpolated sensitivity and conversion efficiency as shown in equation 2.7 and 2.8:

$$\text{NO mixing ratio} = \frac{\text{NO measurement - Background measurement}}{\text{Sensitivity}} \quad \text{(Eq. 2.7)}$$

$$\text{NO}_2\text{ mixing ratio} = \frac{\text{NO}_x\text{ measurement - NO measurement}}{\text{Sensitivity} \times \text{CE}} \quad \text{(Eq. 2.8)}$$

The NO and NO_2 BLC concentrations are corrected by subtracting the interpolated artefacts described in sections 2.2.4.4.1 and 2.2.4.4.2. If the difference between two subsequent NO artefact measurements vary by more than the mean ± 2σ of the differences in NO artefacts determined from January

2014 – August 2019 (0.0 ± 6.2 pptV), the measurements made between are not used for further analysis due to a potential step change between the determinations.

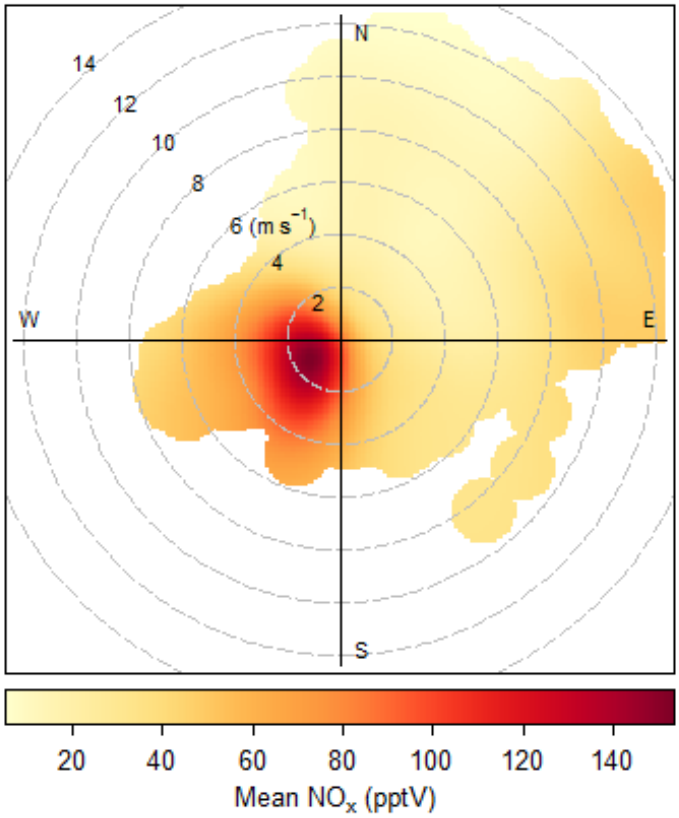

Figure 2.5: Total NO_x from June 2017 to August 2019 plotted as a function of wind speed and direction.

Hourly averages of all the measurements are determined. If data coverage during the hour is less than 50%, the hour is flagged and discarded from the data analysis. The hourly NO_x (NO + NO_2 PLC) concentrations between June 2017 and August 2019 are plotted as a function of wind speed and direction in Figure 2.5. It can be observed that the concentrations are enhanced at low wind speed and when the air crosses the island (from the southwest). Measurements made at a wind speed <2 m s^{-1} or from a wind direction 100-360° are, therefore, flagged as suspected of local contamination and are not used in the analysis. Extreme mixing ratios outside the mean ± 4σ of the 5-

year for NO and 2-year period for NO_2 are flagged as suspicious (see Table 2.2 for boundaries). Lastly, inconsistencies in the measurements such as differences outside the mean $\pm$ 4σ between the mean and median of a measurement (see Table 2.2 for boundaries) and differences between the two NO_2 measurements are flagged as suspicious (0.4 $\pm$ 32.2 pptV). The data remaining to analyse after these removals are 88% of the original NO and NO_2 BLC dataset and 83% of the NO_2 PLC dataset.

2.3.1 Corrections

As described above, excited NO_2 can be quenched by other sampled molecules, giving a lower observed mixing ratio than the real value. Water molecules are effective quenchers and therefore a correction is usually applied depending on the humidity in the instrument [133, 134]. However, since the calibrations at the CVAO are performed by standard addition, and a Nafion dryer is placed in front of the instrument, this is not necessary.

Additionally, NO can react with O_3 in the ambient air in the inlet and manifold giving an overestimation of NO_2 and an underestimation of NO due to the lack of NO_2 photolysis in the sampling line. To correct for this the following equations are used [135]:

$$[\mathrm{NO}]_0 = [\mathrm{NO}]_{\mathrm{E1}} \times \mathrm{e}^{k_{\mathrm{O3}} \times \mathrm{t}_{\mathrm{E1}}} \quad \text{(Eq. 2.9)}$$

$$[\mathrm{NO_2}]_0 = \left(\frac{k_{\mathrm{O3}} + j_{\mathrm{C}}}{j_{\mathrm{C}}}\right) \times \left(\frac{[\mathrm{NO}]_{\mathrm{E2}} - [\mathrm{NO}]_{\mathrm{E1}} \times \mathrm{e}^{-(k_{\mathrm{O3}} \times (\mathrm{t}_{\mathrm{C2}} - \mathrm{t}_{\mathrm{C1}}) + j_{\mathrm{C}} \times \mathrm{t}_{\mathrm{C2}})}}{1 - \mathrm{e}^{(-(k_{\mathrm{O3}} + j_{\mathrm{C}}) \times \mathrm{t}_{\mathrm{C2}})}}\right) - [\mathrm{NO}]_0 \quad \text{(Eq. 2.10)}$$

where $[\mathrm{NO}]_0$ is the corrected NO mixing ratio, $[\mathrm{NO}]_{\mathrm{E1}}$ is the uncorrected NO mixing ratio, $[\mathrm{NO_2}]_0$ is the corrected NO_2 mixing ratio, $[\mathrm{NO}]_{\mathrm{E2}}$ is the uncorrected NO mixing ratio when the converter is on, k_{O3} is the rate of the reaction

between NO and O_3 ($k(O_3+NO) \times [O_3] \times 10^{-9} \times M$), t_{E1} is the sum of the residence time from the inlet to the entry of the converter and the time the air is in the converter, t_{C1} and t_{C2} are the time the air is in the converter when the converter is on and off, respectively, and j_C is the photolysis rate inside the converter. The residence time from the inlet to the entry of the converter has been 2.3 s since 2015 and the time the air is in each of the converters is 0.96 s (with and without the converter on). The O_3 mixing ratio measured at the CVAO has varied between 5 and 60 ppbV (with an uncertainty of 0.07 ppbV) between 2014 and 2019. The ozone correction is calculated for each hour using a rate coefficient of 1.8×10^{-14} cm^3 $molecule^{-1}$ s^{-1} at 298K [19]. This gives an average O_3 correction $\pm$ 2σ of 6.8 $\pm$ 3.0%, 1.7 $\pm$ 11.0%, and 1.3 $\pm$ 7.1% for NO, NO_2 BLC, and NO_2 PLC, respectively, when the measured mixing ratio of NO or NO_2 is above 0.1 pptV (See Appendix A for an example of the calculation and a detailed derivation of Eq. 2.9 and 2.10). Thus, at the low mixing ratios of O_3 present at Cabo Verde and the short residence time for sampling, the corrections for O_3 are well within the noise of the measurements (see below), but are still included in the final calculated mixing ratios.

2.4 Uncertainty Analysis

To be able to evaluate the NO_x measurements made at the CVAO an extensive uncertainty analysis is performed. The uncertainty of a measurement is given as an interval at a confidence level, which describes how certain it is that the true value is within the interval. The interval can be determined from the spread of data, which can be described by several probability distributions. The most common are normal and rectangular distributions. A normal distribution is used when most of the measurements are centred around the mean. The signal-to-noise is reduced by approximately $1/\sqrt{\text{number of averaging points}}$ when averaging the measurements. The uncertainty in the mean of the measurements are estimated using equation 2.11.

To get an uncertainty at the 95 percent confidence interval 2 standard deviations (σ) are used. A rectangular distribution is when the probability of each measurement is equal. The 1σ uncertainty is estimated from the half-width of the distribution and the 2σ uncertainty is estimated from the full width of the distribution as shown in equation 2.12. The hourly precision and uncertainty of the instrument are estimated to characterize the uncertainties at the 95 percent confidence interval [136].

$$\text{Normal distrbution uncertainty (u)} = \frac{2\sigma}{\sqrt{\text{number of averaging points}}} \tag{Eq. 2.11}$$

$$\text{Rectangular distribution uncertainty} = \frac{\text{full width}}{\sqrt{3}} \tag{Eq. 2.12}$$

The hourly precision is estimated from the zero count variability, which is directly related to the photon-counting precision of the PMT. The hourly mean ($\overline{x}$) of the zero measurements is subtracted from each individual measurement of the respective hour ($x\text{-}\overline{x}$) to give hourly frequency distributions. Photon-counting frequency distributions are best described by a Poisson distribution, however, at high photon-counting rates they become indistinguishable from a Gaussian distribution [137]. With a yearly mean background count rate of 1400-3000 count s^{-1} between 2014 and 2019, the frequency distributions can be assumed as Gaussian. Examples of hourly frequency distributions can be observed in Figure 2.6. The standard deviation of each hourly frequency distribution is calculated and divided by the interpolated sensitivity to give a 2σ NO precision for 1 s data of 23.4 $\pm$ 20.3 pptV for the hours between January 2014 and August 2019. The 2σ NO precision for hourly averaged data is 1.0 $\pm$ 0.9 pptV. The hourly precisions reported here are in good agreement with the previously reported 1σ precision of 0.30 pptV [44] and the 2σ precision of 0.6-1.7 pptV [23] for the same instrument. The NO_2 precisions are determined by taking the conversion efficiency of the respective converters

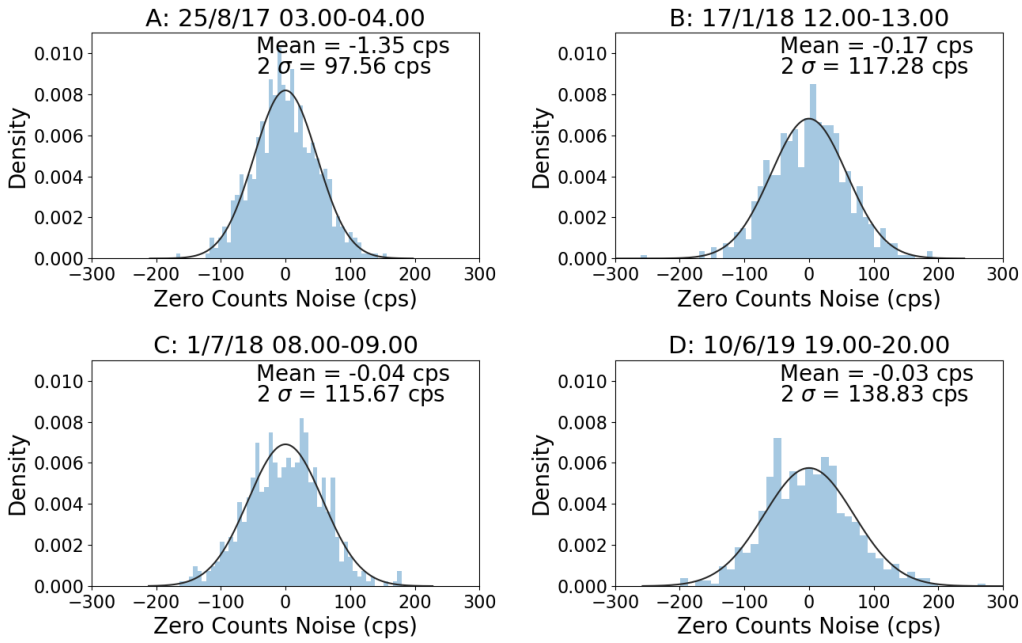

Figure 2.6: Examples of hourly frequency distributions of the calculated zero variability.

into account. The hourly 2σ NO_2 precision for hourly averaged data between March 2017 and August 2019 becomes 1.5 ± 0.8 pptV and 2.7 ± 2.2 pptV for the BLC and PLC, respectively. The determined NO_2 precisions are within the interval of previously reported precisions for the same instrument [23, 44]. The uncertainty of the hourly measurements is estimated by combining all the uncertainties associated with the measurements. This includes uncertainties in the calibrations, artefact determinations, and O_3 corrections as well as the precision of the instrument. The precision of the NO and NO_2 measurements are both included in the total uncertainty of the NO_2 measurements as the NO measurements are subtracted from the NO_2 measurements. Each term is converted into pptV to be able to combine them. All the uncertainties are combined using uncertainty propagation:

$$\text{Accuracy} = \sqrt{\text{Precision}^2 + \text{Artefact}^2 + \text{Calibration}^2 + \text{O}_3\ \text{Correction}^2} \quad \text{(Eq. 2.13)}$$

Uncertainty in the calibrations is caused by uncertainty in the flow of the calibration gas, the concentration of the calibration gas, the sensitivity and the conversion efficiency of the instrument as well as the drift in the sensitivity and conversion efficiency between each calibration. The total uncertainty in the calibrations is determined as the propagation of each term. Each term is calculated as a percentage to be able to combine them before converting the total calibration uncertainty to pptV to combine it with the other uncertainty terms. According to the manufacturers the sample and calibration mass flow controllers have an uncertainty of 1%, which has been confirmed by a gillibrator bubble flowmeter. The uncertainty of the concentration of the NO standard used for calibration is known to ±1% (British Oxygen Company (BOC), certified to UK National Physical Laboratory (NPL) standard) (BOC certifies that NO/N_2 standards are stable for 5 years). To estimate the uncertainty in the sensitivity and conversion efficiency, the uncertainties in each measurement used to determine them must be estimated. Equation 2.4 and 2.5 describe the calculation of the sensitivity and conversion efficiency of the instrument, respectively. The spread of each type of measurement used can be described by a normal distribution. The percentage uncertainty in the sensitivity and the conversion efficiency can therefore be determined by equation 2.14 and 2.15, respectively.

$$\text{Sensitivity uncertainty} = \frac{u_{NO_{(1)}}}{NO_{(1)}} \qquad \text{(Eq. 2.14)}$$

$$\text{CE uncertainty} = \sqrt{\left(\frac{u_{NO.c_{(1)}}}{NO.c_{(1)}}\right)^2 + \left(\frac{u_{NO.c_{(2)}}}{NO.c_{(2)}}\right)^2 + \left(\frac{u_{NO_{(1)}}}{NO_{(1)}}\right)^2 + \left(\frac{u_{NO_{(2)}}}{NO_{(2)}}\right)^2} \qquad \text{(Eq. 2.15)}$$

The drift between calibrations contains two terms; one for the sensitivity and one for the conversion efficiency when estimating the uncertainty for NO_2. Both terms are determined as the absolute difference between two measurements. The distribution is assumed to be rectangular as only two measure-

ments are known – each calibration. The differences are therefore divided by $\sqrt{3}$ to get the uncertainties. To get them as percentages they are divided by the last determined sensitivity and conversion efficiency, respectively. The total uncertainty in the calibration is estimated to be 2.78 ± 8.05 % for NO, 3.44 ± 9.32 % for NO_2 using the BLC, and 3.52 ± 8.67 % for NO_2 using the PLC for the calibrations between January 2014 and August 2019. The individual terms and final uncertainties in the calibrations are summarized in Table 2.3.

Table 2.3: Calculated uncertainties associated with the calibrations. The values in bold are the combined uncertainties for each type of measurement. Each uncertainty is given as the mean uncertainty ± 2 standard deviations of the calibration data between January 2014 and August 2019 for NO and from March 2017 to August 2019 for both NO_2 measurements.

Source of uncertainty	Probability distribution	Uncertainty (%)
Flow	Normal	1.00
Cal. gas concentration	Normal	1.00
Sensitivity	Normal	0.16 ± 0.11
Drift sensitivty	Rectangular	2.01 ± 8.45
CE BLC	Normal	0.44 ± 0.45
Drift CE BLC	Rectangular	1.24 ± 5.61
CE PLC	Normal	0.45 ± 0.39
Drift CE PLC	Rectangular	1.43 ± 4.86
Cal. uncertainty NO		**2.78 ± 8.05**
Cal. uncertainty NO_2 BLC		**3.44 ± 9.32**
Cal. uncertainty NO_2 PLC		**3.52 ± 8.67**

The NO artefact is determined every night using the measurements between 21.00-03.00 UTC-1 (local time). The uncertainty can be described by a normal distribution and the uncertainty is, therefore, estimated from the standard deviation and number of the measurements used to determine the artefact. The NO_2 artefact is determined from measurements of PAG Zero air every 61 hours, where only 3 measurements are used for the artefact. The uncertainty is assumed to be rectangular due to the low amount of measurements used. The difference between the highest and lowest of the PAG Zero measurements is used to get the full-width. As the BLC artefact is corrected using the

PLC measurement, the uncertainty in the correction is also determined in the same way and used in the propagation of uncertainties. The drift between the artefacts is estimated in the same way as the drift between the calibrations assuming a rectangular probability distribution. The total uncertainty in the NO and NO_2 BLC artefacts are estimated to be 1.1 ± 3.4 pptV and 7.2 ± 7.2 pptV, respectively. The individual terms and final uncertainties in the artefacts are summarized in Table 2.4.

Table 2.4: Calculated uncertainties associated with the artefact determinations. The values in bold are the combined uncertainties for each type of measurement. Each uncertainty is given as the mean uncertainty ± 2 standard deviations of the artefact data between January 2014 and August 2019 for NO and from March 2017 to August 2019 for both NO_2 measurements.

Source of uncertainty	Probability distribution	Uncertainty (pptV)
NO artefact	Normal	0.6 ± 1.1
Drift NO artefact	Rectangular	0.7 ± 3.4
NO artefact uncertainty		**1.1 ± 3.4**
NO_2 artefact	Rectangular	4.6 ± 5.6
NO_2 artefact correction	Rectangular	0.1 ± 1.6
Drift NO_2 artefact	Rectangular	3.0 ± 6.7
NO_2 artefact uncertainty		**7.2 ± 7.2**

Lastly, the uncertainty associated with correcting the measurements for O_3 reactions in the inlet is estimated from the uncertainties in the rate coefficient and the O_3 concentration. The rate coefficient used is 1.8×10^{-14} with an uncertainty of 20% at 298K, which has been evaluated based on 6 studies of the reaction [19]. The uncertainty in the O_3 concentration is ±0.07 ppbV. With measured concentrations in the range 5-60 ppbV, the uncertainty becomes 0.1-1.4%. The combined uncertainty using propagation of uncertainties, therefore, becomes 20 ± 0.001%.

The total hourly uncertainty for each of the three measurements are determined by combining all the uncertainties summarised in Table 2.5 using propagation of uncertainties as described in equation 2.13. The precisions are already calculated as hourly precisions in pptV. The calibration uncertainties

Table 2.5: Calculated uncertainties associated with the NO_x measurements. The values in bold are the combined uncertainties for each type of measurement. Each uncertainty is given as the mean uncertainty ± 2 standard deviations of the data between January 2014 and August 2019 for NO and from March 2017 to August 2019 for both NO_2 measurements.

Source of Uncertainty	Probability Distribution	Uncertainty (%)	Uncertainty (pptV)
Hourly precision/repeatability NO	Normal		1.0 ± 0.9
Hourly precision/repeatability NO_2 BLC	Normal		1.5 ± 0.9
Hourly precision/repeatability NO_2 PLC	Normal		2.7 ± 2.2
Total calibration uncertainty NO		2.78 ± 8.05	0.0 ± 0.3
Total calibration uncertainty NO_2 BLC		3.44 ± 9.32	0.3 ± 1.3
Total calibration uncertainty NO_2 PLC		3.52 ± 8.67	0.4 ± 1.3
Total NO artefact uncertainty			1.1 ± 3.4
Total NO_2 artefact uncertainty			7.2 ± 7.2
Hourly O_3 correction uncertainty NO	Normal	20.00 ± 0.001	0.3 ± 1.1
Hourly O_3 correction uncertainty NO_2 BLC	Normal	20.00 ± 0.001	2.5 ± 6.8
Hourly O_3 correction uncertainty NO_2 PLC	Normal	20.00 ± 0.001	2.6 ± 6.4
Total hourly uncertainty NO			**1.4 ± 1.5**
Total hourly uncertainty NO_2 BLC			**8.4 ± 7.5**
Total hourly uncertainty NO_2 PLC			**4.4 ± 5.8**

are interpolated between each calibration and multiplied by the hourly concentrations of NO and NO_2 to get hourly uncertainties in pptV. The artefact uncertainties are interpolated between each artefact determination. And the uncertainty due to ozone corrections are determined by multiplying the determined uncertainties in percentage with the hourly concentrations of NO and NO_2. The hourly uncertainties are determined to be 1.4 ± 1.5 pptV, 8.4 ± 7.5 pptV, and 4.4 ± 5.8 pptV for NO, NO_2 BLC, and NO_2 PLC, respectively. Approximately half of the PLC uncertainty is caused by a bias from the O_3 correction, however, both the NO and BLC measurement uncertainties are dominated by noise from the precision and artefact determinations.

2.5 Results: Example of Data

The first year of data (August 1st 2017 to July 31st 2018) is chosen as an example of the resulting NO and NO_2 datasets. October 2017, December 2017, and April 2018 are used to highlight the seasonality in the mixing ratios observed during a year of measurements. Panel A in Figure 2.7 and 2.8 show the full O_3 corrected time series for NO and NO_2, respectively. Panel B, C, and D in the two figures show the time series for the three chosen months and panel E, F, and G show the 3-hour rolling average diurnal cycles for the same months. Monthly diurnal cycles for NO and NO_2 for the entire year can be found in Figure D.1 and D.2, respectively.

Clear seasonality can be observed in the diurnal cycles of NO measurements with a maximum of $\sim$7.5 pptV in Winter and a minimum of $\sim$2 pptV in the spring and summer. This is in good agreement with that reported by Lee et al. (2009) [23], however, the seasonal diurnal cycles reported by Reed et al. (2017) [44] show less variability, which can be explained by interannual variation in the air masses arriving at the CVAO. The two NO_2 measurements are in general in good agreement when looking at the time series in Figure 2.8. Offsets of up to 10 pptV between the two measurements can be seen over

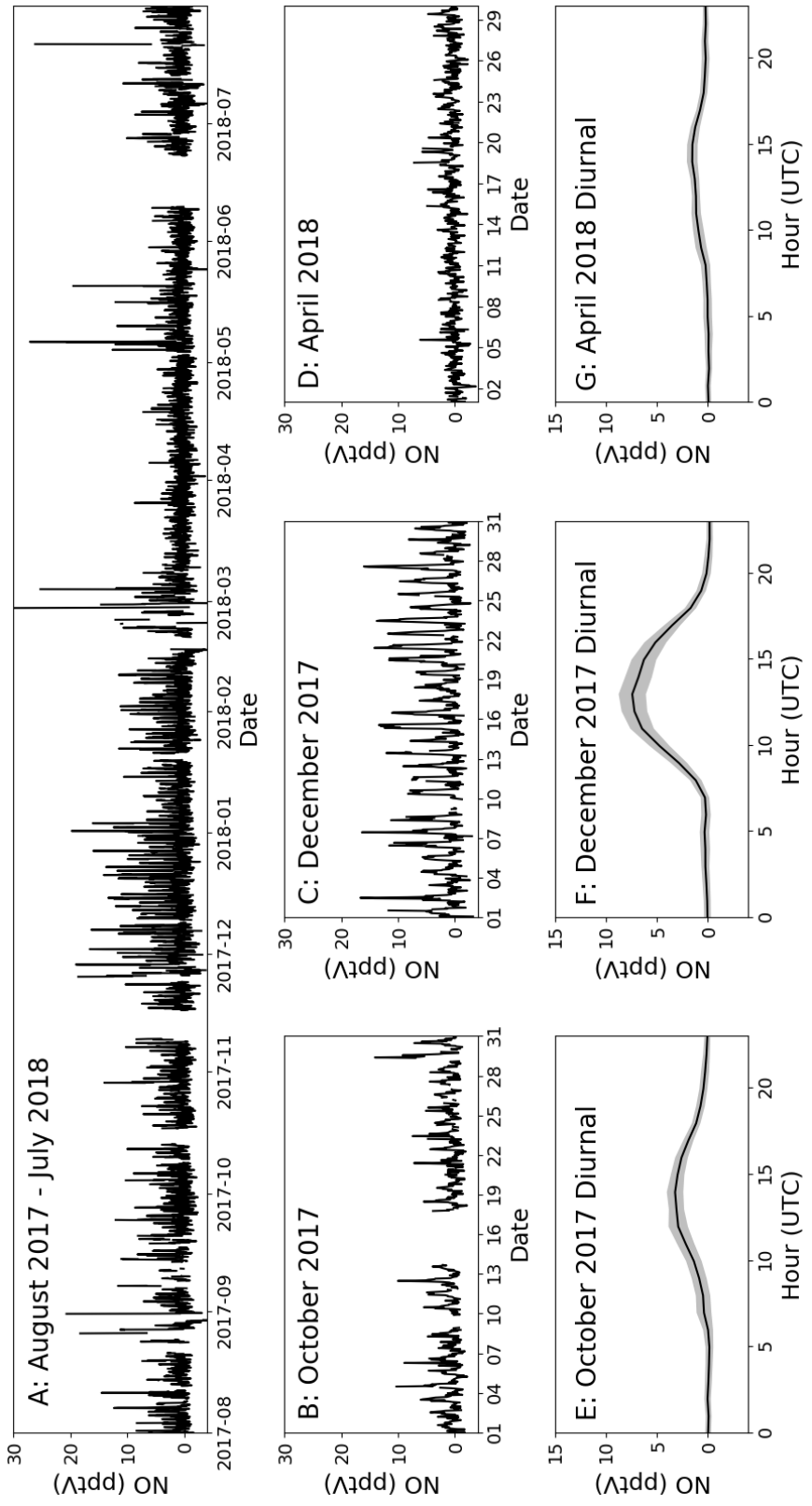

Figure 2.7: Panel A show the time series for filtered O_3 corrected NO from August 1st 2017 to July 31st 2018. Panel B, C and D zoom in on October 2017, December 2017 and April 2018, respectively. Panel E, F and G show the average diurnal cycle of NO for October 2017, December 2017 and April 2018, respectively, with the coloured areas being ± 2 standard errors. If there are less than 15 measurements available for the hour, it is not included in the diurnal.

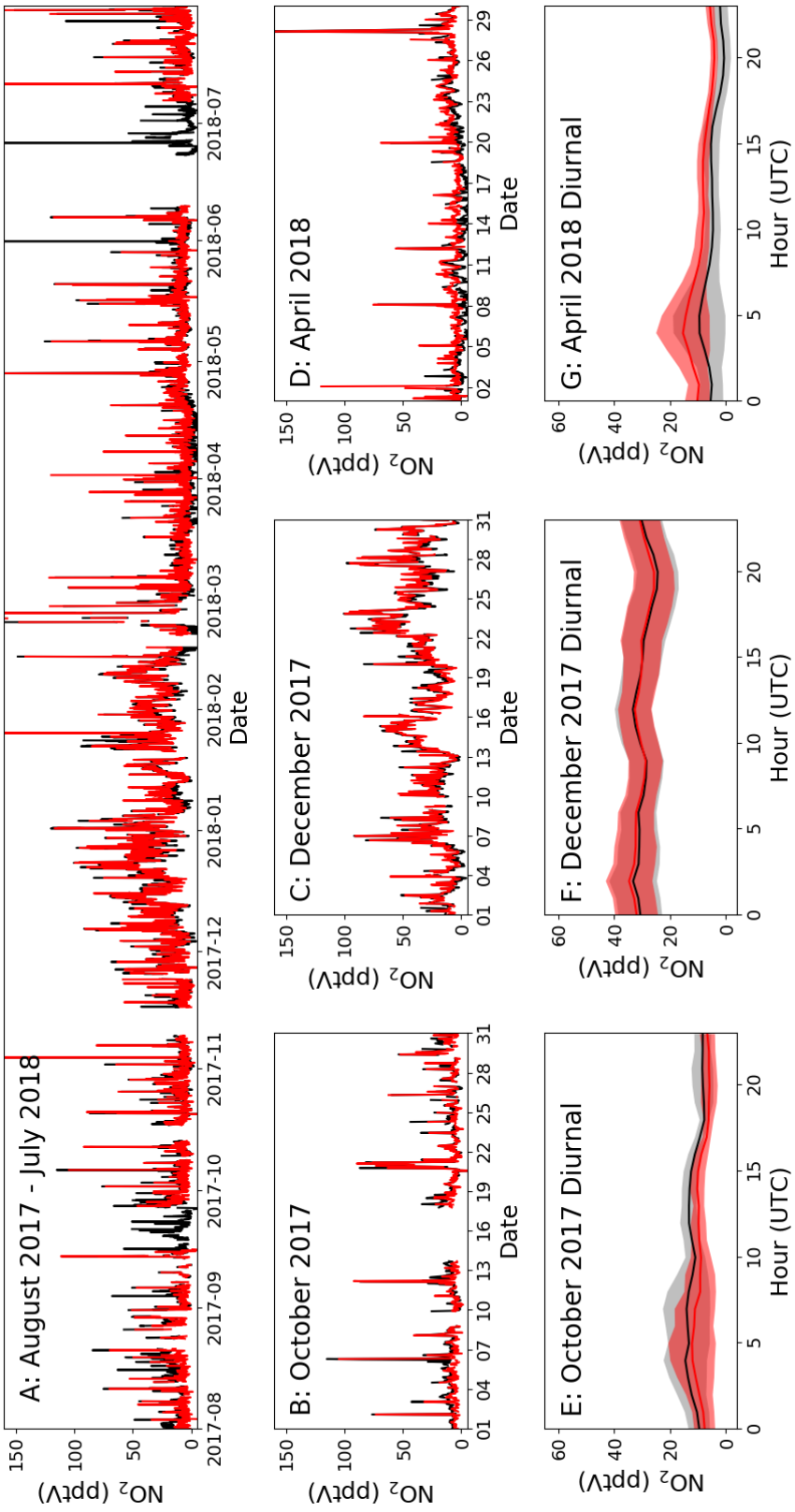

Figure 2.8: Panel A show the time series of filtered O_3 corrected NO_2 from August 1st 2017 to July 31st 2018 for the BLC (black) and PLC (red). Panel B, C and D zoom in on October 2017, December 2017 and April 2018, respectively, with the red line being the PLC and the black being the BLC. Panel E, F and G show the average diurnal cycle of NO_2 for October 2017, December 2017 and April 2018, respectively, with the red line being the PLC and the black being the BLC and the coloured areas being ± 2 standard errors. If there are less than 15 measurements available for the hour, it is not included in the diurnal.

some time periods (E.g. April, Panel D), which are most likely caused by the calculated BLC artefact for those periods either being too high or too low due to potential differences in the composition of the ambient and PAG air. This is supported by the diurnal cycles having the same shape, but with an offset. Monthly diurnal cycles of the two NO_2 measurements agree within 2 standard errors except in August 2017, where the offset between the two measurements is larger than for the remaining months. It is currently unknown why August 2017 differs from the other reported months. NO_2 would be expected to decrease during the day due to photolysis, however, the measurements show a fairly flat diurnal cycle for most months and a small increase in daytime NO_2 is even evident in some months. Reed et al. (2017) [44] reported more pronounced seasonal daytime increases in NO_2 at the CVAO in 2014-2015 than what is observed here, which was proposed to be caused by photolysis of particulate nitrate (see chapter 4 for further details). Spikes in the early morning are noticeable in the NO_2 diurnal cycles for July-November, which correspond to the months with an average lower wind speed than the rest of the year (the diurnal cycle for April also shows a spike, however, it is caused by data from one morning). These spikes could be caused by local fishing boats passing upwind of the observatory in the morning hours, which will give a more prominent spike at low wind speed. Monthly wind speed diurnal cycles can be found in Figure D.3. The good agreement between the two NO_2 measurements observed in Figure 2.8 can also be observed in Figure 2.9, where the two are plotted against each other. The data points are scattered around the 1:1 line shown in black. A linear least squares regression (with uncertainty in the BLC measurements) and an orthogonal distance regression (ODR) (with uncertainty in both measurements) are performed to evaluate the scatter of the data points between August 2017 and 2019. The resulting regression lines are displayed in red (BLC = 0.99 × PLC + 0.7 pptV) and blue (BLC = 1.08 × PLC – 0.6 pptV), respectively. The deviation in the slope from 1 for both regressions are consistent with the uncertainty in the measured NO_2 artefact

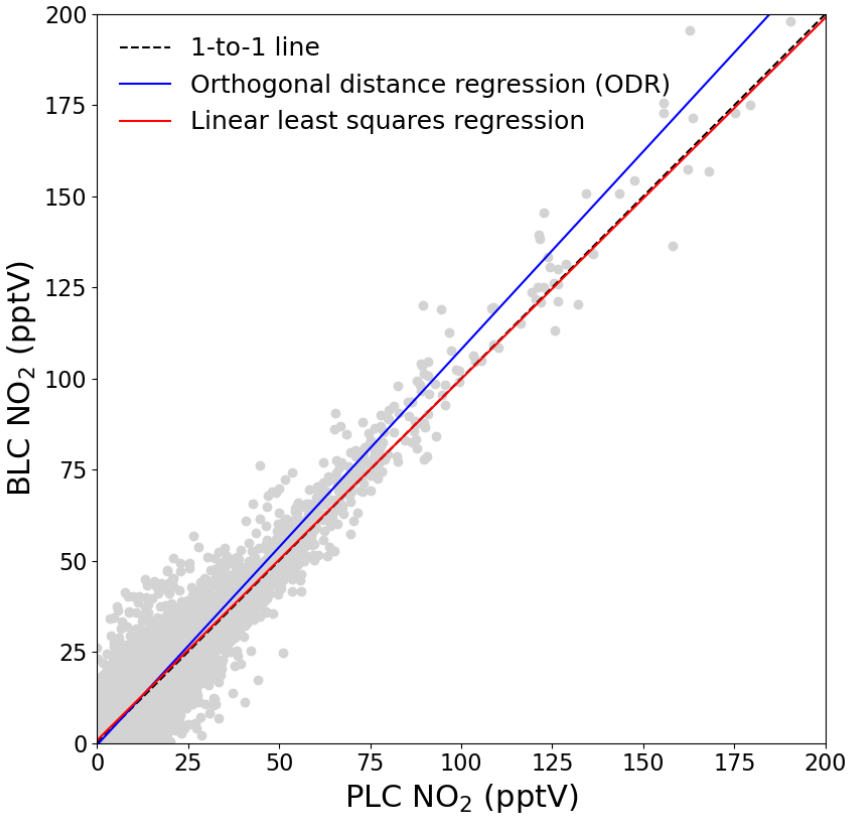

Figure 2.9: The BLC NO_2 mixing ratio is plotted against the PLC NO_2 mixing ratio. The black dashed line shows the 1-to-1 relationship. The red line is the linear least square regression of the hourly data with uncertainty in y and the blue line is the orthogonal distance regression with uncertainties in both the x and y.

which has been determined to be 7.2 ± 7.2 pptV.

The seasonality of the NO measurements can be explained by a combination of the variation of the origin of the air masses arriving at the CVAO, meteorology, photolysis rates, and seasonality of emissions. Back trajectories of the three months used as examples are shown in Figure 2.10. FLEXPART version 10.4 is used in backwards mode, driven by pressure level data from Global Forecast System (GFS) reanalyses at $0.5° \times 0.5°$ resolution [138, 139]. 10-day back-trajectory simulations are initialised every 6 hours, releasing 1000 particles from the CVAO site. Further information on FLEXPART can be found in Appendix B. During the winter maximum (December) the back-trajectories

indicate that the air reaching the CVAO is largely dominated by African air, compared to during the spring minimum (April), which is dominated by Atlantic marine air. Large west African cities such as Dakar and Nouakchott, and/or the shipping lanes to the east/northeast of Cabo Verde, are potential candidates for the source of elevated NO_x. The NO mixing ratios measured in October are higher than those in April and lower than in December. This may be due in part to the influence of polluted African air arriving at Cabo Verde, which is more prominent in October than in April, but less so than in December. The NO_2 and the total NO_x (NO + PLC NO_2, Figure 2.11) similarly show higher levels in December than April, but the mixing ratios observed in October are similar to those in April. It should be noted that some of the days with high percentages of African air have missing data or wind directions from other places than the north east.

From Table 2.6 it can be observed that the NO, NO_2, and NO_x measurements at the CVAO compare well to the few other measurements in the remote marine boundary layer as well as background sites in Alert, Canada and measurements in the free troposphere. A wintertime seasonal increase in NO, NO_2, and NO_x can be observed during December-February, which corresponds to the months when surface air masses arrive at Cabo Verde from western Africa [23, 114].

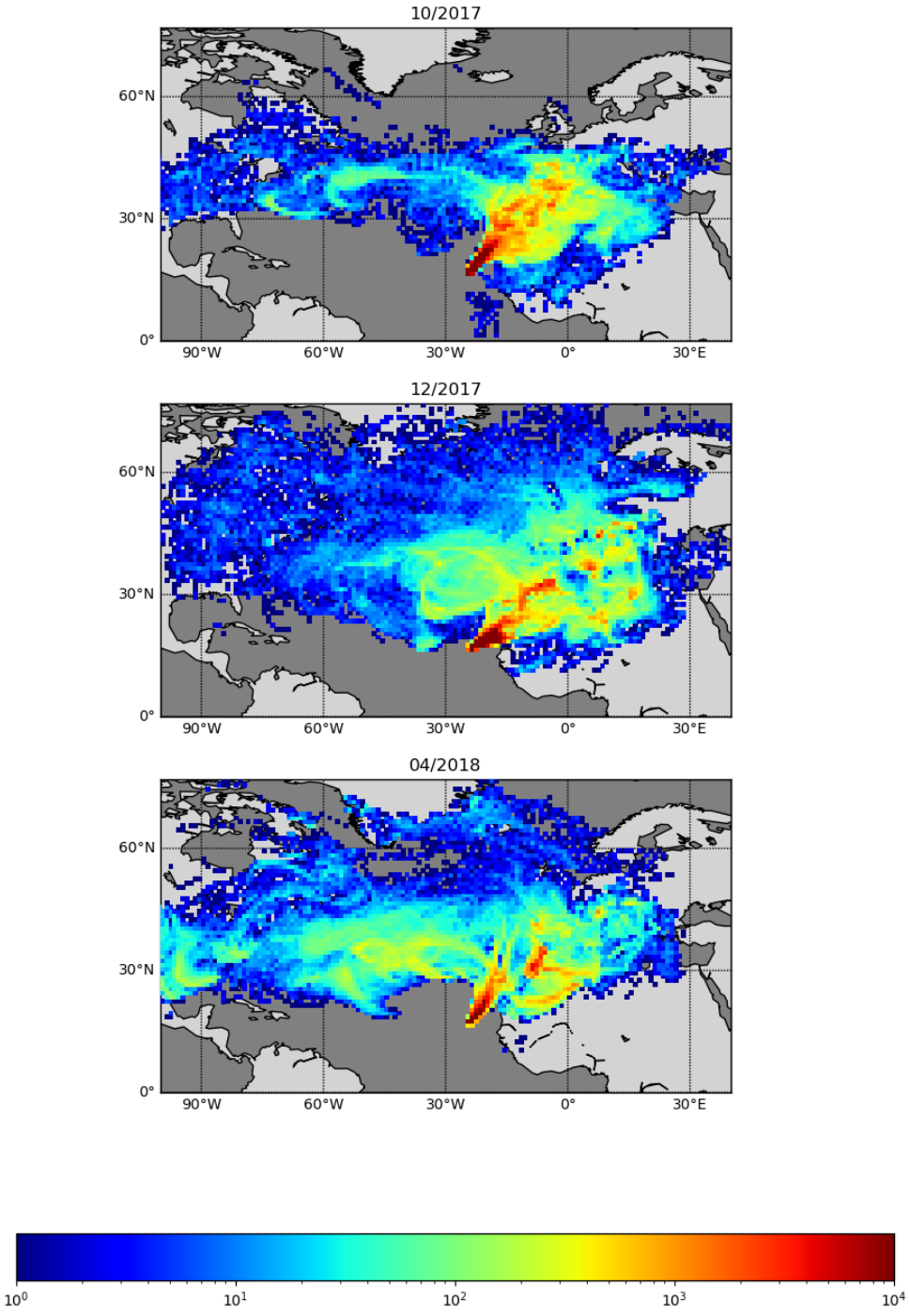

Figure 2.10: Back trajectories estimated for October 2017, December 2017, and April 2018. FLEXPART version 10.4 is used in backwards mode, driven by pressure level data from Global Forecast System (GFS) reanalyses at $0.5^\circ \times 0.5^\circ$ resolution [138, 139]. 10-day back-trajectory simulations are initialised every 6 hours, releasing 1000 particles from the CVAO site.

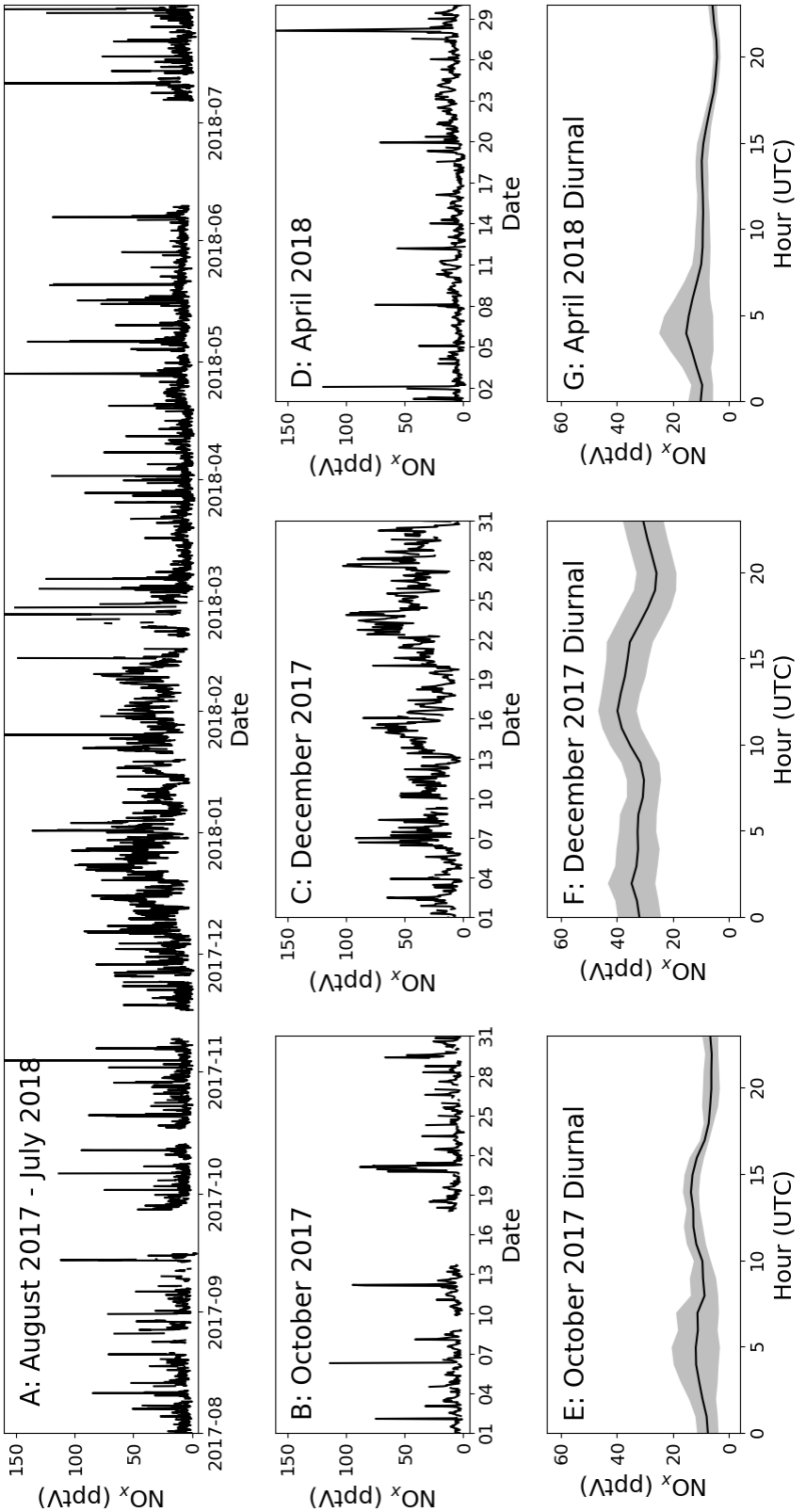

Figure 2.11: Panel A show the time series for total NO_x ($NO + NO_2$ PLC) from August 1st 2017 to July 31st 2018. Panel B, C and D zoom in on October 2017, December 2017 and April 2018, respectively. Panel E, F and G show the average diurnal cycle of NO_x for October 2017, December 2017 and April 2018, respectively, with the coloured areas being ± 2 standard errors. If there are less than 15 measurements available for the hour, it is not included in the diurnal.

Table 2.6 NO, NO_2, and NO_x mixing ratios at different low NO_x sites.

	NO (pptV)	NO_2 (pptV)	NO_x (pptV)	Reference
Tropospheric Marine				
CVAO, Cape Verde 2017-2018[a]	2-10	5-50	7-60	This study
Cape Grim, Australia[a]	1-6	3-6	4-12	[43]
SAGA3, Pacific Ocean, Cruise[b]	2.9 ± 0.1			[140]
ASTEX, North Atlantic, Cruise[c]	5 ± 4	29 ± 8		[141]
WOCE, Indian Ocean, Cruise[d]	~ 5	18-40		[142]
Background Sites				
Alert, Canada[e]	0.2-2.8	1.3-10.8		[143]
South Pole[f]	~ 10			[144]
Free Troposphere				
Mauna Loa, USA[g]	9.4	29.6	32	[145]
Pico Mountain, Portugal[h]	0-9	19-30	20-37	[146]
NASA GTE, Pacific Ocean, Aircraft[i]	~ 1			[147]
Svalbard, Norway[j]			27.7 ± 24	[148]

[a]Measurements made during the SOAPEX (Southern Ocean Atmospheric Photochemistry EXperiment) campaign during Austral summer in 1995. [b]Measurements from the Soviet-American Gases and Aerosols (SAGA) campaign between Hawaii and American Samoa between February and March. [c]Measurements from 6 clean days on the Atlantic Stratocumulus Transition Experiment (ASTEX). [d]Measurements from the World Ocean Circulation Experiment (WOCE) between South Africa and Sri Lanka. [e]Measurements made during 24-hour darkness and in spring. [f]Measurements made from January-March 1997 at the German Antarctic research station, Neumayer. [g]Measurements made during the Mauna Loa Observatory Photochemistry Experiment (MLOPEX) in May 1988. [h]Measurements made at Mount Pico between July 2002 and August 2005. [i]Measurements made in the upper marine boundary layer from 13 flights between California and west of Hawaii. [j]Measurements made at the Ny-Ålesund Zeppelin mountain station on Svalbard during a spring campaign in 1994. [k]Daytime values.

2.6 Conclusions

NO_2 was measured at a remote marine site by photolytic conversion to NO followed by chemiluminesence detection, using two different methods for conversion. A photolytic NO_2 converter with external diodes and a quartz photolysis cell (PLC) has been installed at the Cape Verde Atmospheric Observatory and the NO_2 measurements have been compared to those of the historical BLC used at the site, which has internal diodes and a reaction chamber made of Teflon-like barium doped material. The two measurements show good agreement (BLC = 0.99 × PLC + 0.7 pptV, linear least squares analysis) with small differences due to uncertainties in the estimations of the BLC NO_2 artefact. Even though the PLC has a lower conversion efficiency (CE= 52 ± 4%) than the BLC (CE= 85 ± 4%), it is preferred due to its assumed negligible artefact as a consequence of having non-porous/non-reactive walls. The assumption of a zero artefact causes the hourly uncertainty of the NO_2 measurements to be roughly halved. With 2σ hourly precisions of 1.0 ± 0.9 pptV, 1.5 ± 0.8 pptV, and 2.7 ± 2.2 pptV and 2σ hourly uncertainties of 1.4 ± 1.5 pptV, 8.4 ± 7.5 pptV, and 4.4 ± 5.8 pptV for NO, NO_2 BLC, and NO_2 PLC, respectively, the instrument has a high repeatability and low uncertainties for all the measurements. The mixing ratios observed at the CVAO (NO: 2-10 pptV, NO_2: 5-50 pptV, and NO_x: 7-60 pptV at midday) are in good agreement with previous measurements at the CVAO as well as other remote measurements around the world. However, NO_2 and NO_x show a slight increase during the day, which would not be expected from established NO_x chemistry. This suggests a photolytic source of NO_x, which has previously been proposed to be photolysis of particulate nitrate. This potential source is discussed and investigated in details in chapter 4.

Long-term remote measurements, which are not subject to local pollution, are ideal to test our current knowledge on. The measurements shown in this chapter together with additional years of data and other measurements are

used in chapter 3 to investigate the photostationary state of NO_x and O_3 in the remote MBL.

Chapter 3

Fundamental Oxidation Processes in the Remote Marine Atmosphere Investigated Using the NO-NO_2-O_3 Photostationary State

Luis Neves has done the day-to-day maintenance of instruments, while I have had the overall responsibility of running the NO_x instrument while Shalini Punjabi (University of York) and Katie Read (University of York) have run the remaining instruments. Lisa Whalley (University of Leeds) has helped Katie with processing the photolysis measurements. Beth Nelson (University of York) has run the chemical box model, Matthew Rowlinson (University of York) has run the FLEXPART back trajectories, and Tomás Sherwen (Universiy of York) has run the GEOS-Chem model. I have used the measurements and the model outputs to do the data analysis.

3.1 Introduction

Tropospheric NO, NO_2 and O_3 are rapidly interconverted during the day via reactions (R3.1-R3.3), where NO is oxidised by O_3 into NO_2, which is then photolyzed into NO and $O(^3P)$, followed by a fast reaction of $O(^3P)$ with O_2 to return O_3.

$$NO + O_3 \longrightarrow NO_2 + O_2 \tag{R3.1}$$

$$NO_2 + h\nu (\leq 410\,\text{nm}) \longrightarrow NO + O(^3P) \tag{R3.2}$$

$$O(^3P) + O_2 + M \longrightarrow O_3 + M \tag{R3.3}$$

The photostationary state (PSS) equilibrium between NO and NO_2 is reached within minutes [149] if it is not impacted by fresh NO_x emissions and if the photolysis rate does not change quickly such as under rapidly changing cloud coverage [150]. The photostationary state can be described by the Leighton ratio [149] (Eq. 3.1), where jNO_2 is the photolysis rate of NO_2 and φ is the PSS parameter.

$$\varphi = \frac{jNO_2[NO_2]}{k_{3.1}[NO][O_3]} \tag{Eq. 3.1}$$

Under very polluted conditions, where O_3 is the only oxidant converting NO to NO_2, φ is equal to 1 and the NO_2 at PSS can be estimated from the measured NO, O_3, and jNO_2 (Eq. 3.2).

$$[NO_2]_{PSS} = \frac{k_{3.1}[NO][O_3]}{jNO_2} \tag{Eq. 3.2}$$

Deviations from $\varphi = 1$ suggest the presence of additional chemistry occurring [151], particularly the conversion of NO to NO_2 by reaction with an other oxidant than O_3, such as hydroperoxy radicals (HO_2) and peroxy radicals (RO_2) (R3.4-R3.5, where R in the peroxy radicals represents any organic functional group) or with halogen oxides (IO, BrO; R3.6-R3.7) in the marine

atmosphere.

$$RO_2 + NO \longrightarrow NO_2 + RO \quad \text{(R3.4)}$$

$$HO_2 + NO \longrightarrow NO_2 + OH \quad \text{(R3.5)}$$

$$IO + NO \longrightarrow NO_2 + I \quad \text{(R3.6)}$$

$$BrO + NO \longrightarrow NO_2 + Br \quad \text{(R3.7)}$$

By including these additional NO oxidation reactions, the NO_2 concentration at PSS can be estimated using equation (3.3). The photostationary state of NO-NO_2-O_3 can also be used to estimate the sum of HO_2 and RO_2 (RO_x) or the sum of BrO and IO (XO) in the atmosphere using equation (3.4) and (3.5) and assuming that $k_{3.4} = k_{3.5}$ and $k_{3.6} = k_{3.7}$, respectively:

$$[NO_2]_{\text{PSS ext.}} = \frac{(k_{3.1}[O_3] + k_{3.4}[RO_2] + k_{3.5}[HO_2] + k_{3.6}[IO] + k_{3.7}[BrO])[NO]}{jNO_2} \quad \text{(Eq. 3.3)}$$

$$[RO_2] + [HO_2] = \frac{jNO_2[NO_2] - (k_{3.1}[O_3] + k_{3.6}[IO] + k_{3.7}[BrO])[NO]}{k_{3.4,3.5}[NO]} \quad \text{(Eq. 3.4)}$$

$$[IO] + [BrO] = \frac{jNO_2[NO_2] - (k_{3.1}[O_3] + k_{3.4}[RO_2] + k_{3.5}[HO_2])[NO]}{k_{3.6,3.7}[NO]} \quad \text{(Eq. 3.5)}$$

Previous studies reporting deviations in the PSS parameter to estimate RO_x concentrations in the atmosphere are summarised in Table 3.1, which compares $[RO_x]_{PSS}$ against measured and/or modelled $[RO_x]$. Measurements of RO_x are predominantly conducted using chemical amplification, where each RO_2 and HO_2 molecule in ambient air leads to the formation of several NO_2 molecules by chain reactions caused by the addition of high concentrations of NO and CO [152]. As halogen oxides also convert NO to NO_2, the chemical amplification techniques should also be sensitive to them. The resultant NO_2 can be detected and converted back to a RO_x concentration by quantification

of the chain length of the reactions via calibration, typically using known concentrations of CH_3O_2 or peroxyacetyl ($CH_3C(O)O_2$) radicals [152–154]. Since the basis of the chemical amplification technique is detection of RO_x radicals from their ability to oxidise NO to NO_2 (R3.4 and R3.5), which is also used to estimate RO_x from the PSS, the RO_x concentrations determined from these methods would be expected to agree reasonably well. However, PSS-derived RO_x concentrations are generally higher than both measured and modelled values in rural conditions [150,155–158] with exceptions such as in the Pearl River Delta where PSS-derived and measured RO_x were comparable [157]. During campaigns in relatively clean regions with moderate influence from pollution (Amazon Basin and Arabian Peninsula), PSS-derived RO_x levels have been shown to be in good agreement with modelled RO_x [159, 160]. In the remote marine boundary layer (MBL), PSS-derived RO_x has been observed to be 1.27 times higher than the measured RO_x over the South Atlantic Ocean, however, the measured RO_x was approximately 4 times higher than modelled [161].

The difference between measured, modelled, and PSS-derived RO_x can be due to a variety of reasons. RO_x concentrations calculated by box models rely on comprehensive constraint from co-measured trace gases and a reaction scheme which accurately represents the most important photochemical processes. Incomplete characterization of ambient trace gases and/or reaction schemes can therefore result in uncertain RO_x predictions. Large deviations (factor of ~ 3) between modelled and measured RO_x levels in a pine forest in the Rocky Mountains were attributed to a combination of a missing photolytic source of HO_2 at midday and a missing reaction forming RO_2 independently of sunlight in the model scheme [166]. PSS-derived RO_x can be significantly over- or underestimated if the PSS has not been established, for example due to rapidly changing photolysis rates or local sources of NO_x [150]. Another reason for overestimation of PSS-derived RO_x is NO_2 measurement artefacts [170, 171], which results in overestimated NO_2 concentrations. These are common in chemiluminescence instruments and can be due to photolytic

Table 3.1: Summary of previous studies which have compared $[RO_x]_{PSS}$ against measured and/or modelled $[RO_x]$ in rural, marine and remote conditions.

Location	NO_x Instrument	NO_x	φ[a]	$\frac{[RO_x]_{PSS}}{[RO_x]_{Measured}}$[b]	$\frac{[RO_x]_{PSS}}{[RO_x]_{Modelled}}$[b]	$\frac{[RO_x]_{Measured}}{[RO_x]_{Modelled}}$[b]	Ref.
Rural conditions							
Hohenpeissenberg, Germany	CLD with PLC[c]	NO; 50-7000 pptV	2-5.7[d]	2-3[e]	-	-	[150]
Pearl River Delta, China	CLD with PLC[c]	NO; 50-4000 pptV	1-8.5[d]	~ 1[e]	2-10	~ 2[e]	[157]
Pabstthum, Germany	CLD with PLC[c]	1-7 ppbV	1.1-3.0[d]	~ 4[e]	-	-	[158]
Idaho Hill, Colorado	CLD with PLC[c]	38 pptV-21.3 ppbV	-	2.1 (mean)[e]	-	~ 1[e]	[155,162]
Pine forest, Alabama	CLD with PLC[c]	1-5 ppbV	-	1-2[e]	-	~ 1[e]	[156,163, 164]
Essex, England	CLD with Mo[g]	NO; 0.3-9.9 ppbV	-	-	-	~ 1.4[e]	[165]
Ponderosa pine forest, Rocky Mountains	CLD with PLC[c]	NO; 100-150 pptV	-	-	-	<3[h]	[166]
Marine/Remote with pollution							
Arabian Peninsula	CLD with PLC[c] and CRDS[i]	$<$50 pptV - $>$10 ppbV	-	-	~ 1	-	[159]
Amazon Basin (Manau)	CLD with PLC[c]	100 pptV-30 ppbV	-	-	~ 1[k]	-	[160]
Remote/Marine conditions							
South Atlantic Ocean	CLD with PLC[c]	NO_2; 3-20 pptV	1-12.5[l]	1.27[e]	~ 5	~ 4[e]	[161]
Mauna Loa, Hawaii	CLD with PLC[c]	20-60 pptV	1.4-2.2	1.5-3.0[e]	2-3.5	1.2-2[e]	[167]
Mace Head, Ireland	CLD with TC[m]	NO $<$ 10 pptV	-	-	-	~ 0.25[e]	[168,169]
Cape Grim, Tasmania	CLD with PLC[c]	NO , 5 pptV	-	-	-	~ 0.4[e]	[168,169]
Cabo Verde	CLD with PLC[c]	$<$ 50 pptV	0.45-12.0[d]	-	1.5 (median)	-	This study

[a]Without radicals and halogens. [b]$[RO_x] = [HO_2] + [RO_2]$. [c]CLD with PLC = Detection by chemiluminescence with photolytic converter for NO_2. [d]Increasing φ with decreasing [NO], $[NO_2]$ or $[NO_x]$. [e]$[RO_x]$ measured by chemical amplification. [f]Calculated/modelled using steady state theory. [g]CLD with Mo = Detection by chemiluminescence with molybdenum converter. [h]$[RO_x]$ measured by Peroxy Radical Chemical Ionization Mass Spectrometry (PeRCIMS). [i]CRDS = Cavity Ring down spectroscopy. [k]PSS derived $[RO_x]$ was within the range of the modelled values. [l]Increasing φ with increasing $[NO_2]$. [m]CLD with TC = Detection by chemiluminescence with thermal converter.

or thermal decomposition of HONO, peroxyacetyl nitrate (PAN), and other nitrate molecules in the atmosphere [107, 108, 132, 170, 172–174].

Measurements of RO_x are also not without challenges due to effects from e.g. the high reactivity of RO_x, humidity, non-linearity of the NO_2 detection, and formation of organic nitrates and nitrites. In the first chemical amplification instruments, NO_2 was detected by luminol chemiluminescence, which has a non-linear response to NO_2 resulting in the need for a multipoint calibration [155]. However, more recent instruments use Cavity Attenuated Phase Shift (CAPS) [154, 175], Laser Induced Fluorescence (LIF) [176], or Cavity Ring-Down Spectroscopy (CRDS) [177] for detection of NO_2, all of which have been shown to have a linear response. Chemical amplifiers are usually only calibrated for one or two types of peroxy radicals. However, the chain length of each peroxy radical varies, resulting in a different amount of NO_2 production depending on the mixture of peroxy radicals present, which most likely lead to underestimations due to a lower sensitivity to other peroxy radicals than CH_3O_2, which most amplification instruments are calibrated for. Additionally, the chain length is significantly affected by humidity due to the increase in HO_2 wall loss on wet surfaces and to an enhanced termination rate of HO_2 by reaction with NO to give HNO_3. HO_2 has been shown to form a complex with H_2O ($HO_2{\cdot}H_2O$), which reacts 4-8 times faster with NO, creating HNO_3, at 50% relative humidity (RH) compared to under dry conditions [175, 178, 179]. This leads to the measured chain length decreasing by a factor of two when going from dry conditions to 40% RH and by a factor of three at 70% RH [175, 180]. Finally, the chain length is impacted by the gas reagents (NO and CO). Peroxy radicals and alkoxy radicals (RO) can react with NO to create organic nitrates and nitrites, which terminates the chain reaction, preventing further radical propagation processes. This is favoured by longer chain peroxy radicals, and at high NO concentrations. The formation yield of organic nitrates and nitrites differs from a few percent to up to $\sim$23% depending on the nature of the R group present [175]. It is therefore important to determine the optimal

concentrations of reagent gas for each individual instrument as it could vary with what material has been used in the reactor. Some of these challenges can be overcome by using RO_xLIF (laser induced fluorescence), where the sum of RO_x is determined without the amplification step, which removes the problem with varying chain lengths [181].

In the presence of sufficient levels of NO, additional ambient peroxy radicals not accounted for in photochemical models should lead to an underestimation of the simulated production rate of O_3, which occurs via reactions (R3.4) and (R3.5) followed by photolysis of NO_2. The production of O_3 ($P(O_3)$) can be calculated using equation (3.6):

$$P(O_3) = k_{3.4}[NO][RO_2] + k_{3.5}[NO][HO_2] \qquad \text{(Eq. 3.6)}$$

Volz-Thomas et al. (2003) calculated O_3 production rates from PSS-derived and chemical amplification-measured RO_x during the BERLIOZ campaign in Pabstthum, Germany, resulting in an average of ~ 20 ppbV h^{-1} and ~ 2 ppbV h^{-1} across the campaign, respectively. The large difference was credited to an unknown process that converts NO into NO_2 without causing additional O_3 production [158]. This is possible if NO is oxidised by an oxidant which also destroys O_3, similarly to halogen atoms/halogen oxides. This hypothesis is consistent with observations by Parrish et al. (1986) at a mountain station in Colorado, where a missing oxidant of photolytic origin was identified [164]. It was shown that if the NO to NO_2 oxidation was completely due to RO_x, the increased O_3 production would result in O_3 mixing ratios significantly higher than measured, yet if the oxidant exhibited similar reaction mechanisms to IO, extremely high (70 pptV) mixing ratios of IO would be needed [164]. These IO levels are more than an order of magnitude higher than observations in the marine atmosphere [13, 182–184] and would have a massive impact on the OH/HO_2 ratio.

In regions where the net O_3 production is negligible or negative during

the day due to very low NO levels, it is more relevant to compare the net ozone production rate (NOPR) to the observed change in O_3. The chemical NOPR can be calculated as the difference between the photochemical processes producing and destroying O_3:

$$\mathrm{NOPR} = \mathrm{P}(O_3) - \mathrm{L}(O_3) \qquad \text{(Eq. 3.7)}$$

where $\mathrm{P}(O_3)$ is determined using equation (3.6) and the loss rate of O_3 ($\mathrm{L}(O_3)$), is usually determined from reactions (R3.8-R3.12). Additionally, halogens have previously been shown to cause an O_3 loss of 0.23 ± 0.05 ppbV h^{-1} in the MBL (initiated by R3.13) [13], which is in line with other studies suggesting that halogens can have a significant impact on O_3 in marine environments [185–187].

$$O_3 + h\nu(\leq 340\,\mathrm{nm}) \longrightarrow O_2 + O(^1D) \qquad \text{(R3.8)}$$

$$O(^1D) + H_2O \longrightarrow 2\,OH \qquad \text{(R3.9)}$$

$$O(^1D) + M \longrightarrow O(^3P) \qquad \text{(R3.10)}$$

$$OH + O_3 \longrightarrow HO_2 + O_2 \qquad \text{(R3.11)}$$

$$HO_2 + O_3 \longrightarrow OH + 2\,O_2 \qquad \text{(R3.12)}$$

$$X(X{=}Br,Cl,I) + O_3 \longrightarrow XO + O_2 \qquad \text{(R3.13)}$$

The actual rate of change of O_3 within the planetary boundary layer is also impacted by the physical processes of advection, deposition and entrainment, which complicates comparisons with the NOPR. However, if these physical processes change only negligibly over the course of a day, such as in marine well mixed air masses, their net influence can be deduced from the net night time change in O_3 [13, 188, 189], allowing a calculation of the NOPR from observations. A comparison of the observed and calculated NOPR gives an indication of whether production and loss rates of O_3 from known processes are sufficient to explain the photochemical regime [13].

From the studies shown in Table 3.1, there is clearly widespread evidence of

enhanced PSS-derived RO_x compared to measurements and models, however, all methods to derive RO_x are not without challenges as described above. The large uncertainties associated with RO_x measurements, especially at high humidities where the chain length is significantly impacted by enhanced wall loss and the production of HNO_3, suggest that measurements could be underestimating RO_x in the atmosphere. Previous studies also find that the additional conversion of NO to NO_2 caused by the extra "RO_2" should only produce minimal additional O_3, or at least lead to additional O_3 destruction, thus inferring an unknown missing oxidant which exhibits different chemical behaviour to peroxy radicals.

Up to 25% of methane removal occurs in the tropical MBL due to the high photochemical activity and humidity resulting in high OH radical concentrations and the high temperatures, which increases the rate coefficient for the OH+CH_4 reaction [7]. Thus it is crucially important to understand the fundamental oxidation processes, such as the NO_x-O_3 cycle, occurring in this region. However, remote NO_x measurements are rare due to the difficulty in measuring very low (pptV) mixing ratios. Most previous remote NO_x measurements have taken place during short campaigns and do not give information on seasonal changes and long-term trends [121, 141, 142, 190]. Here, we investigate the photostationary state under clean marine conditions from three years of observations (2017-2020) at the Cape Verde Atmospheric Observatory (CVAO) in the tropical east Atlantic, representing a unique dataset to investigate NO_x-O_3 chemistry in the remote MBL [23, 114, 191]. We also compare the chemical NOPR calculated from a box model with NOPR derived from the observed net O_3 rate of change, in order to evaluate the possibility of missing peroxy radicals in this remote environment.

3.2 Methods

3.2.1 Measurements

Year-round measurements of meteorological parameters and trace gases including NO, NO_2, alkanes, and alkenes have been conducted at the CVAO (16° 51' N, 24° 52' W) since October 2006. The CVAO is located on the north eastern coast of São Vicente, Cabo Verde. The air sampled predominantly comes from the northeast (see Figure 3.1) and has travelled over the Atlantic Ocean for multiple days since the last exposure to anthropogenic emissions, with the potential exception of ship emissions [13, 114]. This makes it an ideal location to investigate fundamental photochemistry in an ultra-clean environment.

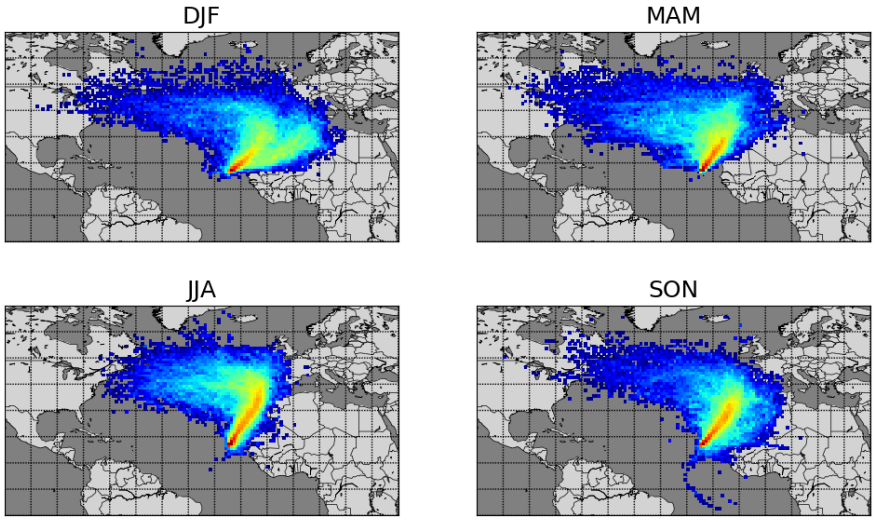

Figure 3.1: Seasonal average back trajectories for the CVAO determined using FLEXPART as described in Appendix B

Wind speed (m/s), wind direction (°), temperature (°C), relative humidity (%), barometric pressure (mbar) and solar radiation (W m^{-2}) are measured at a height of 10 m using an automatic weather station from Campbell Scientific. NO and NO_2 have been measured using an ultra-high sensitivity NO chemiluminescence instrument, which measures NO_2 by photolytic conversion to NO, at the CVAO since 2006 [23]. The technique and data analysis have been de-

scribed in detail in chapter 2. O_3 is measured using a Thermo Scientific 49i Ozone monitor as described in Read et al. (2008). Photolysis rates of a variety of species were measured in 2020 using a spectral radiometer (a 2-pi sr quartz diffuser coupled to an Ocean Optics QE65000 spectrometer via a 10 m fibre optic cable). Prior to 2020, photolysis rates are calculated in this study based on the correlation between the measured photolysis rates in 2020 and the total solar radiation, as described in Appendix E. Average $j\mathrm{NO_2}$ and $j\mathrm{O(^1D)}$ for different seasons are shown in Table 3.2. Volatile organic compounds (VOCs) are measured using a dual channel Agilent 7890A gas chromatograph coupled with a Flame Ionization Detector (GC-FID) and a MARKES Thermal Desorption Unit with an ozone precursor trap that is cooled to -30°C [192]. Details of the calibration and uncertainties are given in the World Calibration Centre (WCC)-VOC audit report [193]. Examples of the VOCs measured at the CVAO can be found in Table 3.2. Carbon monoxide (CO), and methane (CH_4), are measured using CRDS, G2401 manufactured by Picarro Inc, following the Global Atmosphere Watch (GAW) recommended technique for long term remote measurements. The instrument is highly linear, has a precision of 1 ppbV over 10 minutes and no measurable drift [194,195].

Time series of NO, NO_2, O_3, $j\mathrm{NO_2}$, $j\mathrm{O(^1D)}$, temperature, CO, propene, benzene and CH_4 for July 2017 – June 2020 are shown in figures F.1-F.3. The specifics of each instrument and their respective measurements can be found in Table 3.2 and a full description of the CVAO site and associated measurements is given in Carpenter et al. (2010).

3.2.1.1 NO_2 Measurement Artefact

One of the drawbacks of measuring NO_2 by photolytic conversion to NO is it can be subject to artefacts. These could either be of a photolytic or thermal origin [132, 170, 172–174]. Photolytic artefacts occur when other compounds containing -NO, -NO_2, or -NO_3 photolyse to form NO over a similar wavelength range as NO_2 and thereby produce an overestimate of NO_2 in the sample [107].

Table 3.2 Overview of instruments and measurements used from the CVAO.

Instrument	Measurement	Accuracy	DJF[a]	MAM[a]	JJA[a]	SON[a]	Ref.[b]
AQD	NO (pptV)	1.4	5.3 ± 7.8	1.9 ± 4.2	2.7 ± 5.6	3.6 ± 5.9	[191]
	NO_2 (pptV)	4.4	27.0 ± 35.8	10.0 ± 13.5	10.2 ± 16.8	10.6 ± 15.7	
Thermo Scientific 49i	O_3 (ppbV)	0.07	38.9 ± 8.8	39.2 ± 12.1	29.9 ± 11.9	31.2 ± 11.1	[13]
Oceans Optics QE650000	jNO_2 (10^{-3} s^{-1})	15%	7.8 ± 2.7	9.3 ± 2.2	8.9 ± 2.5	8.7 ± 2.4	[c]
	$jO(^1D)$ (10^{-5} s^{-1})	15%	1.7 ± 1.2	3.0 ± 1.3	2.6 ± 1.2	2.6 ± 1.2	
Picarro	CO ppbV	1.0	99.0 ± 20.2	103 ± 17	80.0 ± 19.3	84.5 ± 16.6	[194,
	CH_4 (ppbV)	1.0	1916 ± 26	1914 ± 29	1886 ± 34	1896 ± 30	195]
GC-FID	Ethane (pptV)	5.2%	1438 ± 600	1204 ± 608	518 ± 267	660 ± 449	[193]
	Ethene (pptV)	5.0%	31.2 ± 18.6	23.2 ± 9.8	27.5 ± 15.1	28.9 ± 19.6	
	Acetylene (pptV)	10.7%	134 ± 86	86.9 ± 82.4	22.6 ± 22.2	38.1 ± 38.5	
	Propane (pptV)	5.6%	336 ± 259	148 ± 195	20.6 ± 18.7	71.0 ± 133	
	Propene (pptV)	6.9%	8.6 ± 8.6	8.8 ± 11.5	8.0 ± 6.2	7.2 ± 6.1	
	Iso-butane (pptV)	6.4%	40.4 ± 39.5	11.0 ± 20.0	3.2 ± 4.3	8.4 ± 15.5	
	n-butane (pptV)	5.0%	82.8 ± 80.7	19.4 ± 36.0	6.0 ± 7.3	22.1 ± 40.5	
	Iso-pentane (pptV)	4.6%	11.1 ± 14.9	3.6 ± 6.2	5.2 ± 9.5	4.0 ± 6.7	
	n-pentane (pptV)	6.4%	8.7 ± 11.4	2.9 ± 4.7	1.7 ± 2.6	3.5 ± 5.2	
	Benzene (pptV)	4.8%	40.1 ± 30.5	22.9 ± 23.3	11.1 ± 10.5	17.3 ± 11.5	
	Toluene (pptV)	6.3%	4.6 ± 5.4	3.0 ± 4.2	2.9 ± 2.8	3.4 ± 3.1	
	Methanol (pptV)	20.7%	486 ± 563	698 ± 734	677 ± 603	857 ± 655	
	Acetone (pptV)	12.2%	506 ± 263	614 ± 274	767 ± 332	681 ± 213	
Campbell Scientific weather station	Temperature (°C)	0.4°C at 5-40°C	22.0 ± 2.3	21.7 ± 1.4	24.5 ± 2.5	25.8 ± 2.1	[114]
	Pressure (hPa)	1.0 hPa at 0-40°C	1016 ± 4	1016 ± 3	1015 ± 4	1014 ± 3	
	Relative humidity (%)	2% at 10-90%	74.9 ± 12.8	77.2 ± 10.4	82.8 ± 8.8	81.1 ± 11.9	
	Solar radiation (W m^{-1})	5%	615 ± 312	785 ± 251	737 ± 283	716 ± 273	

[a]Midday (12.00-15.00 UTC, local +1) mean ± 2σ for July 2017 – June 2020. [b]For further information on the instrument and the data processing. [c]See Appendix E.

Thermal artefacts are caused by thermally labile compounds which decompose in photolytic converters when they heat up and release NO that is measured by the detector or NO_2 which is immediately photolytically converted to NO and then detected [108]. The maximum potential NO_2 artefact can be estimated using measured or modelled mixing ratios of a range of potential interfering compounds. The photolytic contribution can be estimated based on the absorbtion cross section (ACS) of NO_2 and the potential interferents around the peak wavelength of the diodes used to convert NO_2 into NO (385 nm). The ACS of NO_2 and some known interfering compounds over the wavelength range 380-390 nm are shown in Table 3.3. NO_2 and most of the interferents, with the exception of HONO, show relatively invariant ACSs across these wavelengths. When the ACSs of both NO_2 and the particular interferent are invariant over the spectral output of the diodes, the ratio at the peak wavelength is used to estimate the potential artefact. However, since HONO varies significantly over the range, it has been estimated assuming a Gaussian output of the diodes over the wavelengths. It is also important to distinguish between the products formed from the photolysis of the potential interferents. If NO_2 is the product then it will be photolysed to NO with the same efficiency as NO_2 in the ambient air, however, if NO is the product then 1 converted molecule will be detected as 2 NO_2 molecules if the conversion efficiency of NO_2 is 50%. Organic nitrates, HNO_3, and NO_3 do not photolyse at 385 nm and have therefore not been included in the evaluation of photolytic artefacts.

The main potential photolytic artefact for the CVAO NO_2 measurements is HONO. Measurements of HONO at the CVAO using a Long Path Absorption Photometer (LOPAP) show levels of up to $\sim$5 pptV (see [44] and chapter 4), indicating an NO_2 artefact of up to 0.63 pptV. However, these measurements were made using a thermostated inlet system with reactive HONO stripping, where loss of HONO to the sample lines is minimised. The NO_x instrument at the CVAO samples at the end of the manifold making it highly likely that a significant fraction of HONO is lost on the manifold before the air is introduced

Table 3.3 Potential sources of NO_2 artefacts at the CVAO.

	ACS at 380 nm (10^{-20}cm^2)[a]	ACS at 385 nm (10^{-20}cm^2)[a]	ACS at 390 nm (10^{-20}cm^2)[a]	Conversion efficiency (%)[b]	Measured at the CVAO at midday (pptV)[c]	Modelled by GEOS-Chem at midday (pptV)[c]	Potential artefact (pptV)
$NO_2 \xrightarrow{h\nu} NO$	59.24	59.42	62.0	50	-	-	-
$BrONO_2 \xrightarrow{h\nu} NO_2$	3.85	3.37	2.97	2.8	-	0.5-1.5	0.014-0.042
$ClONO_2 \xrightarrow{h\nu} NO_2$	0.121	0.137	0.091	0.1	-	0.5-1	0.0005-0.001
$ClNO \xrightarrow{h\nu} NO$	8.86	7.82	6.86	6.6	-	-	-
$ClNO_2 \xrightarrow{h\nu} NO_2$	0.3593	0.2687	0.2008	0.2	-	~ 0	-
$BrNO_2 \xrightarrow{h\nu} NO_2$	17	17	16	14.3	-	~ 0	-
$HONO \xrightarrow{h\nu} NO$	9.2	14.5	2.4	6.3	3-5	0.2-0.4	0.38-0.63
$PAN \xrightarrow{\Delta} NO_2$	-	-	-	~ 5	< 6	~ 20	< 0.3
Total	-	-	-	-	-	-	**0.69-0.97**

[a]All absorption cross sections (ACSs) have been reported by IUPAC [49]. [b]The reported conversion efficiencies have been calculated based on a NO_2 CE of 50%. [c]Midday is defined as 12.00-15.00 UTC (local+1).

to the NO_x instrument due to the high surface reactivity of HONO [196]. Thus, we regard the potential HONO-induced artefact of 0.63 pptV as an upper limit. No other potential photolytic artefacts have been measured at the CVAO, however, using the GEOS-Chem model (see section 3.2.2.2) we calculated seasonal cycles of 20 potential interfering compounds at the CVAO (Figure 3.2). None of these compounds exhibit major seasonal differences, indicating that any measurement artefact will be fairly constant across the year. The contribution from photolytic degradation of compounds other than HONO is predicted to be less than 0.05 pptV using the estimated conversion efficiency of each compound in Table 3.3 and the modelled mixing ratios at the CVAO.

Peroxyacetyl nitrate (PAN) is produced in polluted areas and transported to remote regions, where it can thermally decompose into peroxy radicals and NO_2. 5.8% of the available PAN has been shown to thermally decompose in blue light converters (BLC) switched on 40% of the time [108]. This can cause significant overestimations of NO_2 in colder regions where PAN can build up in the atmosphere due to its long lifetime [197], however, in warmer regions such as Cabo Verde the overestimation will be substantially lower due to the much shorter lifetime ($\sim$40-230 minutes at 25°C) [197,198], and hence lower concentration of PAN. At the CVAO, PAN has been measured using gas chromatography as described by Whalley et al. (2004) [199], however, all measurements were below the limit of detection (LOD) of 6 pptV. The photolytic converter (PLC) used at the CVAO is only switched on 20% of the time, so a thermal decomposition efficiency of 5% for PAN is used to estimate a potential artefact of 0.3 pptV from PAN. Combining photolytic and thermal artefact contributions gives a maximum potential NO_2 artefact of 0.97 pptV at the CVAO, which is within the uncertainty previously reported for the NO_2 measurements, see Table 3.2 and chapter 2.

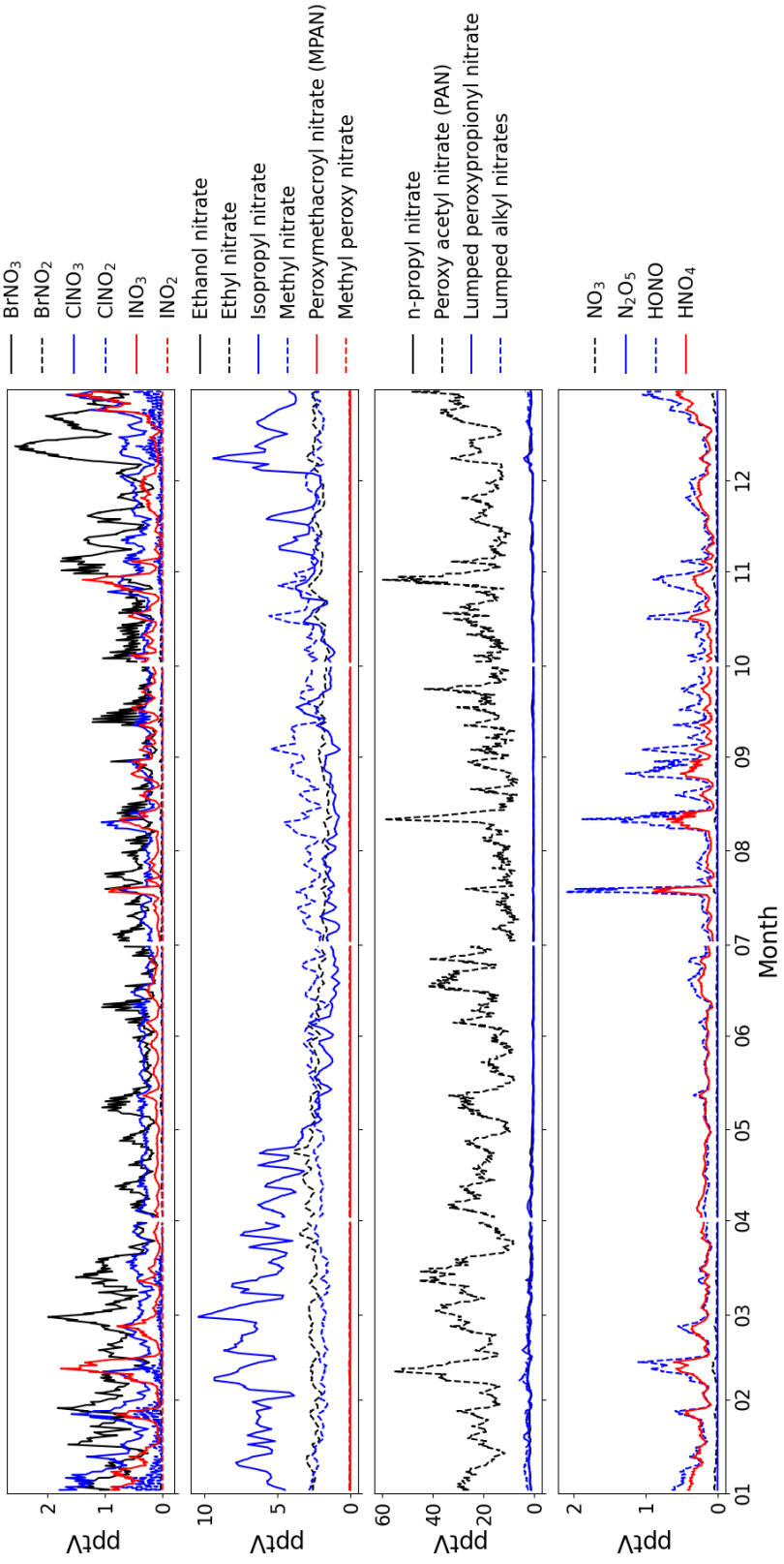

Figure 3.2: GEOS-Chem model output for potential NO_2 interfering compounds in 2019.

3.2.2 Modelling

3.2.2.1 Chemical Box Model

A tailored zero-dimensional chemical box model of the lower atmosphere previously used in Nelson et al. (2021) [200], incorporating a subset of the Master Chemical Mechanism (MCM) v3.3.1 [201] into the AtChem2 modelling toolkit [202], was used to estimate concentrations of OH, HO_2 and RO_2 and daily chemical production and loss of O_3 at the CVAO. The MCM describes the detailed atmospheric chemical degradation of 143 VOCs, through 17,500 reactions of 6900 species. More details can be found on the MCM website (http://mcm.york.ac.uk, last access: 4^{th} March 2022). A fixed deposition rate of 1.2×10^{-5} s^{-1} was applied to all model generated species, giving them a lifetime of approximately 24 hours. The model was constrained to 34 observationally derived photolysis rates, temperature, pressure, and relative humidity, along with a range of observed chemical species, defined in Table 3.2. Heterogeneous reactions on aerosols have not been included in the model.

3.2.2.2 GEOS-Chem

Concentrations of 20 different chemical species were extracted every hour during 2019 at nearest point in space and time from the GEOS-Chem model (v12.9.0, DOI:10.5281/zenodo.3950327). The v12.9.0 model as described by Wang et al. (2021) was run at a nested horizontal resolution of 0.25×0.3125 degrees over the region (-32.0 to 15.0 °E, 0.0 to 34.0 °N), with boundary conditions provided by a separate global model run spun up for one year and with acid uptake on dust considered as described by Fairlie et al. (2010) [203, 204].

3.3 Results and Discussion

Monthly diurnal cycles of HO_2, RO_2, and OH were modelled by constraining the box model to the measurements described in Table 3.2 (except NO_2) using

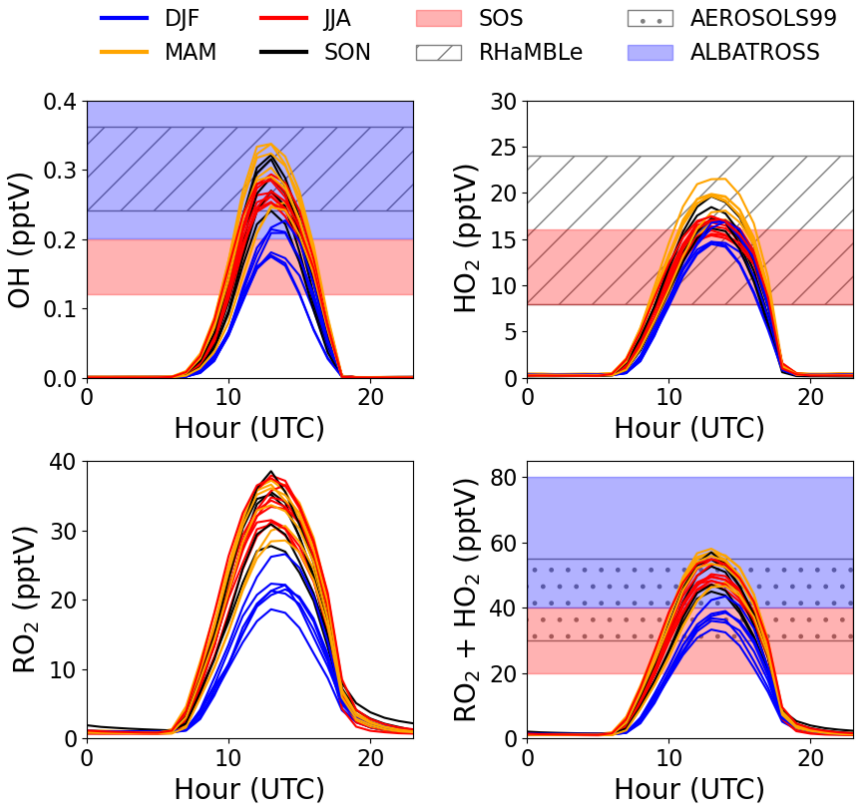

Figure 3.3: Average monthly diurnal cycles of modelled OH, HO_2, RO_2, and HO_2+RO_2 from the chemical box model coloured by season compared to midday measurements during SOS (February, May, September, and November) [114,205], RHaMBLe (May and June) [48], AEROSOLS99 (January and February) [206], and ALBATROSS (November and December) [207].

hourly median concentrations for each month from July 2017 – June 2020 where all the trace gas measurements were available. When measured $jO(^1D)$ was not available, the hourly average from the same month across the other years was used. Calculated photolysis rates based on total solar radiation (see appendix E) were used up to December 2019 for all other photolysis rates than $jO(^1D)$.

The modelled OH, HO_2 and RO_2 concentrations agree reasonably well with previous measurements from short term field campaigns based at the CVAO and from various cruises in the Atlantic Ocean (see Figure 3.3). All the previous measurements of RO_x (HO_2 + RO_2) shown in Figure 3.3 were conducted

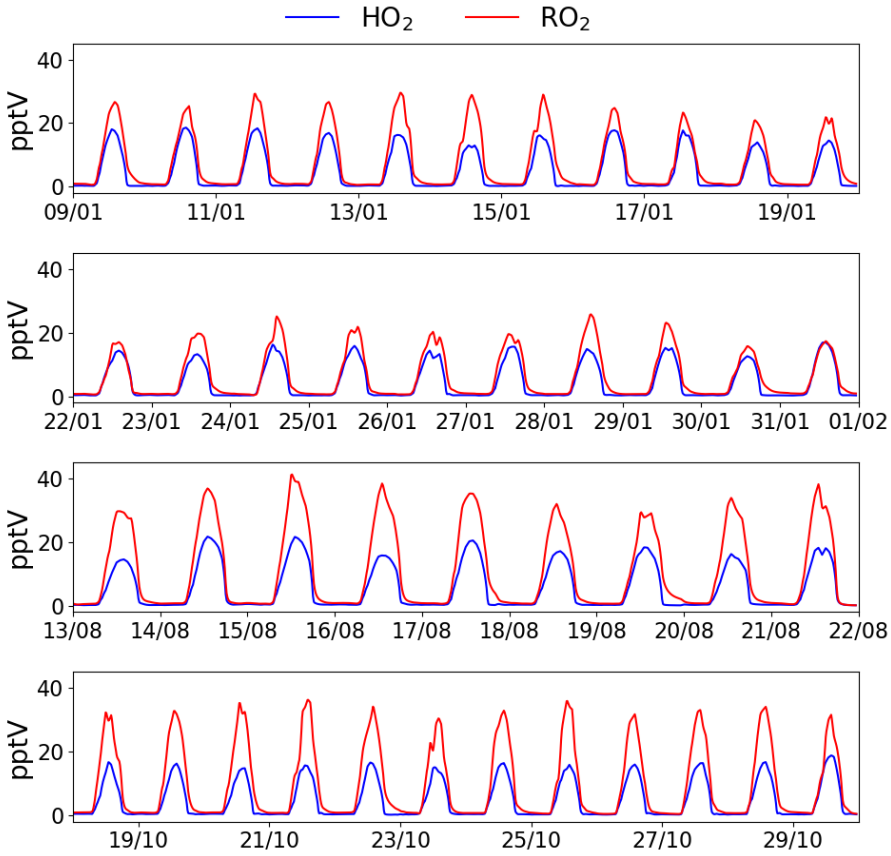

Figure 3.4: Daily modelled HO_2 (blue) and RO_2 (red) for January 2018, August 2017, and October 2017.

using the chemical amplifier technique, which is subject to high uncertainties due to the challenges described above. Daily diurnal cycles of RO_2 and HO_2 for 9 days in August 2017, 12 days in October 2017, and 20 days in January 2018 were modelled to investigate their daily variability (see Figure 3.4). Seasonal differences can be observed from the daily outputs, but no major day to day changes within a given month.

3.3.1 Comparison of Measured and PSS-Derived NO_2 Mixing Ratios

Daily midday (12.00-15.00 UTC, local+1) NO_2 mixing ratios were calculated from the Leighton ratio using equation 3.2 ($[NO_2]_{PSS}$), the measured NO, O_3,

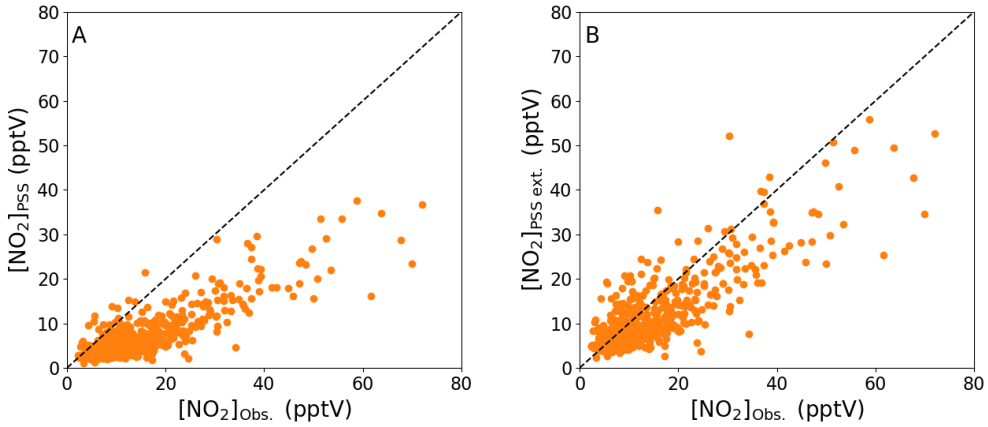

Figure 3.5: Midday (12.00-15.00 UTC, local+1) daily averages of $[NO_2]_{PSS}$ (A) and $[NO_2]_{PSS\ ext.}$ (B) plotted against the observed NO_2 using measurements from July 2017 – June 2020. The black dashed lines show the 1:1 ratio.

and jNO_2 and $k_{3.1} = 2.07 \times 10^{-12} \times e^{(-1400/T)}$ [49] for a three-year period (July 2017 – June 2020). Measurements of NO and NO_2 below the limit of detection (LOD) have not been included in the midday averages used. Midday averages have been used to ensure that jNO_2 was stable across the time period used to make sure that PSS was established. Figure 3.5A shows that $[NO_2]_{PSS}$ significantly underestimates the measured NO_2, indicating that additional oxidants are needed to convert NO into NO_2. Daily midday values of $[NO_2]_{PSS\ ext.}$ was calculated using equation 3.3, where a midday average of each modelled monthly diurnal cycle of HO_2 and RO_2 in Figure 3.3 was used for all days of their respective month together with previous yearly averaged midday measurements of IO (1.4 ± 0.8 pptV) and BrO (2.5 ± 1.1 pptV) [13, 183] at the CVAO. RO_2 was assumed to be equivalent to CH_3O_2, making $k_{3.4} = 2.3 \times 10^{-12} \times e^{(360/T)}$, $k_{3.5} = 3.45 \times 10^{-12} e^{(270/T)}$, $k_{3.6} = 7.15 \times 10^{-12} \times e^{(300/T)}$, and $k_{3.7} = 8.7 \times 10^{-12} \times e^{(260/T)}$ [49]. $[NO_2]_{PSS\ ext.}$ was calculated using a midday average of the modelled monthly $[HO_2]$ and $[RO_2]$ in Figure 3.3 as well as the modelled daily midday averages from the diurnal cycles in Figure 3.4 for August 2017, October 2017, and January 2018. A scatter plot of monthly vs. daily calculated $[NO_2]_{PSS\ ext.}$ around the 1:1 line

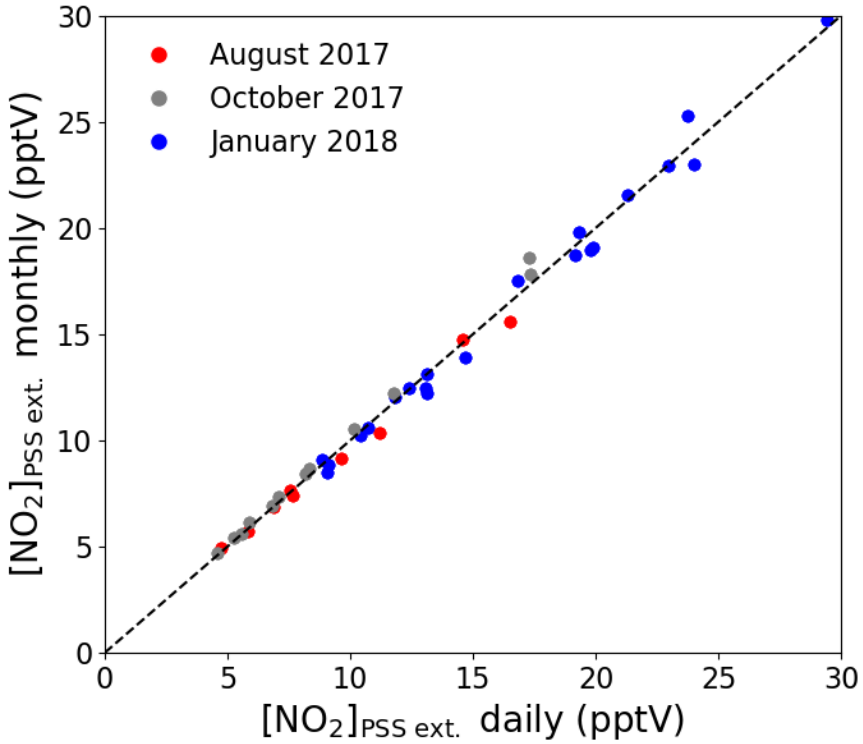

Figure 3.6: $[NO_2]_{PSS\ ext.}$ using monthly modelled diurnal cycles of RO_2 and HO_2 for August 2017 (red), October 2017 (grey), and January 2018 (blue) have been plotted against $[NO_2]_{PSS\ ext.}$ using daily modelled diurnal cycles. The dashed black line shows the 1:1 ratio.

(see Figure 3.6) verifies the use of monthly calculated $[HO_2]$ and $[RO_2]$ for the remaining analyses.

Figure 3.5B shows that the agreement between measured and calculated NO_2 was improved significantly by including modelled additional oxidants. At NO_2 mixing ratios below 20 pptV, the scatter of $[NO_2]_{PSS\ ext.}$ vs $[NO_2]_{Obs.}$ was close to the 1:1 line, however, at higher NO_2 mixing ratios $[NO_2]_{PSS\ ext.}$ under-predicts the observed NO_2 mixing ratio by on average 9.5 pptV. NO_2 mixing ratios above 20 pptV are predominantly observed at the CVAO from December-February (see chapter 2), which coincides with the arrival of predominantly African air to the site (see Figure 3.1).

We next investigate the effects of seasons and the abundance of NO on the ability of the full PSS equation (equation 3.3) to predict NO_2. Daily midday

averages of $[NO_2]_{Obs.}/[NO_2]_{PSS\ ext.}$ are plotted as a function of NO in Figure 3.7. A ratio of 1 would be expected if all relevant reaction mechanisms has been taken into account. The deviations from 1 in the ratio can be observed to increase with decreasing NO mixing ratio during March-December. The data is coloured by year; 2017 (blue), 2018 (red), 2019 (orange), 2020 (grey) to be able to distinguish interannual variability. In April the high data points when [NO] < 5 pptV can be observed to be 2019 and 2020, where 2018 is scattered around the 1:1 line. The dashed lines in Figure 3.7 visualise the effect of a constant NO_2 artefact of 0.97 pptV (our calculated upper limit) on the $[NO_2]_{Obs.}/[NO_2]_{PSS\ ext.}$ ratio, showing that the artefact, while small, can explain some of this observed trend. However, only a small dependence on the NO mixing ratio is seen for January and February, where enhancements of $[NO_2]_{Obs.}/[NO_2]_{PSS\ ext.}$ above 1 continue out to 10 pptV of NO. At Hohenpeissenberg, Germany, similar trends with increasing NO_2/NO ratio with decreasing NO have been observed, which were partly explained by measurement uncertainty in NO and partly by the PSS not being established after being perturbed by NO_x emissions or variable jNO_2 [150]. A similar study to the one presented here was conducted on a cruise in the South Atlantic Ocean, where they observed increasing deviations in $[NO_2]_{Obs.}/[NO_2]_{PSS\ ext.}$ with increasing NO_2 from 3-20 pptV [161], which was explained by a missing photolytic oxidation process. When doing the same plot for the measurements obtained at the CVAO (see Figure 3.8) a similar trend can be observed when looking at the entire measurement range of NO_2, however, $[NO_2]_{Obs.}/[NO_2]_{PSS\ ext.}$ at the CVAO only reaches half of what was observed by Hosaynali Beygi et al. (2011) [161]. When using the same range of $[NO_2]_{Obs.}/[NO_2]_{PSS\ ext.}$ and NO_2 as in the other study (see Panel B), a more flat profile can be observed here, where the ratio seem to flatten out around 1.5-2. The differences observed between the two studies can be due to different measurement techniques and filtering of data.

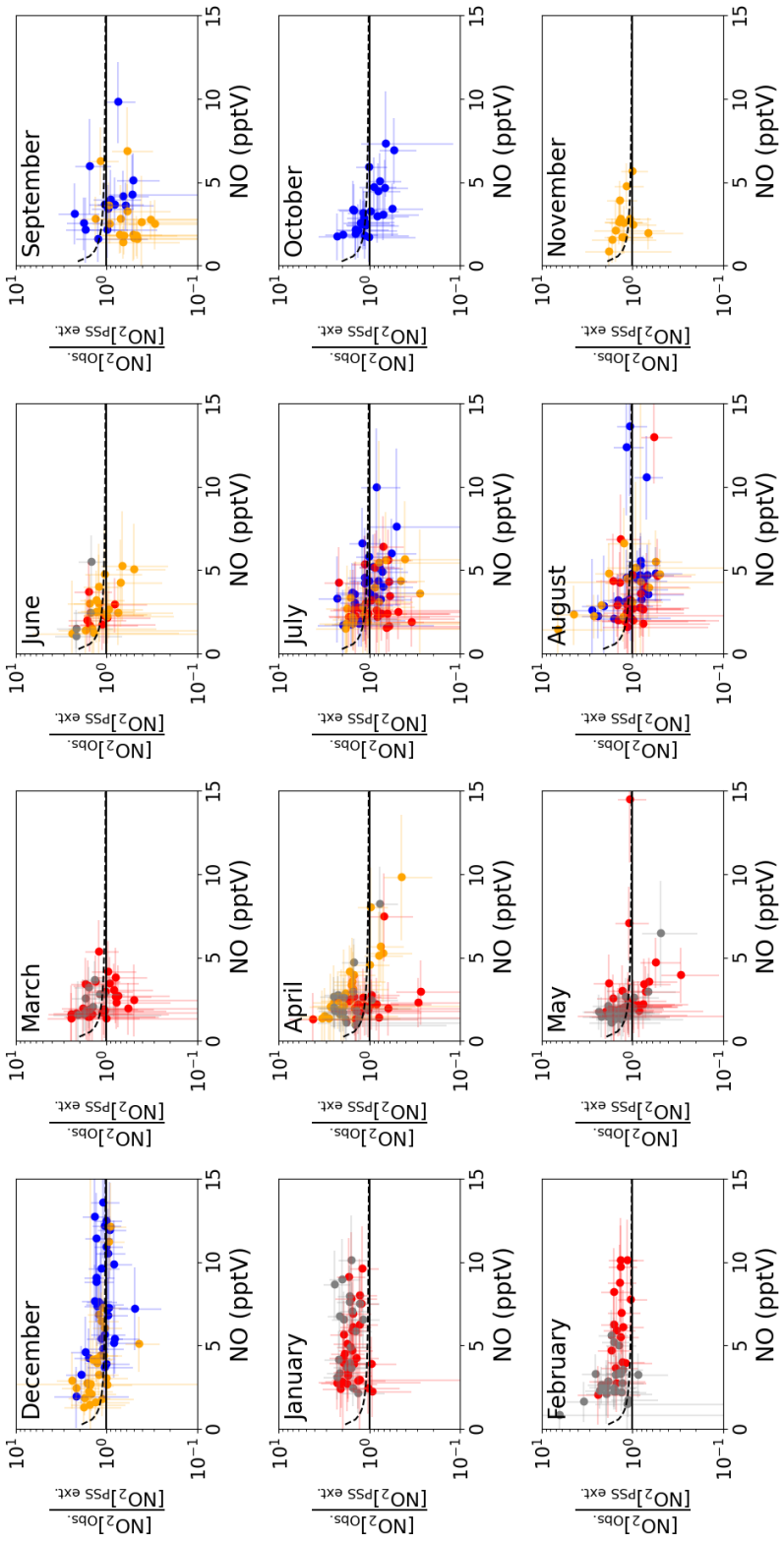

Figure 3.7: Monthly plots of midday (12.00-15.00 UTC, local+1) daily averages of $[NO_2]_{Obs.}/[NO_2]_{PSS\ ext.}$ vs. the measured NO mixing ratio. The data is coloured by year; 2017 (blue), 2018 (red), 2019 (orange), 2020 (grey). The solid lines represent a ratio of 1 between the observed and predicted NO_2. The error bars represent $\pm$ 2σ on the calculated ratio and measured NO. The dashed lines represent ($[NO_2]_{PSS\ ext.}$ + 0.97 pptV)/$[NO_2]_{PSS\ ext.}$ to visualise the effect of a NO_2 artefact of 0.97 pptV on the ratio using the average measured $j$$NO_2$ and O_3 and modelled HO_2 and RO_2 for each month and the annually average measured IO and BrO for the CVAO. The uncertainty of each data point has been determined from measurement uncertainties in Table 3.2, the uncertainties in the measured BrO and IO described in the text, and 20% uncertainty on all the rate coefficients. The uncertainty in the modelled radicals has not been included.

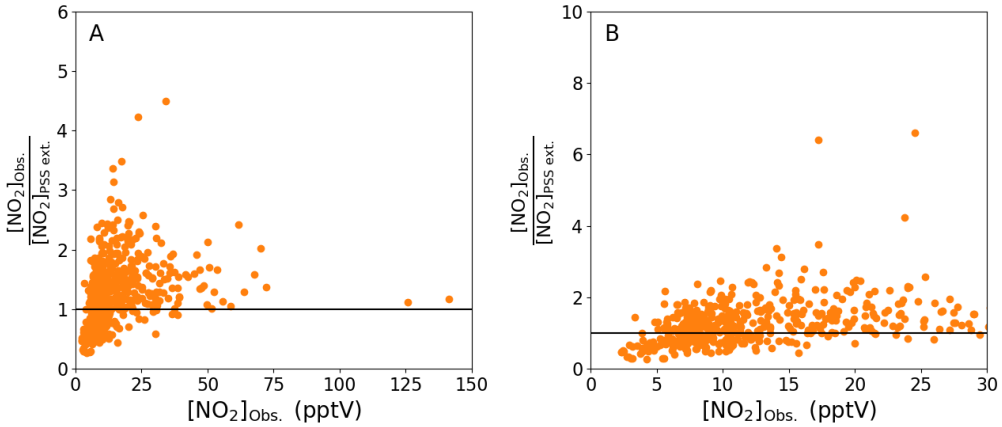

Figure 3.8: Midday (12.00-15.00 UTC, local +1) daily averages of $[NO_2]_{Obs.}/[NO_2]_{PSS\ ext.}$ from July 2017 to June 2020 plotted against $[NO_2]_{Obs.}$. (A) shows the entire measuring range of NO_2 and (B) shows the same range as used in Hosaynali Beygi et al. (2011) [161]. The black line shows the 1:1 ratio.

3.3.2 NO_2 Artefact or Missing Oxidant?

Deviations between $[NO_2]_{Obs.}$ and $[NO_2]_{PSS\ ext.}$ are usually attributed to an unaccounted artefact in the NO_2 measurements or a missing oxidant converting NO into NO_2 [158, 161, 167, 170, 171, 208, 209]. As discussed above, we show that below 5 pptV of ambient NO, our calculated maximum NO_2 artefact of 0.97 pptV starts to have an impact on the $[NO_2]_{Obs.}/[NO_2]_{PSS\ ext.}$ ratio and the deviation at very low NO can on most days be explained by the measurement uncertainty in NO ($\sim$1.4 pptV), however, it is not enough to explain the enhancements observed, especially in wintertime at the CVAO.

The production of RO_2 and HO_2 radicals is dependent on the abundance of their VOC and CO precursors as well as on photochemical activity. When modelling RO_2 and HO_2 radicals, they are also highly dependent on the reaction scheme in the model being complete. To investigate whether the availability of VOCs, CO or sunlight was related to the discrepancy between $[NO_2]_{Obs.}$ and $[NO_2]_{PSS\ ext.}$, $[NO_2]_{Obs.}/[NO_2]_{PSS\ ext.}$ was plotted against different precursors and meteorological parameters in Figure 3.9. The high deviations in $[NO_2]_{Obs.}/[NO_2]_{PSS\ ext.}$ can be observed to be associated with higher mea-

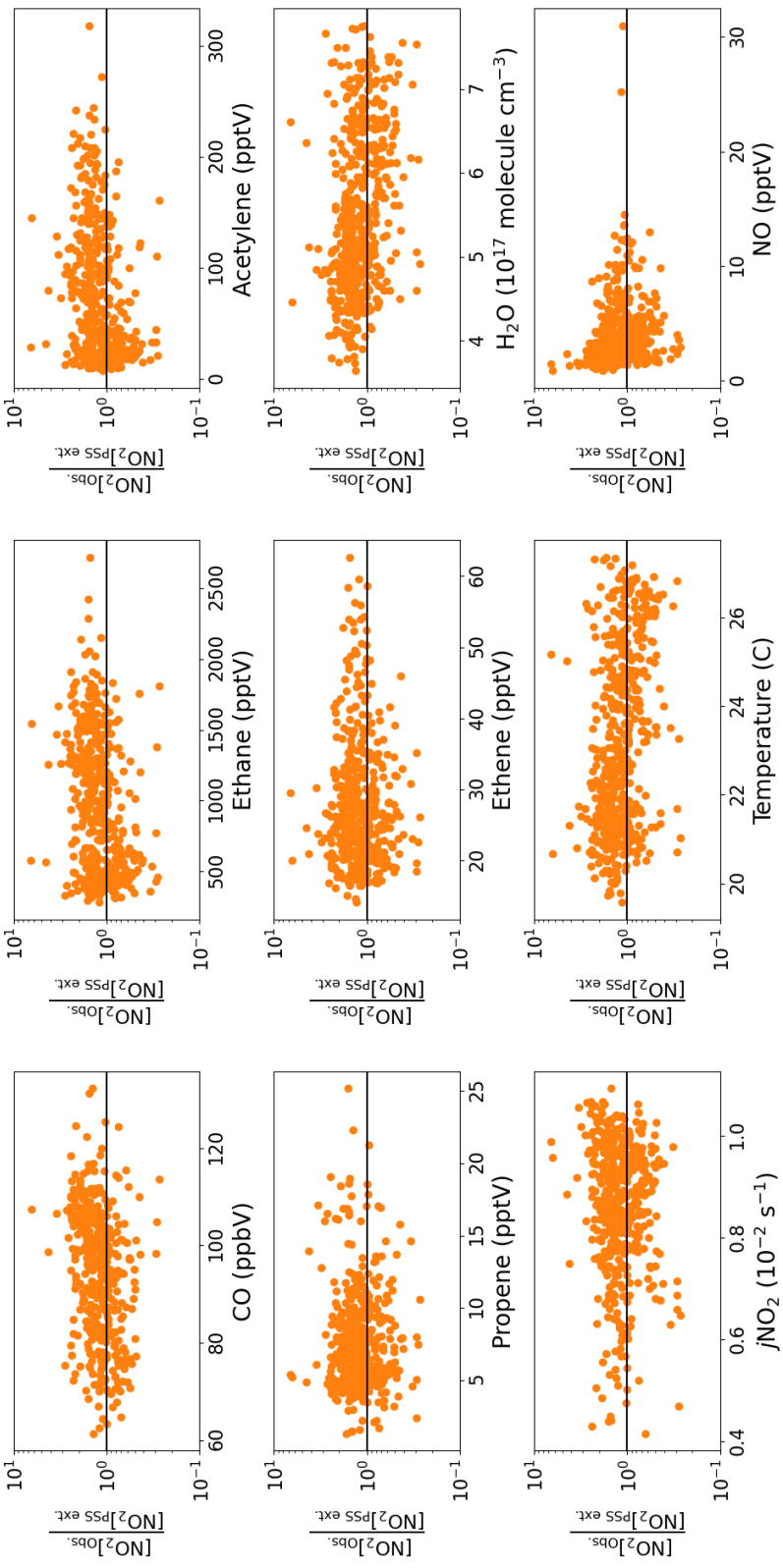

Figure 3.9: Midday (12.00-15.00 UTC, local +1) daily averages of $[NO_2]_{Obs.}/[NO_2]_{PSS\ ext.}$ from July 2017 to June 2020 plotted against five measured precursors for either HO_2 or RO_2, H_2O, jNO_2, and temperature. The line represent a ratio of 1.

sured mixing ratios of CO, ethane, and acetylene, and lower midday temperature. No obvious trend can be observed for the dependence on jNO_2, even though Hosaynali Beygi et al. (2011) [161] observed the largest deviations in $[NO_2]_{Obs.}/[NO_2]_{PSS\ ext.}$ at similar jNO_2 as observed at the CVAO at midday ($>0.007\ s^{-1}$). Figure 3.9 shows that the abundances of ethene and propene, both of which have atmospheric lifetimes of less than 3 days, do not seem to affect the deviation of $[NO_2]_{Obs.}/[NO_2]_{PSS\ ext.}$ from 1. Conversely, high abundances of CO, ethane, and acetylene, which all have atmospheric lifetimes above 6 weeks [210], are observed to be associated with higher $[NO_2]_{Obs.}/[NO_2]_{PSS\ ext.}$ ratios. This could indicate that long-range transport of pollutants supplies additional peroxy radicals (or other NO to NO_2 oxidants) at the CVAO, which are not predicted from known sources and photochemistry.

To further evaluate the impact of pollution, $[NO_2]_{Obs.}/[NO_2]_{PSS\ ext.}$ was separated into three categories based on CO mixing ratios; CO $<$ 90 ppbV, 90 ppbV $<$ CO $<$ 100 ppbV, and CO $>$ 100 ppbV. These splits were chosen based on the median $[NO_2]_{Obs.}/[NO_2]_{PSS\ ext.}$ over 10 ppbV increments in the CO mixing ratio, where each category had to have a similar amount of measurements. The deviations of $[NO_2]_{Obs.}/[NO_2]_{PSS\ ext.}$ from 1 increase with increasing [CO], with 50^{th} (25^{th}-75^{th}) percentiles of 1.10 (0.82-1.37) for CO $<$ 90 ppbV, 1.20 (0.97-1.54) for 90 ppbV $<$ CO $<$ 100 ppbV, and 1.50 (1.18-1.78) for CO $>$ 100 ppbV. The small deviation from 1, which is within the uncertainty of our measurements (see below), for CO $<$ 90 ppbV is strong evidence that fundamental oxidation processes in ultra-clean marine air, where the main precursors of RO_2 and HO_2 are CH_4 and CO giving CH_3O_2 and HO_2, respectively, are well understood.

An NO_2 artefact of 0.7 pptV would reduce the ratio of 1.10 to 1.00 in air masses with CO $<$ 90 ppbV. Since the minimum value of the artefact is 0 pptV (if there was no conversion of interferent compounds to NO or NO_2), and our estimated upper limit is 0.97 pptV, we therefore consider it a reasonable assumption that the NO_2 artefact of our instrument at the CVAO is

0.7 pptV. We make the simple *a priori* assumption that this applies across all measurements during the period of analyses. Such an artefact is insignificant when considering total NO_x concentrations, however, it has a non-negligible impact when investigating NO_2/NO ratios in this very low NO_x environment.

Subtracting 0.7 pptV from all the NO_2 observations results in median (25^{th}-75^{th} percentiles) ratios of 1.00 (0.76-1.29) for CO $<$ 90 ppbV, 1.14 (0.89-1.47) for 90 ppbV $<$ CO $<$ 100 ppbV, and 1.42 (1.12-1.68) for CO $>$ 100 ppbV. Distributions of each category are plotted in Figure 3.10A. When CO is between 90 and 100 ppbV, the distribution of $[NO_2]_{Obs.}/[NO_2]_{PSS\ ext.}$ shows the highest occurrences at ratios of $\sim$1 and $\sim$1.5. When CO $>$ 100 ppbV, it is evident that either additional oxidants are needed to convert NO to NO_2, or an additional NO_2 artefact of the order of 4.4 pptV is present in these air masses. As an artefact of 0.7 pptV has already been subtracted, and measurements of HONO and PAN and modelled mixing ratios of halogen nitrates indicate a fairly stable artefact across the year (see Figure 3.2), 4.4 pptV of additional artefact seems highly unlikely. This leaves the possibility of a missing oxidant when the sampled air is enhanced in CO.

Using equation (3.4) and (3.5), the required RO_x (RO_2 + HO_2) and XO (IO + BrO) concentrations needed to reconcile $[NO_2]_{Obs.}$ with $[NO_2]_{PSS\ ext.}$ can be estimated using $k_{3.4,3.5} = 2.3\times10^{-12}\times e^{(360/T)}$ and $k_{3.6,3.7} = 8.7\times10^{-12}\times e^{(260/T)}$ [49]. CH_3O_2 and its rate coefficient with NO has been used as a proxy for all RO_x in these calculations due to it representing over 90% of all the modelled peroxy radicals at midday. Our calculations are based on two scenarios: (1) that the measured [BrO] and [IO] are correct and there is missing RO_x, or (2) that the modelled $[RO_x]$ is correct and there is missing [XO]. Due to the similar rate coefficients for IO and BrO reacting with NO, a combined XO can be estimated. The results are summarised in Table 3.4 based on the three CO categories. The median required RO_x was determined to be 65.0 (33.68 - 112.5, 25^{th}-75^{th} percentile) pptV and 109.7 (63.14 - 149.5, 25^{th}-75^{th} percentile) pptV for 90 ppbV $<$ CO $<$ 100 ppbV and CO $>$ 100 ppbV, respectively. RO_x

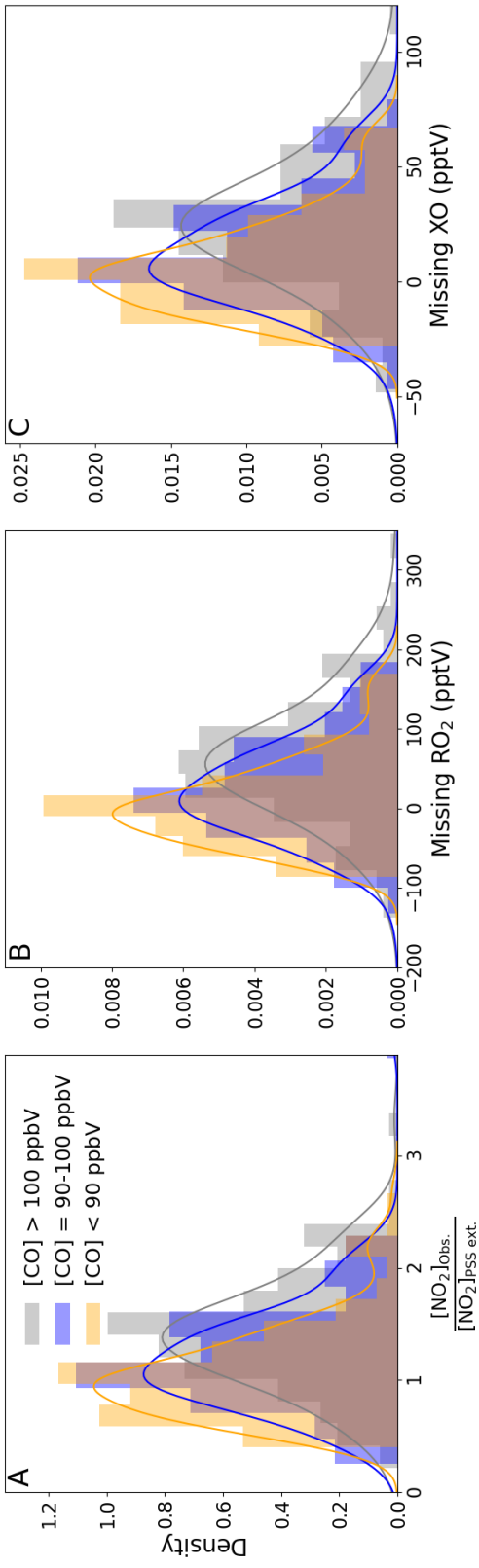

Figure 3.10: Density distributions of (A) $[NO_2]_{Obs.}/[NO_2]_{PSS\ ext.}$, (B) missing RO_2, and (C) missing XO separated by measured CO mixing ratios. An NO_2 artefact of 0.7 pptV has been subtracted from all data.

measurements during the ALBATROSS cruise varied from 40-80 pptV while in the North Atlantic, however, with a reported uncertainty of 25% (1σ) they could be as high as 100 pptV [207]. Such concentrations are comparable to the required median RO_x in this study of 109.7 pptV when CO > 100 ppbV. The uncertainty reported for ALBATROSS is similar to many other studies which have reported 10-36% (1σ) uncertainty on chemical amplification RO_x measurements [155,158,161,206,211,212], however, a recent study in the Pearl River Delta reported an uncertainty of 60% (1σ) [157]. This combined with measurements up to ∼150 pptV of RO_x in the South Atlantic Ocean [161] indicates that our required RO_x levels of ∼100 pptV may not be unrealistic in the MBL. Other peroxy radicals such as $C_2H_5O_2$, *n*- and *i*-$C_3H_7O_2$, and $C_2H_5(O)O_2$ have slightly faster reactions rates with NO at 298 K [210] which would result in less required RO_2, however, they are not expected to be the dominant peroxy radical specie at the CVAO.

The median required RO_x ($[RO_x]_{PSS}$) can be observed to be ∼2.5 times higher than those modelled for air masses where CO > 100 ppbV, whereas the required [XO] is a factor of ∼6.5 higher than previous observations at the CVAO [13, 183] due to the lower rate coefficients for halogen oxides with NO. Across the three categories, the daily median ratio of $[RO_x]_{PSS}/[RO_x]_{Model}$ is 1.5, which is similar to those observed in previous studies both in remote and rural regions (see Table 3.1). The missing XO required to reconcile $[NO_2]_{Obs.}$ with $[NO_2]_{PSS\ ext.}$ was determined for each CO category by subtracting the previous measured average concentration of 3.9 pptV (2.5 pptV BrO + 1.4 pptV IO) from the required XO. Since CO, the main precursor for HO_2, is constrained by measurements in the model and is in good agreement with previous measurements (see Figure 3.3), the calculated $[HO_2]$ is assumed to be correct. Thus, we estimate the required and missing RO_2 assuming it is all in

Table 3.4: Summary over the required additional artefact, RO_2, and XO to give $[NO_2]_{Obs.}/[NO_2]_{PSS\ ext.} = 1$ given as 50^{th} (25^{th}-75^{th}) percentile when subtracting a NO_2 artefact of 0.7 pptV.

	[CO] < 90 ppbV	90 ppbV < [CO] < 100 ppbV	[CO] > 100 ppbV
$\frac{[NO_2]_{Obs.}}{[NO_2]_{PSS\ ext.}}$	1.00 (0.76 - 1.29)	1.14 (0.89 - 1.47)	1.42 (1.12 - 1.68)
Required additional artefact (pptV)	0.00 (-2.65 - 1.70)	1.90 (0.92 - 5.27)	4.40 (0.95 - 9.27)
Case I: Using BrO = 2.5 pptV and IO = 1.4 pptV			
Required RO_x (pptV)[a]	49.45 (16.18 - 87.63)	65.00 (33.68 - 112.5)	109.7 (63.14 - 149.5)
Modelled RO_x (pptV)	48.89 (46.01 - 53.35)	45.60 (35.69 - 54.71)	44.99 (37.31 - 54.70)
Required RO_2 (pptV)[b]	31.77 (-1.79 - 69.99)	47.53 (16.81 - 93.93)	90.49 (45.04 - 128.5)
Modelled RO_2 (pptV)	33.66 (30.07 - 34.43)	29.89 (21.50 - 36.32)	27.62 (20.93 - 35.42)
Missing RO_2 (pptV)[c]	-0.25 (-31.85 - 39.69)	20.19 (-14.23 - 66.44)	61.33 (18.53 - 104.3)
Case II: Using modelled RO_2 and HO_2			
Required XO (pptV)[d]	3.72 (-7.94 - 18.55)	11.31 (-1.46 - 28.46)	26.58 (10.70 - 42.52)
Missing XO (pptV)[e]	-0.18 (-11.84 - 14.65)	7.41 (-5.36 - 24.56)	22.68 (6.80 - 38.62)

[a]Calculated using equation (IV). [b]Calculated using equation (VIII). [c]Calculated using equation (IX). [d]Calculated using equation (V). [e]Subtracted 3.9 pptV of XO from the required XO (2.5 pptV BrO + 1.4 pptV IO).

the form of CH_3O_2 from:

$$[RO_2]_{\text{Required}} = \frac{jNO_2[NO_2] - (k_{3.1}[O_3] + k_{3.5}[HO_2] + k_{3.6}[IO] + k_{3.7}[BrO])[NO]}{k_{3.4}} \quad \text{(Eq. 3.8)}$$

$$[RO_2]_{\text{Missing}} = [RO_2]_{\text{Required}} - [RO_2]_{\text{Model}} \quad \text{(Eq. 3.9)}$$

Figures 3.10B and C, show that the missing RO_2 or XO level increases with increasing [CO], reaching a median of 61.33 pptV and 22.68 pptV, respectively, for air masses where CO $>$ 100 ppbV, which is approximately 2.2 times the modelled RO_2 and 5.5 times the measured XO in the same air masses. Such an increase in peroxy radicals would, under more polluted conditions, cause a major increase in O_3 production during a day [158]. We next examine the impact of missing RO_2 on the net O_3 production in Cabo Verde.

3.3.3 Chemical O_3 Loss

The daily chemical loss of O_3 between 09.30 (09.00-10.00) and 17.30 (17.00-18.00) UTC was used to evaluate whether the PSS-derived $[RO_2]$ was consistent with the net chemical destruction of O_3 at the CVAO. As discussed above, the measured O_3 mixing ratio in the MBL is affected by loss mechanisms in the form of photolysis, reactions with HO_x and halogens, and deposition, and by production through NO_2 photolysis and by entrainment from the O_3-enriched free troposphere. Due to the very stable meteorological condition of the MBL, the variability in entrainment and deposition between night and day is expected to be negligible [13, 188, 189]. A combined entrainment/deposition term can therefore be estimated from night time O_3 measurements, when there is no photochemical production or loss. An hourly entrainment/deposition term was determined for each month using the average change in O_3 between 22.30

(22.00-23.00) and 03.30 (03.00-04.00) UTC, and found to vary from 0.18 ± 0.30 ppbV h^{-1} in January to 0.35 ± 0.30 ppbV h^{-1} in May, which is in good agreement with previous measurements at the CVAO of 0.18-0.48 ppbV h^{-1} [13]. The observed daily change in O_3 ($\Delta O_{3\ obs.}$) (09.30-17.30) was determined to be -0.40 ± 0.32 ppbV h^{-1} (1σ) across the three years (2017-2020), which is almost identical to the -0.41 ± 0.33 ppbV h^{-1} (1σ) observed at the CVAO in 2007 [13], but roughly 2 times the daily $\Delta O_{3\ obs.}$ in baseline air at Cape Grim (-0.24 ± 0.32 ppbV h^{-1}, 1σ) and Mace Head (-0.20 ± 0.21 ppbV h^{-1}, 1σ) [169] and 2-40 times the modelled O_3 loss at Mauna Loa (-0.01 to -0.21 ppbV h^{-1}) [213, 214].

By subtracting the monthly average entrainment/deposition term from the observed daily ΔO_3, the daily chemical loss of O_3, $\Delta O_{3\ chem.}$, is obtained. The observations were filtered to exclude periods where the change in CO concentration over the interval period, ΔCO, was outside 1 standard deviation of the mean ΔCO, to avoid the ΔO_3 determination being affected by changing air masses. The resulting observed chemical loss of O_3 is averaged by month and plotted in black in Figure 3.11. $\Delta O_{3\ chem.}$ can be observed to follow the photochemical activity, with the lowest $\Delta O_{3\ chem.}$ in October-February, where the lowest photolysis rates are measured (see appendix E and Table 3.2) and highest $\Delta O_{3\ chem.}$ in March-May and September. A small decrease in $\Delta O_{3\ chem.}$ in June-August occurred simultaneously to the small drop in photolysis rates in June-August. Overall, $\Delta O_{3\ chem.}$ varied from -0.48 ppbV h^{-1} in January to -0.88 ppbV h^{-1} in May.

In order to evaluate whether these observationally-derived chemical loss rates of O_3 are consistent with PSS-derived peroxy radical concentrations, $\Delta O_{3\ chem.}$ was estimated using a chemical box model incorporating the MCM, as described in section 3.2.2.1. The model was constrained to all the measurements described in Table 3.2, except NO_2 and O_3, which were left unconstrained. $\Delta O_{3\ chem.}$ was simulated with modelled [RO_2] and [HO_2], with (blue line in Figure 3.11) and without (grey in Figure 3.11) inclusion of the halo-

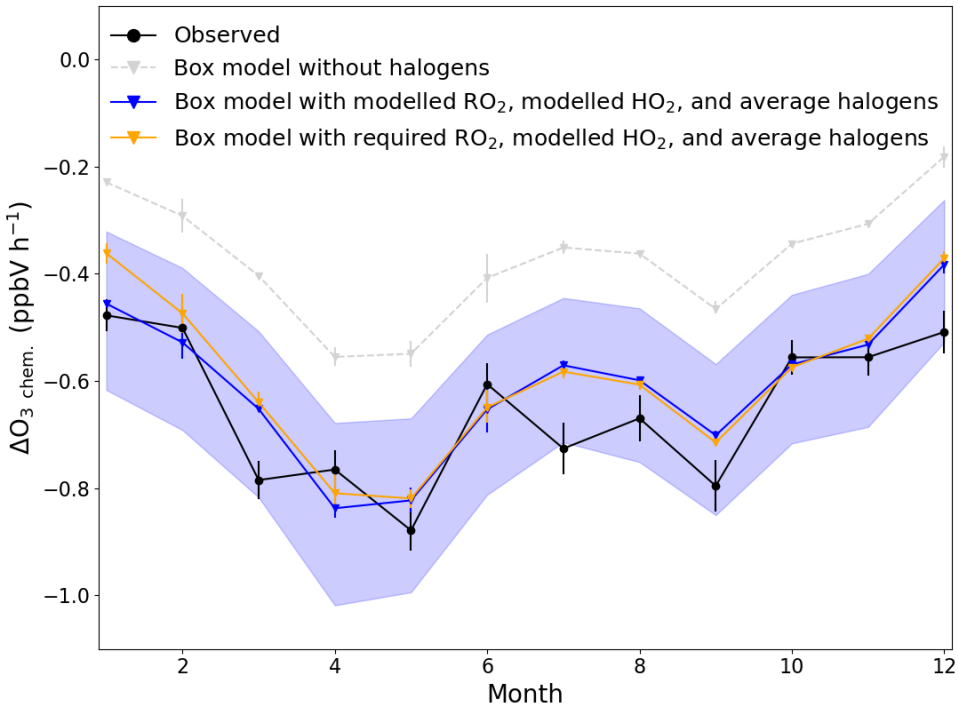

Figure 3.11: Average monthly ΔO_3 due to chemical loss between 09.30 (09.00-10.00) and 17.30 (17.00-18.00) UTC for each month (black) compared to box modelled ΔO_3 due to chemical loss using modelled RO_2 and HO_2 with (blue) and without (grey) halogen monoxides (BrO and IO), and using required RO_2 to get $[NO_2]_{Obs.}/[NO_2]_{PSS\ ext.} = 1$, modelled HO_2, and the annually averaged halogen monoxides (orange). The error bars on the observed chemical loss is the standard error of all the days used for each month and for the box model it is the minimum and maximum ΔO_3 modelled for each month. The blue shaded area show the possible variability in the chemical loss when including the measured halogens at the CVAO (BrO; 2.5 ± 1.1 pptV, IO; 1.4 ± 0.8 pptV) [13].

gen chemistry described in Appendix G, allowing an evaluation of the O_3 loss due to halogens, as previously discussed by Read et al. (2008). Simulations were also performed with $[CH_3O_2]$ constrained to the required RO_2 as modelled $[CH_3O_2]$ is >90% of the modelled $[RO_2]$, modelled $[HO_2]$ and including halogen chemistry (orange in Figure 3.11). In model runs with halogen chemistry, BrO and IO were constrained to previously measured annual averages ± reported uncertainties (blue shaded area in Figure 3.11) [13]. Diurnal cycles of the required RO_2 were constructed using the median of the daily midday averages

for each month determined using equation (3.8) for the peak concentration at midday, 1 pptV overnight and interpolating linearly in between.

Figure 3.11 shows that all three modelled $\Delta O_{3\ chem.}$ exhibited very similar seasonality as the observed $\Delta O_{3\ chem.}$. The difference between running the model with and without halogen chemistry was 0.24 ± 0.02 ppbV h^{-1} (1σ), which is almost equivalent to the results of Read et al. (2008) from the CVAO of 0.23 ± 0.05 ppbV h^{-1} (1σ). From May-December, the modelled $\Delta O_{3\ chem.}$ was almost identical whether using modelled RO_2 or constraining CH_3O_2 to the required RO_2, and both were very similar to observed $\Delta O_{3\ chem.}$. The largest difference in $\Delta O_{3\ chem.}$ between using modelled RO_2 and constraining CH_3O_2 is observed in January where the difference reached 0.09 ppbV h^{-1}, however, this is caused by constraining CH_3O_2 to 100 pptV, which is 5 times more than the modelled RO_2. The average difference between the observed and modelled $\Delta O_{3\ chem.}$ is 0.06 ± 0.07 ppbV h^{-1} (1σ) when constraining CH_3O_2 to the required RO_2 and 0.04 ± 0.07 ppbV h^{-1} (1σ) when using modelled RO_2.

When constraining RO_2 to required CH_3O_2 it also impacts the modelled OH and HO_2 through increasing HO_2+RO_2, which results in a reduction of HO_2+NO and HO_2+O_3. OH can be observed to increase most months when constraining CH_3O_2 to the required RO_2 (see Figure 3.12), where HO_2 decreases, however, they remain within the previous measurements.

Overall, the very small differences in modelled $\Delta O_{3\ chem.}$ whether including the "missing RO_2" or not are a function of the NO_x-limited conditions of the remote MBL, where O_3 production is relatively insensitive to the mixture and abundance of peroxy radicals [215]. Thus, although our analysis shows that peroxy radicals with the equivalent O_3 production potential as CH_3O_2 cannot be ruled out as the missing oxidant in marine air masses with aged pollution, neither does it provide robust evidence that the missing oxidant is O_3-producing. Nevertheless, the deviation between PSS-derived peroxy radicals in this study and previous measurements can potentially be explained by the difficulty in measuring peroxy radicals, as discussed above.

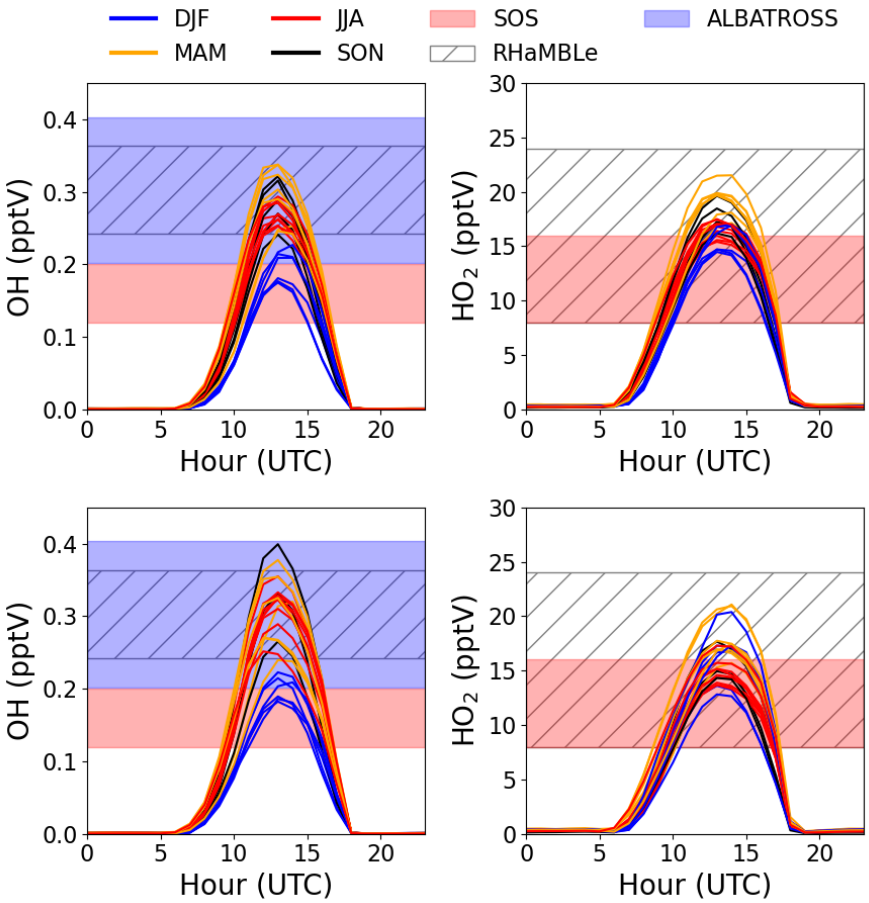

Figure 3.12: Average monthly diurnal cycles of modelled OH and HO_2 with (bottom two panels) and without (top two panels) constraining CH_3O_2 to the required RO_2 from the chemical box model coloured by season compared to midday measurements during SOS (February, May, September, and November) [114, 205], RHaMBLe (May and June) [48], AEROSOLS99 (January and February) [206], and ALBATROSS (November and December) [207].

3.4 Conclusions

In the remote MBL (CO $<$ 90 ppbV, NO_x $<$ 43 pptV) we have shown that the observed NO_2/NO ratio is consistent with fundamental photochemical theory, and that neither missing oxidants nor deviations of the photostationary state are required to reconcile observations with the calculated NO_2/NO ratio. This is to our knowledge the first time this has been shown in a low NO_x environment. However, observed NO_2 levels became increasingly higher than

predicted as the CO mixing ratio increased and the air more influenced by long range transport of air pollution in winter. A detailed analysis of potential NO_2 measurement artefacts at the CVAO showed that such artefacts were unlikely to account for these deviations, thus we evaluated the case for a missing NO to NO_2 oxidant. The required oxidant in air masses with CO $>$ 100 ppbV reached a median of 109.7 pptV when treated as CH_3O_2. These levels are $\sim$2.5 times higher than both our modelled RO_x (RO_2 + HO_2) and previous measurements of RO_x measured by chemical amplification at the CVAO. However, chemical amplification measurements are known to be highly uncertain due to the difficulty in determining the chain length of the mixture of RO_2 in the ambient matrix, and we note that the modelled O_3 production at the CVAO, with the inclusion of these additional peroxy radicals, did not deviate significantly from the observed O_3 production. Overall, we conclude that there is strong evidence for a missing oxidant in remote marine air impacted by long range transport of pollution, and that peroxy radicals cannot be ruled out as to their identity.

Chapter 4

Extensive Field Evidence for the Release of HONO from the Photolysis of Nitrate Aerosols

Ground-based measurements of NO_x, HONO, particulate nitrate, and photolysis rates have been conducted by me, Roberto Sommariva (University of Birmingham), TROPOS, and Katie Read (University of York). I have organised, sampled, and analysed the airborne aerosol measurements. Chris Reed (FAAM) has run the NO_x and HONO instrument on the aircraft and calibrated it together with Graham Boustead (University of Leeds) and Lauren Fleming (University of Leeds), while the processing of the raw data from the campaigns and the calibration was performed by me. Graeme Nott (FAAM) measured and processed aerosol surface area on the aircraft. Lisa Whalley (University of Leeds) processed the photolysis measurements from the aircraft. Tomás Sherwen (University of York) modelled OH concentrations and photolysis rates using GEOS-Chem. I ran HYSPLIT back trajectories for the aircraft measurements. All data analysis was conducted by me.

4.1 Introduction

Nitrous acid (HONO) has a key role in tropospheric chemistry as an important source of NO_x ($NO + NO_2$) and of the hydroxyl radical (OH) [44, 51, 66–73]. NO_x regulates the abundance of atmospheric oxidants (O_3 and OH) as well as being essential for the formation of secondary atmospheric aerosols, and OH controls the self-cleansing capacity of the atmosphere via degradation of pollutants and greenhouse gases such as methane [72].

Primary HONO emission sources include vehicle exhaust, wildfires and soils [65–67], but it is also produced through the gas-phase reaction of NO and OH radicals (R4.1). Photolysis (R4.2), reaction with OH radicals (R4.3) and dry deposition (R4.4) are the major loss mechanisms for HONO:

$$NO + OH + M \longrightarrow HONO + M \tag{R4.1}$$

$$HONO + h\nu(\leq 390\,\text{nm}) \longrightarrow NO + OH \tag{R4.2}$$

$$HONO + OH \longrightarrow NO_2 + H_2O \tag{R4.3}$$

$$HONO \xrightarrow{\text{deposition}} \tag{R4.4}$$

In the remote oceanic troposphere, NO_x levels are too low to supply any significant levels of HONO from (R4.1) and primary HONO emission sources are absent. A recent study by Crilley et al. (2021) has investigated whether the ocean surface is a source of HONO and their findings suggest that the rate of conversion from NO_2 to HONO by the ocean is negligible [68]. Reactions on aerosol surfaces have historically been suggested to make only moderate contributions to daytime HONO formation [69], although there is evidence for NO_2 to HONO conversion on aerosols in polluted to semi-polluted regions [70,71,73]. Laboratory studies have also showed that illuminated TiO_2 particles in the presence of 34-200 parts per billion by volume (ppbV) NO_2 produces HONO [216–218] with reported HONO yields per lost NO_2 molecule as high as $\sim 75\%$ [218]. No known studies have investigated this process with NO_2 mixing

ratios in the order of parts per trillion by volume (pptV), however, it is not expected to have a significant impact as it depends on the start concentration of NO_2.

Over the past 20 years several laboratory studies have suggested that photolysis of particulate nitrate (pNO_3^-) on different surfaces such as trees, metal, glass, urban grime and aerosols could be a significant source of HONO and NO_x compared to photolysis of gaseous HNO_3 [219–225]:

$$pNO_3^- + h\nu \longrightarrow x\,HONO + y\,NO_2 \tag{R4.5}$$

As the photolysis rate of pNO_3^-, $j pNO_3^-$, cannot be measured directly like gas phase photolysis rates due to the absorption cross section for pNO_3^- being red-shifted and broader compared to that of gas phase HNO_3 [220], it is usually reported as an enhancement factor compared to that of gaseous HNO_3; $f = j pNO_3^- / j HNO_3$. There is a very high uncertainty in f, with laboratory studies reporting values spanning three orders of magnitude ($\sim$10–1700) depending on the surface (Table 4.1).

Recent field observations of HONO in the marine atmosphere offers a method to diagnose the presence of any missing sources but are so far limited to only a few days of measurements, which have reported enhancement factors of $\sim$25–300 for photolysis of pNO_3^- associated with sea-salt aerosols [44, 51, 52]. The marine field observations are well within the range reported in laboratory experiments. However, recent experiments using suspended nitrate particles [228] and calculations derived from observed ratios of NO_x/HNO_3 in the polluted boundary layer [226] have derived much smaller f of 1-30. Thus, there is as yet no consensus on whether 'renoxification' offers a limited or a highly significant role in the NO_x and OH budgets of remote environments, nor field evidence for HONO production from photolysis of pNO_3^- occurring on ambient aerosol other than sea-salt aerosol.

The renoxification process has been shown to be impacted by multiple

Table 4.1 Overview of previous studies investigating the photolysis of surface adsorbed nitrate.

Study type	Surface	$[pNO_3^-]$ $(10^{-9}\,mol\,m^{-3})^b$	$jpNO_3^-$ $(10^{-5}\,s^{-1})^e$	$jpNO_3^- \rightarrow HONO$ $(10^{-5}\,s^{-1})^f$	Enhancement factor $(f)^g$	Airmass origin	Ref.
Field	Aerosols	0.04-2.0		20	150-450	Marine	[51]
Field/Laboratory	Aerosols	0.7-39.5	0.62-50.0		8-700	Urban, rural, remote	[223]
Field/Model	Aerosols	40-265[c]			1-30		[226]
Global Model	Aerosols	0.4-40			25-100	Marine	[227]
Laboratory	Aerosols[a]	1600-9700			<10		[228]
Field/Laboratory	Aerosols	5-15			18-54[h]	Marine	[52]

Study type	Surface	$D_{HNO_3^-}$ $(10^{-7}\,mol\,m^{-2})^d$	$jpNO_3^-$ $(10^{-5}\,s^{-1})^e$	$jpNO_3^- \rightarrow HONO$ $(10^{-5}\,s^{-1})^f$	Enhancement factor $(f)^g$	Airmass origin	Ref.
Laboratory	Glass	0.5-12.5	2.2-6.0	0.16-1.4	10-100		[224]
Laboratory	Urban grime		120		1700	Urban	[219]
Laboratory	Aluminium	4-251	5.7-15.3		8-220		[222]
Laboratory	Oak	3-174	1.6-37.0		20-530		[222]
Laboratory	Maple	22-380	0.9-4.9		10-70		[222]
Laboratory	Pyrex glass	11-250	0.5-2.1	0.34-1.6	7-30		[229]
Laboratory	Glass	2.5-55		0.024	0.34		[230]

[a]Pure nitrate salts added to Teflon chambers. [b]Concentrations of pNO_3^- given in other units than moles m^{-3} have been converted using T = 298 K and P = 1 atm. [c]pNO_3^- here is the sum of pNO_3^- and HNO_3 (5^{th}-95^{th} percentile). [d]Density of pNO_3^- on surface. [e]Determined from the production of $HONO+NO_2$. [f]Determined from the production of HONO. [g]Estimated using $jHNO_3 = 7 \times 10^{-7}$ s^{-1} if not reported in the study. [h]25^{th}-75^{th} percentile.

different parameters such as acidity of the aerosols, relative humidity, temperature, location of pNO_3^- in the aerosol, and coexisting chemical species (eg. halide ions and organics) [220, 221, 225, 231–238]. Acidity does not affect the photolysis rate constant, but it does affect which products are formed. Scharko et al. (2014) observed decreasing production of HONO with increasing pH with a maximum at a pH of approximately 2 and no HONO production at pH $\geq$ 4, which can be explained by HONO having a pK_a value of 3.2 [221]. NO_2 production was observed to be constant across all pH. Relative humidity can impact the process by regulating the NO_3^- concentration in the liquid phase of the aerosol as well as the HONO production through the H_2O+NO_2 reaction and temperature has been shown to impact the quantum yield of the products [231, 232].

Laboratory studies suggest that renoxification is driven by photolysis of surface-bound pNO_3^-. The absorption cross section of nitrate adsorbed on to aluminium, ice, and silica surfaces has been shown to be up to two orders of magnitude larger than for gas phase HNO_3 due to optimal alignment and orientation of nitrate molecules on surfaces resulting in a red-shift of the absorption cross section compared to in gas phase. At the same time the quantum yield of the photolysis only drops from close to 1 to $\geq$ 0.6 on surfaces, leading to significantly enhanced pNO_3^- photolysis compared to bulk aqueous or gas phase HNO_3 [220, 225, 238]. However, it should be noted that one study has estimated the quantum yield of the production of HONO to be orders of magnitude lower [230]. Knowledge about quantum yields and absorption cross sections is important to be able to extrapolate laboratory studies to atmospherically relevant enhancement factors. Furthermore, Wingen et al. (2008) showed increasing production of NO_2 in the gas phase from nitrate photolysis when mixing $NaNO_3$ and NaCl, with increasing NaCl/$NaNO_3$ ratio [237]. This was attributed to the nitrate ion being enhanced in the air-aqueous interface due to the known surface affinity of halide ions pulling sodium cations closer, and thereby drawing NO_3^- to the interface, where it experiences a reduced

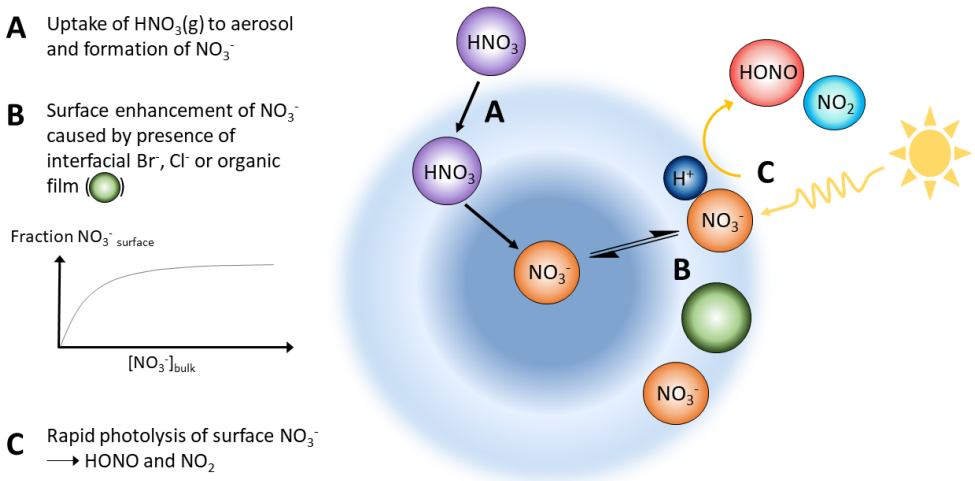

Figure 4.1: Proposed mechanism for renoxification on nitrate aerosol.

solvent cage effect compared to in the bulk [236, 237]. This surface-enhanced mechanism is summarised in Figure 4.1. HNO_3 has also been shown to be taken up on organic films, where it at least partially dissociates into H^+ and NO_3^- when in the presence of water vapour [235]. Addition of HNO_3 and HCl to acridine showed a protonation of acridine in both cases, however when photolyzed, deprotonation occurred significantly faster for HNO_3 suggesting the presence of photochemistry and the possibility of organics acting as photosensitizers [234].

Renoxification is important because it offers a rapid route for recycling of NO_x from inorganic nitrate, which has historically been thought to be slow due to the low photolysis frequency of gas phase HNO_3. If renoxification supplies a substantial amount of NO_x to remote oceanic regions, where sources have previously been considered to be limited primarily to ship emissions and to transport and decomposition of peroxyacetyl nitrate (PAN), it could have a global scale impact on production of tropospheric oxidants such as O_3 and OH, and hence on methane removal [227]. In this chapter renoxification and NO_2 uptake on aerosols are investigated as potential sources of HONO in the remote marine boundary layer (MBL) using ground-based measurements from

the Cape Verde Atmospheric Observatory (CVAO) and aircraft measurements over the Atlantic Ocean around Cabo Verde during the Atmospheric Reactive Nitrogen over the remote Atlantic (ARNA) field campaigns.

4.2 Location

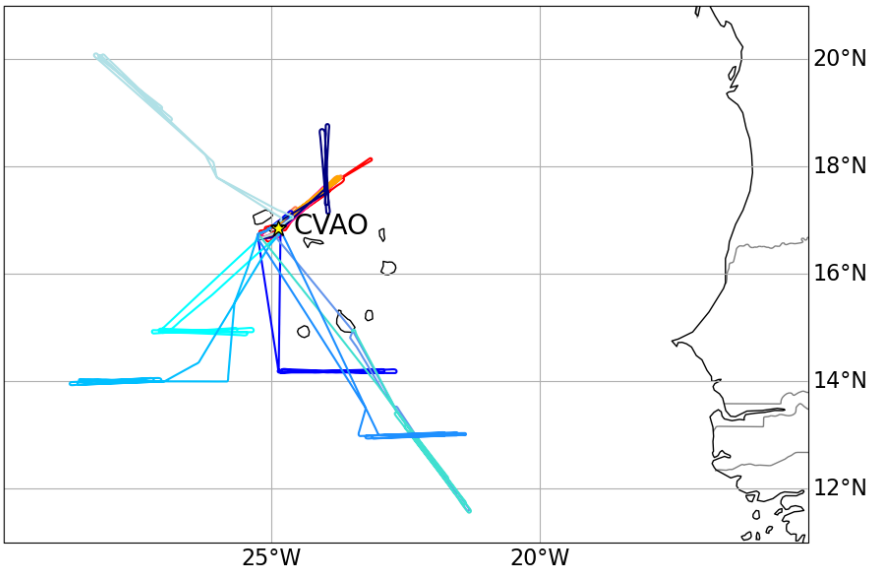

Figure 4.2: Flight tracks of ARNA-1 (coloured in red/orange) and ARNA-2 (coloured in blue colours). The CVAO is shown as the star.

The CVAO and its measurement conditions have been described in chapter 2 and further details can be found in Carpenter et al. (2010) [114]. The FAAM airborne laboratory is a modified BAe-146-301, 4-engine jet aircraft, equipped with instruments to measure a range of gas-phase species, aerosol composition and size distribution, and meteorological parameters in the atmosphere. Four flights north-east of the CVAO were conducted during the ARNA-1 campaign (August 19th-20th 2019). During ARNA-2 (February 5th-12th 2020), flights were targeted on locations where both dust and biomass burning outflow were predicted to be present by 5-day within forecast model predictions, by the NASA GEOS-CF [239] and GEOS-5 models respectively (see flight tracks in Figure 4.2). Multiple straight-and-level-runs (SLRs) of $\sim$20 minutes were

carried out on all flights, at altitudes between 100 ft and 10,000 ft, and the analyses in this study are focused on these data.

4.3 CVAO Measurements

Measurements of NO_x, HONO and the composition of aerosols at the CVAO have been described in detail elsewhere [44,117,191] so only a brief description is given here. The NO_x measurements and uncertainty calculations have been described in chapter 2.

HONO was measured using a Long Path Absorption Photometer (LOPAP-03, Quma GmbH) during three campaigns; November-December 2015 (reported in Reed et al. (2017) [44]), August 2019, and February 2020. HONO is sampled within a stripping coil into an acidic solution and derivatized with an azo dye. Absorption of light (550 nm) by the azo dye is measured with an Ocean Optics spectrometer using an optical path length of 2.4 m. The technique is described in detail in Heland et al. (2001) [240] and the calibration and standard operating procedures are described in Kleffman and Wiesen (2008) [241].

In 2015 the instrument was deployed in the CVAO guest lab sampling at a height of 3 m and the detection limit was 0.2 pptV (2 sigma, 30 seconds), as described in Reed et al. (2017) [44]. The same location was used in 2020 and the detection limit was 0.7 pptV. In 2019, the instrument was deployed on top of the 7.5 m tower and the detection limit was 1.1 pptV (2 sigma, 30 seconds). The relative error of the LOPAP is estimated at 10%. Only measurements from 2019 have been used in the data analysis due to the other two campaigns sampling at low heights, with potential surface and/or enhanced surf zone effects. The measurements from the guest lab averaged $\sim$3.5 and $\sim$2.3 pptV in 2015 and 2020, respectively, compared to 4.7 pptV at the 7.5 m tower in 2020. Figure 4.3 shows the HONO measurements during August 2019.

Aerosol samples have been collected at the CVAO since 2007 and analysed

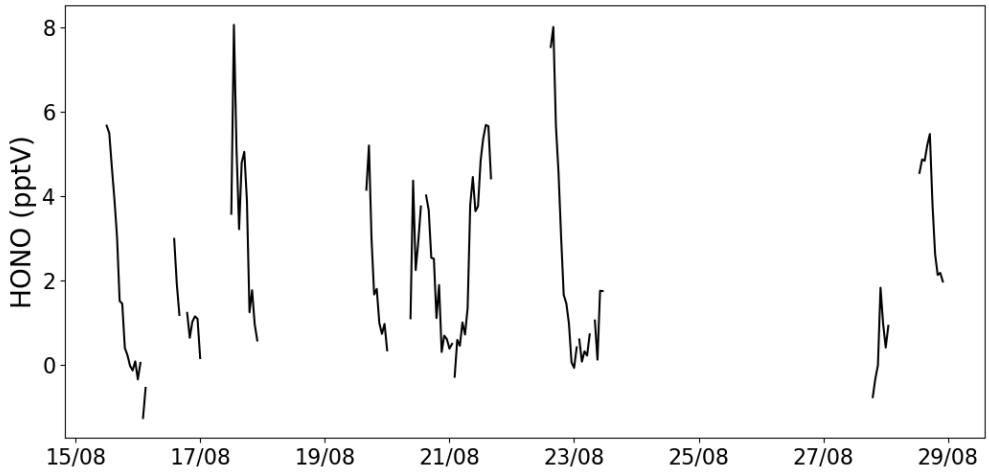

Figure 4.3: HONO measurements made at the CVAO in August 2019.

for Na^+, NH_4^+, K^+, Mg^{2+}, Ca^{2+}, Cl^-, Br^-, NO_3^-, SO_4^{2-} and $C_2O_4^{2-}$ using a standard ion chromatography (IC) technique as described in Fomba et al. (2014) [117]. The detection limits for all ions measured by the conductivity detection technique were less than 0.002 µg m^{-3} except for calcium, which was 0.02 µg m^{-3}. Filters were changed every 24 hours during campaigns and the composition is assumed to be uniform across the sampling period.

The solar actinic UV flux was measured using a spectral radiometer (a 2-pi sr quartz diffuser coupled to an Ocean Optics QE65000 spectrometer via a 10 m fibre optic cable) giving photolysis rates for a variety of species. Photolysis rates were also modelled using GEOS-Chem as explained in section 4.5. A comparison between the measured and modelled photolysis rates is shown in Figure 4.4. Here we use modelled values throughout to avoid discarding data with missing measured photolysis rates. The uncertainty in the modelled photolysis rates is estimated as the average difference between the modelled and measured photolysis rates, as discussed in section 4.5.1.

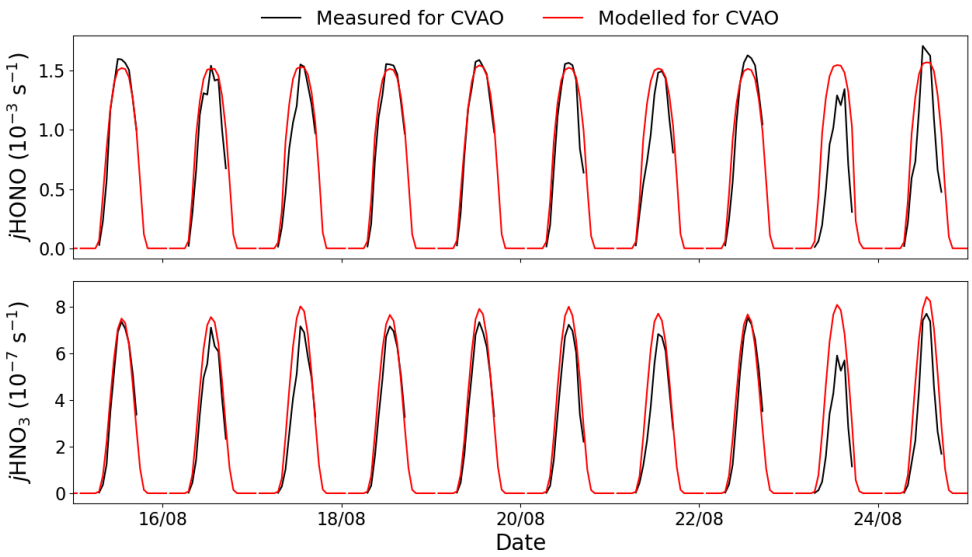

Figure 4.4: Measured and modelled (GEOS-Chem) photolysis rates for HONO and HNO_3 at the CVAO in August 2019. The solar zenith angle at midday was $\sim 6°$.

4.4 FAAM Measurements

4.4.1 NO_x and HONO

NO_x and HONO were measured using differential photolysis [242], where NO_2 and HONO are photolytically converted into NO (R4.6 and R4.2) followed by NO chemiluminescence detection (R4.7-R4.8).

$$NO_2 + h\nu (\leq 410\,\text{nm}) \longrightarrow NO + O(^3P) \quad \text{(R4.6)}$$

$$HONO + h\nu (\leq 390\,\text{nm}) \longrightarrow NO + OH \quad \text{(R4.2)}$$

$$NO + O_3 \longrightarrow NO_2^* + O_2 \quad \text{(R4.7)}$$

$$NO_2^* \longrightarrow NO_2 + h\nu (>600\,\text{nm}) \quad \text{(R4.8)}$$

A dual-channel NO_x chemiluminescence instrument equipped with two custom-built photolytic converters was used, similar in design to that described in Pollack et al. (2010) [107]. Each converter consists of a ~ 40 cm^3 quartz cylinder with two external light emitting diodes (LEDs) to avoid heating up

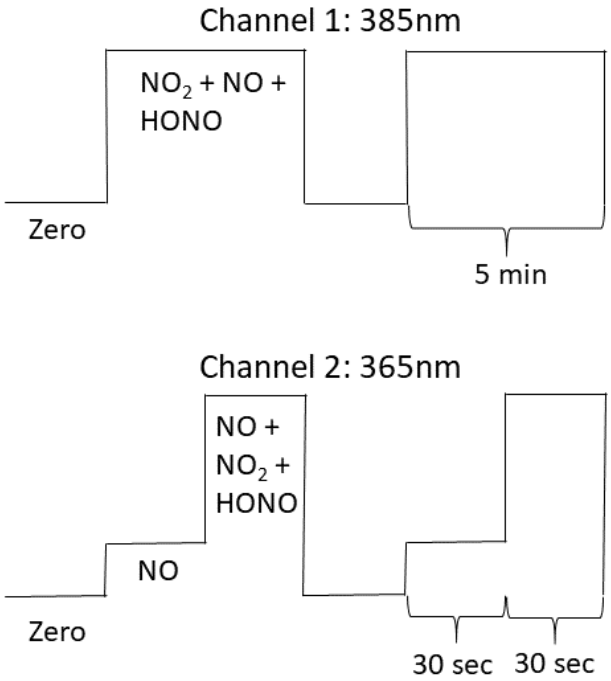

Figure 4.5: Measurement cycles for the differential photolysis instrument on the FAAM BAe-146 aircraft. Every time the diodes in channel 1 is on, the diodes in channel 2 switches on and off 5 times.

the sampled air and causing an NO_2 artefact [108, 191]. Channel 1 and 2 are fitted with 385 nm LEDs (Hamamatsu, jNO_2 1.3 s^{-1}) to optimize the NO_2 conversion and 365 nm LEDs (Hamamatsu, jNO_2 1.0 s^{-1}) to optimize HONO conversion, respectively. Channel 1 switches between zero and NO_x+HONO measurements and channel 2 switches between zero, NO, and NO_x+HONO (see Figure 4.5). Zero measurements are performed to determine the signal due to dark current and interferences. Calibration sequences were conducted multiple times during each flight to determine the NO sensitivity, NO_2 conversion efficiencies, and potential offsets between the two channels. Standard addition of approximately 5 ppbV NO was used to calibrate the sensitivity and conversion efficiencies, where the offset was determined as the difference in measured ambient NO mixing ratio, when running both channels in NO mode at the same time. The sensitivity and conversion efficiencies for both channels were stable during each flight making interpolation between each cal-

ibration appropriate.

The NO mixing ratio is determined from the NO measurements on channel 2 using the in-flight determined sensitivity. The NO_2 mixing ratio is therefore estimated from the NO_x+HONO measurements on channel 1 by subtracting the signal due to NO (from channel 2) and the measured offset in the ambient NO measurements between the two channels using the in-flight sensitivity and NO_2 conversion efficiency of channel 1. The HONO mixing ratio is determined from the difference between the two channels when the LEDs are on using equation (4.1), where $NO^{\dagger}_{2_{365}}$ and $NO^{\dagger}_{2_{385}}$ are the NO_2 mixing ratio of each channel if the entire signal was due to NO_2 and CE^{HONO}_{365} and CE^{HONO}_{385} are the conversion efficiencies of HONO for each channel [242]. As mentioned in chapter 2 and 3 other compounds can photolyse and cause an interference in the measurements. $BrONO_2$ is the interfering specie with the largest absorbtion cross section (ACS) for both wavelength, however, Reed et al. (2016) [242] showed when using 385 and 395 nm LEDs, which have similar ACSs with $BrONO_2$ to LEDs at 365 and 385 nm, that the interference in [HONO] was $\sim$3.4%[$BrONO_2$]. As $BrONO_2$ is typically <1 pptV, the interference from $BrONO_2$ is negligible [242].

$$[\mathrm{HONO}] = \frac{NO^{\dagger}_{2_{365}} - NO^{\dagger}_{2_{385}}}{CE^{HONO}_{365} - CE^{HONO}_{385}} \qquad \text{(Eq. 4.1)}$$

The HONO conversion efficiencies are dependent on the NO_2 conversion efficiencies, so CE^{HONO}_{365}-CE^{HONO}_{385} has been calibrated as one term against UV-vis Cavity Enhanced Absorption Spectroscopy (UV-CEAS) using the Highly Instrumented Reactor for Atmospheric Chemistry (HIRAC) [243] similarly to Reed et al. (2016) [242]. HONO was introduced into the HIRAC chamber from a photolytic source described in Boustead (2019) [244]. Briefly, a humidified mixture of NO in N_2 is illuminated by a low-pressure Mercury vapour lamp emitting at 185 nm. Photolysis of H_2O in the presence of O_2 produces OH and

HO_2, which react with NO forming HONO, NO_2, and OH.

$$H_2O + h\nu(=185\,\text{nm}) \longrightarrow OH + H \quad \text{(R4.9)}$$

$$H + O_2 \longrightarrow HO_2 \quad \text{(R4.10)}$$

$$NO + OH \longrightarrow HONO \quad \text{(R4.1)}$$

$$HO_2 + NO \longrightarrow NO_2 + OH \quad \text{(R4.11)}$$

In addition, unreacted NO remains. A constant flow of HONO in nitrogen was added to the chamber at a rate of approximately 1 L min^{-1} along with a separate flow of nitrogen to balance the sampling rates of the connected instruments to ensure the chamber pressure remained constant at 1000 mbar. This resulted in a gradual increase over time in the HONO concentration present in the chamber. The HONO concentration was monitored by UV-CEAS. The optical cavity was aligned across the diameter of the chamber positioned directly next to the sampling location of the differential photolysis instrument. The CEAS instrument consisted of a probe light produced by a Laser Driven Light Source (LDLS—Energetiq EQ-99X) producing near constant radiance from the near infrared (NIR) to the ultraviolet (UV), <200 nm. The light was then directed into the chamber where the cavity was generated between two cavity mirrors (99.2-99.7% from 330-370 nm). Light exiting the cavity was focused into a fibre optic connected to the detector, a high throughput spectrograph (CP140-103, f/2) coupled to a fast-read (1 kHz) line-array charge-coupled device (CCD) (Hamamatsu S7031).

To prevent saturation of the detector at wavelengths outside the region of interest, a 450 nm cut off filter was used to remove the longer wavelengths and a cuvette filled with acetone removed the peaks in the far UV, <250 nm. Measurements were taken at 30 second intervals. Data were analysed between 330 nm and 370 nm, with the absorption spectrum plotted against the literature cross section. The path length was determined separately by measuring the absorption spectrum of a known concentration of NO_2.

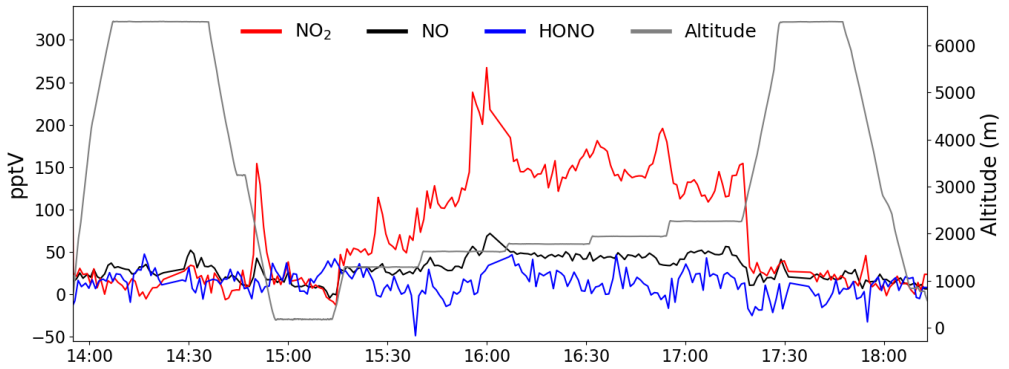

Figure 4.6: Measurements of NO (black), NO_2 (red), and HONO (blue) during an ARNA-2 flight with the vertical profile shown in grey. Negative values can occur for the HONO measurements when measuring very low concentrations since the instrument uses a difference between two channels.

The sensitivity of the FAAM NO_x instrument to HONO was derived from a linear fit ($R^2 = 0.85$, Slope/CE_{365}^{HONO}-$CE_{385}^{HONO} = 0.775$) of UV-CEAS-derived [HONO] against differential-derived [HONO]. Measurements from one of the flights can be seen in Figure 4.6.

4.4.1.1 Uncertainty Analysis

An extensive uncertainty analysis for NO, NO_2 and HONO has been performed for each SLR during the two airborne campaigns. The precision of the measurements have been determined from the zero count variability of each SLR which is directly related to the photon-counting precision of the photomultiplier tube (PMT) [137]:

$$\text{Zero count variability} = x - \overline{x} \qquad \text{(Eq. 4.2)}$$

where x is the individual zero measurements during a run, and $\overline{x}$ is the mean of the measurements on the same run. The 1σ precision of NO, $NO^{\dagger}_{2_{365}}$, and $NO^{\dagger}_{2_{385}}$ were on average 0.6 pptV, 1.2 pptV, and 1.1 pptV for the SLRs, re-

spectively, using equation (4.3):

$$\text{Precision} = \frac{1\sigma}{\sqrt{\text{number of averaging points}}} \qquad \text{(Eq. 4.3)}$$

where σ is the standard deviation of the zero count variability, which is converted into a mixing ratio using the sensitivity and conversion efficiency of each channel. The HONO precision is determined by propagating the precisions of $NO^{\dagger}_{2_{365}}$ and $NO^{\dagger}_{2_{385}}$ while taking the HONO conversion efficiency into account resulting in 2.1 pptV (1σ).

The calibration uncertainty consists of the uncertainties in the sensitivity (S), the drift in sensitivity (S_{drift}), the conversion efficiency (CE), drift in conversion efficiency (CE_{drift}), and the flow (C_{flow}) and concentration (C_{conc}) of the calibration gas (Eq. 4.4 and 4.5). Since the HONO measurements were calibrated on the ground, the uncertainty is estimated from those measurements. The calibration uncertainty of NO, $NO^{\dagger}_{2_{365}}$, and $NO^{\dagger}_{2_{385}}$, and HONO were found to be on average 2.4%, 2.6%, 2.8%, and 15%, respectively.

$$\text{NO cal uncertainty} = \sqrt{S^2 + S^2_{drift} + C^2_{flow} + C^2_{conc}} \qquad \text{(Eq. 4.4)}$$

$$\text{NO}_2\text{ cal uncertainty} = \sqrt{S^2 + S^2_{drift} + C^2_{flow} + C^2_{conc} + CE^2 + CE^2_{drift}} \qquad \text{(Eq. 4.5)}$$

The total absolute uncertainties of NO, NO_2, and HONO are determined by propagating the appropriate measurement precisions and uncertainties in the calibration and drift in measurements using the rules for addition, subtraction, multiplication, and division:

$$X = A \pm B; \qquad (\delta X)^2 = (\delta A)^2 + (\delta B)^2 \qquad \text{(Eq. 4.6)}$$

$$X = c \times (A \times B); \quad \left(\frac{\delta X}{X}\right)^2 = \left(\frac{\delta A}{A}\right)^2 + \left(\frac{\delta B}{B}\right)^2 \qquad \text{(Eq. 4.7)}$$

$$X = c \times \left(\frac{A}{B}\right); \qquad \left(\frac{\delta X}{X}\right)^2 = \left(\frac{\delta A}{A}\right)^2 + \left(\frac{\delta B}{B}\right)^2 \qquad \text{(Eq. 4.8)}$$

The total 1σ uncertainties were on average 0.8 pptV, 3.5 pptV, and 4.4 pptV, for NO, NO_2, and HONO, respectively for the SLRs.

4.4.2 Aerosol Composition

4.4.2.1 Sampling

Aerosol chemical composition was determined by off-line analysis of filter samples. Two identical inlets are mounted on the port side of the aircraft allowing collection of duplicate samples. Air is pumped from the inlets through stacks of filter substrates contained within housings on the inside of the aircraft. The total air flow through the sample lines is monitored by mass flow meters.

During the ARNA campaigns stacks of two 47 mm diameter filters of different pore size were used; a 1 µm filter was placed at the bottom of the stack (ARNA-1: Whatman, PTFE with polypropylene mesh back; ARNA-2: Whatman, polycarbonate, Nuclepore Track-Etch membrane) and an 8 µm filter (Whatman, polycarbonate, Nuclepore Track-Etch membrane, 47mm diameter) at the top, so the aerosols were divided into two size fractions according to the nominal pore size ($>$ 8 µm and 1-8 µm). These fractions broadly correspond to 'coarse' ($>$ 1 µm aerodynamic diameter) and 'fine' ($<$ 1 µm aerodynamic diameter) aerosol [245, 246], which will be used moving forward. To minimise sample contamination, filter holders were washed in deionised water, loaded with filters, stacked together and wrapped in a clean polythene bag pre-flight, and only unwrapped immediately before use. Prior to each flight, the sampling lines were cleaned with deionised water to remove remnant material from the previous flights. Duplicate samples were collected during the flights by inserting a stack of filters into each sample line, zeroing the mass flow meters,

turning on the pump and opening the air flow. Three sets of duplicate samples were taken during each of the four ARNA-1 flights. Usually, two sets of filters were deployed in the boundary layer and a set in the free troposphere. During ARNA-2 a single stack of filters were sampled on each SLR and duplicates were only collected on days with only one flight. At least once a day a set of blank samples was also collected by inserting the stack of filters into the sampling line without turning the air flow on. During ARNA-1 blank samples were collected during one of the free troposphere runs, while during ARNA-2 blank samples were collected either on the way to the sampling region or when returning to São Vicente. Post-flight, the filters were removed from the units and inserted into sterile lab tubes (CORNING Centristar, polypropylene, 50 mL (ARNA-1) and 15 mL (ARNA-2)) and kept cold (5°C) to minimise the aerosols evaporating off the filters. Upon return to the laboratory, filters were stored frozen (-20°C) until extraction.

4.4.2.2 Analysis

Filters were extracted by adding 3 mL ultrapure water ($\geq$18.2 MΩ cm^{-1}) to the filter in the polypropylene storage tube then ultra-sonicating (Fisher scientific, FB15051) for 3 $\times$ 10 min, with one minute of vortex mixing (SciQuip) after every 10 min of sonication. Using a needle and syringe, the aqueous extract was aspirated from the tube and passed through a syringe filter (Milex, 0.22 µm pore size) into a second, pre-cleaned tube (15 mL, CORNING Centristar, polypropylene, cleaned with ultrapure water).

Anions (Cl^-, NO_2^-, NO_3^-, Br^-, SO_4^{2-}, and $C_2O_4^{2-}$) and cations (Na^+, K^+, NH_4^+, Ca^{2+}, and Mg^{2+}) were determined in the aqueous extracts using ion chromatography (IC; Thermo Fischer, Dionex-1100) with isocratic elution and 0.1 mL injection volume. The anions and cations were separated using Dionex IonPac AS14A and CS12A columns, respectively. Eluent was prepared from ultrapure water with Na_2CO_3, and $NaHCO_3$ for anions and methane sulfonic acid for cations. Calibration standards were prepared daily using salts of

the relevant ions (Analytical Reagent grade or better) and ultrapure water. Standards contained between 0 µM and 500 µM of each anion and between 0 µM and 40 (500 for Na^+) µM for each cation. 0.5 mL aliquots of samples and calibration standards were pipetted into polyvials (Thermo Scientific, 0.5 mL) and capped with a plain polyvial cap before loading into the IC autosampler. The samples were run on the IC immediately following extraction.

Each sample was corrected for procedural contamination using the blank samples collected on each flight. Blank corrected extract concentrations below the analytical limit of detection (LOD) were substituted with 0.75 × LOD as described by Chance et al. (2015) [247] before being converted to aerosol loadings using the extraction solvent volume and the air volume passed through each filter. The LOD was calculated as the median of the daily determined analytical LODs from the calibration curves. Aerosol ion concentrations from ARNA-1 and ARNA-2 are compared to previous measurements in the same region in Table 4.2. All the measurements are in the same range as the previous measurements except NH_4^+, which is higher than previously reported. For the winter samples this could be due to the air being sampled having significant contributions from biomass burning, which is a known source of NH_4^+, K^+, and NO_3^- [248, 249]. It is also consistent with an increase in ammonia emissions [250].

Sea-salt and non-sea-salt (NSS) components were calculated from the sea-water ratios between sodium and other ions [251], assuming that all measured sodium was from sea-salt. The measured concentrations of anions and cations for each individual sample are plotted in Figure 4.7 and 4.8, respectively. Previous aerosol measurements made at the CVAO have shown that NSS Ca^{2+} varied from 0.01-4.44 µg m^{-3} over a 5 year period with the maximum concentrations corresponding to Saharan dust events and the minimum concentrations to clean marine air [117].

Table 4.2: Comparison of aerosol composition during the ARNA campaigns, the SHADE campaign [246] and measurements made at the CVAO [117]. The ARNA and CVAO data are given from min-max and the SHADE data is given as 25^{th}-75^{th} percentile. All concentrations are given in $10^{-9}\,\text{mol}\,\text{m}^{-3}$.

	ARNA-1 (Summer)		ARNA-2 (Winter)		SHADE[a] [246]		CVAO[b] [117]
	$< 1\,\mu\text{m}$	$> 1\,\mu\text{m}$	$< 1\,\mu\text{m}$	$> 1\,\mu\text{m}$	$< 1\,\mu\text{m}$	$> 1\,\mu\text{m}$	$< 10\,\mu\text{m}$
Cl^-	7-13.5	31.4-153	Bdl-30.8	Bdl-210	1.3-3.6	1.9-31.3	9.9-597
NO_3^-	1.7-10.1	8.4-23.1	0.6-34.3	Bdl-37.1	0.16-7.8	7.4-33.0	2.3-60.6
SO_4^{2-}	17.7-21.0	9.6-15.7	1.3-25.0	Bdl-46.2	0.8-26.7	2.9-44.0	3.2-76.8
NO_2^-	Bdl	Bdl	Bdl-5.1	Bdl-8.2	-	-	-
$C_2O_4^{2-}$	Bdl-1.0	Bdl	Bdl-8.2	Bdl-7.8	-	-	Bdl-5.2
Na^+	Bdl-17.1	35.7-146	Bdl-34.5	Bdl-179	6.9-14.6	6.5-75.7	10.9-554
NH_4^+	27.4-38.1	1.3-7.4	3.2-69.1	1.0-26.7	0.4-6.4	0.4-6.6	Bdl-9.5
K^+	0.6-3.2	1.9-3.4	0.2-23.2	Bdl-12.1	0.6-2.4	2.7-14.5	Bdl-22.0
Ca^{2+}	Bdl-15.7	12.5-49.3	Bdl-93.1	Bdl-221	2.5-15.9	19.7-196	Bdl-110
Mg^{2+}	Bdl-3.2	5.6-10.3	Bdl-10.2	Bdl-117	0.8-4.1	1.9-25.5	2.1-55.1

Bdl: Below detection limit. [a]All concentrations from the Saharan Dust Experiment (SHADE) have been converted from $\text{ng}\,\text{m}^{-3}$ to $\text{nmol}\,\text{m}^{-3}$. Most samples were taken between 2.5 and 6 km above sea level. [b]Measurements made at the CVAO between 2007 and 2011, which have been converted from $\mu\text{g}\,\text{m}^{-3}$ to $\text{nmol}\,\text{m}^{-3}$.

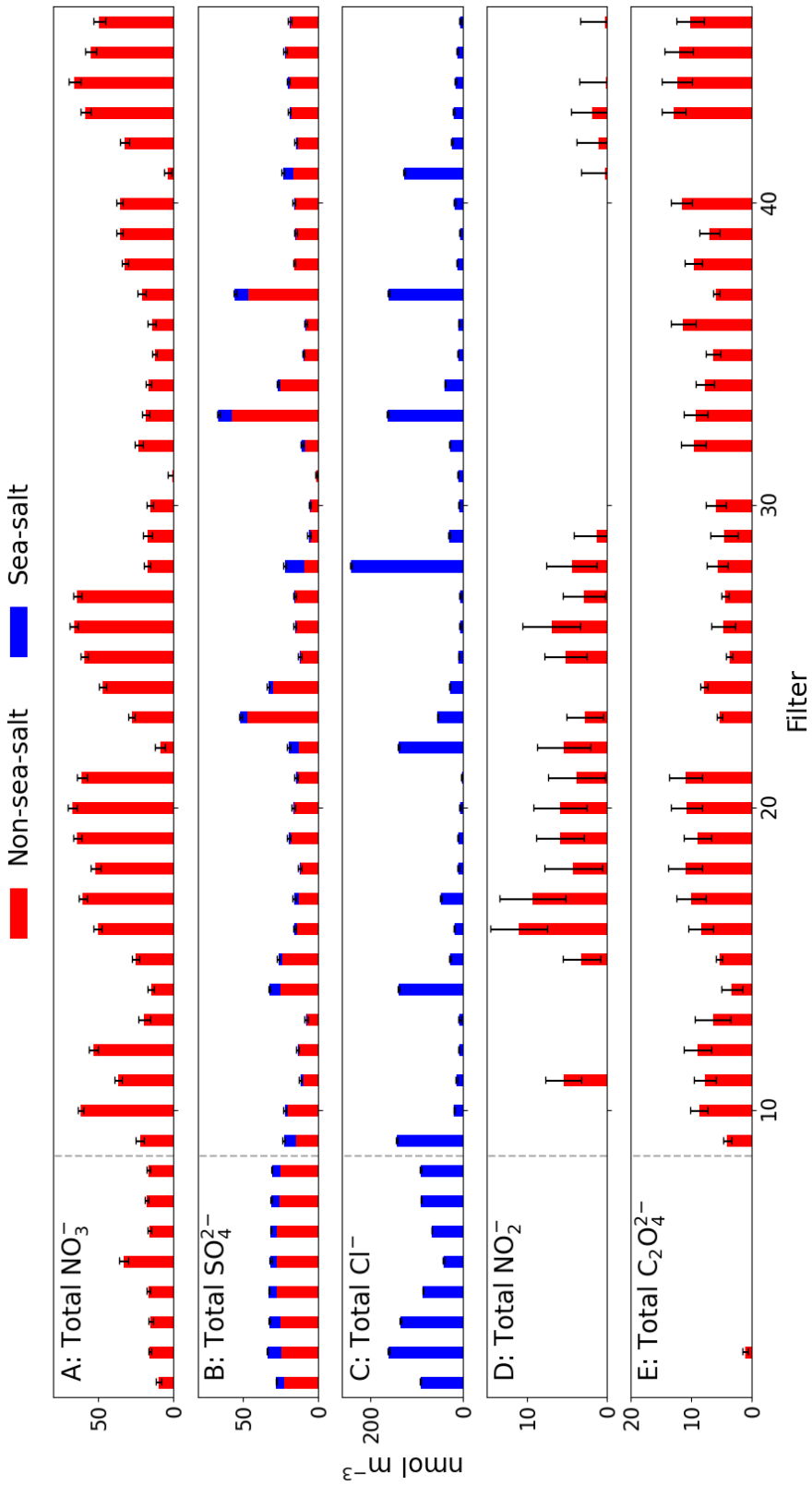

Figure 4.7: Total concentrations (<1 µm + >1 µm) of all the anions measured for each filter during ARNA-1 (1-8) and ARNA-2 (9-46). Sea-salt and NSS components were calculated from the seawater ratios between sodium and other ions [251], assuming that all measured sodium was from sea-salt. The error bars symbolize the uncertainty of the total concentration and the grey dashed vertical lines separate the two campaigns.

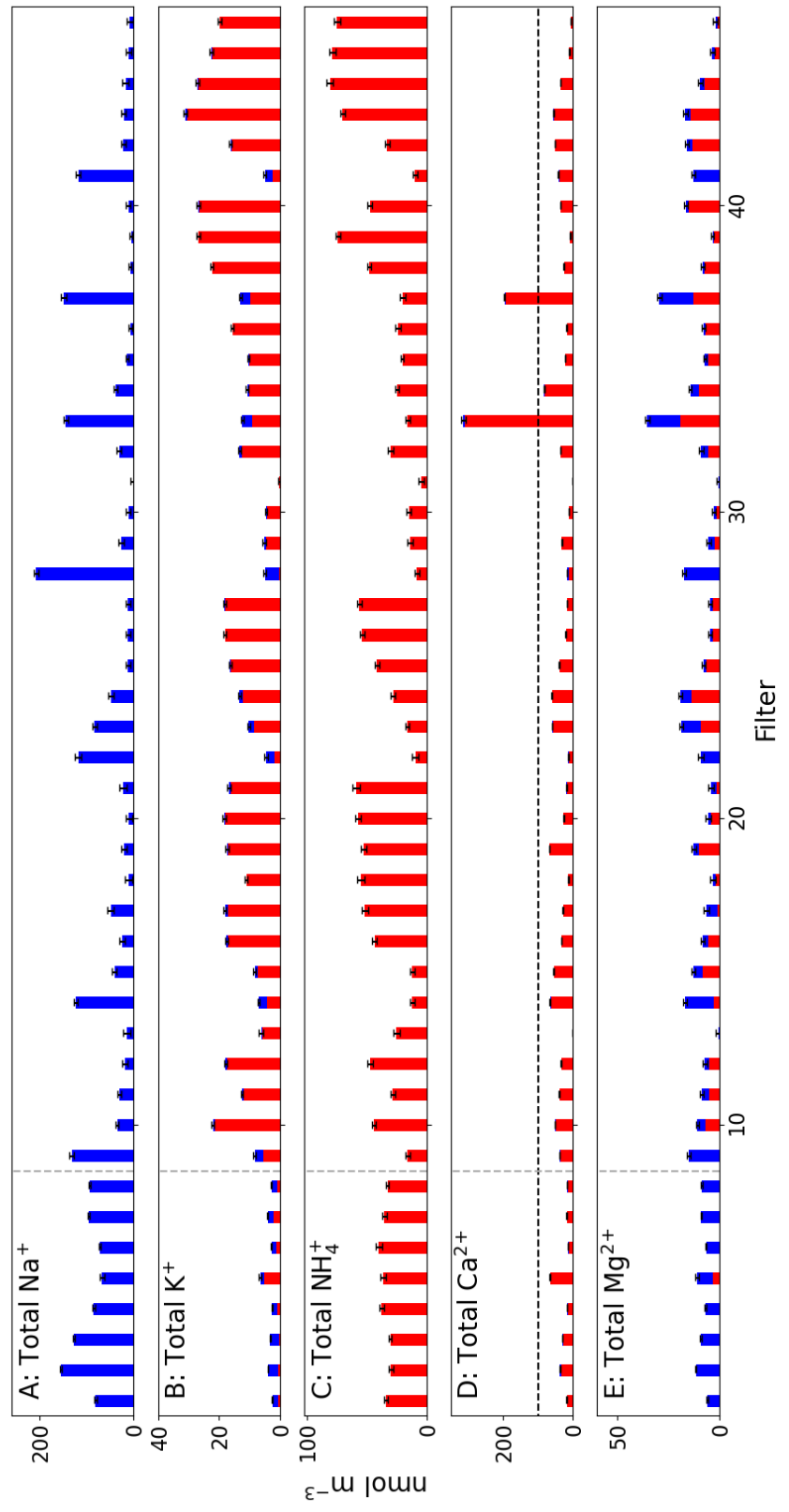

Figure 4.8: Total concentrations (<1 µm + >1 µm) of all the cations measured for each filter during ARNA-1 (1-8) and ARNA-2 (9-46). Sea-salt and NSS components were calculated from the seawater ratios between sodium and other ions [251], assuming that all measured sodium was from sea-salt. The error bars symbolize the uncertainty of the total concentration, the dashed black line marks amount of Ca^{2+} needed for a sample to be categorized as dust and the grey dashed vertical lines separate the two campaigns.

4.4.2.3 Uncertainty Analysis

The total uncertainty in each ion has been estimated by propagation of the uncertainties in the blanks, the calibration curve, and the air volume using equations (4.9) and (4.10). The uncertainty in the blanks was estimated as the standard deviation of all the blanks for each size fraction. The calibration uncertainty is determined as the 1σ confidence interval of the calibration curve by the Chromeleon 7 software used to analyse the IC samples. The uncertainty in the air volume sampled has previously been estimated to be 0.5 L for total sample volumes up to 400 standard litre (stL) for the BAe-146 system [252], however, as the sample volumes measured in this study were significantly higher (900-5000 stL) the uncertainty was set conservatively to 1% of the air volume. The uncertainties associated with each ion is plotted as error bars in Figure 4.7 and 4.8.

$$\mathrm{u}_{\text{Sample-Blank}}(\mu\mathrm{M}) = \sqrt{\mathrm{u}^2_{\text{Calibration}} + \mathrm{u}^2_{\text{Blank}}} \tag{Eq. 4.9}$$

$$\mathrm{u}_{\text{conc}}(\%) = \sqrt{\left(\frac{\mathrm{u}_{\text{Sample-Blank}}}{\text{Sample-Blank}}\right)^2 + \mathrm{u}^2_{\text{Airflow}}} \tag{Eq. 4.10}$$

Additional uncertainty is associated with the sampling efficiency of the inlet lines. Andreae et al. (2000) estimated the sampling efficiency of a similar system on another aircraft to be good for fine aerosols, but only $\sim$35% for coarse aerosols [245]. Sanchez-Marroquin et al. (2019) characterized the inlet system on the BAe-146, where again fine aerosols had a high sampling efficiency but the sampling efficiency of coarse mode aerosols depended on their diameter [253]. However, as the effect has not been quantified it has not been included in the plotted uncertainties.

4.4.3 Aerosol Surface Area

In situ measurements of aerosol particle concentration distributions were made with a Passive Cavity Aerosol Spectrometer Probe (PCASP) and a Cloud Droplet Probe (CDP), both manufactured by Droplet Measurement Technologies (DMT). A description of the processing can be found in Appendix H.

4.4.4 Photolysis Rates

Photolysis rates were measured on the aircraft using two spectral radiometers (a 2-pi sr quartz diffuser coupled to an Ocean Optics QEPro spectrometer via a fibre optic cable); one upward facing and one downward facing to measure the direct solar actinic UV flux and the scattered light. The total photolysis rate is determined as the sum of the two measurements.

4.5 Modelling - GEOS-Chem

Photolysis rates and OH concentrations were extracted for all ground and airborne observations at nearest point in space and time from the GEOS-Chem model (v12.9.0, DOI:10.5281/zenodo.3950327). The model was run at a nested horizontal resolution of 0.25x0.3125 degrees over the region (-32.0 to 15.0 °E, 0.0 to 34.0 °N), with boundary conditions provided by a separate global model run spun up for one year. The photolysis rates are calculated online in quadrature using Fast-JX code [254, 255].

4.5.1 Uncertainty Analysis

A comparison between measured and modelled $j\mathrm{HONO}$ and $j\mathrm{HNO_3}$ photolysis rates during ARNA-1 is shown in Figure 4.9. The uncertainty in the modelled photolysis rates is determined as the difference between the modelled and measured rates for a SLR, which on average was 15 and 11% for $j\mathrm{HONO}$ and $j\mathrm{HNO_3}$, respectively.

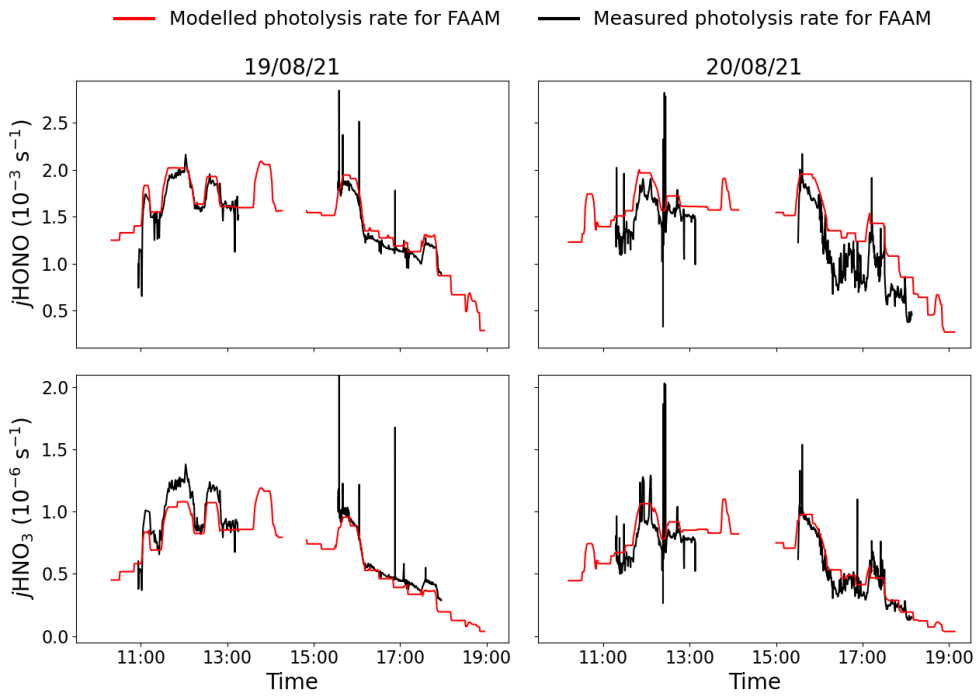

Figure 4.9: Measured (black) and modelled (red; GEOS-Chem) photolysis rates for HNO_3 and HONO aboard the FAAM BAe-146 aircraft. Two flights are plotted each day creating a gap in the middle of the measurements.

GEOS-Chem modelled OH concentrations have previously been compared to observations and been shown to be simulated to within observational uncertainty (74% to 135%, 2σ confidence interval) [256]. As the OH reactions with HONO and NO are minor contributions towards the calculated missing HONO source described below, the OH uncertainty makes a negligible contribution to the overall uncertainty, however, here we use 37% (1σ) for all further uncertainty analysis.

4.6 Trajectory Analysis

For each aerosol sample, 96-hour back trajectories were modelled along the flight track using the Hybrid Single-Particle Langrangian Integrated Trajectory (HYSPLIT) model [257]. Seven out of 8 air samples taken during ARNA-1

only travelled over the Atlantic Ocean during the 4 days before being sampled compared to 3 out of 38 samples taken during ARNA-2 (see Figure 4.10 and 4.11). Modelled precipitation along the back trajectories was used to evaluate whether aerosols could have been rained out before reaching the aircraft. Precipitation was only observed for the ARNA-1 back trajectories.

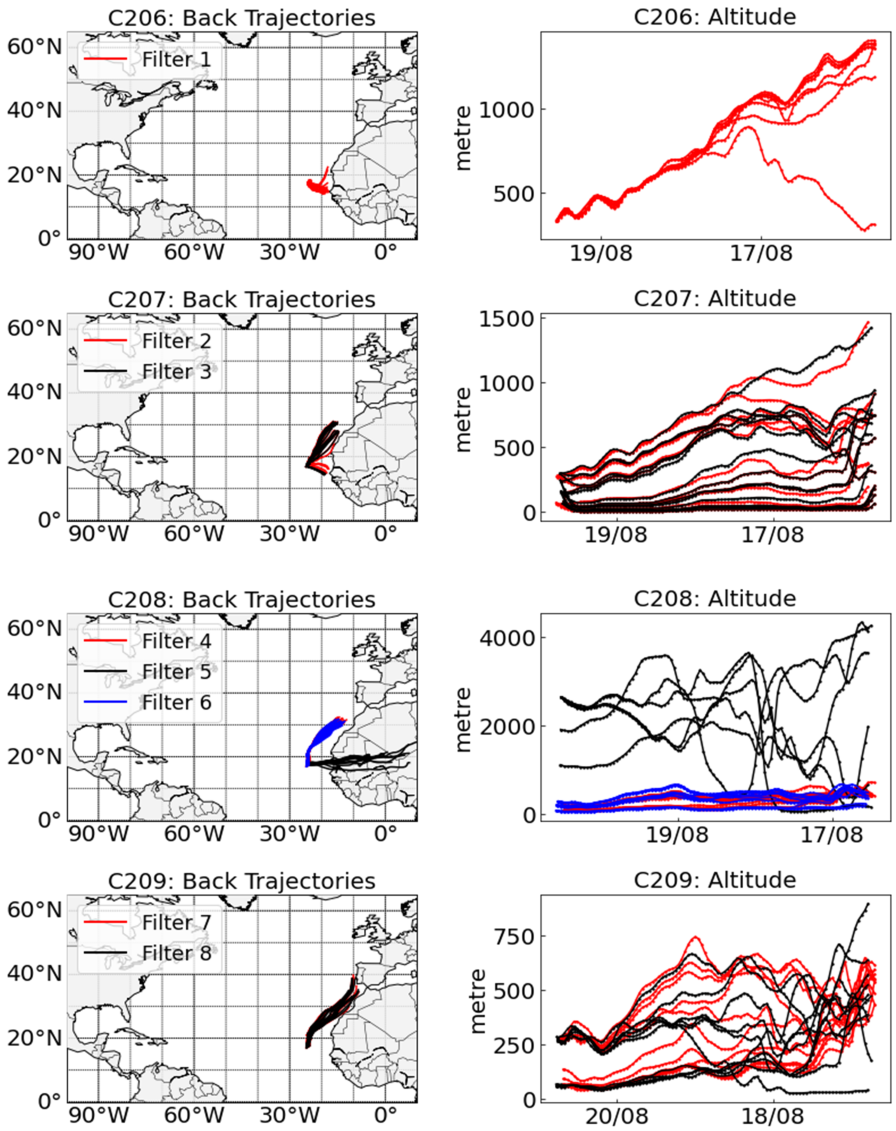

Figure 4.10: 96 h HYSPLIT back trajectories for each aerosol sample during ARNA-1. All trajectories along one SLR are coloured the same colour.

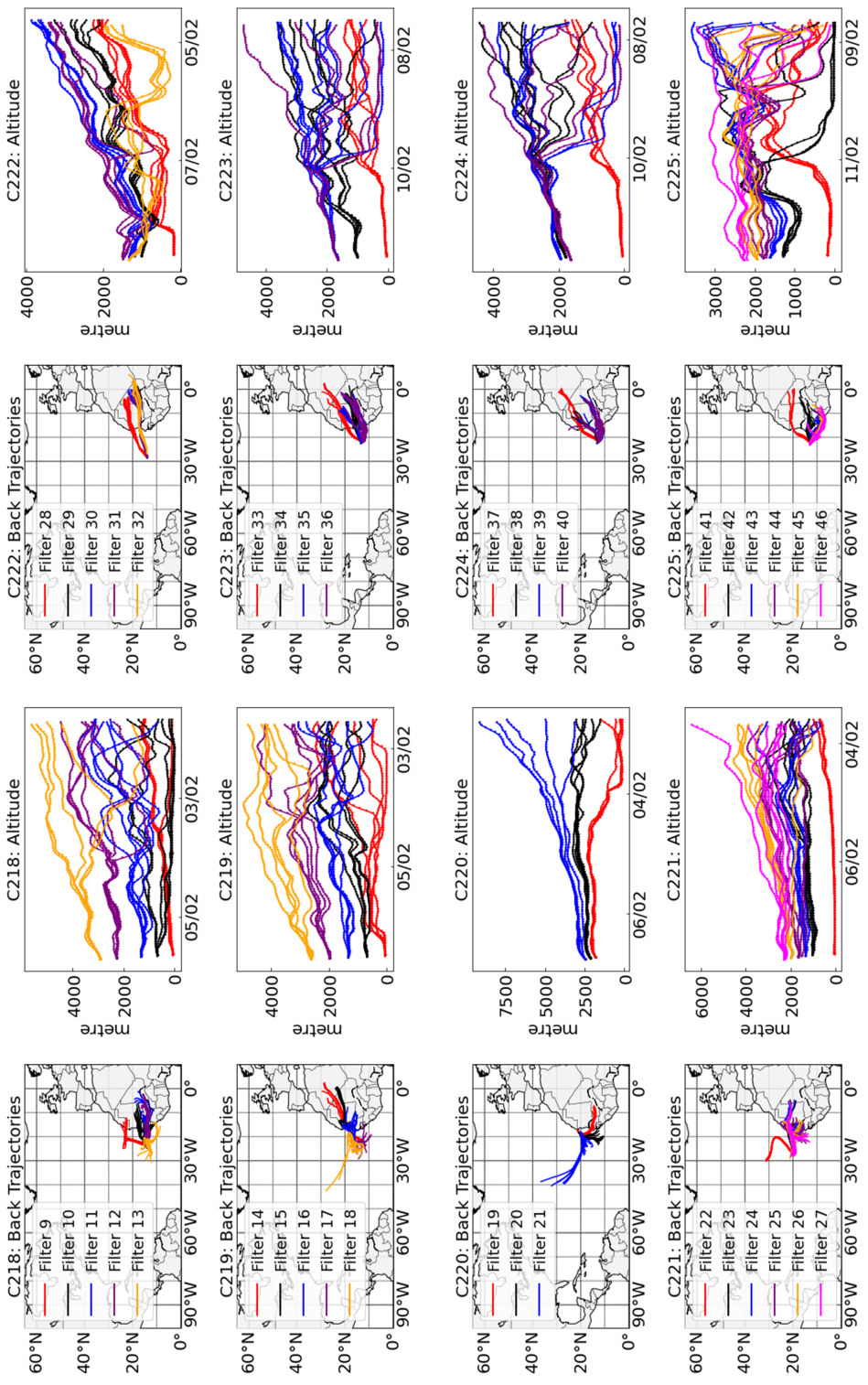

Figure 4.11: 96 h HYSPLIT back trajectories for each aerosol sample during ARNA-2. All trajectories along one SLR are coloured the same colour.

4.7 Aerosol Classification

The aerosol samples were divided into 5 categories based on their composition (Figure 4.7 and 4.8), back trajectories (Figure 4.10 and 4.11) and concurrent gas-phase measurements:

- Dust: Fomba et al. (2014) observed NSS Ca^{2+} in particulate matter with an aerodynamical diameter below 10 μm (PM10) to vary from 0.01-4.44 μg m^{-3} from 2007-2011 at the CVAO and they associated the highest NSS Ca^{2+} measurements with dust episodes [117]. Therefore, we categorised samples as dominated by dust if the back trajectories crossed the Saharan desert in the previous 96 hours and contained >4 μg m^{-3} (99.75 nmol m^{-3}) NSS Ca^{2+}. It should also be noted that the two observed dust samples were also high in sea-salt due to being sampled at low altitude (see back trajectories).

- Sea-salt: These samples contained high concentrations of sea-salt (Na^{+}, Cl^{-}) and low concentrations of NSS Ca^{2+}, NSS K^{+}, and NSS Mg^{2+}. The back trajectories were either completely over the Atlantic Ocean (e.g. ARNA-1 except filter 5) or close to the ocean for an extended amount of time previous to being sampled (e.g. filter 9 and 14).

- Free troposphere: Sample 31 was observed to be low in all anions and cations and the back trajectories associated with this sample were above 1000 m in altitude for the 96 hours before sampling, suggesting that the free troposphere was sampled.

- Biomass burning (BB): The statistical threshold approach described by Lee et al. (2021) [258] was used to determine whether the sampling took place in a biomass burning plume based on CO, O_3, and HCN measurements. The percentage of each SLR spent in BB is plotted in Figure

4.12A. The gas-phase BB filter was combined with the measured composition of the aerosols. Biomass burning releases potassium and nitrate to the atmosphere, and so the ratios of these species to other aerosol constituents may be used as tracers. Elevated ratios of NSS K^+ to NSS Ca^{2+} in fine mode (<1 µm) aerosol have been associated with biomass burning [248]. Similarly, the NO_3^-/NSS SO_4^{2-} ratio in aerosols measured at Barbados from the trade winds from Africa has been reported to be 0.4 during the summer, where the pollution is dominated by fossil fuel combustion in Europe and 1.4 during the winter, where the pollution is dominated by wood and biomass burning in Africa [259]. Here, samples are considered to be influenced by biomass burning when the NSS K^+/NSS Ca^{2+} ratio of the <1 µm fraction was above a threshold value of 0.24 (derived from a crustal K^+/Ca^{2+} of $\sim$0.71 [260] and water solubility of 24% for K^+ and 71% for Ca^{2+} in Saharan dust aerosol [unpublished, data available via GEOTRACES IDP2017 from [261]], see Figure 4.12B), and the NO_3^- to NSS SO_4^{2-} ratio was close to or above 1.4 (see Fig. 4.12C).

- Dust/Biomass burning: The remaining samples were categorised as a mixture of dust and biomass burning.

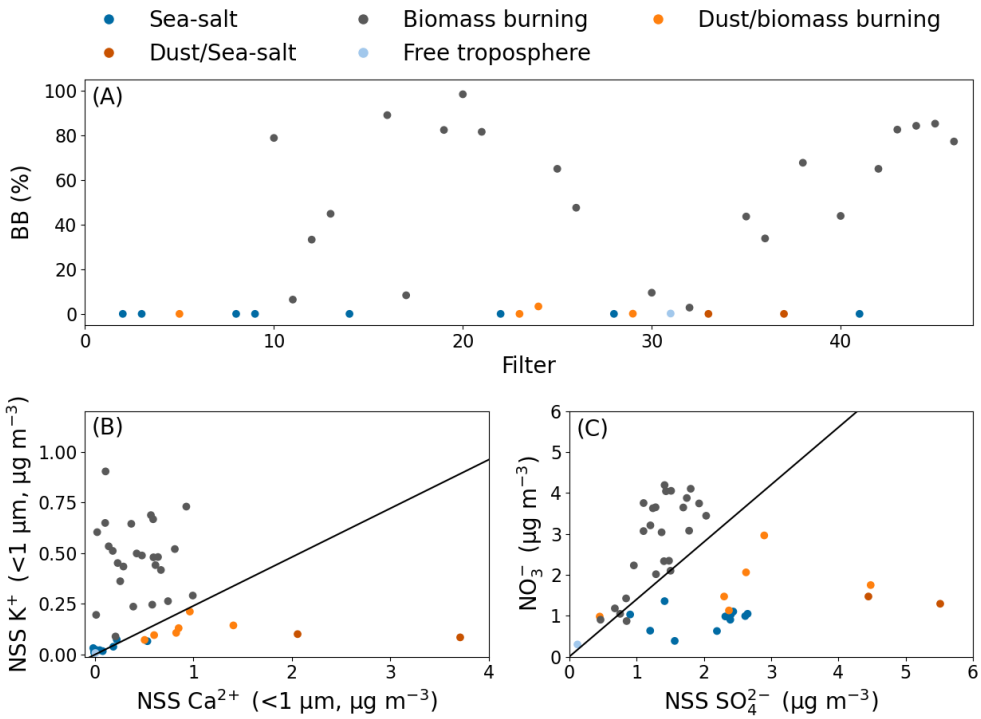

Figure 4.12: Biomass burning tracers for each SLR. (A) shows the percentage of the sampling time spent in a biomass burning plume, defined according to the gas-phase biomass burning filter, for each aerosol sample. (B) shows the NSS K^+ as a function of the NSS Ca^{2+} in the <1 µm size fraction, where the black line is the 0.24 ratio. (C) shows the total NO_3^- as a function of total NSS SO_4^{2-}, where the black line represents NO_3^- = 1.4 × NSS SO_4^{2-}. Each data point is coloured by the determined air mass category based on aerosol composition, back trajectories, and the trace gases sampled.

4.8 Results and Discussion

Vertical profiles of pNO_3^-, NO, NO_2, HONO, and average surface area per cm^3 are plotted in Figure 4.13C-G, where the measurements are coloured the same colour as their respective flight track in Figure 4.13B. Each pNO_3^- datapoint represent a set of filter samples of a SLR. NO, NO_2, HONO, and the average surface area have been calculated as the average over each SLR with a pNO_3^- measurement. The vertical profiles of pNO_3^-, NO, and NO_2 show clear enhancements between 1500-2500 m. The air sampled in this layer predominately originated from over Africa and showed tracers of biomass burning

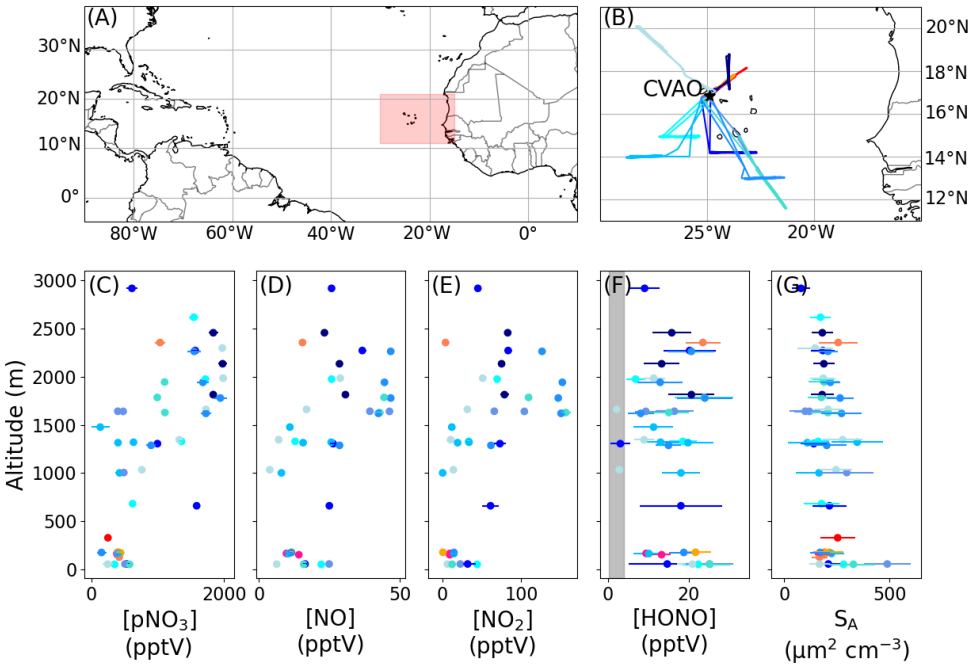

Figure 4.13: Flight tracks and vertical profiles of pNO_3^-, NO, NO_2, HONO, and aerosol surface area during ARNA-1 (August 2019) and ARNA-2 (February 2020). (A) shows a map over the region, where the red box is the area shown in panel (B), (B) shows the flight tracks from ARNA-1 in red colors and ARNA-2 in blue colors. The vertical profiles of (C) total pNO_3^- (<1 µm + >1 µm), (D) NO, (E), NO_2, (F) HONO, and (G) average aerosol surface area per cm^3 are coloured by their respective flight tracks as shown in (B). Each data point is an average of a SLR. The grey vertical area in (F) shows the range of calculated HONO gas-phase source only concentrations for each SLR during the flights using equation 4.11. The error bars represent the uncertainties described in the measurement description.

and dust in the aerosol composition. Small enhancements in HONO can be observed in the NO_x/biomass burning layer as well as in the MBL, however, with few measurements outside these two layers the enhancements are not very clear. The mean mixing ratios of HONO (±1 standard deviation) were 18.2 ± 5.9 pptV in the MBL and 14.2 ± 6.4 pptV above the MBL (0.5-3.0 km). The HONO measurements in the MBL are comparable to those made by Ye et al. (2016) in 2013 [51], where they measured ∼10-15 pptV. However, they only saw ∼1-3 pptV above the MBL, which is significantly lower (a factor of 5) than what we observed. Figure 4.14 shows the average diurnal of HONO measured

at the CVAO in August 2019, which was about a factor of three lower (4.7 ± 1.8 pptV at solar noon) than the MBL aircraft measurements, but similar to previous measurements made at the CVAO (∼3.5 pptV at solar noon) [44] and at Tudor Hill, Bermuda, in marine conditions (∼1-3 pptV) [52].

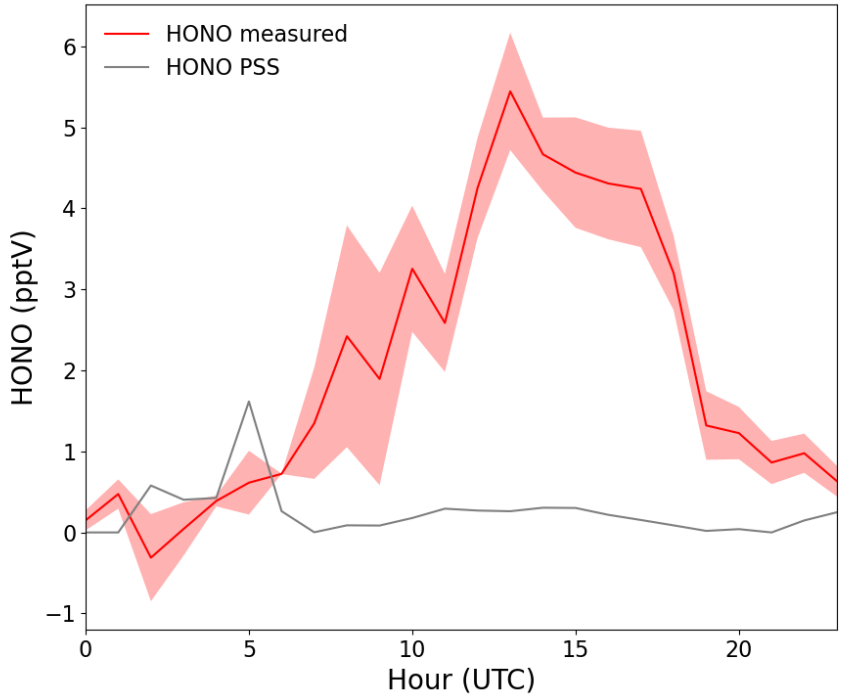

Figure 4.14: Average diurnal cycle of HONO measured at the CVAO in August 2019 (red), where the shaded area shows ± the standard error of the measurements, compared to HONO photostationary state mixing ratios calculated from the average NO diurnal cycle using equation 4.11 (grey).

The photostationary state (PSS) HONO concentrations can be estimated from balancing the known in situ production and loss mechanisms described in (R4.1)-(R4.4) using equation (4.11):

$$[\mathrm{HONO}]_{\mathrm{PSS}} = \frac{k_{4.1}[\mathrm{NO}][\mathrm{OH}]}{k_{4.3}[\mathrm{OH}] + j\mathrm{HONO} + k_{\mathrm{dep}}} \qquad \text{(Eq. 4.11)}$$

where $k_{4.1}$ and $k_{4.3}$ are the rate coefficients for the reaction of OH radicals with NO and HONO, respectively, taken from Atkinson et al. (2004) [19], jHONO is the modelled photolysis rate of HONO and k_{dep} is the calculated dry deposition

rate of HONO. HONO deposition is assumed to be negligible for the aircraft measurements. For calculating $[HONO]_{PSS}$ at the CVAO, k_{dep} was calculated using a value of 3 cm s^{-1} for the HONO deposition velocity [262–265] divided by the effective boundary layer height h, which is the maximum height where dry deposition is still relevant. h was determined to vary from 175-440 m using the average Deardorff velocity (D_v) [266] and the calculated HONO photolysis lifetimes (τ_{HONO}) of approximately 12 minutes. The average Deardorff velocity measured during SLRs at $\sim$100 ft in August 2019 (ARNA-1) was determined to be 0.3 m s^{-1}. The grey area in Figure 4.13F shows the variability of the calculated $[HONO]_{PSS}$ across all the flights and the grey line in Figure 4.14 show $[HONO]_{PSS}$ at the CVAO calculated using an average diurnal cycle of NO during August 2019. Throughout the vertical profile and at the CVAO, measured HONO levels were substantially larger than these calculated levels, which are negligible in this very low NO_x environment, demonstrating the presence of an additional HONO source. The missing HONO source required to supply the observed [HONO] ($P_{HONO_{het}}$) can be estimated assuming steady state of the know sinks and sources:

$$P_{HONO_{het}} = (k_3[OH] + jHONO + k_{dep}) \times [HONO] - k_1[OH][NO] \quad \text{(Eq. 4.12)}$$

In the following sections, NO_2 uptake on aerosols and renoxification are evaluated as possible sources of HONO in the MBL.

4.8.1 NO_2 Uptake on Aerosols

Recent studies in semi-polluted and polluted environments have proposed NO_2 uptake on illuminated aerosols to be an additional source of daytime HONO [70, 216, 267–269]. Here this process is evaluated as a source of HONO in this study. Assuming that all NO_2 taken up on aerosols converts into HONO with a 100% yield, the HONO production rate can be determined using equation (4.13), where k is the reaction rate coefficient for NO_2 uptake described by

equation (4.14) [216]. $\gamma_{NO_2 \rightarrow HONO}$ is the reactive uptake coefficient of NO_2 to generate HONO, S_A is the average surface area per cm^3 of the aerosols sampled, and v is the mean thermal velocity of NO_2.

$$\frac{-\mathrm{d}[NO_2]}{\mathrm{dt}} = \frac{\mathrm{d}[HONO]}{\mathrm{dt}} = k[NO_2] \quad \text{(Eq. 4.13)}$$

$$k = \frac{\gamma_{NO_2 \rightarrow HONO} \times S_A \times v}{4} \quad \text{(Eq. 4.14)}$$

Dyson et al. (2021) [216] found $\gamma_{NO_2 \rightarrow HONO}$ on TiO_2 aerosols to depend on relative humidity and the initial NO_2 mixing ratio with the highest uptake coefficients measured at 25-30% relative humidity and approximately $[NO_2]$ = 50 ppbV. $\gamma_{NO_2 \rightarrow HONO}$ was shown to drop from 1.26×10^{-4} to approximately 4 $\times 10^{-5}$ when going from 50 ppbV to 34 ppbV of initial NO_2. These values are in good agreement with the initial uptake coefficients of NO_2 reported by Li et al. (2019) [270] for mineral dust, however, the steady-state uptake coefficients by Li et al. (2019) were significantly lower. To evaluate an upper limit of the HONO production by NO_2 uptake on aerosols, a $\gamma_{NO_2 \rightarrow HONO}$ of 10^{-4} is used for sea-salt and dust and 10^{-5} is used for biomass burning/soot [216, 270]. Using the maximum observed values for average aerosol surface area per cm^3 and NO_2 concentrations, the HONO production rate from NO_2 uptake on aerosols is estimated to be less than 1 pptV h^{-1} for all three types of aerosols, making it negligible for the conditions of this study.

4.8.2 Renoxification

As discussed above, laboratory experiments suggests that renoxification is a surface process, meaning if the missing source required to balance the measured HONO concentrations is entirely due to renoxification, then it should be equal to the product of $j\mathrm{pNO}_3^-$ and pNO_3^- at the surface [51]:

$$P_{HONO_{het}} = j\mathrm{pNO}_{3\,\mathrm{surface}}^- \times [\mathrm{pNO}_3^-]_{\mathrm{surface}} \quad \text{(Eq. 4.15)}$$

However, like in previous studies [44,51,52], the total (or "bulk") pNO_3^- has been determined as it has not been possible to determine the concentration at the surface. It has therefore been necessary to define an effective photolysis rate of the bulk pNO_3^- and the observationally-derived enhancement factor, f_{obs}:

$$P_{\mathrm{HONO}_{het}} = j\mathrm{pNO}_{3\ \mathrm{effective}}^- \times [\mathrm{pNO}_3^-]_{\mathrm{bulk}} \quad \text{(Eq. 4.16)}$$

$$f_{obs} = \frac{j\mathrm{pNO}_{3\ \mathrm{effective}}^-}{j\mathrm{HNO}_3} \quad \text{(Eq. 4.17)}$$

By combining equation (4.16) and (4.17) f_{obs} can be derived from available parameters:

$$f_{obs} = \frac{P_{\mathrm{HONO}_{het}}}{j\mathrm{HNO}_3 \times [\mathrm{pNO}_3^-]_{\mathrm{bulk}}} \quad \text{(Eq. 4.18)}$$

It should be noted that this definition only considers the production of HONO and ignores the co-production of NO_2. This is important to note when comparing the enhancement factors in this study to laboratory studies which have measured the production of all gaseous oxidised nitrogen products, although it is of limited consequence if the yield of HONO is >0.9 as suggested from a budget analysis of field measurements [271].

$[\mathrm{pNO}_3^-]_{\mathrm{bulk}}$ on the aircraft has been determined as the total nitrate concentration (>1 µm + <1 µm). The ground-based $[\mathrm{pNO}_3^-]_{\mathrm{bulk}}$ are 24-hour averages of PM_{10}. All other relevant measurements on the aircraft have been determined as averages over the time of each aerosol sample and the ground-based have been averaged daily using the midday (11.00-16.00 UTC, local+1) measurements due to the sampling time for the aerosol composition being 24 hours.

Figure 4.15A shows the missing HONO source derived from the aircraft and ground-based HONO observations using equation (4.12) plotted against $j\mathrm{HNO}_3 \times [\mathrm{pNO}_3^-]_{\mathrm{bulk}}$ and coloured by the dominant aerosol type. The observed

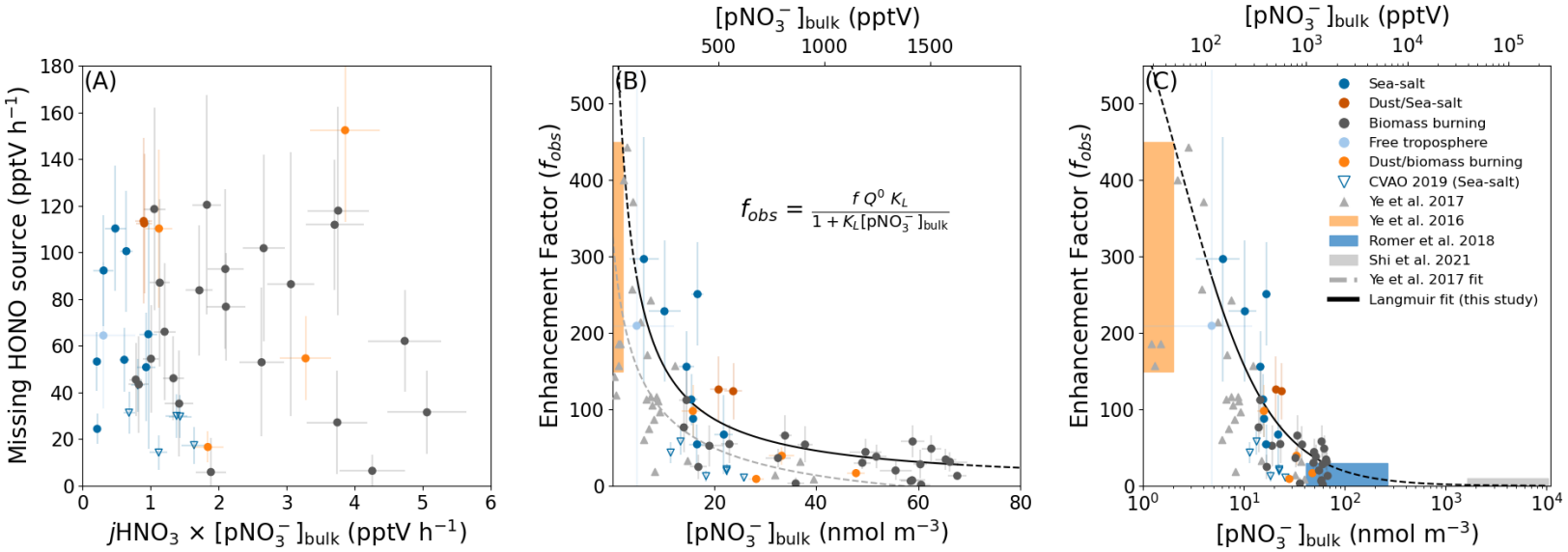

Figure 4.15: (A) Relationship between the calculated missing HONO source ($P_{\mathrm{HONO}_{het}}$) and the photolysis of particulate nitrate. Data points are coloured according to the dominant aerosol classification. (B) Derived enhancement factors, f_{obs}, as a function of $[\mathrm{pNO_3^-}]_{\mathrm{bulk}}$. A Langmuir model (equation 4.21) is used to fit the aircraft data (coloured circles), assuming $f = 100$ to give $Q^0 = 19.48$ nmol m^{-3}, and $K_{\mathrm{L}} = 0.43$ nmol^{-1} m^3 ($\mathrm{R}^2 = 0.66$). $[\mathrm{pNO_3^-}]_{\mathrm{bulk}}$ was converted from nmol m^{-3} to pptV on the second x-axis using surface pressure and temperature. Also shown are the laboratory data of Ye et al. (2017) [223] using aerosol filters (grey triangles) and their fit to the data (grey dashed line) and the aircraft data of Ye et al. (2016) [51] from the remote North Atlantic marine boundary layer (orange rectangle). (C) Same as (B) but a wider comparison of f_{obs} with previously reported values, with the x-axis on a log scale. The $[\mathrm{pNO_3^-}]_{\mathrm{bulk}}$ used is a lower limit meaning the derived f_{obs} are upper limits due to the sampling efficiency of coarse mode aerosols (>1 µm) has been shown to be lower than 100% for aircraft measurements [245, 246, 253]. The effect of the sampling efficiency of coarse mode aerosols have been investigated in Figure 4.16. The error bars represent the propagated uncertainties of all the relevant measurements and 20% uncertainty on all rate coefficients using equation (4.6), (4.7), and (4.8).

enhancement factor, f_{obs}, can be determined as the slope of the plot, however, no linear relationship can be observed from the measurements unlike the study by Ye et al. (2016) [51]. Nevertheless, the ground-based measurements here (Figure 4.14) and in previous studies [44, 52] show unexpectedly high daytime concentrations of HONO, consistent with a photochemical mechanism. The average f_{obs} derived for air masses dominated by sea-salt, dust, and biomass burning were 157 (range 54-296), 125 (two data points), and 38 (range 1.5-112), respectively. The sea-salt and dust-dominated samples give similar values to those derived by Ye et al. (2016) of 150-450 using the same approach as used for Figure 4.15A for airborne measurements over the Atlantic Ocean [51]. However, the values derived for biomass burning and for the ground-based CVAO sea-salt aerosol measurements (f_{obs} of $\sim$10 - 60) are significantly lower, but in good agreement with previous estimates at the CVAO of $\sim$10 [44]. This is not surprising since renoxification has been shown to be dependent on chemical composition, acidity, humidity, temperature, and distribution of pNO_3^- in the aerosols [216, 221, 225, 226, 231–238, 272–274].

Ye et al. (2017) conducted laboratory photolysis experiments on aerosol filter samples collected from urban, suburban/rural, and remote areas, and measured the production of HONO and NO_2 when exposing the filters to light [223]. Their reported $j\mathrm{pNO}_{3\,\mathrm{effective}}^-$ have been converted into enhancement factors using $j\mathrm{HNO}_3 = 7 \times 10^{-7}$ s^{-1}, which corresponds to typical tropical summer conditions on the ground (solar elevation angle $\theta = 0°$) as simulated in their light-exposure experiments and plotted as grey triangles in Figure 4.15B together with their empirical fit to the data (grey dashed line). They observed a strong decrease in enhancement factors with increasing $[\mathrm{pNO}_3^-]_{\mathrm{bulk}}$. The derived f_{obs} from Figure 4.15A is also plotted as a function of measured $[\mathrm{pNO}_3^-]_{\mathrm{bulk}}$ in Figure 4.15B, where f_{obs} can be observed to decrease rapidly with increasing $[\mathrm{pNO}_3^-]_{\mathrm{bulk}}$ by approximately an order of magnitude from $\sim$250 in marine and free tropospheric air with $[\mathrm{pNO}_3^-]_{\mathrm{bulk}} < 10$ nmol m^{-3} (260 pptV) to $\sim$25 in biomass burning air masses associated with $[\mathrm{pNO}_3^-]_{\mathrm{bulk}}$ of > 50 nmol

m^{-3} (1500 pptV).

As discussed above, nitrate has been shown to exhibit surface activity caused by the co-presence of halide ions and/or organic films. The samples dominated by sea salt and dust are expected to be liquid due to the RH of those samples all being above 80%. The other samples were taken at significantly lower RH (5%-70%), which could mean they were solid. However, a study of water uptake on particles showed that pure KNO_3 particles grew continuously when increasing the RH from 0% to 100% without deliquescing [275]. As all the biomass burning samples are high in both potassium and nitrate, it does not seem unlikely that they will contain some water as well. Assuming that nitrate behaves as a surfactant in liquid (deliquesced) aerosol, then the partitioning between the equilibrium surface and equilibrium bulk nitrate can be described using a Langmuir adsorption isotherm:

$$[\mathrm{pNO_3^-}]_{\mathrm{surface}} = \frac{Q^0 \times K_{\mathrm{L}} \times [\mathrm{pNO_3^-}]_{\mathrm{bulk}}}{1 + K_{\mathrm{L}} \times [\mathrm{pNO_3^-}]_{\mathrm{bulk}}} \qquad \text{(Eq. 4.19)}$$

where Q^0 is the maximum loading of adsorbate NO_3^- corresponding to complete monolayer coverage and K_{L} is the Langmuir equilibrium constant of NO_3^-. The concentration of pNO_3^- at the surface reaches a saturation point when full monolayer coverage is reached even if the bulk concentration of pNO_3^- increases. This implies, if renoxification is a surface reaction, that f_{obs} will level off at high $[pNO_3^-]_{\mathrm{bulk}}$ as observed in Figure 4.15B. By combining equation (4.15), (4.18), and (4.19) the dependence of f_{obs} on $[pNO_3^-]_{\mathrm{bulk}}$ can be described:

$$f_{obs} = \frac{P_{\mathrm{HONO}_{het}}}{j\mathrm{HNO_3} \times [\mathrm{pNO_3^-}]_{\mathrm{bulk}}} = \frac{j\mathrm{pNO_3^-}_{\,\mathrm{surface}}}{j\mathrm{HNO_3}} \times \frac{[\mathrm{pNO_3^-}]_{\mathrm{surface}}}{[\mathrm{pNO_3^-}]_{\mathrm{bulk}}} \qquad \text{(Eq. 4.20)}$$

$$f_{obs} = \frac{f \times [\mathrm{pNO_3^-}]_{\mathrm{surface}}}{[\mathrm{pNO_3^-}]_{\mathrm{bulk}}} = \frac{f \times Q^0 \times K_{\mathrm{L}}}{1 + K_{\mathrm{L}} \times [\mathrm{pNO_3^-}]_{\mathrm{bulk}}} \qquad \text{(Eq. 4.21)}$$

where $f = j\mathrm{pNO_3^-}_{\,\mathrm{surface}}/j\mathrm{HNO_3}$.

Equation (4.21) was fitted to the f_{obs} derived from the aircraft measurements (coloured circles) to derive the equation parameters, shown by the black line in Figure 4.15B. The reasonable fit ($R^2 = 0.66$) of the Langmuir model demonstrates a potential explanation for the strong negative dependence of the renoxification enhancement factor on $[pNO_3^-]_{bulk}$. It should be noted that the $[pNO_3^-]_{bulk}$ used is a lower limit meaning the derived f_{obs} are upper limits due to the sampling efficiency of coarse mode aerosols (>1 µm) has been shown to be lower than 100% for aircraft measurements [245, 246, 253]. The effect of the sampling efficiency of coarse mode aerosols have been investigated in Figure 4.16 by varying it from 100% (Figure 4.16A and Figure 4.15B) to 40% (Figure 4.16D). The fit can be observed to essentially be identical whether the sampling efficiency is 100% or 40% for coarse mode aerosols. The fit to the data levels off at a f_{obs} of 837 when reaching $[pNO_3^-]_{bulk} < 0.01$ nmol m^{-3} (0.26 pptV) resulting in a photolytic lifetime of $\sim$28 minutes when assuming $jHNO_3 = 7 \times 10^{-7}$ s^{-1}. This suggests that pNO_3^- can be depleted from aerosols with extremely low $[pNO_3^-]_{bulk}$.

Recent laboratory experiments (grey box in Figure 4.15C) and field observations of NO_x/HNO_3 ratios (blue box) have derived enhancement factors of <30. This has lead them to suggest that renoxification only plays a limited role in atmospheric chemistry and the recycling of NO_x [226, 228]. Both studies were, however, carried out under very high pNO_3^- mass concentrations where the Langmuir model predicts low enhancement factors with a small dependence on pNO_3^- across the concentration ranges explored (Figure 4.15C).

It is evident from the difference in enhancement factors observed for airborne sea-salt samples and measurements at the CVAO, which were also dominated by sea-salt (Figure 4.15B and C), that aerosol parameters other than the nitrate abundance play a significant part in renoxification. One potential reason for the lower enhancements found in ground-based studies compared to aircraft observations is that the surface measurements experience fresh rather than aged sea salt aerosol, due to sampling within the surf zone. As discussed

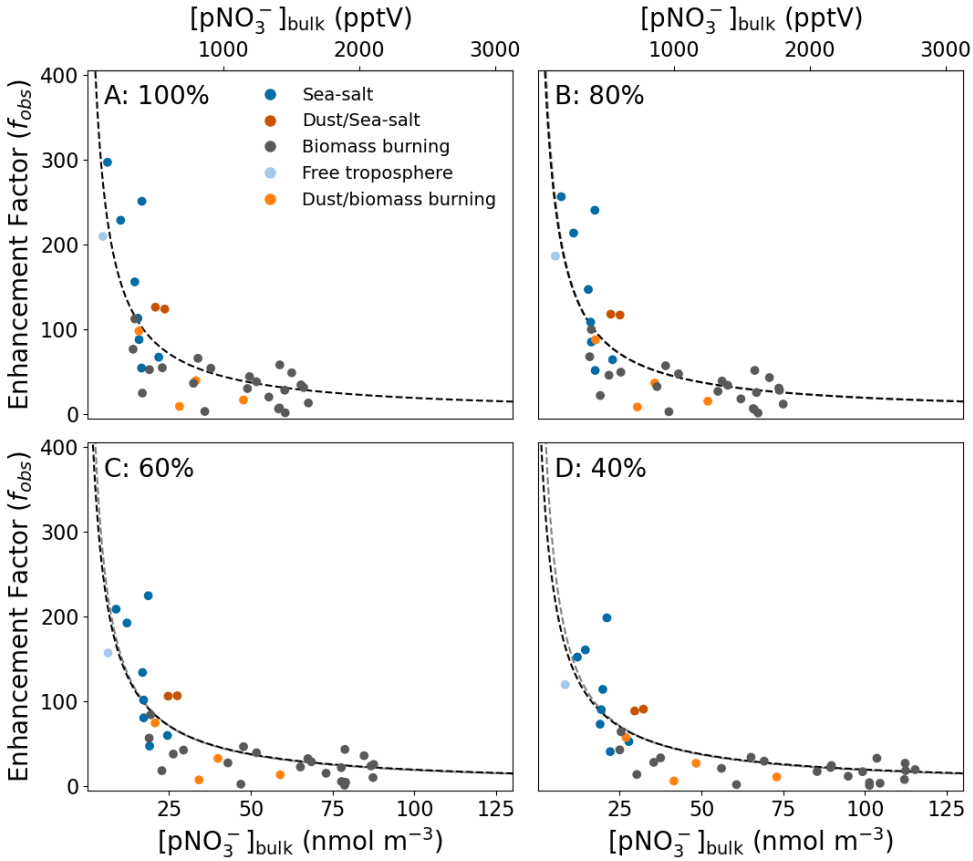

Figure 4.16: Figure 4.15B replotted, where the sampling efficiency of coarse mode aerosols (>1 µm) have been set to 80% (B), 60% (C), and 40% (D) while the fine mode (<1 µm) is set to 100%. The black dashed lines are the Langmuir fit for the data points, and the grey dashed lines in panel B, C, and D are the fit when setting the coarse mode sampling efficiency to 100%.

above, Scharko et al. (2014) observed decreasing HONO production from renoxification with increasing pH until no HONO production was observed at pH $\geq$ 4 [221]. Sea water has been measured to have a pH of approximately 8, however, sea-salt aerosols have been shown to be acidified in less than two minutes from being emitted by sea spray to reach a pH of $\sim$2 for <1 µm aerosols and $\sim$4 for >1 µm aerosols [276]. The ground-based HONO measurements could therefore be representative of renoxification of freshly emitted sea-salt aerosols with a higher pH than the aerosols sampled on the aircraft resulting in a lower HONO production.

4.9 Conclusion

This study shows that the observed enhancement factor of photolysis of pNO_3^- compared to gas-phase HNO_3, when only looking at the production of HONO, decreases rapidly with increasing pNO_3^-. This suggests that a major factor in renoxification is the distribution of pNO_3^-, which can potentially be explained by a Langmuir adsorption isotherm, which reconciles large discrepancies in previously reported enhancement factors. However, it does not exclude that other parameters such as acidity, composition, temperature, and humidity have an impact either on the enhancement of the photolysis rate or on the products formed from the reaction as significant differences can be observed between ground-based and airborne marine measurements. The results suggest that renoxification is an important mechanism for recycling nitric acid in the atmosphere and is an active process on a variety of ambient aerosols, which could have significant implications on atmospheric oxidants.

Chapter 5

Summary and Conclusions

The work presented in this dissertation has improved our knowledge of nitrogen oxides ($NO_x = NO + NO_2$) sources and cycling in the remote marine boundary layer (MBL) by evaluating the reliability of NO_x measurements performed at the Cape Verde Atmospheric Observatory (CVAO) and using the resulting unique dataset together with airborne measurements to explore fundamental processes in the atmosphere.

Atmospheric NO_x has been measured at the CVAO in the tropical Atlantic (16° 51' N, 24° 52' W) since October 2006, where NO_2 is measured via photolytic conversion to nitric oxide (NO) by ultra violet light-emitting diodes followed by chemiluminescence detection. These measurements represent a unique time series of NO_x in the background remote troposphere. However, conversion of NO_2 to NO is often associated with photolytic and/or thermal artefacts causing an overestimation of NO_2 [107, 108, 132, 170, 172–174], which has the potential to significantly affect remote measurements where mixing ratios are of the order of pptV. By changing the NO_2 converter from a blue light converter (BLC) with internal diodes to a custom-built photolytic converter (PLC) with a quartz photolysis cell and external diodes, thermal artefacts were believed to be minimised. NO_2 measurements using the new PLC were shown to be in good agreement with artefact corrected BLC measurements giving

confidence in the quantitative measurement of NO_x at very low levels.

The unique NO_x dataset from the CVAO was utilised in chapter 3 to investigate fundamental oxidation processes in the remote MBL. Deviations in the photostationary state (PSS) equilibrium between NO and NO_2 have previously been used to infer missing oxidants everywhere from highly polluted regions to the extremely clean conditions observed in the remote MBL, which has been interpreted as missing understanding of fundamental photochemistry [158, 161, 164]. Here, contrary to these previous observations, a good agreement between observed NO_2 and PSS-derived NO_2 ($[NO_2]_{\text{PSS ext.}}$) calculated from photochemical model predictions of peroxy radicals (RO_2 and HO_2) and measured NO, O_3, and jNO_2 was observed in extremely clean air containing low levels of CO (< 90 ppbV) and VOCs when considering potential contributions from NO_2 artefacts. In clean air containing small amounts of aged pollution (CO > 100 ppbV), higher levels of NO_2 than inferred from the PSS were observed, with $[NO_2]_{\text{Obs.}}/[NO_2]_{\text{PSS ext.}}$ of 1.12-1.68 (25^{th}-75^{th} percentile). This implied 18.5-104 pptV (25^{th}-75^{th} percentile) of missing RO_2 radicals or an additional artefact which would have to be on average 3 times greater than the maximum calculated from known interferences. The net ozone production rate (NOPR) was calculated using both the modelled and PSS-derived peroxy radicals and compared to the observed to evaluate the effect of the additional RO_2 radicals. If the missing RO_2 radicals have an ozone production efficiency equivalent to that of methyl peroxy radicals (CH_3O_2), then the calculated net ozone production including these additional oxidants is similar to that observed, within estimated uncertainties, once halogen oxide chemistry is accounted for. This implies that peroxy radicals cannot be excluded as the missing oxidant in clean marine air containing aged pollution, however, there is also no robust evidence of the missing oxidant being O_3-producing.

Observed mixing ratios of HONO at the CVAO exceed what would be expected from the extremely low abundance of NO_x at this remote site, suggesting a missing HONO source in the MBL. The origin of the missing HONO

source was investigated in chapter 4 using the CVAO measurements supplemented by HONO measurements together with airborne measurements of HONO, NO_x, particulate nitrate (pNO_3^-), and aerosol surface area. The missing HONO source was determined to vary from $\sim$6.5-140 pptV h^{-1} across the airborne straight-and-level-runs (SLRs). NO_2 uptake on aerosols and photolysis of particulate nitrate were investigated as potential sources. Uptake of NO_2 on aerosols has been proposed as a source of $HONO/NO_x$ in polluted and semi-polluted regions [70, 71, 73], however, with the limited availability of NO_2 in the MBL ($\sim$5-50 pptV), the maximum production rate from this source was calculated as $\sim$1 pptV h^{-1}. Formation of pNO_3^- has long been considered an irreversible sink for NO_x, however, recent studies have proposed that photolysis of pNO_3^- could be an important source of nitrous acid (HONO) and NO_x in the MBL [44, 51, 52]. Enhancement factors (f) of this "renoxification" process, when comparing the photolysis rate of pNO_3^- to the photolysis rate of nitric acid (HNO_3), has been reported to vary by orders of magnitude [51, 52, 219, 222–224, 226, 228, 229], but there has been no mechanistic explanation for why such variability occurs. In chapter 4 the process was investigated using primarily airborne measurements of aerosols with a variety of origins (sea-salt, dust, and biomass burning). No linear relationship was found when assuming that the entire missing HONO source was due to photolysis of pNO_3^-, however, the estimated f_{obs} for each aerosol sample could be observed to decrease with increasing pNO_3^- concentrations. This is consistent with the rate of HONO production being controlled by surface-enhanced nitrate ions, a phenomenon suggested by theoretical and laboratory studies [220, 225, 236–238]. Large discrepancies in reported f across laboratory and field studies can be largely reconciled through this surface-mediated mechanism.

Both the observed missing oxidants in chapter 3 and the HONO production from renoxification on a wide range of aerosols in chapter 4 can have important implications for atmospheric oxidants such as OH and O_3 and their trends in both polluted and clean environments.

5.1 Outlook

Since the biggest uncertainties on NO_x measurements are due to noise in the form of precision and artefact measurements, the obvious way to improve the measurements would be to change to a direct measurement technique such as Laser Induced Fluorescence (LIF). LIF instruments have a better precision than chemiluminescence and excites NO and NO_2 at wavelengths where there should be no artefact.

In the future it would be useful to identify the source of the spikes in the dataset, which are currently being removed before doing any data analysis as they are not representative of the background measurements. One possible source could be local fishing boats. It has therefore been discussed to hire one of them to sail past the observatory for a few hours and follow the measurements. Another measurement that would be useful when investigating remote NO_x chemistry is total NO_y. There are plans to add this in the Autumn/Winter of 2022.

It is evident from the deviations from NO-NO_2-O_3 photostationary state when CO $>$ 100 ppbV discussed in chapter 3, that year-long HO_2 and RO_2 measurements at the CVAO could help determine the origin of the "missing RO_2". While total RO_x (HO_2+RO_2) measurements conducted by chemical amplification would be a start, the measurements would still be subject to the same challenges as previous measurements from short field campaigns in the same region. The ideal solution would be having a direct measurement, which does not depend on chemical amplification and can differentiate between different types of peroxy radicals, so the different rate coefficient can be taken into account. Chemical Ionization Mass Spectrometry (CIMS) has been shown to be able to measure different peroxy radicals (eg. CH_3O_2, $CH_3C(O)O_2$, $(CH_3)_3CO_2$, and c$-C_6H_{11}O_2$) simultaneously [277], however, the reported limit of detection for each radical makes it unsuitable for use in the field at this stage. Measurements of methyl peroxy (CH_3O_2), which is expected to be the most

abundant peroxy radical in the MBL and is one of the few peroxy radicals used for chemical amplification calibrations, could be used to validate model predictions and thereby help bridge the gap in our current understanding of fundamental oxidation processes. CH_3O_2 concentrations as low as 1.1×10^8 molecule cm^{-3} ($\sim$4 pptV) has been detected by fluorescence assay by gas extension (FAGE) in the laboratory when averaging over an hour, which is comparable to ambient concentrations [278].

Most HONO instruments were developed to measure HONO in urban areas, where the concentrations observed are significantly higher than those observed in the remote MBL, however, the measurements shown in chapter 4 clearly shows a need for an airborne instrument with the limit of detection (LOD) of a Long Path Absorption Photometer (LOPAP), but with a higher resolution and which can either be calibrated in-flight or at the very least directly before and after a flight. The HONO LOD of the differential photolysis instrument used in chapter 4 is approximately 2.1 pptV (1σ) when averaging over a SLR ($\sim$20 min), which is good enough if no rapid changes in concentration are observed. However, it currently cannot be calibrated while on field work. This could be solved by bringing a portable calibration unit like the one described by Lao et al. (2020) [279].

Appendix A

O_3 Correction

NO and NO_2 are in photostationary state in the atmosphere, where NO reacts with O_3 to give NO_2 and NO_2 is photolysed to NO:

$$NO + O_3 \xrightarrow{k_{NO+O3}} NO_2 + O_2 \quad \text{(RA.1)}$$

$$NO_2 + h\nu (\leq 410\,\text{nm}) \xrightarrow{j_C} NO + O(^3P) \quad \text{(RA.2)}$$

When measuring NO and NO_2, NO continues to react with ambient O_3 in the sample line to the instrument, however, no photolysis occurs in the sample line causing an underestimation of NO and an overestimation of NO_2. This can be corrected using the equations described below.

A.1 NO Correction

Since NO only reacts with O_3 in the line and is not photolysed back to NO as it would be in the atmosphere during daylight, the decrease in NO can be described by a simple rate equation:

$$\frac{d[NO]}{dt} = -k_{NO+O3}[O_3][NO] = -k_{O3}[NO] \quad \text{(Eq. A.1)}$$

where $k_{NO+O3}[O_3] = k_{O3}$. By integrating between time = 0 and the time it takes to reach the reaction cell (t = t_{E1}) the following is obtained:

$$\ln\left(\frac{[NO]_{E1}}{[NO]_0}\right) = -k_{O3} \times t_{E1} \quad \text{(Eq. A.2)}$$

$$[NO]_0 = [NO]_{E1} \times e^{k_{O3} \times t_{E1}} \quad \text{(Eq. A.3)}$$

where $[NO]_0$ and $[NO]_{E1}$ are the NO mixing ratio at the inlet and that measured by the PMT, respectively.

A.2 NO_2 Correction

NO_2 is measured by converting it photolytically into NO and reacting the NO with O_3 to produce excited state NO_2 which emits chemiluminescent light as it drops to the ground state. The measured mixing ratio of NO_2 is calculated from the NO signals with ($[NO]_{E2}$) and without ($[NO]_{E1}$) the converter on and the conversion efficiency of the converter (SC):

$$[NO_2]_M = \frac{[NO]_{E2} - [NO]_{E1}}{S_C} \quad \text{(Eq. A.4)}$$

To correct the measured NO_2 mixing ratio for reactions with O_3, the following needs to be taken into account:

- NO reacts with O_3 in the line before reaching the converter.

- NO_2 is photolysed into NO at the same time as NO continues to react with O_3 inside the converter.

The photostationary state of NO and NO_2 inside the converter can be described by the following equations:

$$[NO]_{PSS} = [NO]_0 + \Delta[NO] \quad \text{(Eq. A.5)}$$

$$[NO_2]_{PSS} = [NO_2]_0 - \Delta[NO_2] \quad \text{(Eq. A.6)}$$

where $[NO]_{PSS}$ and $[NO_2]_{PSS}$ are the photostationary state mixing ratios of NO and NO_2, respectively, $[NO]_0$ and $[NO_2]_0$ are the mixing ratios of NO and NO_2 at the entrance of the inlet, and ΔNO and ΔNO_2 are the change in NO and NO_2 inside the converter. The change in NO and NO_2 will be equal since the only reactions occurring are reactions RA.1 and RA.2. Thus, the photo-stationary state can be written as:

$$[NO]_{PSS} = [NO]_0 + [NO_2]_0 - [NO_2]_{PSS} \quad \text{(Eq. A.7)}$$

$$[NO_2]_{PSS} = [NO_2]_0 - ([NO]_{PSS} - [NO]_0) = [NO_2]_0 + [NO]_0 - [NO]_{PSS} \quad \text{(Eq. A.8)}$$

In photostationary state, reactions A.1 and A.2 react with the same rate, which can be written as:

$$k_{O3} \times [NO]_{PSS} = j_C \times [NO_2]_{PSS} \quad \text{(Eq. A.9)}$$

where j_C is the photolysis rate of the converter. Combining equation A.8 and A.9 gives the following equations for the photostationary state of NO:

$$[NO]_{PSS} = \frac{j_C}{k_{O3}} \times [NO_2]_{PSS} = \frac{j_C}{k_{O3}} \times ([NO_2]_0 + [NO]_0 - [NO]_{PSS}) \quad \text{(Eq. A.10)}$$

$$[NO]_{PSS} = \frac{j_C}{k_{O3}} \times ([NO_2]_0 + [NO]_0) - \frac{j_C}{k_{O3}} \times [NO]_{PSS} \quad \text{(Eq. A.11)}$$

$$\left(1 + \frac{j_C}{k_{O3}}\right) \times [NO]_{PSS} = \left(\frac{k_{O3} + j_C}{k_{O3}}\right) \times [NO]_{PSS} = \frac{j_C}{k_{O3}} \times ([NO_2]_0 + [NO]_0) \quad \text{(Eq. A.12)}$$

$$[\mathrm{NO}]_{\mathrm{PSS}} = \left(\frac{k_{\mathrm{O3}}}{k_{\mathrm{O3}} + j_{\mathrm{C}}}\right) \times \frac{j_{\mathrm{C}}}{k_{\mathrm{O3}}} \times ([\mathrm{NO_2}]_0 + [\mathrm{NO}]_0)$$
$$= \left(\frac{j_{\mathrm{C}}}{k_{\mathrm{O3}} + j_{\mathrm{C}}}\right) \times ([\mathrm{NO_2}]_0 + [\mathrm{NO}]_0) \quad \text{(Eq. A.13)}$$

By combining equations (A.9) and (A.13), the photostationary state of NO_2 in the converter can be obtained:

$$[\mathrm{NO_2}]_{\mathrm{PSS}} = \frac{k_{\mathrm{O3}}}{j_{\mathrm{C}}} \times [\mathrm{NO}]_{\mathrm{PSS}} = \frac{k_{\mathrm{O3}}}{j_{\mathrm{C}}} \times \left(\frac{j_{\mathrm{C}}}{k_{\mathrm{O3}} + j_{\mathrm{C}}}\right) \times ([\mathrm{NO_2}]_0 + [\mathrm{NO}]_0) \quad \text{(Eq. A.14)}$$

$$[\mathrm{NO_2}]_{\mathrm{PSS}} = \left(\frac{k_{\mathrm{O3}}}{k_{\mathrm{O3}} + j_{\mathrm{C}}}\right) \times ([\mathrm{NO_2}]_0 + [\mathrm{NO}]_0) \quad \text{(Eq. A.15)}$$

The photolysis rate inside the converter is given by:

$$j_{\mathrm{C}} = \frac{-\ln(1 - \mathrm{S_C})}{\mathrm{t_{C2}}} \quad \text{(Eq. A.16)}$$

where t_{C2} is the time the air is in the converter while it is on.

Inside the converter, the NO mixing ratio moves towards photostationary state ($[NO]_{PSS}$) with a rate of $k_{O3} + j_C$ since some of the NO_2 being photolysed to NO in the converter will react with O_3 in the sample to regenerate NO_2. This can be described by equation (A.17), where $[NO]_L$ is the NO mixing ratio at the entrance of the converter:

$$[\mathrm{NO}]_{\mathrm{E2}} = [\mathrm{NO}]_{\mathrm{PSS}} - ([\mathrm{NO}]_{\mathrm{PSS}} - [\mathrm{NO}]_{\mathrm{L}}) \times \mathrm{e}^{(-(k_{\mathrm{O3}} + j_{\mathrm{C}}) \times \mathrm{t_{C2}})} \quad \text{(Eq. A.17)}$$

$$[\mathrm{NO}]_{\mathrm{E2}} = [\mathrm{NO}]_{\mathrm{PSS}} - [\mathrm{NO}]_{\mathrm{PSS}} \times \mathrm{e}^{(-(k_{\mathrm{O3}} + j_{\mathrm{C}}) \times \mathrm{t_{C2}})} - [\mathrm{NO}]_{\mathrm{L}} \times \mathrm{e}^{(-(k_{\mathrm{O3}} + j_{\mathrm{C}}) \times \mathrm{t_{C2}})} \quad \text{(Eq. A.18)}$$

$$[\mathrm{NO}]_{\mathrm{E2}} = [\mathrm{NO}]_{\mathrm{PSS}} \times (1 - \mathrm{e}^{(-(k_{\mathrm{O3}} + j_{\mathrm{C}}) \times \mathrm{t_{C2}})}) - [\mathrm{NO}]_{\mathrm{L}} \times \mathrm{e}^{(-(k_{\mathrm{O3}} + j_{\mathrm{C}}) \times \mathrm{t_{C2}})} \quad \text{(Eq. A.19)}$$

The NO mixing ratio at the entrance of the converter can be estimated from the loss of NO to O_3 in the line in the same way as the ozone corrected

NO mixing ratio could be determined:

$$[\mathrm{NO}]_{\mathrm{L}} = [\mathrm{NO}]_0 \times \mathrm{e}^{(-k_{\mathrm{O3}} \times \mathrm{t_L})} = [\mathrm{NO}]_{\mathrm{E1}} \times \mathrm{e}^{(k_{\mathrm{O3}} \times \mathrm{t_{E1}})} \times \mathrm{e}^{(-k_{\mathrm{O3}} \times \mathrm{t_L})} \quad \text{(Eq. A.20)}$$

$$[\mathrm{NO}]_{\mathrm{L}} = [\mathrm{NO}]_{\mathrm{E1}} \times \mathrm{e}^{(k_{\mathrm{O3}} \times \mathrm{t_{C1}})} \quad \text{(Eq. A.21)}$$

Equations (A.19) and (A.21) are combined to give equation (A.22):

$$[\mathrm{NO}]_{\mathrm{E2}} = [\mathrm{NO}]_{\mathrm{PSS}} \times (1 - \mathrm{e}^{(-(k_{\mathrm{O3}}+j_{\mathrm{C}}) \times \mathrm{t_{C2}})}) - [\mathrm{NO}]_{\mathrm{E1}} \times \mathrm{e}^{(k_{\mathrm{O3}} \times \mathrm{t_{C1}} - (k_{\mathrm{O3}}+j_{\mathrm{C}}) \times \mathrm{t_{C2}})} \quad \text{(Eq. A.22)}$$

$[\mathrm{NO}]_{\mathrm{PSS}}$ is isolated to give equation (A.23):

$$[\mathrm{NO}]_{\mathrm{PSS}} = \frac{[\mathrm{NO}]_{\mathrm{E2}} - [\mathrm{NO}]_{\mathrm{E1}} \times \mathrm{e}^{(k_{\mathrm{O3}} \times \mathrm{t_{C1}} - (k_{\mathrm{O3}}+j_{\mathrm{C}}) \times \mathrm{t_{C2}})}}{(1 - \mathrm{e}^{(-(k_{\mathrm{O3}}+j_{\mathrm{C}}) \times \mathrm{t_{C2}})})} \quad \text{(Eq. A.23)}$$

Lastly equations (A.13) and (A.23) are combined to give equation (A.24) and rearranged to give the ozone corrected mixing ratio in equation (A.25):

$$\left(\frac{j_{\mathrm{C}}}{k_{\mathrm{O3}} + j_{\mathrm{C}}}\right) \times ([\mathrm{NO_2}]_0 + [\mathrm{NO}]_0) = \frac{[\mathrm{NO}]_{\mathrm{E2}} - [\mathrm{NO}]_{\mathrm{E1}} \times \mathrm{e}^{(k_{\mathrm{O3}} \times \mathrm{t_{C1}} - (k_{\mathrm{O3}}+j_{\mathrm{C}}) \times \mathrm{t_{C2}})}}{(1 - \mathrm{e}^{(-(k_{\mathrm{O3}}+j_{\mathrm{C}}) \times \mathrm{t_{C2}})})} \quad \text{(Eq. A.24)}$$

$$[\mathrm{NO_2}]_0 = \left(\frac{k_{\mathrm{O3}} + j_{\mathrm{C}}}{j_{\mathrm{C}}}\right) \times \left(\frac{[\mathrm{NO}]_{\mathrm{E2}} - [\mathrm{NO}]_{\mathrm{E1}} \times \mathrm{e}^{(k_{\mathrm{O3}} \times \mathrm{t_{C1}} - (k_{\mathrm{O3}}+j_{\mathrm{C}}) \times \mathrm{t_{C2}})}}{(1 - \mathrm{e}^{(-(k_{\mathrm{O3}}+j_{\mathrm{C}}) \times \mathrm{t_{C2}})})}\right) - [\mathrm{NO}]_0 \quad \text{(Eq. A.25)}$$

A.3 Low O_3 Concentration

At low O_3 concentrations k_{O3} tends towards 0 and becomes very small compared to j_C, such that the calculations for NO and NO_2 become:

$$[NO]_0 = [NO]_{E1} \quad \text{(Eq. A.26)}$$

$$[NO_2]_0 = \left(\frac{j_C}{j_C}\right) \times \left(\frac{[NO]_{E2} - [NO]_{E1} \times e^{(-j_C \times t_{C2})}}{1 - e^{(-j_C \times t_{C2})}}\right) - [NO]_0 \quad \text{(Eq. A.27)}$$

$$[NO_2]_0 = \frac{[NO]_{E2} - [NO]_{E1} \times e^{(-j_C \times t_{C2})} - [NO]_{E1} + [NO]_{E1} \times e^{(-j_C \times t_{C2})}}{1 - e^{(-j_C \times t_{C2})}} \quad \text{(Eq. A.28)}$$

$$[NO_2]_0 = \frac{[NO]_{E2} - [NO]_{E1}}{(1 - e^{(-j_C \times t_{C2})})} = \frac{[NO]_{E2} - [NO]_{E1}}{1 - e^{\left\{-\left(\frac{\ln(1-S_C)}{t_{C2}}\right) \times t_{C2}\right\}}} = \frac{[NO]_{E2} - [NO]_{E1}}{S_C} \quad \text{(Eq. A.29)}$$

A.4 Example Calculation

An example calculation of the O_3 corrections is shown below, assuming a conversion efficiency of 50% (SC = 50%), a time of 3.3 s from the inlet to the converter (t_L = 3.3 s), a residence time of 1 s for the sample in the converter whether the converter is on or not ($t_{C1} = t_{C2}$ = 1 s), an ozone mixing ratio of 30 ppbV, a temperature of at 298 K and therefore, using k(O_3 + NO) = 1.8 × 10^{-14} cm^3 $molecule^{-1}$ s^{-1}, a k_{O3} = 0.013 s^{-1}. We start with uncorrected mixing ratios (i.e. measured mixing ratios) of $[NO]_M$ = 10 pptV and $[NO_2]_M$ = 30 pptV:

$$[NO]_{E1} = 10\text{pptV} \quad \text{(Eq. A.30)}$$

$$[NO]_{E2} = 30\text{pptV} \times 0.5 + 10\text{pptV} = 25\text{pptV} \quad \text{(Eq. A.31)}$$

$$j_C = \frac{-\ln(1 - S_C)}{t_{C2}} = \frac{-\ln(1 - 0.5)}{1\text{s}} = 0.69\text{s}^{-1} \quad \text{(Eq. A.32)}$$

$$[NO]_0 = [NO]_{E1} \times e^{k_{O3} \times t_{E1}} = 10\,\text{pptV} \times e^{0.013\,\text{s}^{-1} \times 4.3\,\text{s}} = 10.6\,\text{pptV} \quad \text{(Eq. A.33)}$$

$$
\begin{aligned}
&[\mathrm{NO_2}]_0 = \\
&\left(\frac{k_{\mathrm{O3}} + j_{\mathrm{C}}}{j_{\mathrm{C}}}\right) \times \left(\frac{[\mathrm{NO}]_{\mathrm{E2}} - [\mathrm{NO}]_{\mathrm{E1}} \times \mathrm{e}^{(k_{\mathrm{O3}} \times \mathrm{t_{C1}} - (k_{\mathrm{O3}} + j_{\mathrm{C}}) \times \mathrm{t_{C2}})}}{(1 - \mathrm{e}^{(-(k_{\mathrm{O3}} + j_{\mathrm{C}}) \times \mathrm{t_{C2}})})}\right) - [\mathrm{NO}]_0 \\
&= \left(\frac{0.69\,\mathrm{s^{-1}} + 0.013\,\mathrm{s^{-1}}}{0.69\,\mathrm{s^{-1}}}\right) \times \\
&\left(\frac{25\,\mathrm{pptV} - 10\,\mathrm{pptV} \times \mathrm{e}^{(0.013\,\mathrm{s^{-1}} \times 1\,\mathrm{s} - (0.013\,\mathrm{s^{-1}} + 0.69\,\mathrm{s^{-1}} \times 1\,\mathrm{s})}}{(1 - \mathrm{e}^{(-(0.013\,\mathrm{s^{-1}} + 0.69\,\mathrm{s^{-1}}) \times 1\,\mathrm{s})})}\right) - 10.6\,\mathrm{pptV} \\
&\qquad = 1.02 \times 39.6\,\mathrm{pptV} - 10.6\,\mathrm{pptV} = 29.7\,\mathrm{pptV} \quad \text{(Eq. A.34)}
\end{aligned}
$$

This gives a small increase in NO mixing ratio (0.6 pptV or 5.7%) and a small decrease (0.3 pptV or 1%) in $\mathrm{NO_2}$ mixing ratio under these conditions.

Appendix B

FLEXPART Description

The FLEXPART back-trajectories were run by Matthew Rowlinson, Univeristy of York, and the description was written by him.

Back-trajectories are produced using FLEXPART, a Lagrangian particle dispersion model [138, 139]. Although originally designed to simulate dispersion of pollutants from a point source, FLEXPART has been developed into a comprehensive tool for simulating atmospheric transport. FLEXPART is run offline using meteorological reanalyses or forecasts and can be run either forwards or backwards in time, sampling particles on a global longitude-latitude-altitude grid and enabling analysis of the source regions of a plume [280]. The planetary boundary layer (PBL) height is calculated using a Richardson number threshold [281], turbulence is parameterised using the standard gaussian model [138] and the convection parameterisation is based on Emanuel and Živković-Rothman (1999) [282]. FLEXPART has been extensively evaluated and shown to be a useful and reliable resource [139, 283–285], particularly for investigating transport and sources of pollution [286, 287].

Here, FLEXPART version 10.4 is used in backwards mode, driven by pressure level data from Global Forecast System (GFS) reanalyses at $0.5^\circ \times 0.5^\circ$ resolution. 10-day back-trajectory simulations are initialised every 6 hours, releasing 1000 particles from the CVAO site.

Appendix C

NO_x Measurement Parameters

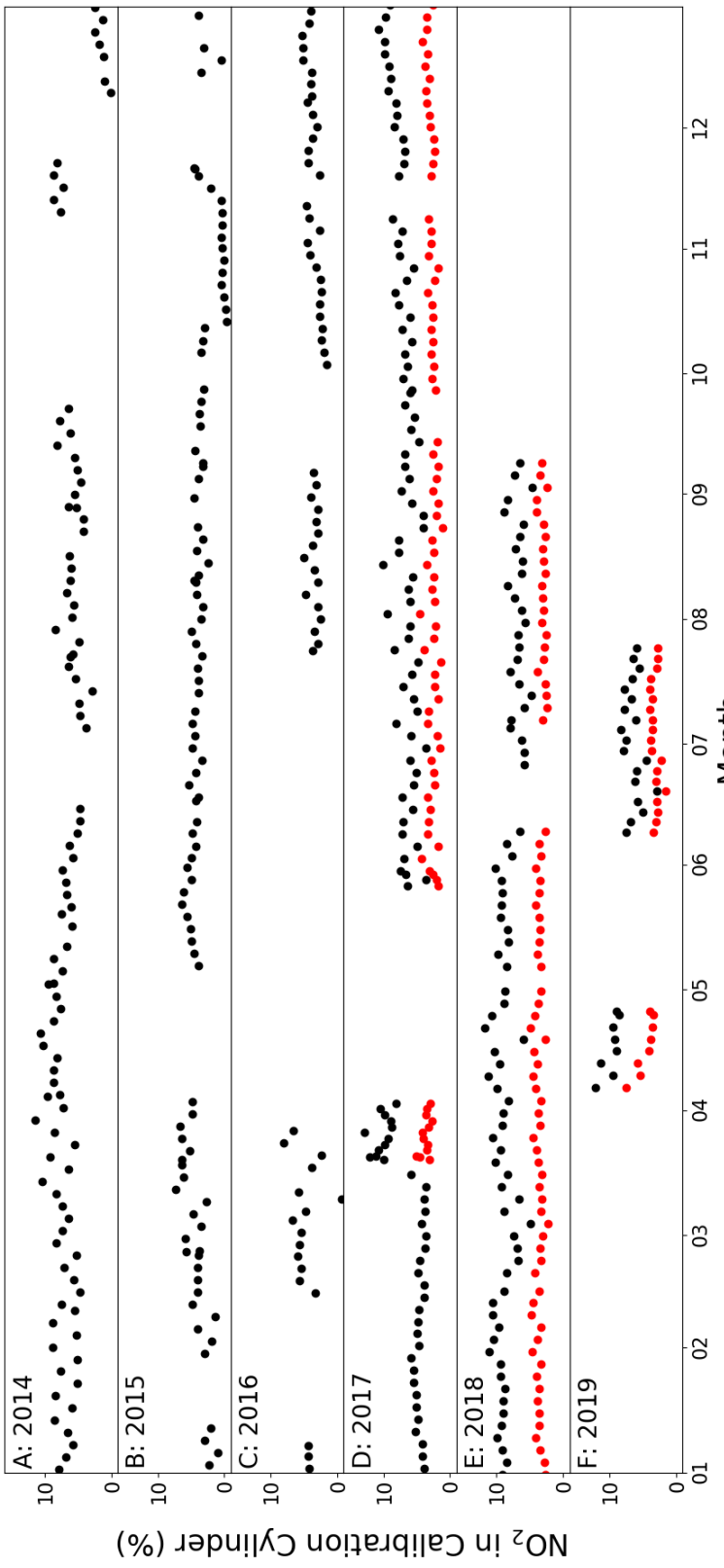

Figure C.1: Percentage of NO_x in the calibration cylinder measured as NO_2 between January 2014 and August 2019. The black circles symbolise the measurements made by the BLC and the red circles symbolise the measurements made by the PLC.

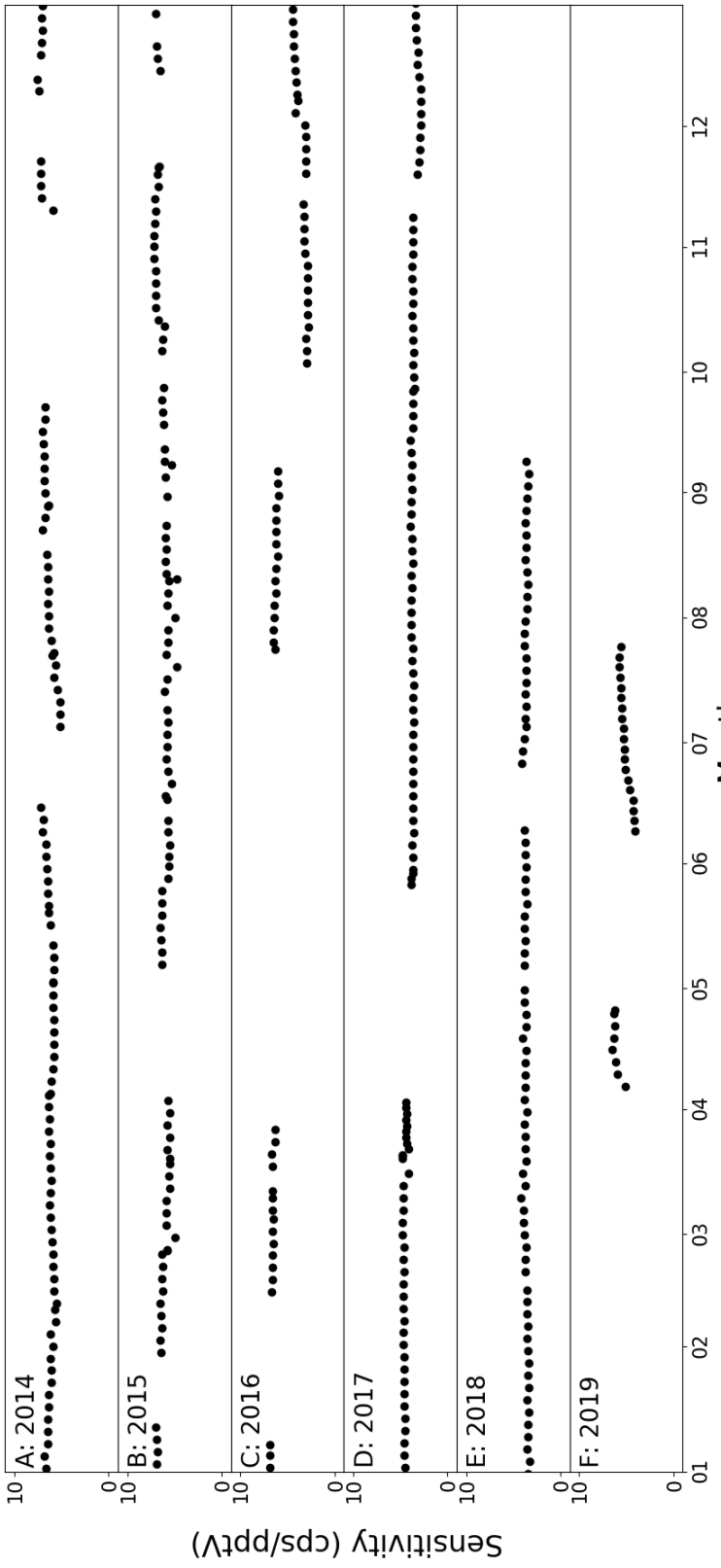

Figure C.2: Calculated sensitivities between January 2014 and August 2019.

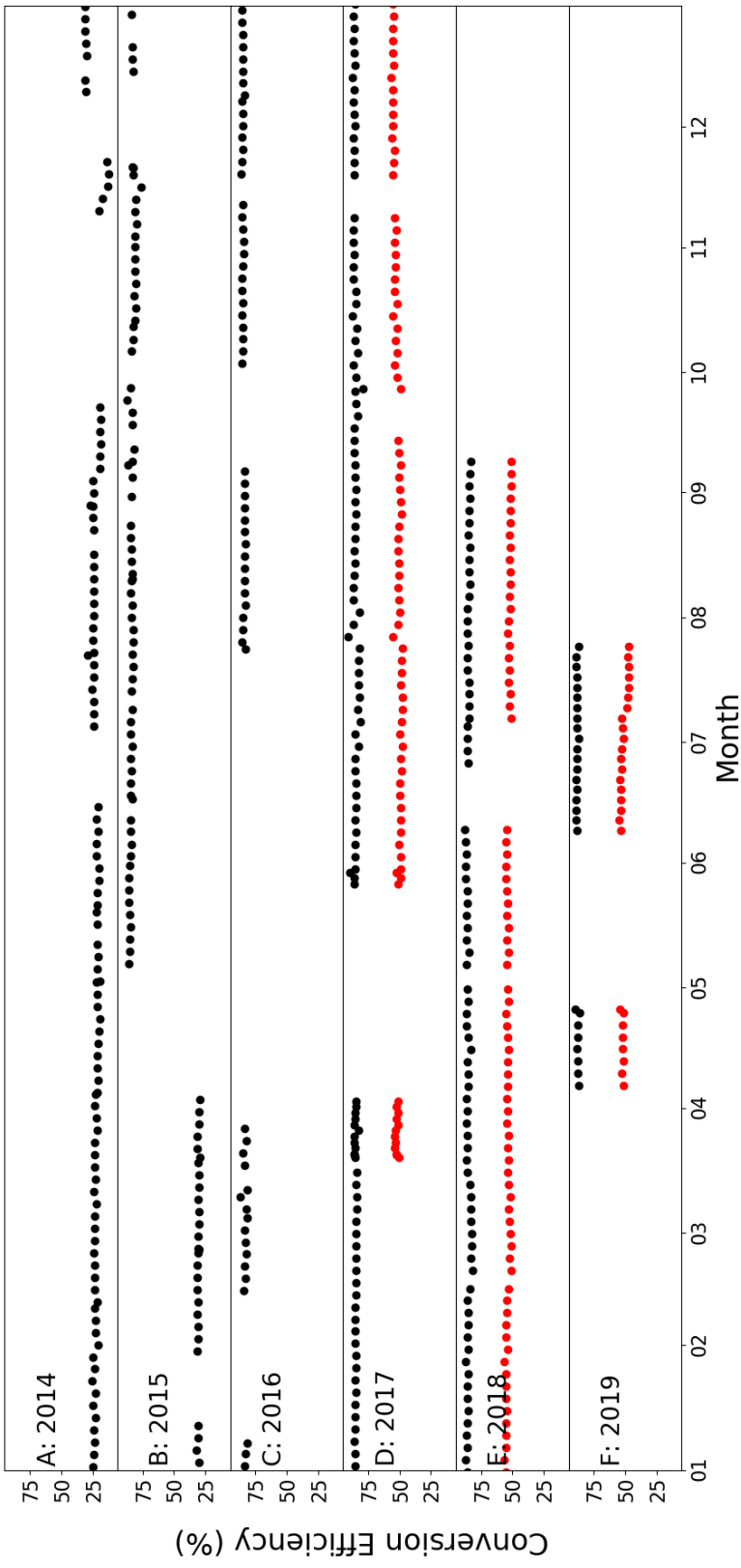

Figure C.3: Calculated conversion efficiencies for the BLC (black) and PLC (red) from January 2014 to August 2019.

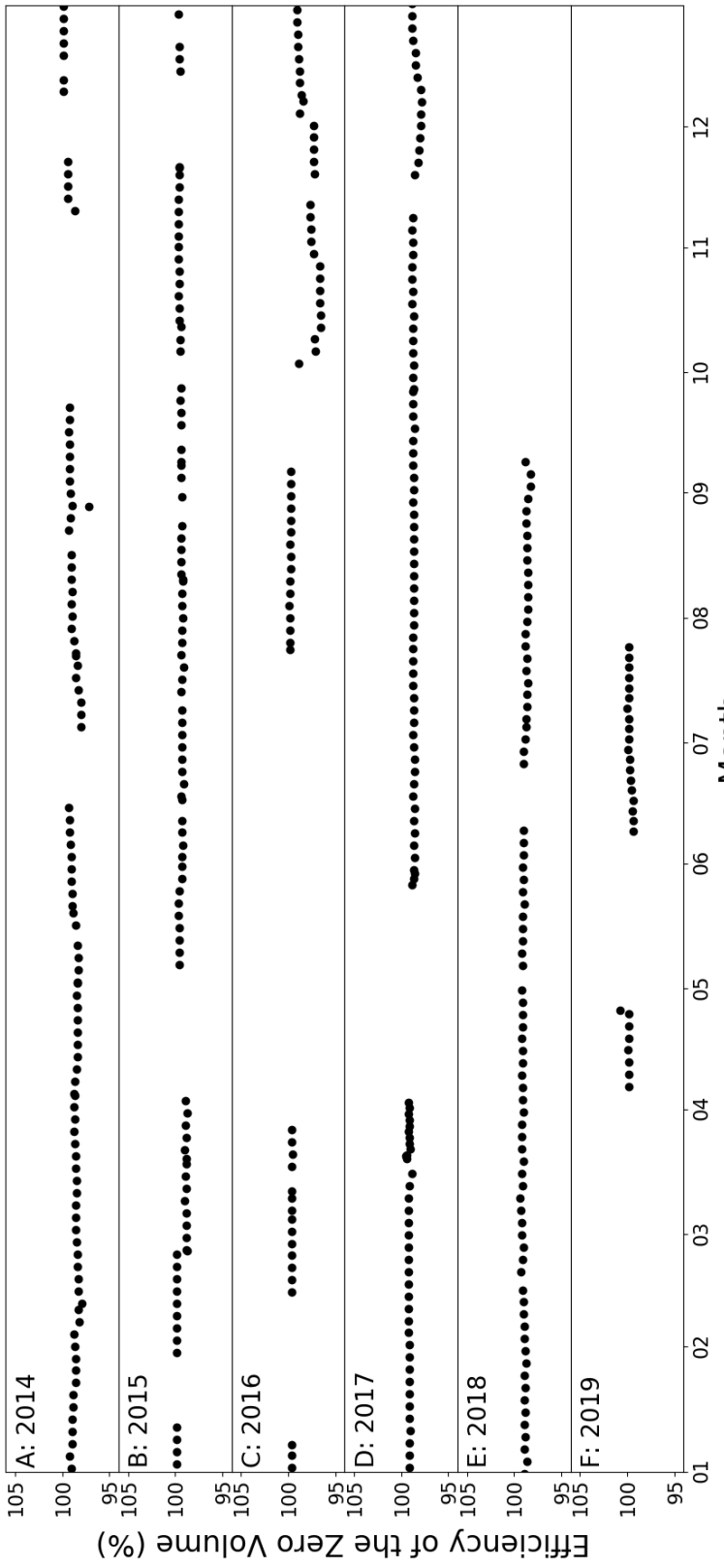

Figure C.4: The efficiency of the zero volume plotted over time from January 2014 to August 2019.

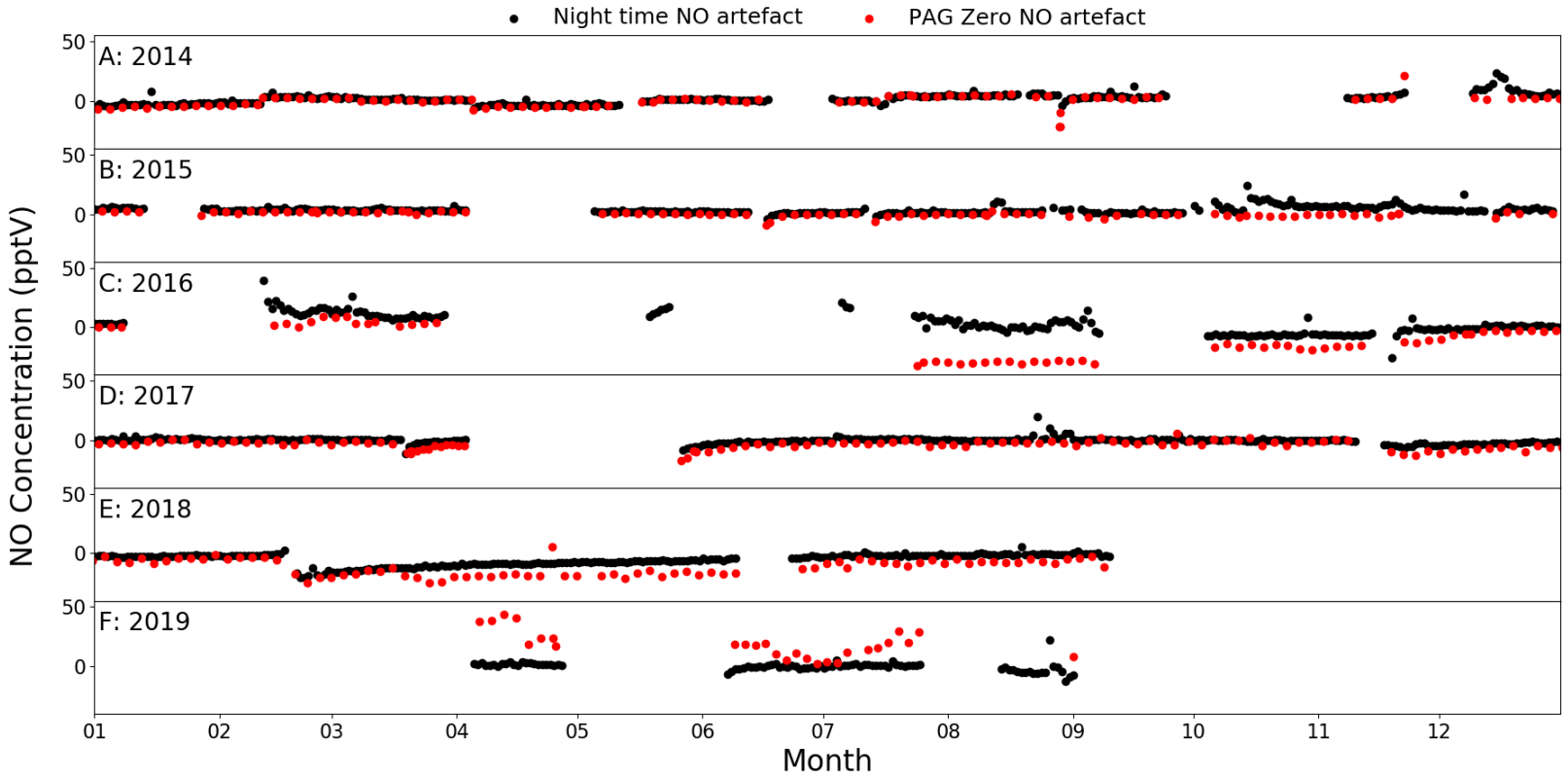

Figure C.5: NO artefact from January 2014 to August 2019, where the black is the average night time measurements and the red are the measurements from the pure air generator (PAG). The PAG measurements can be observed to be significantly higher than the nocturnal measurements in 2019, which can be explained by issues with the compressor supplying the PAG. In 2016 it can be observed to be significantly lower than the nocturnal measurements, which could be due to contaminations, however, the NO_2 measurements from the PAG (Figure C.6) are not significantly different from other measurements, suggesting an interference in the background measurement during that period.

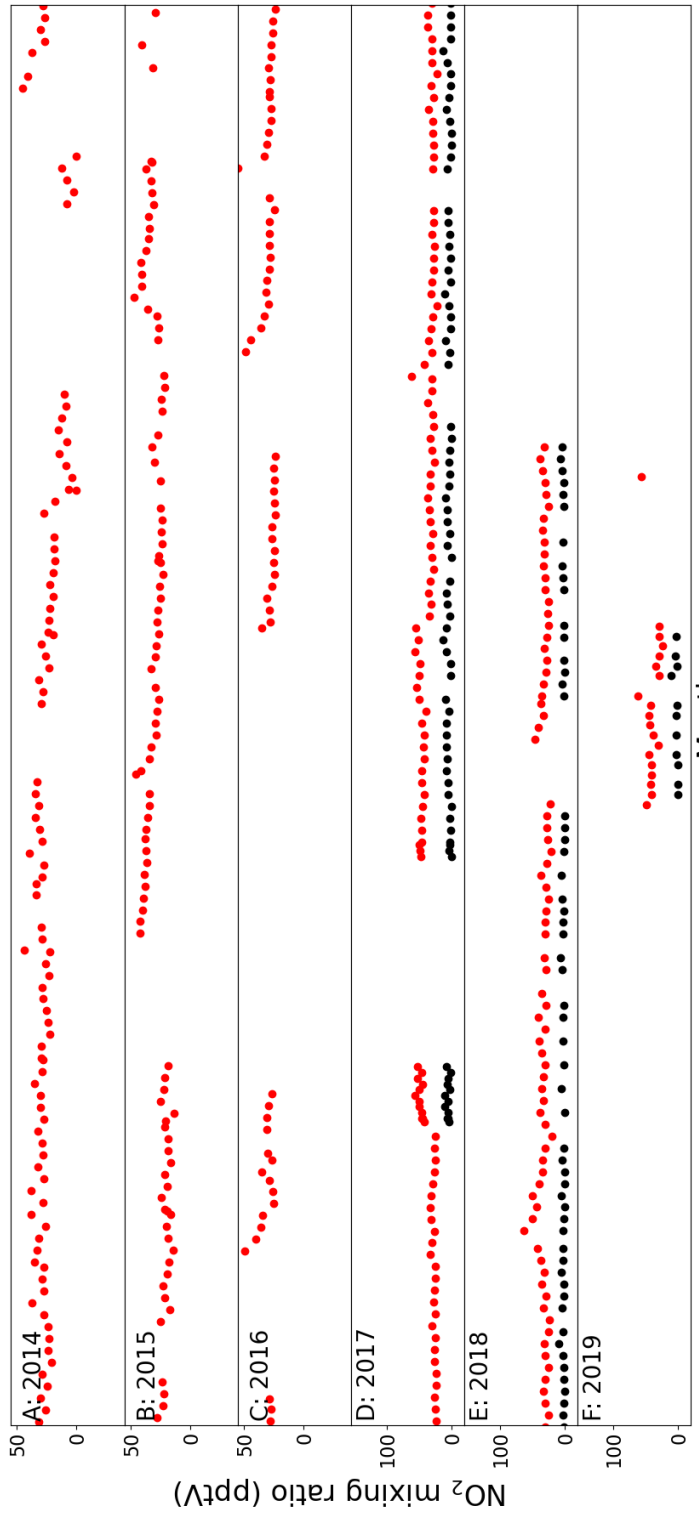

Figure C.6: NO_2 PAG artefact measurements from January 2014 to August 2019, where the black is the PLC measurements and the red is the BLC measurements before correcting for NO_2 in the PAG air.

Appendix D

Monthly Diurnal Cycles at the CVAO

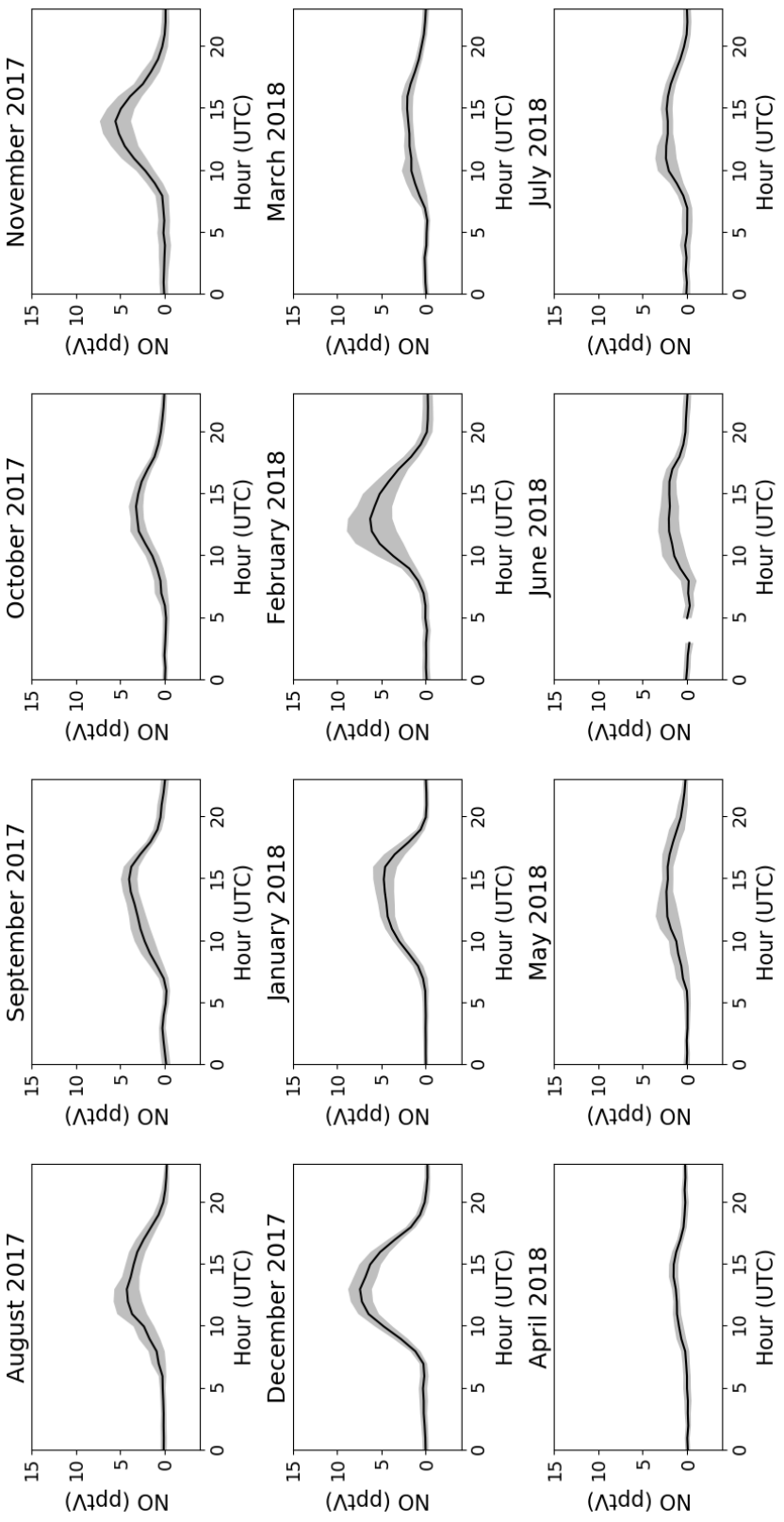

Figure D.1: NO diurnal cycles for August 2017-July 2018. The coloured area is ±2 standard errors. If there are less than 15 measurements available for the hour, it is not included.

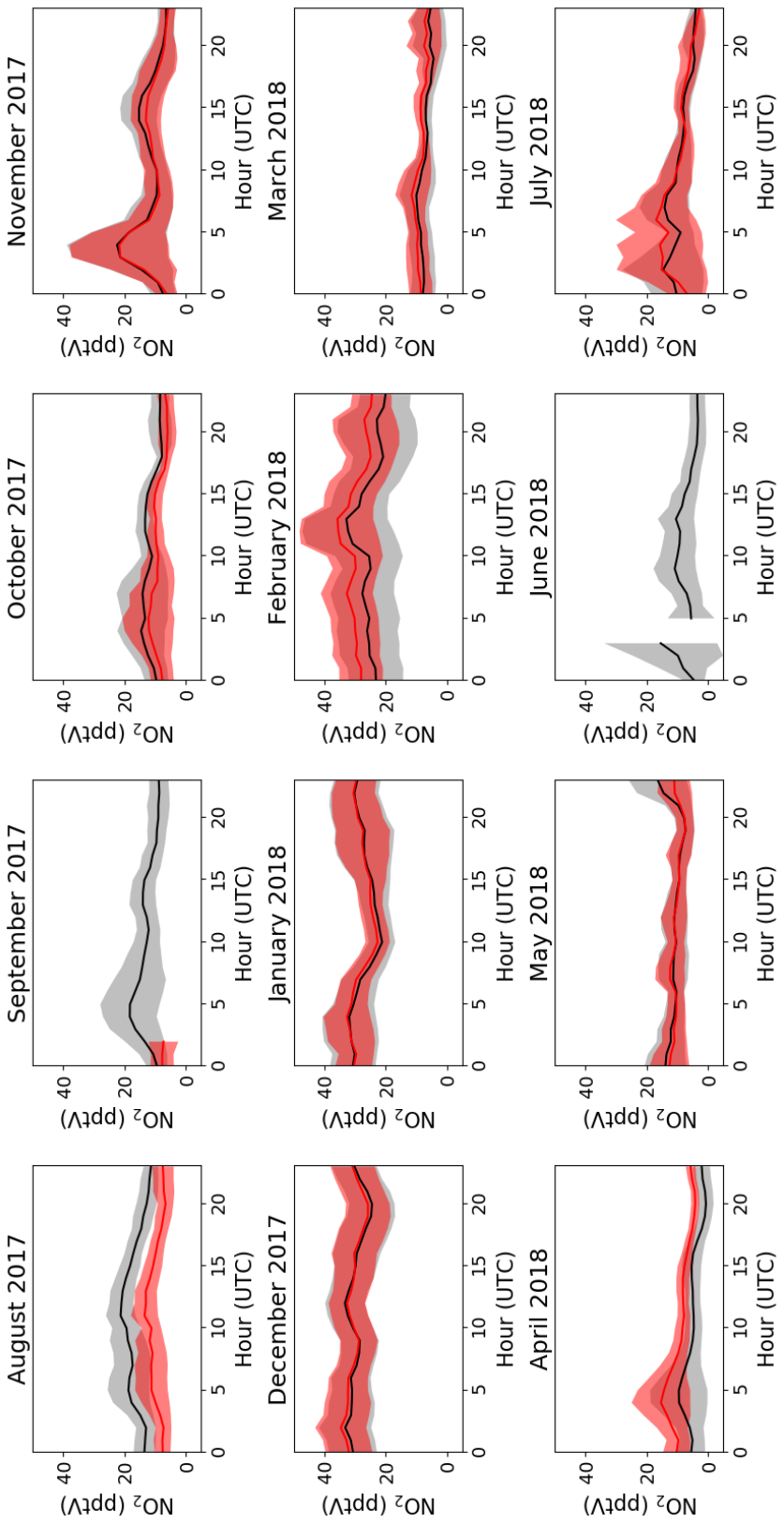

Figure D.2: NO_2 diurnal cycles for August 2017-July 2018 for the BLC (black) and PLC (red). The coloured area is ± 2 standard errors. If there are less than 15 measurements available for the hour, it is not included.

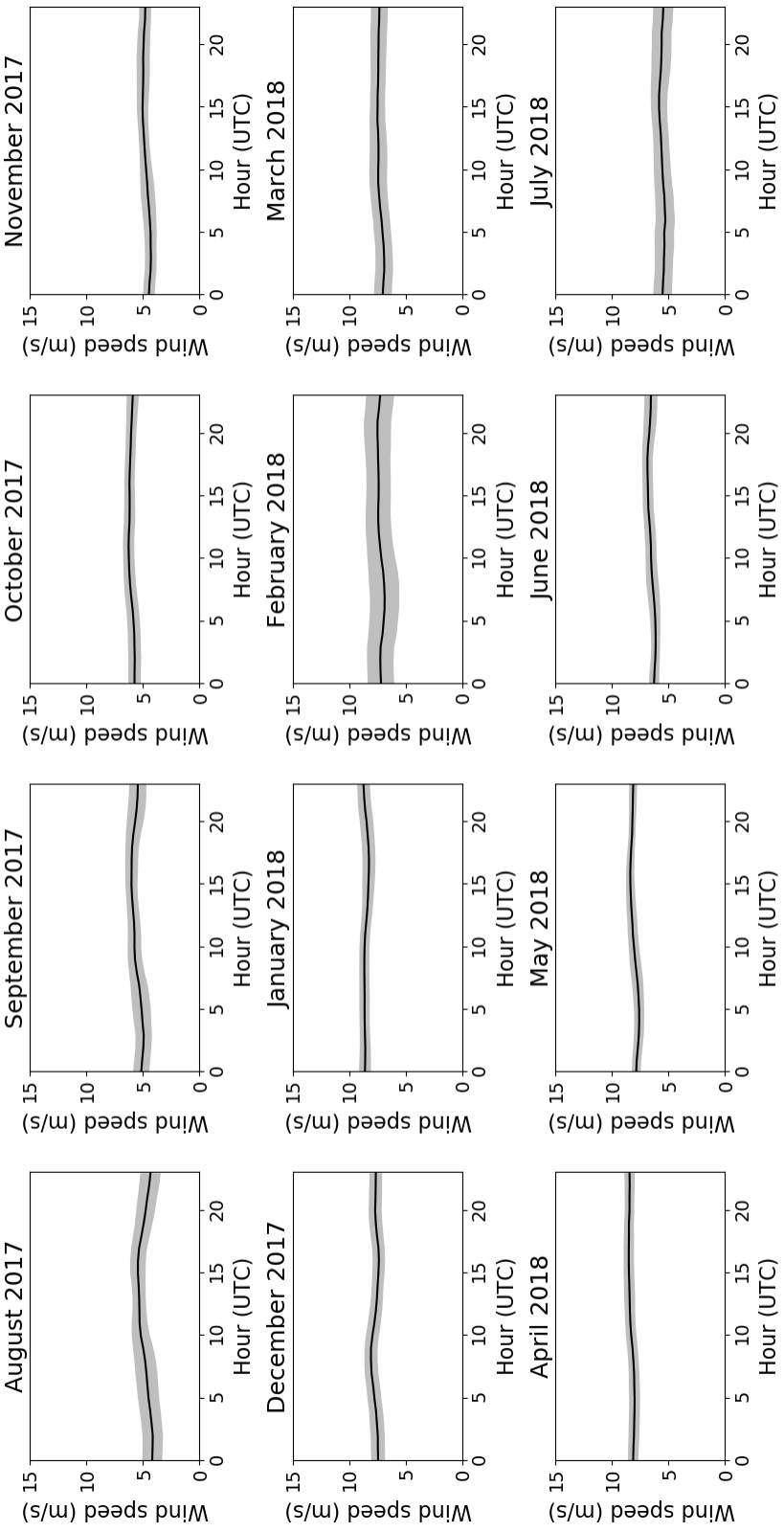

Figure D.3: Wind speed diurnal cycles for August 2017-July 2018. The coloured area is ± 2 standard errors. If there are less than 15 measurements available for the hour, it is not included.

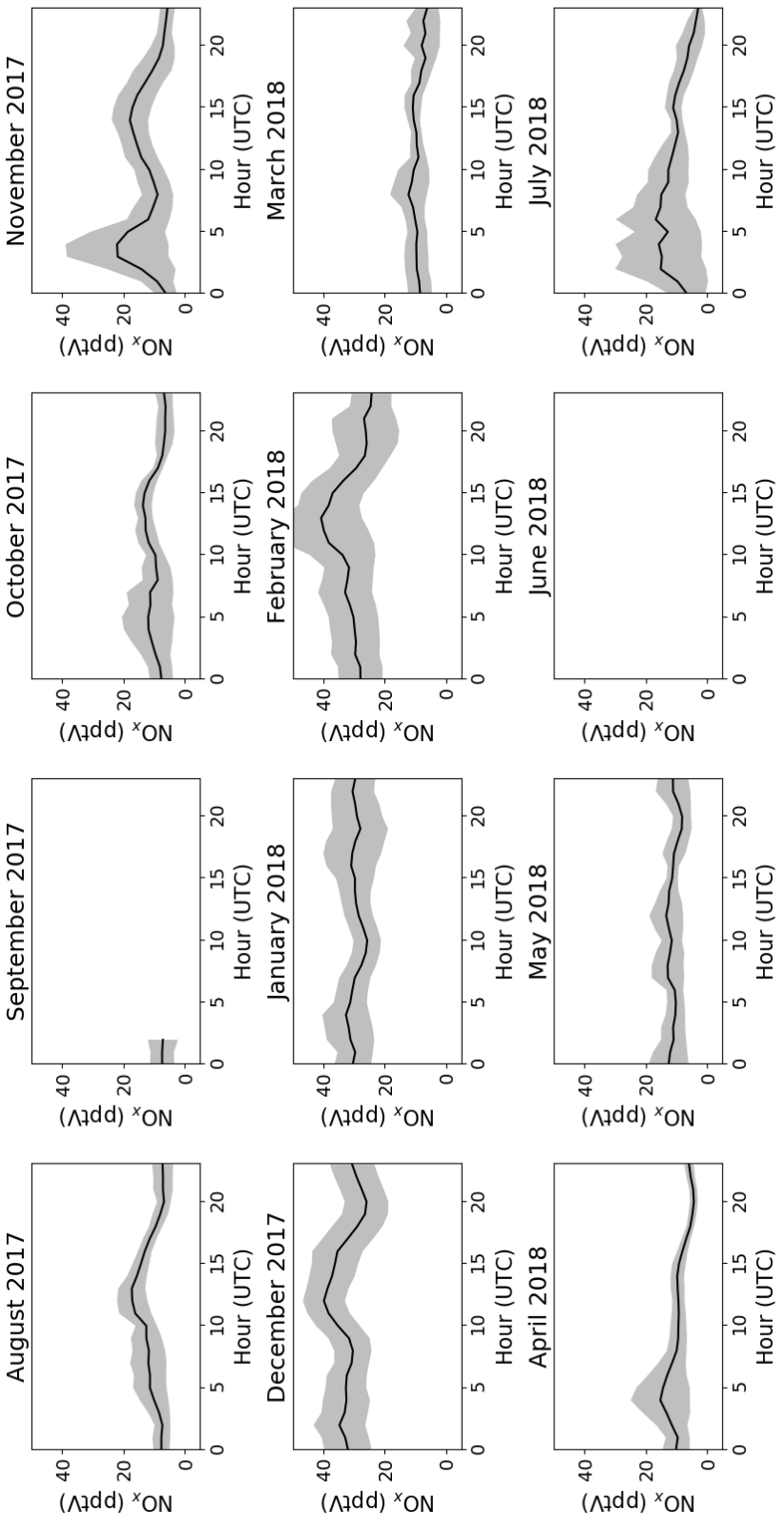

Figure D.4: NO_x diurnal cycles for August 2017-July 2018. The coloured area is ± 2 standard errors. If there are less than 15 measurements available for the hour, it is not included.

Appendix E

Calculations of Photolysis Rates

The photolysis rates at the CVAO has been processed and described by Dr. Katie A. Read, NCAS and University of York. Calibrations have been performed by Dr. Lisa K. Whalley, NCAS and University of Leeds.

E.1 Photolysis Frequencies

The spectral radiometer located at a height of 7.5m provides a direct measurement of solar actinic UV flux and thus determination of atmospheric photolysis frequencies. The instrument consists of a 2-pi sr quartz diffuser coupled to an Ocean Optics spectrometer via a 10m fibre optic cable. It operates between 200 and 1000nm, calibrated between 250-750nm at 1 nm resolution. It utilises a Hamamatsu, back-thinned FFT-CCD detector with >90% quantum efficiency at 700nm. It has an integration time of 1 minute.

The instrument was calibrated in 2016 and again in 2019 against a 1000 Watt (FEL) quartz-halogen tungsten coiled coil filament lamp at the University of Leeds (Gooch and Housego NIST traceable FEL 1000-Watt lamp Standard of Spectral Irradiance (OL FEL-A)) bearing the designation F-1128. Providing the fibre optic cable isn't changed the calibration is relatively constant over a number of years (∼7% drift in 10 years, [288]).

47 photolysis rates are calculated using Python code developed by L. K.

Whalley at the University of Leeds based on accurate absorption cross section and quantum yield from literature (http://chmlin9.leeds.ac.uk/MCMv3.3.1/parameters/photolysis.htt)

Solar radiation is measured from the same location with a Campbell Scientific sensor, SP-110 pyranometer. The sensor measures total sun and sky solar radiation over a spectral range 360 to 1120 nm encompassing most of the shortwave radiation reaching the surface. It measures a maximum of 1000 W m-2 (200mV) in full sun, 0.2mV per W m^{-2} at 5% accuracy.

E.2 $j\mathrm{O}(^1\mathrm{D})$ Calibration

Due to the errors in the measurement of $j\mathrm{O}(^1\mathrm{D})$ at lower wavelengths using the spectral radiometer, for 1 month in 2020 $j\mathrm{O}(^1\mathrm{D})$ was further evaluated using a co-located measurement made with a $j\mathrm{O}(^1\mathrm{D})$ 2pi filter radiometer (Metcon GmbH) [288].

The $j\mathrm{O}(^1\mathrm{D})$ filter radiometer output is proportional to the corresponding photolysis frequencies and the absolute calibration was determined during an intercomparison exercise when the instrument was run alongside a reference spectroradiometer [288]. The data from the two instruments is shown below in Figure E.1.

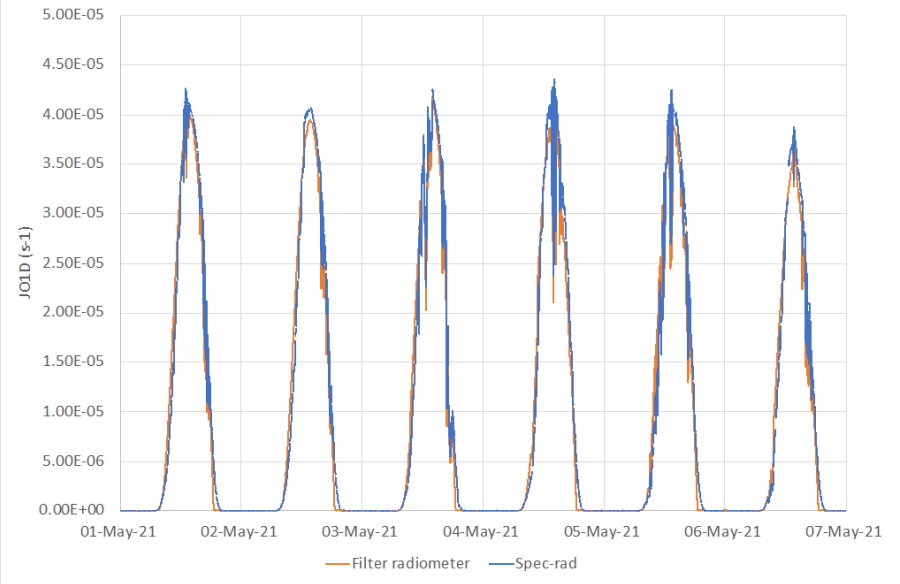

Figure E.1: Comparison of $jO(^1D)$ measurements using a filter radiometer and a spec-rad.

E.3 Other Photolysis Rates

The calibration of the spectral radiometer in 2019 is assumed to be accurate for the calibration of other photolysis rates which photolyse further into the visible spectrum however the earlier calibration in 2016 may have been affected by reflections due to some issues with the calibration procedure. During this earlier calibration the spectral radiometer observed more light through reflections than that directly emitted by the lamp, leading to a higher sensitivity than reality and under reading of the measurements in the early years. Therefore, we have used the correlation of photolysis rates with solar radiation in 2020 between the hours of 09.00-17.00 to calculate the photolysis rates prior to this date. An example of the correlation for jNO_2 can be observed in Figure E.2 and the calculated photolysis rates are compared to the measured photolysis rates in Figure E.3.

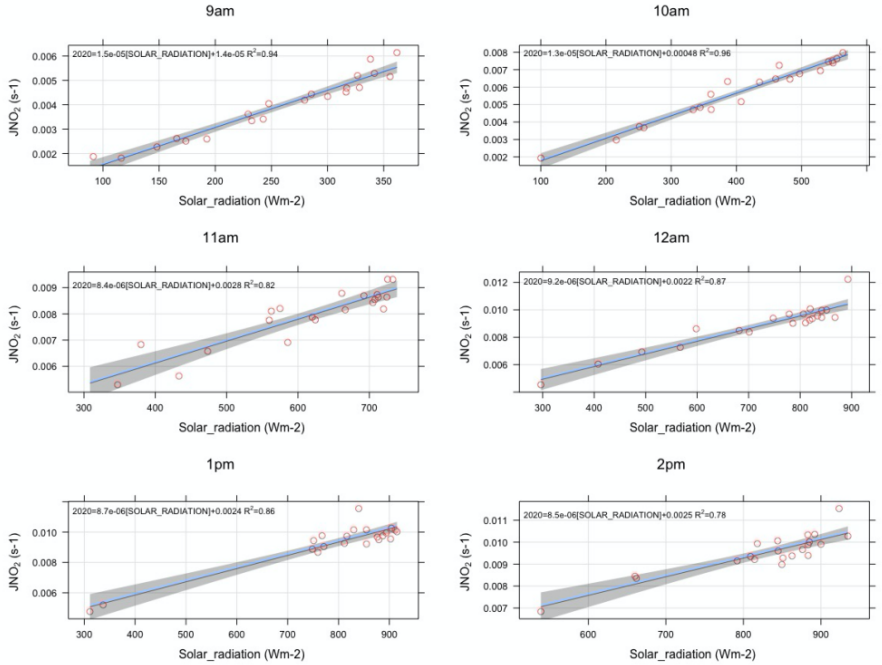

Figure E.2: Correlation between measured jNO_2 from the spec-rad and total solar radiation.

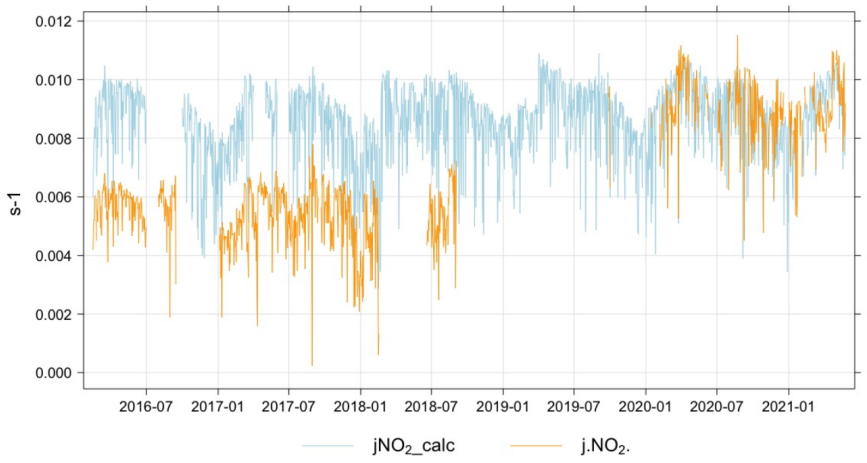

Figure E.3: Comparison of measured jNO_2 and calculated jNO_2 for measurements at 14.00.

Appendix F

Time Series from the CVAO 2017-2020

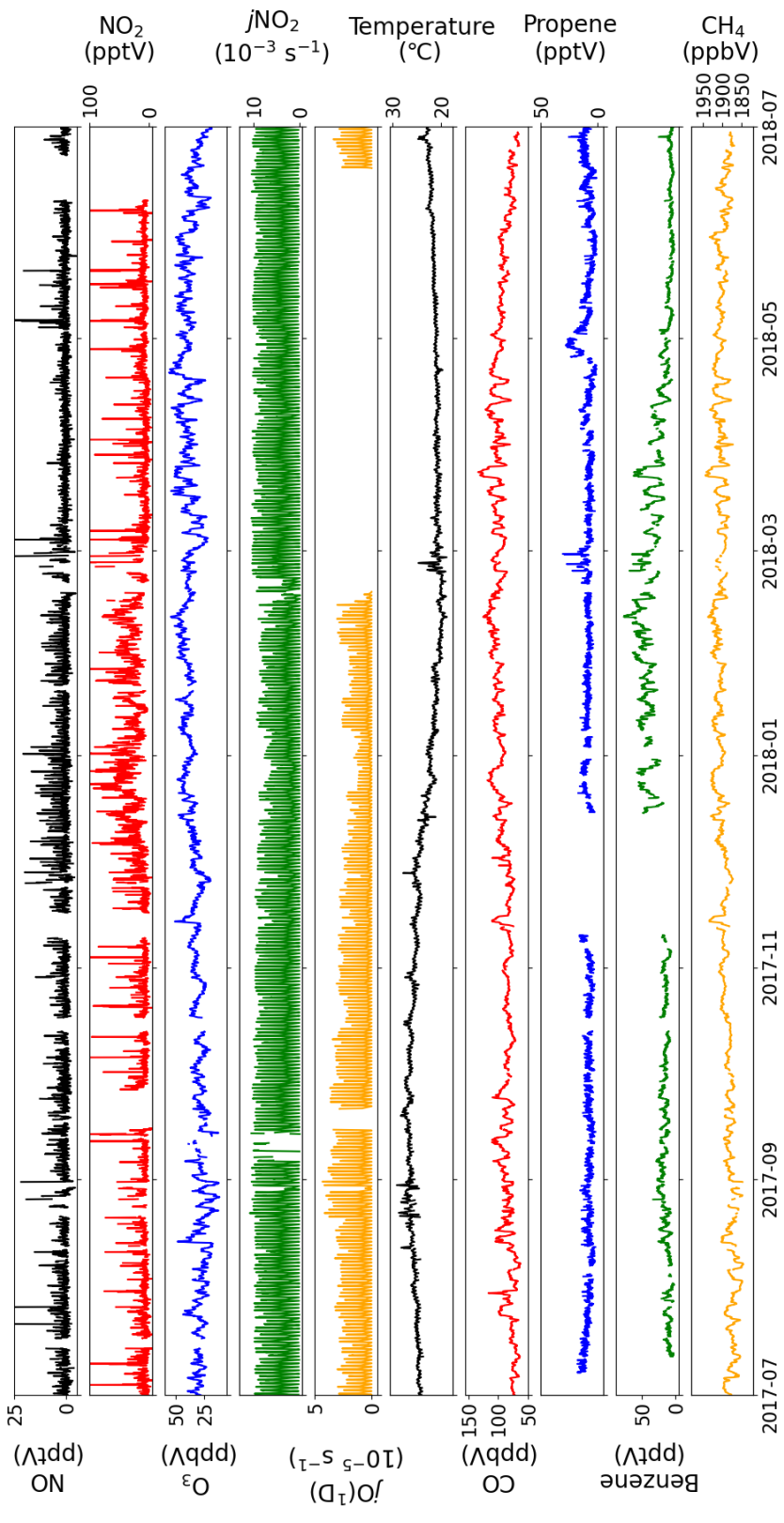

Figure F.1: Time series of NO, NO_2, O_3, jNO_2, $jO(^1D)$, Temperature, CO, propene, benzene, and CH_4 at the CVAO from July 2017 – June 2018.

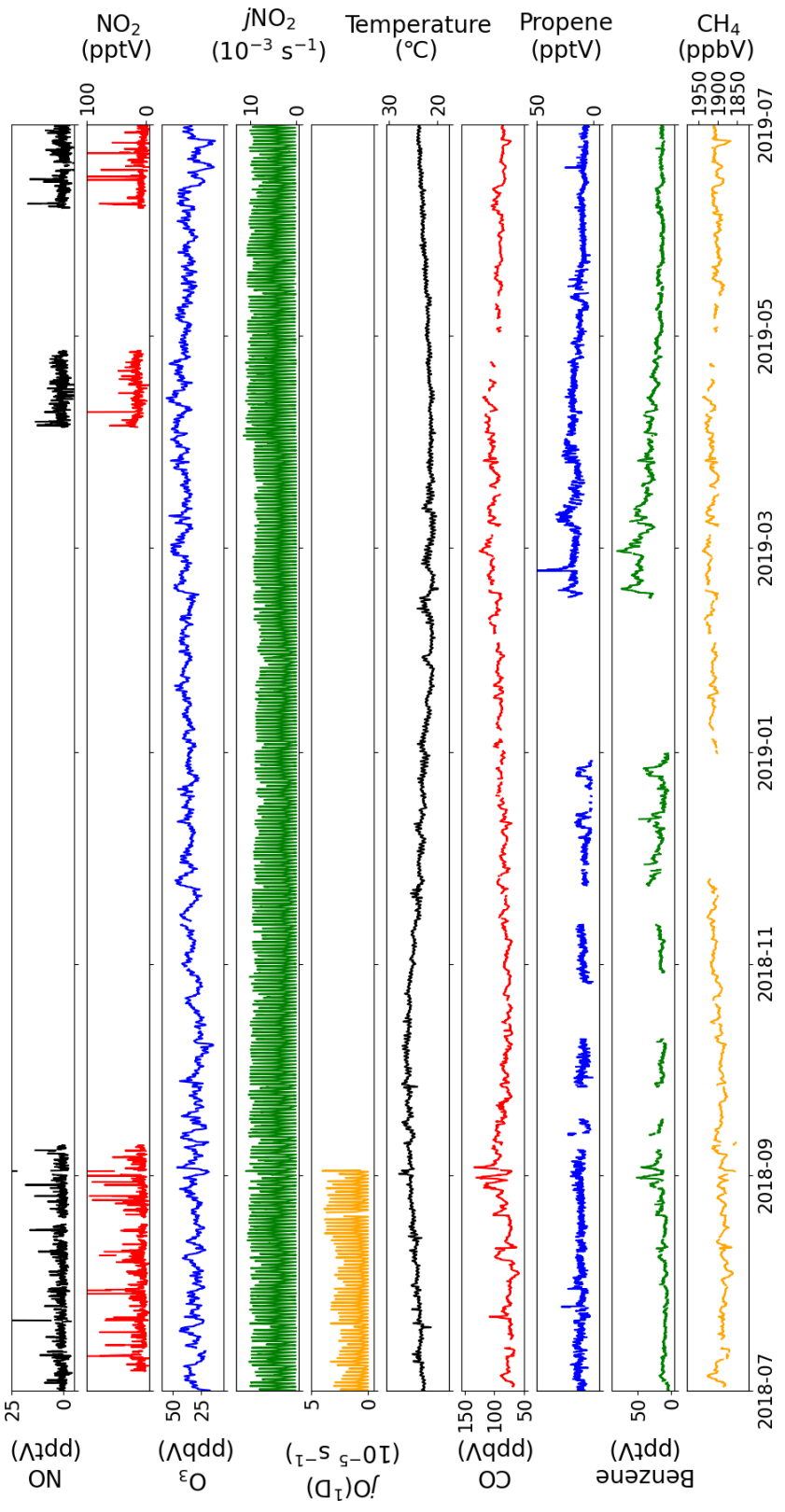

Figure F.2: Time series of NO, NO_2, O_3, jNO_2, $jO(^1D)$, Temperature, CO, propene, benzene, and CH_4 at the CVAO from July 2018 – June 2019.

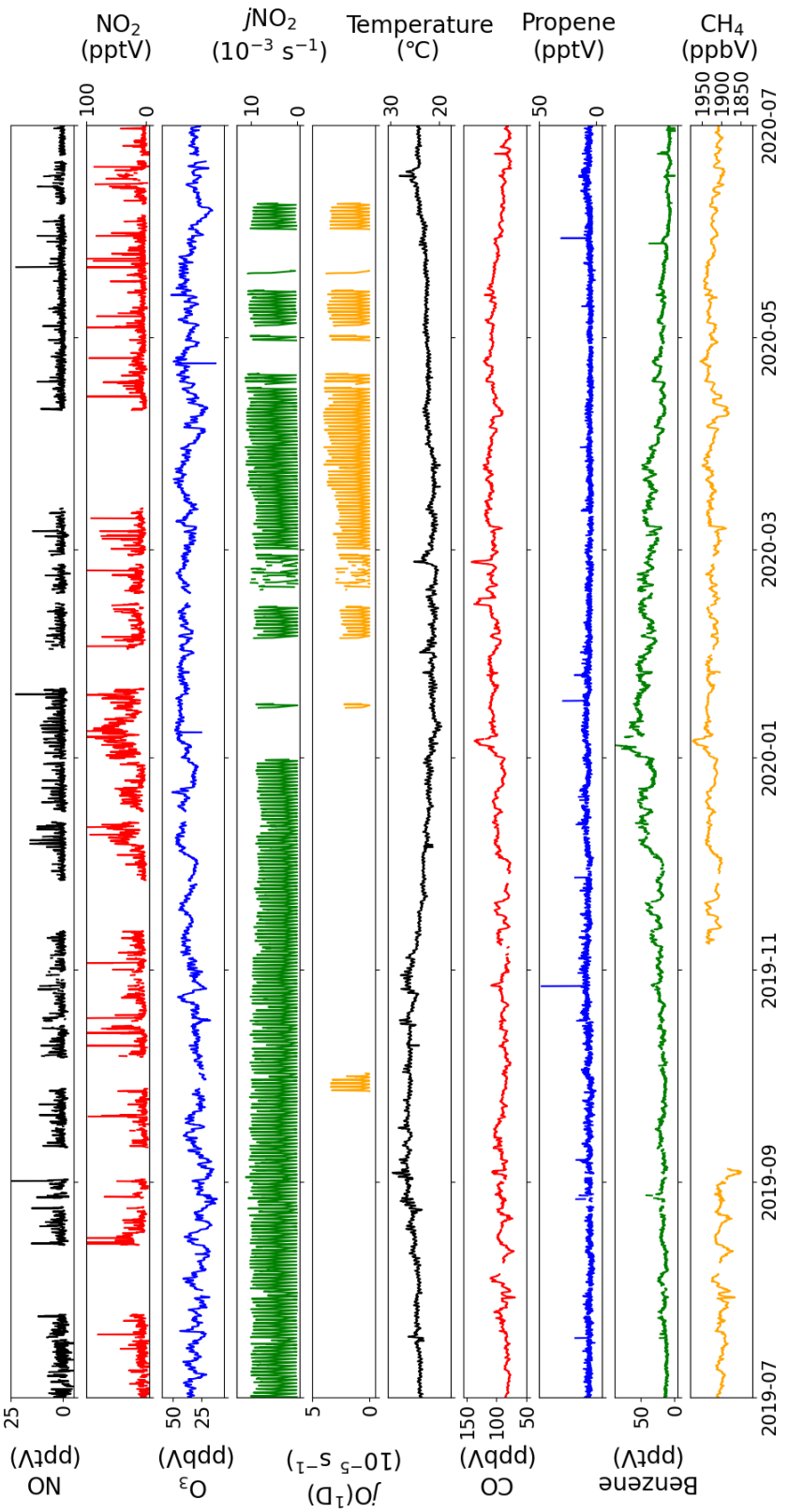

Figure F.3: Time series of NO, NO_2, O_3, jNO_2, $jO(^1D)$, Temperature, CO, propene, benzene, and CH_4 at the CVAO from July 2019 – June 2020.

Appendix G

Halogen Chemistry

Table G.1 Bimolecular reaction mechanisms added to the MCM.

	Rate coefficient (cm^{-3} $molecule^{-1}$ s^{-1})	Ref.
$Br + O_3 \rightarrow BrO + O_2$	$1.6 \times 10^{-11} \times e^{(-780/T)}$	[289]
$BrO + HO_2 \rightarrow HOBr + O_2$	$4.5 \times 10^{-12} \times e^{(460/T)}$	[289]
$Br + HO_2 \rightarrow HBr + O_2$	$4.8 \times 10^{-12} \times e^{(-310/T)}$	[289]
$HBr + OH \rightarrow Br + H_2O$	$5.5 \times 10^{-12} \times e^{(200/T)}$	[289]
$BrO + NO \rightarrow Br + NO_2$	$8.8 \times 10^{-12} \times e^{(260/T)}$	[289]
$BrO + BrO \rightarrow 2\ Br + O_2$	$2.4 \times 10^{-12} \times e^{(40/T)}$	[289]
$BrO + BrO \rightarrow Br_2 + O_2$	$2.8 \times 10^{-14} \times e^{(860/T)}$	[289]
$Br + CH_3CHO \rightarrow HBr + CH_3CO$	$1.8 \times 10^{-11} \times e^{(-460/T)}$	[210]
$Br + HCHO \rightarrow HBr + HCO$	$7.7 \times 10^{-12} \times e^{(-580/T)}$	[210]
$I + HO_2 \rightarrow HI + O_2$	$1.5 \times 10^{-11} \times e^{(-1090/T)}$	[289]
$OH + HI \rightarrow I + H_2O$	3.0×10^{-11}	[289]
$IO + NO \rightarrow I + NO_2$	$8.6 \times 10^{-12} \times e^{(230/T)}$	[289]
$I + O_3 \rightarrow IO + O_2$	$2.0 \times 10^{-11} \times e^{(-830/T)}$	[289]
$IO + HO_2 \rightarrow HOI + O_2$	$1.4 \times 10^{-11} \times e^{(540/T)}$	[290]
$HOI + OH \rightarrow IO + H_2O$	5.0×10^{-12}	[291]
$IO + IO \rightarrow I + OIO$	$5.4 \times 10^{-11} \times e^{(180/T)} \times 0.38$	[290]
$IO + IO \rightarrow I_2O_2$	$5.4 \times 10^{-11} \times e^{(180/T)} \times 0.62$	[290]
$IONO_2\ (+M) \rightarrow IO + NO_2\ (+M)$	$1.1 \times 10^{15} \times e^{(12060/T)}$	[290]
$OIO + OIO \rightarrow$ products	1.5×10^{-10}	[292]
$IO + OIO \rightarrow$ products	1.5×10^{-10}	[292]
$BrO + IO \rightarrow Br + 0.8\ OIO + 0.2\ I + 0.2\ O_2$	$1.5 \times 10^{-11} \times e^{(510/T)}$	[290]

Table G.2 Termolecular reaction mechanisms added to the MCM.

	$n = (1 + (\log_{10}(k_0 \times [M]/k_\infty))^2)^{-1}$ $k = (k_0[M]/(1 + k_0[M]/k_\infty)) \times 0.6^n$	Ref.
OH + OH (+M) →	$k_0 = 6.9 \times 10^{-31} \times (T/298)^{-1}$	
H_2O_2 (+M)	$k_\infty = 2.6 \times 10^{-11}$	[289]
BrO + NO_2 (+M) →	$k_0 = 5.5 \times 10^{-31} \times (T/298)^{-3.1}$	
$BrONO_2$ (+M)	$k_\infty = 6.6 \times 10^{-11} \times (T/298)^{-2.9}$	[289]
Br + NO_2 (+M) →	$k_0 = 4.3 \times 10^{-31} \times (T/298)^{-2.4}$	
$BrNO_2$ (+M)	$k_\infty = 2.7 \times 10^{-11}$	[289]
IO + NO_2 (+M) →	$k_0 = 7.7 \times 10^{-31} \times (T/298)^{-3.5}$	
$IONO_2$ (+M)	$k_\infty = 7.7 \times 10^{-12} \times (T/298)^{-1.5}$	[289]

Table G.3 Thermal decomposition reaction mechanism added to the MCM.

	Rate coefficient (s^{-1})	Ref.
$BrONO_2 \rightarrow BrO + NO_2$	$2.8 \times 10^{13} \times e^{(-12360/T)}$	[293]

Table G.4 Photolysis rates of gas phase species added to the MCM.

	Reference for absorption cross section and quantum yield
$BrO + h\nu \rightarrow Br + O$	[19]
$HOBr + h\nu \rightarrow Br + OH$	[19]
$BrONO_2 + h\nu \rightarrow BrO + NO_2$	[19]
$BrONO_2 + h\nu \rightarrow Br + NO_3$	[19]
$BrNO_2 + h\nu \rightarrow Br + NO_2$	[19]
$HOI + h\nu \rightarrow I + OH$	[19]
$IO + h\nu \rightarrow I + O$	[19]
$OIO + h\nu \rightarrow I + O_2$	[19]

Appendix H

Aerosol Surface Area

The aerosol surface area measurements were conducted and processed by Dr. Graeme J. Nott, FAAM Airborne Laboratory, and this description was written by him.

In situ measurements of aerosol particle concentration distributions were made with the Passive Cavity Aerosol Spectrometer Probe (PCASP) and the Cloud Droplet Probe (CDP), both manufactured by Droplet Measurement Technologies (DMT). These instruments are both laser scattering based optical particle counters, operating at 632.8 nm and 658 nm for the PCASP and CDP respectively. Nominal particle size ranges are 0.1-3 µm and 3-50 µm and a composite particle size distribution was constructed using the two instruments to cover the entire size range. Both instruments had a sample rate of 1 Hz. They were mounted on underwing pylons, the CDP is open path while the PCASP uses a pump and very short inlet. The same CDP was used for both campaigns while different PCASPs were used due to changes in instrument serviceability.

The instruments were calibrated as described by Rosenberg et al. (2012) [294]. The CDP was cleaned and calibrated throughout the campaigns on every flying day. An average calibration was calculated for each campaign and applied to all flights in that campaign. The PCASP was calibrated in the

laboratory before or after the campaigns with each calibration applied to all flights within the campaign. The sample flow rate through the PCASP was calibrated with a Gilibrator-2 Calibrator (Sensidyne). The size calibration determines the range of scattering cross-sections associated with each of the thirty bins of both instruments. For computational simplicity, spherical particles were assumed so that Mie theory could be used to calculate equivalent particle diameters. The predominant aerosol type was identified as described in section 6 for each run. Size calibrations were calculated for three different types of aerosol runs; runs in sea salt aerosol, runs in mineral dust, and runs in a combination of biomass burning aerosol and dust. Despite any mix of particle type in a single run, the most appropriate size calibration was applied to all particles in that run.

Sea salt dominated runs were at altitudes less than 300 m above the sea surface. The OPAC database [295,296] includes the optical properties for both accumulation and coarse mode sea salt aerosols as a function of scattering wavelength and relative humidity. Relative humidity for the sea salt runs was determined from the GEOS-chem model as 79% ± 3% so the OPAC data for 80% relative humidity was used for all sea salt runs. The accumulation mode refractive index applied to the PCASP calibrations and that of the coarse mode, applied to the CDP calibrations, were both 1.35+2.0e-8i.

The optical properties of aged mineral dust transported from the sub-Saharan region have been measured at the ground station in Cabo Verde and during previous aircraft campaigns based in the region. Ryder et al.(2018) [297] lists such campaigns since 2006. Here we use a range of size-invariant refractive indices based on previous measurements. Weinzierl et al. (2011) [298] use a non-absorbing refractive index for particles larger than 3 µm, however, this has not been done here. Ryder et al. (2019) [299] use values for the real and imaginary parts of the refractive index ranging over 1.53-1.55 and 0.001-0.0024i and we use values based on these. The real part is biased a little smaller than the 1.55 (all reported values have been corrected for the wavelengths used

here) from airborne measurements reported by Weinzierl et al. (2011) [298] and from ground-based electron microscopy measurements by Kandler et al. (2011) [300]. A sensitivity study in Ryder et al. (2018) [297] suggest that a $\pm$ 0.05 change will result in a change in derived effective diameter of $< 5\%$ and so has only a small influence on the derived particle sizes. Weinzierl et al. (2011) [298] finds imaginary refractive indices of 0.0014 and 0.001 for 632.8 and 658 nm for sizes less than 2.5 µm. Ryder et al.(2018) [297] uses a constant 0.001. Ground-based measurements at the CVAO suggest somewhat larger values of 0.0026 and 0.0025 [301]. Again sensitivity studies for values from 0 to 0.006 suggest changes in effective diameter of between 1 % [298] and 5 % [297] depending on the condition of the study.

Uncertainties in the refractive index have been included in the bin size calibrations [294] by calculating the bin diameters from the bin scattering cross-sections over the range of values, 1.53-1.55 and 0.001-0.0024i. The resulting uncertainties of bin centre and widths are larger than for a single value refractive index and propagated through to the derived property uncertainties. Similarly to studies quoted above, this additional uncertainty has a minor impact on the run-averaged sizes and their uncertainties.

Transported biomass burning aerosols with a strongly absorbing soot content were assumed to be concentrated in the small size range [302, 303]. A strong accumulation mode, not seen in either the mineral dust or sea salt runs, was a feature of the area concentration distributions when sampling biomass burning plumes. A two-part calibration was applied in this case [302]; for particles nominally smaller than 300 nm a biomass specific refractive index of 1.57 + 0.043i was used while for larger particles the mineral dust refractive index was used [298].

Uncertainties of the PCASP measurements were derived from the counting statistics and an assumed 10% uncertainty in the sample flow rate. The impact of uncertainties of the externally measured ambient conditions was found to be small so errors in the ambient pressure and temperature were ignored. The

gain stage for the smallest particles of the PCASP used during ARNA-1 failed between the campaign and the post-campaign calibration. The calibration of this gain stage was taken from a subsequent calibration and used for these bins, the uncertainties associated with these bins was doubled as a precaution.

The sample area of the CDP was determined by the manufacturer using a droplet gun as described by Lance et al. (2010) [304], no uncertainties were given so 20% has been assumed here. The collection optics operated over solid angles subtended by 1.7-14 deg. Counting statistics were again included in the propagated errors and uncertainties in the measured true air speed were omitted.

To obtain particle surface area concentrations over the entire size range sampled a composite number concentration distribution was determined. Firstly the bins either side of the gain stage cross-overs of the PCASP were merged [294] and the first bin for both instruments discarded due to uncertainty of the lower bound of the first bins. Any overlapping bins were resampled to match the CDP bins and an average, taken weighted by the associated uncertainties in the number concentration. For particles at the upper limits of the PCASP measurement range, uncertainties of PCASP number concentrations were significantly larger than those of the CDP at these sizes. Bin centre diameters were used to calculate the particle surface areas assuming spherical particles. The bin width added in quadrature with the error in the centre and width, determined the uncertainty in the particle diameter and this was propagated through to the calculated bulk properties.

For each run, outliers of the bulk properties with a z-score of ≥ 5 were discarded as questionable, less than 1 % of the data of any run were discarded. Run averages were calculated weighted by the uncertainties of the bulk parameters in each 1 s sample. The uncertainties of the run averages are thus a combination of the propagated uncertainties of the 1 s data and the natural variability along each run. These two are uncorrelated and so were added in quadrature to obtain a final uncertainty for each bulk parameter calculated.

Except for cases with very low counts and so large counting errors, the along-run variability tended to dominate the uncertainty calculated.

The effective diameter, d_{eff} (or surface mean diameter in Hinds (1999) [305]), over the entire size range measured tend to be larger than those reported by Weinzierl et al. (2011) [298] but for mineral dust are comparable with those of Ryder et al. (2019) [299]. There is little correlation with altitude. Limiting the bulk parameters to the accumulation mode, here those approximately less than 2.5 µm, the average of all d_{eff} for dust, sea salt, and biomass burning runs were 0.59 ± 0.09, 0.39 ± 0.12, and 0.25 ± 0.18 µm respectively.

References

[1] J. Ciencewicki and I. Jaspers. Air pollution and respiratory viral infection. *Inhalation Toxicology*, 19(14):1135–1146, 2007.

[2] L. D. Emberson, H. Pleijel, E. A. Ainsworth, M. van den Berg, W. Ren, S. Osborne, G. Mills, D. Pandey, F. Dentener, P. Büker, F. Ewert, R. Koeble, and R. Van Dingenen. Ozone effects on crops and consideration in crop models. *European Journal of Agronomy*, 100:19–34, 2018.

[3] Health Effects Institute. State of global air 2020. special report. Report, 2020.

[4] D. Li, D. Shindell, D. Ding, X. Lu, L. Zhang, and Y. Zhang. Surface ozone impacts on major crop production in China from 2010 to 2017. *Atmos. Chem. Phys.*, 22(4):2625–2638, 2022.

[5] R. G. Derwent, D. S. Stevenson, W. J. Collins, and C. E. Johnson. Intercontinental transport and the origins of the ozone observed at surface sites in Europe. *Atmospheric Environment*, 38(13):1891–1901, 2004.

[6] H. Ritchie and M. Roser. Land use. *Our World in Data*, 2013. https://ourworldindata.org/land-use.

[7] W. J. Bloss, M. J. Evans, J. D. Lee, R. Sommariva, D. E. Heard, and M. J. Pilling. The oxidative capacity of the troposphere: Coupling of field measurements of OH and a global chemistry transport model. *Faraday Discussions*, 130(0):425–436, 2005.

[8] L. W. Horowitz, S. Walters, D. L. Mauzerall, L. K. Emmons, P. J. Rasch, C. Granier, X. Tie, J.-F. Lamarque, M. G. Schultz, G. S. Tyndall, J. J. Orlando, and G. P. Brasseur. A global simulation of tropospheric ozone and related tracers: Description and evaluation of MOZART, version 2. *Journal of Geophysical Research: Atmospheres*, 108(D24), 2003.

[9] D. J Jacob. *Introduction to atmospheric chemistry*. Princeton University Press, 1999.

[10] P. S. Monks. Gas-phase radical chemistry in the troposphere. *Chemical Society Reviews*, 34(5):376–395, 2005.

[11] B. J. Finlayson-Pitts and J. N. Pitts Jr. *Chemistry of the upper and lower atmosphere: theory, experiments, and applications*. Elsevier, 1999.

[12] Y. Zhang, D. J. Seidel, and S. Zhang. Trends in planetary boundary layer height over Europe. *Journal of Climate*, 26(24):10071–10076, 2013.

[13] K. A. Read, A. S. Mahajan, L. J. Carpenter, M. J. Evans, B. V. E. Faria, D. E. Heard, J. R. Hopkins, J. D. Lee, S. J. Moller, A. C. Lewis, L. Mendes, J. B. McQuaid, H. Oetjen, A. Saiz-Lopez, M. J. Pilling, and J. M. C. Plane. Extensive halogen-mediated ozone destruction over the tropical Atlantic Ocean. *Nature*, 453(7199):1232–1235, 2008.

[14] S. Chapman. A theory of upper-atmospheric ozone. *Mem. Roy. Meteor.*, 3:103–125, 1930.

[15] P. J. Crutzen. Estimates of possible future ozone reductions from continued use of fluoro-chloro-methanes (CF_2Cl_2, $CFCl_3$). *Geophysical Research Letters*, 1(5):205–208, 1974.

[16] M. J. Molina and F. S. Rowland. Stratospheric sink for chlorofluoromethanes: chlorine atom-catalysed destruction of ozone. *Nature*, 249(5460):810–812, 1974.

[17] J. C. Farman, B. G. Gardiner, and J. D. Shanklin. Large losses of total ozone in Antarctica reveal seasonal ClO_x/NO_x interaction. *Nature*, 315(6016):207–210, 1985.

[18] D. W. Tarasick, T. K. Carey-Smith, W. K. Hocking, O. Moeini, H. He, J. Liu, M. K. Osman, A. M. Thompson, B. J. Johnson, S. J. Oltmans, and J. T. Merrill. Quantifying stratosphere-troposphere transport of ozone using balloon-borne ozonesondes, radar windprofilers and trajectory models. *Atmospheric Environment*, 198:496–509, 2019.

[19] R. Atkinson, D. L. Baulch, R. A. Cox, J. N. Crowley, R. F. Hampson, R. G. Hynes, M. E. Jenkin, M. J. Rossi, and J. Troe. Evaluated kinetic and photochemical data for atmospheric chemistry: Volume i - gas phase reactions of O_x, HO_x, NO_x and SO_x species. *Atmospheric Chemistry and Physics*, 4(6):1461–1738, 2004.

[20] R. Atkinson. Atmospheric chemistry of VOCs and NO_x. *Atmospheric Environment*, 34(12):2063–2101, 2000.

[21] L. Jaeglé, D. J. Jacob, W. H. Brune, D. Tan, I. C. Faloona, A. J. Weinheimer, B. A. Ridley, T. L. Campos, and G. W. Sachse. Sources of HO_x and production of ozone in the upper troposphere over the United States. *Geophysical Research Letters*, 25(10):1709–1712, 1998.

[22] J. A. Logan. Tropospheric ozone: Seasonal behavior, trends, and anthropogenic influence. *Journal of Geophysical Research: Atmospheres*, 90(D6):10463–10482, 1985.

[23] J. D. Lee, S. J. Moller, K. A. Read, A. C. Lewis, L. Mendes, and L. J. Carpenter. Year-round measurements of nitrogen oxides and ozone in the tropical North Atlantic marine boundary layer. *Journal of Geophysical Research: Atmospheres*, 114(D21), 2009.

[24] P. Sicard. Ground-level ozone over time: An observation-based global overview. *Current Opinion in Environmental Science & Health*, 19:100226, 2021.

[25] U. Schumann and H. Huntrieser. The global lightning-induced nitrogen oxides source. *Atmos. Chem. Phys.*, 7(14):3823–3907, 2007.

[26] M. Val Martin, R. E. Honrath, R. C. Owen, and K. Lapina. Large-scale impacts of anthropogenic pollution and boreal wildfires on the nitrogen oxides over the central North Atlantic region. *Journal of Geophysical Research: Atmospheres*, 113(D17), 2008.

[27] E. A. Davidson and W. Kingerlee. A global inventory of nitric oxide emissions from soils. *Nutrient Cycling in Agroecosystems*, 48(1):37–50, 1997.

[28] R. Delmas, D. Serça, and C. Jambert. Global inventory of NO_x sources. *Nutrient Cycling in Agroecosystems*, 48(1):51–60, 1997.

[29] F. Berkes, N. Houben, U. Bundke, H. Franke, H.-W. Pätz, F. Rohrer, A. Wahner, and A. Petzold. The IAGOS NO_x instrument - design, operation and first results from deployment aboard passenger aircraft. *Atmospheric Measurement Techniques*, 11(6):3737–3757, 2018.

[30] D. C. Carslaw. Evidence of an increasing NO_2/NO_X emissions ratio from road traffic emissions. *Atmospheric Environment*, 39(26):4793–4802, 2005.

[31] N. A. Mazzeo, L. E. Venegas, and H Choren. Analysis of no, NO_2, O_3 and NO_x concentrations measured at a green area of buenos aires city during wintertime. *Atmospheric Environment*, 39(17):3055–3068, 2005.

[32] S. K. Pandey, K.-H. Kim, S.-Y. Chung, S.-J. Cho, M.-Y. Kim, and Z.-H. Shon. Long-term study of NO_x behavior at urban roadside and back-

ground locations in Seoul, Korea. *Atmospheric Environment*, 42(4):607–622, 2008.

[33] K. Miyazaki, H. Eskes, K. Sudo, K. F. Boersma, K. Bowman, and Y. Kanaya. Decadal changes in global surface nox emissions from multi-constituent satellite data assimilation. *ACP*, 17(2):807–837, January 2017.

[34] Lee T. Murray, Jennifer A. Logan, and Daniel J. Jacob. Interannual variability in tropical tropospheric ozone and oh: The role of lightning. *J. Geophys. Res. Atmos.*, 118(19):11,468–11,480, October 2013.

[35] T. Stavrakou, J.-F. Müller, K. F. Boersma, A. van der R. J., J. Kurokawa, T. Ohara, and Q. Zhang. Key chemical NO_x sink uncertainties and how they influence top-down emissions of nitrogen oxides. *ACP*, 13(17):9057–9082, September 2013.

[36] K. Miyazaki, H. J. Eskes, K. Sudo, and C. Zhang. Global lightning NO_x production estimated by an assimilation of multiple satellite data sets. *ACP*, 14(7):3277–3305, April 2014.

[37] J. J. Yienger and H. Levy II. Empirical model of global soil-biogenic NO_x emissions. *Journal of Geophysical Research: Atmospheres*, 100(D6):11447–11464, 1995.

[38] Lyatt Jaeglé, Linda Steinberger, Randall V. Martin, and Kelly Chance. Global partitioning of NO_x sources using satellite observations: Relative roles of fossil fuel combustion, biomass burning and soil emissions. *Faraday discussions*, 130:407–423, 2005.

[39] G. C. M. Vinken, K. F. Boersma, J. D. Maasakkers, M. Adon, and R. V. Martin. Worldwide biogenic soil NO_x emissions inferred from omi no₂ observations. *ACP*, 14(18):10363–10381, September 2014.

[40] R. V. Martin, D. J. Jacob, K. Chance, T. P. Kurosu, P. I. Palmer, and M. J. Evans. Global inventory of nitrogen oxide emissions constrained by space-based observations of NO_2 columns. *Journal of Geophysical Research: Atmospheres*, 108(D17), 2003.

[41] P. S. Kasibhatla, H. Levy II, and W. J. Moxim. Global NO_x, HNO_3, PAN, and NOy distributions from fossil fuel combustion emissions: A model study. *Journal of Geophysical Research: Atmospheres*, 98(D4):7165–7180, 1993.

[42] S. J. Pai, C. L. Heald, and J. G. Murphy. Exploring the global importance of atmospheric ammonia oxidation. *ACS Earth and Space Chemistry*, 5(7):1674–1685, 2021.

[43] P. S. Monks, L. J. Carpenter, S. A. Penkett, G. P. Ayers, R. W. Gillett, I. E. Galbally, and C.P. (Mick) Meyer. Fundamental ozone photochemistry in the remote marine boundary layer: the soapex experiment, measurement and theory. *Atmospheric Environment*, 32(21):3647–3664, 1998.

[44] C. Reed, M. J. Evans, L. R. Crilley, W. J. Bloss, T. Sherwen, K. A. Read, J. D. Lee, and L. J. Carpenter. Evidence for renoxification in the tropical marine boundary layer. *Atmospheric Chemistry and Physics*, 17(6):4081–4092, 2017.

[45] H. B. Singh and L.J. Salas. Peroxyacetyl nitrate in the free troposphere. *Nature*, 302(5906):326–328, 1983.

[46] J. L. Neu, M. J. Lawler, M. J. Prather, and E. S. Saltzman. Oceanic alkyl nitrates as a natural source of tropospheric ozone. *Geophysical Research Letters*, 35(13), 2008.

[47] S. Beirle, U. Platt, R. von Glasow, M. Wenig, and T. Wagner. Estimate of nitrogen oxide emissions from shipping by satellite remote sensing. *Geophysical Research Letters*, 31(18), 2004.

[48] L. K. Whalley, K. L. Furneaux, A. Goddard, J. D. Lee, A. Mahajan, H. Oetjen, K. A. Read, N. Kaaden, L. J. Carpenter, A. C. Lewis, J. M. C. Plane, E. S. Saltzman, A. Wiedensohler, and D. E. Heard. The chemistry of OH and HO_2 radicals in the boundary layer over the tropical Atlantic Ocean. *Atmos. Chem. Phys.*, 10(4):1555–1576, 2010.

[49] R. Atkinson, D. L. Baulch, R. A. Cox, J. N. Crowley, R. F. Hampson, R. G. Hynes, M. E. Jenkin, M. J. Rossi, and J. Troe. Iupac task group on atmospheric chemical kinetic data evaluation. *Atmos. Chem. Phys.*, 4, 2004.

[50] S. M. Kane, F. Caloz, and M.-T. Leu. Heterogeneous uptake of gaseous N_2O_5 by $(NH_4)_2SO_4$, NH_4HSO_4, and H_2SO_4 aerosols. *The Journal of Physical Chemistry A*, 105(26):6465–6470, 2001.

[51] C. Ye, X. Zhou, D. Pu, J. Stutz, J. Festa, M. Spolaor, C. Tsai, C. Cantrell, R. L. Mauldin, T. Campos, A. Weinheimer, R. S. Hornbrook, E. C. Apel, A. Guenther, L. Kaser, B. Yuan, T. Karl, J. Haggerty, S. Hall, K. Ullmann, J. N. Smith, J. Ortega, and C. Knote. Rapid cycling of reactive nitrogen in the marine boundary layer. *Nature*, 532:489, 2016.

[52] Y. Zhu, Y. Wang, X. Zhou, Y. Elshorbany, C. Ye, M. Hayden, and A. J. Peters. An investigation into the chemistry of HONO in the marine boundary layer at Tudor Hill marine atmospheric observatory in Bermuda. *Atmos. Chem. Phys. Discuss.*, 2021:1–33, 2021.

[53] R. Atkinson and J. Arey. Atmospheric degradation of volatile organic compounds. *Chemical Reviews*, 103(12):4605–4638, 2003.

[54] Y. Zhang and J. R. Morris. Hydrogen abstraction probability in reactions of gas-phase NO_3 with an OH-functionalized organic surface. *The Journal of Physical Chemistry C*, 119(26):14742–14747, 2015.

[55] N. L. Ng, S. S. Brown, A. T. Archibald, E. Atlas, R. C. Cohen, J. N. Crowley, D. A. Day, N. M. Donahue, J. L. Fry, H. Fuchs, R. J. Griffin, M. I. Guzman, H. Herrmann, A. Hodzic, Y. Iinuma, J. L. Jimenez, A. Kiendler-Scharr, B. H. Lee, D. J. Luecken, J. Mao, R. McLaren, A. Mutzel, H. D. Osthoff, B. Ouyang, B. Picquet-Varrault, U. Platt, H. O. T. Pye, Y. Rudich, R. H. Schwantes, M. Shiraiwa, J. Stutz, J. A. Thornton, A. Tilgner, B. J. Williams, and R. A. Zaveri. Nitrate radicals and biogenic volatile organic compounds: oxidation, mechanisms, and organic aerosol. *Atmos. Chem. Phys.*, 17(3):2103–2162, 2017.

[56] A. E. Perring, A. Wisthaler, M. Graus, P. J. Wooldridge, A. L. Lockwood, L. H. Mielke, P. B. Shepson, A. Hansel, and R. C. Cohen. A product study of the isoprene+NO_3 reaction. *Atmos. Chem. Phys.*, 9(14):4945–4956, 2009.

[57] A. W. Rollins, A. Kiendler-Scharr, J. L. Fry, T. Brauers, S. S. Brown, H. P. Dorn, W. P. Dubé, H. Fuchs, A. Mensah, T. F. Mentel, F. Rohrer, R. Tillmann, R. Wegener, P. J. Wooldridge, and R. C. Cohen. Isoprene oxidation by nitrate radical: alkyl nitrate and secondary organic aerosol yields. *Atmos. Chem. Phys.*, 9(18):6685–6703, 2009.

[58] J. F. Müller, J. Peeters, and T. Stavrakou. Fast photolysis of carbonyl nitrates from isoprene. *Atmos. Chem. Phys.*, 14(5):2497–2508, 2014.

[59] R. Suarez-Bertoa, B. Picquet-Varrault, W. Tamas, E. Pangui, and J. F. Doussin. Atmospheric fate of a series of carbonyl nitrates: Photolysis frequencies and OH-oxidation rate constants. *Environmental Science & Technology*, 46(22):12502–12509, 2012.

[60] C. M. Boyd, J. Sanchez, L. Xu, A. J. Eugene, T. Nah, W. Y. Tuet, M. I. Guzman, and N. L. Ng. Secondary organic aerosol formation from the β-pinene+NO_3 system: effect of humidity and peroxy radical fate. *Atmos. Chem. Phys.*, 15(13):7497–7522, 2015.

[61] J. L. Fry, A. Kiendler-Scharr, A. W. Rollins, P. J. Wooldridge, S. S. Brown, H. Fuchs, W. Dubé, A. Mensah, M. dal Maso, R. Tillmann, H. P. Dorn, T. Brauers, and R. C. Cohen. Organic nitrate and secondary organic aerosol yield from NO_3 oxidation of β-pinene evaluated using a gas-phase kinetics/aerosol partitioning model. *Atmos. Chem. Phys.*, 9(4):1431–1449, 2009.

[62] J. L. Fry, A. Kiendler-Scharr, A. W. Rollins, T. Brauers, S. S. Brown, H. P. Dorn, W. P. Dubé, H. Fuchs, A. Mensah, F. Rohrer, R. Tillmann, A. Wahner, P. J. Wooldridge, and R. C. Cohen. SOA from limonene: role of NO_3 in its generation and degradation. *Atmos. Chem. Phys.*, 11(8):3879–3894, 2011.

[63] J. L. Fry, D. C. Draper, K. C. Barsanti, J. N. Smith, J. Ortega, P. M. Winkler, M. J. Lawler, S. S. Brown, P. M. Edwards, R. C. Cohen, and L. Lee. Secondary organic aerosol formation and organic nitrate yield from NO_3 oxidation of biogenic hydrocarbons. *Environmental Science & Technology*, 48(20):11944–11953, 2014.

[64] T. Nah, J. Sanchez, C. M. Boyd, and N. L. Ng. Photochemical aging of α-pinene and β-pinene secondary organic aerosol formed from nitrate radical oxidation. *Environmental Science & Technology*, 50(1):222–231, 2016.

[65] J. N. Pitts, H. W. Biermann, A. M. Winer, and E. C. Tuazon. Spectroscopic identification and measurement of gaseous nitrous acid in dilute auto exhaust. *Atmospheric Environment (1967)*, 18(4):847–854, 1984.

[66] H. Su, Y. Cheng, R. Oswald, T. Behrendt, I. Trebs, F. X. Meixner, M. O. Andreae, P. Cheng, Y. Zhang, and U. Pöschl. Soil nitrite as a source of atmospheric HONO and OH radicals. *Science*, page 1207687, 2011.

[67] N. Theys, R. Volkamer, J. F. Müller, K. J. Zarzana, N. Kille, L. Clarisse, I. De Smedt, C. Lerot, H. Finkenzeller, F. Hendrick, T. K. Koenig, C. F. Lee, C. Knote, H. Yu, and M. Van Roozendael. Global nitrous acid emissions and levels of regional oxidants enhanced by wildfires. *Nature Geoscience*, 13(10):681–686, 2020.

[68] L. R. Crilley, L. J. Kramer, F. D. Pope, C. Reed, J. D. Lee, L. J. Carpenter, L. D. J. Hollis, S. M. Ball, and W. J. Bloss. Is the ocean surface a source of nitrous acid (HONO) in the marine boundary layer? *Atmos. Chem. Phys.*, 21(24):18213–18225, 2021.

[69] X. Li, F. Rohrer, A. Hofzumahaus, T. Brauers, R. Häseler, B. Bohn, S. Broch, H. Fuchs, S. Gomm, F. Holland, J. Jäger, J. Kaiser, F. N. Keutsch, I. Lohse, K. Lu, R. Tillmann, R. Wegener, G. M. Wolfe, T. F. Mentel, A. Kiendler-Scharr, and A. Wahner. Missing gas-phase source of HONO inferred from zeppelin measurements in the troposphere. *Science*, 344(6181):292–296, 2014.

[70] Z. Liu, Y. Wang, F. Costabile, A. Amoroso, C. Zhao, L. G. Huey, R. Stickel, J. Liao, and T. Zhu. Evidence of aerosols as a media for rapid daytime HONO production over China. *Environmental Science & Technology*, 48(24):14386–14391, 2014.

[71] X. Lu, Y. Wang, J. Li, L. Shen, and J. C. H. Fung. Evidence of heterogeneous HONO formation from aerosols and the regional photochemical impact of this HONO source. *Environmental Research Letters*, 13(11):114002, 2018.

[72] P. S. Monks, C. Granier, S. Fuzzi, A. Stohl, M. L. Williams, H. Akimoto, M. Amann, A. Baklanov, U. Baltensperger, I. Bey, N. Blake, R. S. Blake, K. Carslaw, O. R. Cooper, F. Dentener, D. Fowler, E. Fragkou, G. J. Frost, S. Generoso, P. Ginoux, V. Grewe, A. Guenther, H. C. Hansson, S. Henne, J. Hjorth, A. Hofzumahaus, H. Huntrieser, I. S. A. Isaksen, M. E. Jenkin, J. Kaiser, M. Kanakidou, Z. Klimont, M. Kulmala, P. Laj, M. G. Lawrence, J. D. Lee, C. Liousse, M. Maione, G. McFiggans, A. Metzger, A. Mieville, N. Moussiopoulos, J. J. Orlando, C. D. O'Dowd, P. I. Palmer, D. D. Parrish, A. Petzold, U. Platt, U. Pöschl, A. S. H. Prévôt, C. E. Reeves, S. Reimann, Y. Rudich, K. Sellegri, R. Steinbrecher, D. Simpson, H. ten Brink, J. Theloke, G. R. van der Werf, R. Vautard, V. Vestreng, Ch Vlachokostas, and R. von Glasow. Atmospheric composition change – global and regional air quality. *Atmospheric Environment*, 43(33):5268–5350, 2009.

[73] N. Zhang, X. Zhou, P. B. Shepson, H. Gao, M. Alaghmand, and B. Stirm. Aircraft measurement of HONO vertical profiles over a forested region. *Geophysical Research Letters*, 36(15), 2009.

[74] W. A. McClenny, E. J. Williams, R. C. Cohen, and J. Stutz. Preparing to measure the effects of the NO_x SIP call– methods for ambient air monitoring of NO, NO_2, NOy, and individual NOz species. *null*, 52(5):542–562, May 2002.

[75] U. Platt, D. Perner, and H. W. Pätz. Simultaneous measurement of atmospheric CH_2O, O_3, and NO_2 by differential optical absorption. *Journal of Geophysical Research: Oceans*, 84(C10):6329–6335, 1979.

[76] J. Stutz and U. Platt. Improving long-path differential optical absorption spectroscopy with a quartz-fiber mode mixer. *Applied optics*, 36(6):1105–1115, 1997.

[77] A. A. Kosterev, A. L. Malinovsky, F. K. Tittel, C. Gmachl, F. Capasso, D. L. Sivco, J. N. Baillargeon, A. L. Hutchinson, and A. Y. Cho. Cavity ringdown spectroscopic detection of nitric oxide with a continuous-wave quantum-cascade laser. *Applied Optics*, 40(30):5522–5529, 2001.

[78] A. O'Keefe and D. A. G. Deacon. Cavity ring-down optical spectrometer for absorption measurements using pulsed laser sources. *Review of Scientific Instruments*, 59(12):2544–2551, 1988.

[79] H. D. Osthoff, S. S. Brown, T. B. Ryerson, T. J. Fortin, B. M. Lerner, E. J. Williams, A. Pettersson, T. Baynard, W. P. Dubé, S. J. Ciciora, and A. R. Ravishankara. Measurement of atmospheric NO_2 by pulsed cavity ring-down spectroscopy. *Journal of Geophysical Research: Atmospheres*, 111(D12), 2006.

[80] P. L. Kebabian, E. C. Wood, S. C. Herndon, and A. Freedman. A practical alternative to chemiluminescence-based detection of nitrogen dioxide: Cavity attenuated phase shift spectroscopy. *Environ. Sci. Technol.*, 42(16):6040–6045, August 2008.

[81] P. L. Kebabian, S. C. Herndon, and A. Freedman. Detection of nitrogen dioxide by cavity attenuated phase shift spectroscopy. *Anal. Chem.*, 77(2):724–728, January 2005.

[82] A. W. Rollins, P. S. Rickly, R. S. Gao, T. B. Ryerson, S. S. Brown, J. Peischl, and I. Bourgeois. Single-photon laser-induced fluorescence detection of nitric oxide at sub-parts-per-trillion mixing ratios. *Atmos. Meas. Tech.*, 13(5):2425–2439, 2020.

[83] W. J. Tango, J. K. Link, and R. N. Zare. Spectroscopy of K_2 using laser-induced fluorescence. *The Journal of Chemical Physics*, 49(10):4264–4268, 1968.

[84] J. A. Thornton, P. J. Wooldridge, R. C. Cohen, E. J. Williams, D. Hereid, F. C. Fehsenfeld, J. Stutz, and B. Alicke. Comparisons of in situ and long path measurements of NO_2 in urban plumes. *Journal of Geophysical Research: Atmospheres*, 108(D16), 2003.

[85] J. W. Drummond, A. Volz, and D. H. Ehhalt. An optimized chemiluminescence detector for tropospheric NO measurements. *Journal of Atmospheric Chemistry*, 2(3):287–306, 1985.

[86] N. A. Marley, J. S. Gaffney, R. V. White, L. Rodriguez-Cuadra, S. E. Herndon, E. Dunlea, R. M. Volkamer, L. T. Molina, and M. J. Molina. Fast gas chromatography with luminol chemiluminescence detection for the simultaneous determination of nitrogen dioxide and peroxyacetyl nitrate in the atmosphere. *Review of Scientific Instruments*, 75(11):4595–4605, 2004.

[87] Y. Q. Li, K. L. Demerjian, M. S. Zahniser, D. D. Nelson, J. B. McManus, and S. C. Herndon. Measurement of formaldehyde, nitrogen dioxide, and sulfur dioxide at Whiteface mountain using a dual tunable diode laser system. *Journal of Geophysical Research: Atmospheres*, 109(D16), 2004.

[88] M. S. Zahniser, D. D. Nelson, B. McManus, P. L. Kebabian, and D. Lloyd. Measurement of trace gas fluxes using tunable diode laser spectroscopy. *Philosophical Transactions of the Royal Society of London. Series A: Physical and Engineering Sciences*, 351(1696):371–382, 1995.

[89] D. Mihelcic, P. Müsgen, and D. H. Ehhalt. An improved method of measuring tropospheric NO_2 and RO_2 by matrix isolation and electron spin resonance. *Journal of atmospheric chemistry*, 3(3):341–361, 1985.

[90] G. Dooly, C. Fitzpatrick, and E. Lewis. Deep UV based DOAS system for the monitoring of nitric oxide using ratiometric separation techniques. *Sensors and Actuators B: Chemical*, 134(1):317–323, 2008.

[91] Y. Li, X. Zhang, X. Li, Z. Cui, and H. Xiao. Detection of ozone and nitric oxide in decomposition products of air-insulated switchgear using ultraviolet differential optical absorption spectroscopy (UV-DOAS). *Applied Spectroscopy*, 72(8):1244–1251, 2018.

[92] A. Al-Jalal, W. Al-Basheer, K. Gasmi, and M. S. Romadhon. Measurement of low concentrations of NO_2 gas by differential optical absorption spectroscopy method. *Measurement*, 146:613–617, 2019.

[93] A. Seyler, A. C. Meier, F. Wittrock, L. Kattner, B. Mathieu-Üffing, E. Peters, A. Richter, T. Ruhtz, A. Schönhardt, S. Schmolke, and J. P. Burrows. Studies of the horizontal inhomogeneities in NO_2 concentrations above a shipping lane using ground-based multi-axis differential optical absorption spectroscopy (MAX-DOAS) measurements and validation with airborne imaging DOAS measurements. *Atmos. Meas. Tech.*, 12(11):5959–5977, 2019.

[94] R. K. Jha. Non-dispersive infrared gas sensing technology: A review. *IEEE Sensors Journal*, 22(1):6–15, 2022.

[95] H. Sumizawa, H. Yamada, and K. Tonokura. Real-time monitoring of nitric oxide in diesel exhaust gas by mid-infrared cavity ring-down spectroscopy. *Applied Physics B*, 100(4):925–931, 2010.

[96] N. Sobanski, J. Schuladen, G. Schuster, J. Lelieveld, and J. N. Crowley. A five-channel cavity ring-down spectrometer for the detection of NO_2, NO_3, N_2O_5, total peroxy nitrates and total alkyl nitrates. *AMT*, 9(10):5103–5118, October 2016.

[97] J. Matsumoto, J. Hirokawa, H. Akimoto, and Y. Kajii. Direct measurement of NO_2 in the marine atmosphere by laser-induced fluorescence technique. *Atmospheric Environment*, 35(16):2803–2814, 2001.

[98] J. Matsumoto and Y. Kajii. Improved analyzer for nitrogen dioxide by laser-induced fluorescence technique. *Atmospheric Environment*, 37(34):4847–4851, 2003.

[99] J. A. Thornton, P. J. Wooldridge, and R. C. Cohen. Atmospheric NO_2: In situ laser-induced fluorescence detection at parts per trillion mixing ratios. *Anal. Chem.*, 72(3):528–539, February 2000.

[100] Y. Maeda, K. Aoki, and M. Munemori. Chemiluminescence method for the determination of nitrogen dioxide. *Analytical Chemistry*, 52(2):307–311, 1980.

[101] T. J. Kelly, C. W. Spicer, and G. F. Ward. An assessment of the luminol chemiluminescence technique for measurement of NO_2 in ambient air. *Atmospheric Environment. Part A. General Topics*, 24(9):2397–2403, 1990.

[102] A. Fontijn, A. J. Sabadell, and R. J. Ronco. Homogeneous chemiluminescent measurement of nitric oxide with ozone. implications for continuous selective monitoring of gaseous air pollutants. *Anal. Chem.*, 42(6):575–579, May 1970.

[103] D Kley and M McFarland. Chemiluminescence detector for NO and NO_2. *Atmos. Technol.;(United States)*, 12, 1980.

[104] E. J. Dunlea, S. C. Herndon, D. D. Nelson, R. M. Volkamer, F. San Martini, P. M. Sheehy, M. S. Zahniser, J. H. Shorter, J. C. Wormhoudt, B. K. Lamb, E. J. Allwine, J. S. Gaffney, N. A. Marley, M. Grutter, C. Marquez, S. Blanco, B. Cardenas, A. Retama, C. R. Ramos Villegas, C. E. Kolb, L. T. Molina, and M. J. Molina. Evaluation of nitrogen dioxide

chemiluminescence monitors in a polluted urban environment. *Atmospheric Chemistry and Physics*, 7(10):2691–2704, 2007.

[105] D. Grosjean and J. Harrison. Response of chemiluminescence NO_x analyzers and ultraviolet ozone analyzers to organic air pollutants. *Environ. Sci. Technol.*, 19(9):862–865, September 1985.

[106] A. M. Winer, J. W. Peters, J. P. Smith, and J. N. Pitts. Response of commercial chemiluminescent nitric oxide-nitrogen dioxide analyzers to other nitrogen-containing compounds. *Environ. Sci. Technol.*, 8(13):1118–1121, December 1974.

[107] I. B. Pollack, B. M. Lerner, and T. B. Ryerson. Evaluation of ultraviolet light-emitting diodes for detection of atmospheric NO_2 by photolysis - chemiluminescence. *Journal of Atmospheric Chemistry*, 65(2):111–125, 2010.

[108] C. Reed, M. J. Evans, P. Di Carlo, J. D. Lee, and L. J. Carpenter. Interferences in photolytic NO_2 measurements: explanation for an apparent missing oxidant? *Atmospheric Chemistry and Physics*, 16(7):4707–4724, 2016.

[109] J. M. Hoell, G. L. Gregory, M. A. Carroll, M. McFarland, B. A. Ridley, D. D. Davis, J. Bradshaw, M. O. Rodgers, A. L. Torres, G. W. Sachse, G. F. Hill, E. P. Condon, R. A. Rasmussen, M. C. Campbell, J. C. Farmer, J. C. Sheppard, C. C. Wang, and L. I. Davis. An intercomparison of carbon monoxide, nitric oxide, and hydroxyl measurement techniques: Overview of results. *Journal of Geophysical Research: Atmospheres*, 89(D7):11819–11825, 1984.

[110] J. M. Hoell Jr., G. L. Gregory, D. S. McDougal, A. L. Torres, D. D. Davis, J. Bradshaw, M. O. Rodgers, B. A. Ridley, and M. A. Carroll.

Airborne intercomparison of nitric oxide measurement techniques. *Journal of Geophysical Research: Atmospheres*, 92(D2):1995–2008, 1987.

[111] I. Bourgeois, J. Peischl, J. A. Neuman, S. S. Brown, H. M. Allen, P. Campuzano-Jost, M. M. Coggon, J. P. DiGangi, G. S. Diskin, J. B. Gilman, G. I. Gkatzelis, H. Guo, H. Halliday, T. F. Hanisco, C. D. Holmes, L. G. Huey, J. L. Jimenez, A. D. Lamplugh, Y. R. Lee, J. Lindaas, R. H. Moore, J. B. Nowak, D. Pagonis, P. S. Rickly, M. A. Robinson, A. W. Rollins, V. Selimovic, J. M. St. Clair, D. Tanner, K. T. Vasquez, P. R. Veres, C. Warneke, P. O. Wennberg, R. A. Washenfelder, E. B. Wiggins, C. C. Womack, L. Xu, K. J. Zarzana, and T. B. Ryerson. Comparison of airborne measurements of NO, NO_2, HONO, NOy and CO during FIREX-AQ. *AMTD*, 2022:1–47, January 2022.

[112] F. C. Fehsenfeld, J. W. Drummond, U. K. Roychowdhury, P. J. Galvin, E. J. Williams, M. P. Buhr, D. D. Parrish, G. Hübler, A. O. Langford, J. G. Calvert, B. A. Ridley, F. Grahek, B. G. Heikes, G. L. Kok, J. D. Shetter, J. G. Walega, C. M. Elsworth, R. B. Norton, D. W. Fahey, P. C. Murphy, C. Hovermale, V. A. Mohnen, K. L. Demerjian, G. I. Mackay, and H. I. Schiff. Intercomparison of NO_2 measurement techniques. *Journal of Geophysical Research: Atmospheres*, 95(D4):3579–3597, 1990.

[113] G. L. Gregory, J. M. Hoell Jr., M. A. Carroll, B. A. Ridley, D. D. Davis, J. Bradshaw, M. O. Rodgers, S. T. Sandholm, H. I. Schiff, D. R. Hastie, D. R. Karecki, G. I. Mackay, G. W. Harris, A. L. Torres, and A. Fried. An intercomparison of airborne nitrogen dioxide instruments. *Journal of Geophysical Research: Atmospheres*, 95(D7):10103–10127, 1990.

[114] L. J. Carpenter, Z. L. Fleming, K. A. Read, J. D. Lee, S. J. Moller, J. R. Hopkins, R. M. Purvis, A. C. Lewis, K. Müller, B. Heinold, H. Herrmann, K. Wadinga Fomba, D. van Pinxteren, C. Müller, I. Tegen, A. Wiedensohler, T. Müller, N. Niedermeier, E. P. Achterberg, M. D. Patey, E. A.

Kozlova, M. Heimann, D. E. Heard, J. M. C. Plane, A. Mahajan, H. Oetjen, T. Ingham, D. Stone, L. K. Whalley, M. J. Evans, M. J. Pilling, R. J. Leigh, P. S. Monks, A. Karunaharan, S. Vaughan, S. R. Arnold, J. Tschritter, D. Pöhler, U. Frieß, R. Holla, L. M. Mendes, H. Lopez, B. Faria, A. J. Manning, and D. W. R. Wallace. Seasonal characteristics of tropical marine boundary layer air measured at the Cape Verde atmospheric observatory. *Journal of Atmospheric Chemistry*, 67(2):87–140, 2010.

[115] D. B. Ryall, R. G. Derwent, A. J. Manning, P. G. Simmonds, and S. O'Doherty. Estimating source regions of european emissions of trace gases from observations at Mace Head. *Atmospheric Environment*, 35(14):2507–2523, 2001.

[116] I. Chiapello, G. Bergametti, L. Gomes, B. Chatenet, F. Dulac, J. Pimenta, and E. Santos Suares. An additional low layer transport of Sahelian and Saharan dust over the north-eastern Tropical Atlantic. *Geophysical Research Letters*, 22(23):3191–3194, 1995.

[117] K. W. Fomba, K. Müller, D. van Pinxteren, L. Poulain, M. van Pinxteren, and H. Herrmann. Long-term chemical characterization of tropical and marine aerosols at the Cape Verde atmospheric observatory (CVAO) from 2007 to 2011. *Atmospheric Chemistry and Physics*, 14(17):8883–8904, 2014.

[118] M. J. A. Rijkenberg, C. F. Powell, M. Dall'Osto, M. C. Nielsdottir, M. D. Patey, P. G. Hill, A. R. Baker, T. D. Jickells, R. M. Harrison, and E. P. Achterberg. Changes in iron speciation following a Saharan dust event in the tropical North Atlantic Ocean. *Marine Chemistry*, 110(1):56–67, 2008.

[119] P. N. Clough and B. A. Thrush. Mechanism of chemiluminescent reaction between nitric oxide and ozone. *Trans. Faraday Soc.*, 63:915–925, 1967.

[120] M. A. A. Clyne, B. A. Thrush, and R. P. Wayne. Kinetics of the chemiluminescent reaction between nitric oxide and ozone. *Trans. Faraday Soc.*, 60:359–370, 1964.

[121] M. C. Peterson and R. E. Honrath. NO_x and NOy over the northwestern North Atlantic: Measurements and measurement accuracy. *Journal of Geophysical Research: Atmospheres*, 104(D9):11695–11707, 1999.

[122] M. Val Martín, R. E. Honrath, R. C. Owen, G. Pfister, P. Fialho, and F. Barata. Significant enhancements of nitrogen oxides, black carbon, and ozone in the North Atlantic lower free troposphere resulting from North American boreal wildfires. *Journal of Geophysical Research: Atmospheres*, 111(D23), 2006.

[123] M. P. Buhr. Solid-state light source photolytic nitrogen dioxide converter, 2007.

[124] B. A. Ridley and F. E. Grahek. A small, low flow, high sensitivity reaction vessel for NO chemiluminescence detectors. *Journal of Atmospheric and Oceanic Technology*, 7(2):307–311, 1990.

[125] M. S. Alam, L. R. Crilley, J. D. Lee, L. J. Kramer, C. Pfrang, M. Vázquez-Moreno, M. Ródenas, A. Muñoz, and W. J. Bloss. Interference from alkenes in chemiluminescent NO_x measurements. *Atmospheric Measurement Techniques*, 13(11):5977–5991, 2020.

[126] B. J. Finlayson, J. N. Pitts, and R. Atkinson. Low-pressure gas-phase ozone-olefin reactions. chemiluminescence, kinetics, and mechanisms. *J. Am. Chem. Soc.*, 96(17):5356–5367, August 1974.

[127] F. Su, J. G. Calvert, and J. H. Shaw. A ft ir spectroscopic study of the ozone-ethene reaction mechanism in oxygen-rich mixtures. *The Journal of Physical Chemistry*, 84(3):239–246, 1980.

[128] H. Ohoyama, T. Kasai, Y. Yoshimura, H. Kimura, and K. Kuwata. Initial distribution of vibration of the OH radicals produced in the H + O_3 → OH($X^2\pi_{1/2,3/2}$) + O_2 reaction. chemiluminescence by a crossed beam technique. *Chemical Physics Letters*, 118(3):263–266, 1985.

[129] I. E. Galbally. Nitrogen oxides (NO, NO_2, NOy) measurements at Cape Grim: A technical manual. Technical report, CSIRO, Australia, 2020.

[130] Ralf Schwarzwald, Penelope Monkhouse, and Jürgen Wolfrum. Picosecond fluorescence lifetime measurement of the oh radical in an atmospheric pressure flame. *Chemical Physics Letters*, 142(1):15–18, 1987.

[131] L. F. Keyser, S. Z. Levine, and F. Kaufman. Kinetics and mechanism of no2 fluorescence. *J. Chem. Phys.*, 54(1):355–363, January 1971.

[132] T. B. Ryerson, E. J. Williams, and F. C. Fehsenfeld. An efficient photolysis system for fast-response NO_2 measurements. *Journal of Geophysical Research: Atmospheres*, 105(D21):26447–26461, 2000.

[133] R. D. Matthews, R. F. Sawyer, and R. W. Schefer. Interferences in chemiluminescent measurement of nitric oxide and nitrogen dioxide emissions from combustion systems. *Environ. Sci. Technol.*, 11(12):1092–1096, November 1977.

[134] B. A. Ridley, F. E. Grahek, and J. G. Walega. A small high-sensitivity, medium-response ozone detector suitable for measurements from light aircraft. *Journal of Atmospheric and Oceanic Technology*, 9(2):142–148, 1992.

[135] S. Gilge, C. Plass-Dülmer, F. Rohrer, M. Steinbacher, A. M. Fjaeraa, F. Lagler, and J. Walden. WP4-NA4: Trace gases networking: Volatile organic carbon and nitrogen oxides deliverable D4.10: Standardized operating procedures (SOPs) for NOxy measurements. Technical report, ACTRIS, 2014.

[136] S. Bell. A beginner's guide to uncertainty of measurement. techreport 11, National Physical laboratory (NPL), Teddington, Middlesex, United Kingdom, TW11 0LW, 2001.

[137] D. Silvia and J. Skilling. *Data Analysis: A Bayesian Tutorial*. Oxford Univ. Press, Oxford, U. K., 2nd edition, 2006.

[138] I. Pisso, E. Sollum, H. Grythe, N. I. Kristiansen, M. Cassiani, S. Eckhardt, D. Arnold, D. Morton, R. L. Thompson, C. D. Groot Zwaaftink, N. Evangeliou, H. Sodemann, L. Haimberger, S. Henne, D. Brunner, J. F. Burkhart, A. Fouilloux, J. Brioude, A. Philipp, P. Seibert, and A. Stohl. The lagrangian particle dispersion model FLEXPART version 10.4. *Geoscientific Model Development*, 12(12):4955–4997, 2019.

[139] A. Stohl, M. Hittenberger, and G. Wotawa. Validation of the lagrangian particle dispersion model FLEXPART against large-scale tracer experiment data. *Atmospheric Environment*, 32(24):4245–4264, 1998.

[140] A. L. Torres and A. M. Thompson. Nitric oxide in the equatorial Pacific boundary layer: SAGA 3 measurements. *Journal of Geophysical Research: Atmospheres*, 98(D9):16949–16954, 1993.

[141] T. P. Carsey, D. D. Churchill, M. L. Farmer, C. J. Fischer, A. A. Pszenny, V. B. Ross, E. S. Saltzman, M. Springer-Young, and B. Bonsang. Nitrogen oxides and ozone production in the North Atlantic marine boundary layer. *Journal of Geophysical Research: Atmospheres*, 102(D9):10653–10665, 1997.

[142] K. P. Rhoads, P. Kelley, R. R. Dickerson, T. P. Carsey, M. Farmer, D. L. Savoie, and J. M. Prospero. Composition of the troposphere over the Indian Ocean during the monsoonal transition. *Journal of Geophysical Research: Atmospheres*, 102(D15):18981–18995, 1997.

[143] H. J. Beine, R. E. Honrath, F. Dominé, W. R. Simpson, and J. D. Fuentes. NO_x during background and ozone depletion periods at Alert: Fluxes above the snow surface. *Journal of Geophysical Research: Atmospheres*, 107(D21):ACH 7–1–ACH 7–12, 2002.

[144] A. E. Jones, R. Weller, A. Minikin, E. W. Wolff, W. T. Sturges, H. P. McIntyre, S. R. Leonard, O. Schrems, and S. Bauguitte. Oxidized nitrogen chemistry and speciation in the Antarctic troposphere. *Journal of Geophysical Research: Atmospheres*, 104(D17):21355–21366, 1999.

[145] M. A. Carroll, B. A. Ridley, D. D. Montzka, G. Hubler, J. G. Walega, R. B. Norton, B. J. Huebert, and F. E. Grahek. Measurements of nitric oxide and nitrogen dioxide during the Mauna Loa observatory photochemistry experiment. *Journal of Geophysical Research: Atmospheres*, 97(D10):10361–10374, 1992.

[146] M. Val Martin, R. E. Honrath, R. C. Owen, and Q. B. Li. Seasonal variation of nitrogen oxides in the central North Atlantic lower free troposphere. *Journal of Geophysical Research: Atmospheres*, 113(D17), 2008.

[147] B. A. Ridley, M. A. Carroll, and G. L. Gregory. Measurements of nitric oxide in the boundary layer and free troposphere over the Pacific Ocean. *Journal of Geophysical Research: Atmospheres*, 92(D2):2025–2047, 1987.

[148] H. J. Beine, M. Engardt, D. A. Jaffe, Ø. Hov, K. Holmén, and F. Stordal. Measurements of NO_x and aerosol particles at the NY-Ålesund Zeppelin mountain station on Svalbard: Influence of regional and local pollution sources. *Atmospheric Environment*, 30(7):1067–1079, 1996.

[149] P. A. Leighton. *Photochemistry of Air Pollution*. Academic Press, 1961.

[150] K. Mannschreck, S. Gilge, C. Plass-Duelmer, W. Fricke, and H. Berresheim. Assessment of the applicability of NO-NO_2-O_3 photosta-

tionary state to long-term measurements at the Hohenpeissenberg GAW station, Germany. *Atmos. Chem. Phys.*, 4(5):1265–1277, 2004.

[151] J. G. Calvert and W. R. Stockwell. Deviations from the O_3–NO–NO_2 photostationary state in tropospheric chemistry. *Canadian Journal of Chemistry*, 61(5):983–992, 1983.

[152] C. A. Cantrell, R. E. Shetter, J. A. Lind, A. H. McDaniel, J. G. Calvert, D. D. Parrish, F. C. Fehsenfeld, M. P. Buhr, and M. Trainer. An improved chemical amplifier technique for peroxy radical measurements. *Journal of Geophysical Research: Atmospheres*, 98(D2):2897–2909, 1993.

[153] K. Miyazaki, A. E. Parker, C. Fittschen, P. S. Monks, and Y. Kajii. A new technique for the selective measurement of atmospheric peroxy radical concentrations of HO_2 and RO_2 using a denuding method. *Atmos. Meas. Tech.*, 3(6):1547–1554, 2010.

[154] E. C. Wood and J. R. Charest. Chemical amplification - cavity attenuated phase shift spectroscopy measurements of atmospheric peroxy radicals. *Analytical Chemistry*, 86(20):10266–10273, 2014.

[155] C. A. Cantrell, R. E. Shetter, J. G. Calvert, F. L. Eisele, E. Williams, K. Baumann, W. H. Brune, P. S. Stevens, and J. H. Mather. Peroxy radicals from photostationary state deviations and steady state calculations during the tropospheric OH photochemistry experiment at Idaho Hill, Colorado, 1993. *Journal of Geophysical Research: Atmospheres*, 102(D5):6369–6378, 1997.

[156] C. A. Cantrell, R. E. Shetter, J. G. Calvert, D. D. Parrish, F. C. Fehsenfeld, P. D. Goldan, W. Kuster, E. J. Williams, H. H. Westberg, G. Allwine, and R. Martin. Peroxy radicals as measured in ROSE and estimated from photostationary state deviations. *Journal of Geophysical Research: Atmospheres*, 98(D10):18355–18366, 1993.

[157] Y. Ma, K. Lu, C. C. K. Chou, X. Li, and Y. Zhang. Strong deviations from the NO-NO_2-O_3 photostationary state in the pearl river delta: Indications of active peroxy radical and chlorine radical chemistry. *Atmospheric Environment*, 163:22–34, 2017.

[158] A. Volz-Thomas, H.-W. Pätz, N. Houben, S. Konrad, D. Mihelcic, T. Klüpfel, and D. Perner. Inorganic trace gases and peroxy radicals during BERLIOZ at Pabstthum: An investigation of the photostationary state of NO_x and O_3. *Journal of Geophysical Research: Atmospheres*, 108(D4):PHO 4–1–PHO 4–15, 2003.

[159] I. Tadic, J. N. Crowley, D. Dienhart, P. Eger, H. Harder, B. Hottmann, M. Martinez, U. Parchatka, J. D. Paris, A. Pozzer, R. Rohloff, J. Schuladen, J. Shenolikar, S. Tauer, J. Lelieveld, and H. Fischer. Net ozone production and its relationship to nitrogen oxides and volatile organic compounds in the marine boundary layer around the Arabian Peninsula. *Atmos. Chem. Phys.*, 20(11):6769–6787, 2020.

[160] I. Trebs, O. L. Mayol-Bracero, T. Pauliquevis, U. Kuhn, R. Sander, L. Ganzeveld, F. X. Meixner, J. Kesselmeier, P. Artaxo, and M. O. Andreae. Impact of the Manaus urban plume on trace gas mixing ratios near the surface in the Amazon Basin: Implications for the NO-NO_2-O_3 photostationary state and peroxy radical levels. *Journal of Geophysical Research: Atmospheres*, 117(D5), 2012.

[161] Z. Hosaynali Beygi, H. Fischer, H. D. Harder, M. Martinez, R. Sander, J. Williams, D. M. Brookes, P. S. Monks, and J. Lelieveld. Oxidation photochemistry in the Southern Atlantic boundary layer: unexpected deviations of photochemical steady state. *Atmos. Chem. Phys.*, 11(16):8497–8513, 2011.

[162] E. J. Williams, J. M. Roberts, K. Baumann, S. B. Bertman, S. Buhr, R. B. Norton, and F. C. Fehsenfeld. Variations in NOy composition at

Idaho Hill, Colorado. *Journal of Geophysical Research: Atmospheres*, 102(D5):6297–6314, 1997.

[163] C. A. Cantrell, J. A. Lind, R. E. Shetter, J. G. Calvert, P. D. Goldan, W. Kuster, F. C. Fehsenfeld, S. A. Montzka, D. D. Parrish, E. J. Williams, M. P. Buhr, H. H. Westberg, G. Allwine, and R. Martin. Peroxy radicals in the ROSE experiment: Measurement and theory. *Journal of Geophysical Research: Atmospheres*, 97(D18):20671–20686, 1992.

[164] D. D. Parrish, M. Trainer, E. J. Williams, D. W. Fahey, G. Hübler, C. S. Eubank, S. C. Liu, P. C. Murphy, D. L. Albritton, and F. C. Fehsenfeld. Measurements of the NO_x-O_3 photostationary state at Niwot Ridge, Colorado. *Journal of Geophysical Research: Atmospheres*, 91(D5):5361–5370, 1986.

[165] K. M. Emmerson, N. Carslaw, D. C. Carslaw, J. D. Lee, G. McFiggans, W. J. Bloss, T. Gravestock, D. E. Heard, J. Hopkins, T. Ingham, M. J. Pilling, S. C. Smith, M. Jacob, and P. S. Monks. Free radical modelling studies during the UK TORCH campaign in summer 2003. *Atmos. Chem. Phys.*, 7(1):167–181, 2007.

[166] G. M. Wolfe, C. Cantrell, S. Kim, R. L. Mauldin Iii, T. Karl, P. Harley, A. Turnipseed, W. Zheng, F. Flocke, E. C. Apel, R. S. Hornbrook, S. R. Hall, K. Ullmann, S. B. Henry, J. P. DiGangi, E. S. Boyle, L. Kaser, R. Schnitzhofer, A. Hansel, M. Graus, Y. Nakashima, Y. Kajii, A. Guenther, and F. N. Keutsch. Missing peroxy radical sources within a summertime ponderosa pine forest. *Atmos. Chem. Phys.*, 14(9):4715–4732, 2014.

[167] D. A. Hauglustaine, S. Madronich, B. A. Ridley, J. G. Walega, C. A. Cantrell, R. E. Shetter, and G. Hübler. Observed and model-calculated photostationary state at Mauna Loa observatory during MLOPEX 2.

Journal of Geophysical Research: Atmospheres, 101(D9):14681–14696, 1996.

[168] R. A. Cox. Ozone and peroxy radical budgets in the marine boundary layer: Modeling the effect of NO_x. *Journal of Geophysical Research: Atmospheres*, 104(D7):8047–8056, 1999.

[169] L. J. Carpenter, P. S. Monks, B. J. Bandy, S. A. Penkett, I. E. Galbally, and C. P. Meyer. A study of peroxy radicals and ozone photochemistry at coastal sites in the northern and southern hemispheres. *Journal of Geophysical Research: Atmospheres*, 102(D21):25417–25427, 1997.

[170] J. Bradshaw, D. Davis, J. Crawford, G. Chen, R. Shetter, M. Müller, G. Gregory, G. Sachse, D. Blake, B. Heikes, H. Singh, J. Mastromarino, and S. Sandholm. Photofragmentation two-photon laser-induced fluorescence detection of NO_2 and NO: Comparison of measurements with model results based on airborne observations during PEM-Tropics A. *Geophysical Research Letters*, 26(4):471–474, 1999.

[171] J. Crawford, D. Davis, G. Chen, J. Bradshaw, S. Sandholm, G. Gregory, G. Sachse, B. Anderson, J. Collins, D. Blake, H. Singh, B. Heikes, R. Talbot, and J. Rodriguez. Photostationary state analysis of the NO_2-NO system based on airborne observations from the western and central North Pacific. *Journal of Geophysical Research: Atmospheres*, 101(D1):2053–2072, 1996.

[172] R. S. Gao, E. R. Keim, E. L. Woodbridge, S. J. Ciciora, M. H. Proffitt, T. L. Thompson, R. J. Mclaughlin, and D. W Fahey. New photolysis system for NO_2 measurements in the lower stratosphere. *J. Geophys. Res.*, 99(D10):20673–20681, October 1994.

[173] D. D. Parrish, C. H. Hahn, D. W. Fahey, E. J. Williams, M. J. Bollinger, G. Hübler, M. P. Buhr, P. C. Murphy, M. Trainer, E. Y. Hsie, S. C.

Liu, and F. C. Fehsenfeld. Systematic variations in the concentration of NO_x (NO + NO_2) at Niwot Ridge, Colorado. *Journal of Geophysical Research: Atmospheres*, 95(D2):1817–1836, 1990.

[174] B. A. Ridley, M. A. Carroll, G. L. Gregory, and G. W. Sachse. NO and NO_2 in the troposphere: Technique and measurements in regions of a folded tropopause. *Journal of Geophysical Research: Atmospheres*, 93(D12):15813–15830, 1988.

[175] M. Duncianu, A. Lahib, A. Tomas, P. S. Stevens, and S. Dusanter. Characterization of a chemical amplifier for peroxy radical measurements in the atmosphere. *Atmospheric Environment*, 222:117106, 2020.

[176] Y. Sadanaga, J. Matsumoto, K.-I. Sakurai, R. Isozaki, S. Kato, T. Nomaguchi, H. Bandow, and Y. Kajii. Development of a measurement system of peroxy radicals using a chemical amplification/laser-induced fluorescence technique. *Review of Scientific Instruments*, 75(4):864–872, 2004.

[177] Y. Liu and J. Zhang. Atmospheric peroxy radical measurements using dual-channel chemical amplification cavity ringdown spectroscopy. *Analytical Chemistry*, 86(11):5391–5398, 2014.

[178] N. Butkovskaya, A. Kukui, and G. Le Bras. Hno3 forming channel of the HO_2 + NO reaction as a function of pressure and temperature in the ranges of 72-600 torr and 223-323 K. *The Journal of Physical Chemistry A*, 111(37):9047–9053, 2007.

[179] N. Butkovskaya, M.-T. Rayez, J.-C. Rayez, A. Kukui, and G. Le Bras. Water vapor effect on the HNO_3 yield in the HO_2 + NO reaction: Experimental and theoretical evidence. *The Journal of Physical Chemistry A*, 113(42):11327–11342, 2009.

[180] C. M. Mihele and D. R. Hastie. The sensitivity of the radical amplifier to ambient water vapour. *Geophysical Research Letters*, 25(11):1911–1913, 1998.

[181] H. Fuchs, F. Holland, and A. Hofzumahaus. Measurement of tropospheric RO_2 and HO_2 radicals by a laser-induced fluorescence instrument. *Review of Scientific Instruments*, 79(8):084104, August 2008.

[182] S. Inamdar, L. Tinel, R. Chance, L. J. Carpenter, P. Sabu, R. Chacko, S. C. Tripathy, A. U. Kerkar, A. K. Sinha, P. V. Bhaskar, A. Sarkar, R. Roy, T. Sherwen, C. Cuevas, A. Saiz-Lopez, K. Ram, and A. S. Mahajan. Estimation of reactive inorganic iodine fluxes in the Indian and Southern Ocean marine boundary layer. *Atmos. Chem. Phys.*, 20(20):12093–12114, 2020.

[183] A. S. Mahajan, J. M. C. Plane, H. Oetjen, L. Mendes, R. W. Saunders, A. Saiz-Lopez, C. E. Jones, L. J. Carpenter, and G. B. McFiggans. Measurement and modelling of tropospheric reactive halogen species over the tropical Atlantic Ocean. *Atmos. Chem. Phys.*, 10(10):4611–4624, 2010.

[184] C. Prados-Roman, C. A. Cuevas, T. Hay, R. P. Fernandez, A. S. Mahajan, S. J. Royer, M. Galí, R. Simó, J. Dachs, K. Großmann, D. E. Kinnison, J. F. Lamarque, and A. Saiz-Lopez. Iodine oxide in the global marine boundary layer. *Atmos. Chem. Phys.*, 15(2):583–593, 2015.

[185] A. Saiz-Lopez, J. M. C. Plane, A. R. Baker, L. J. Carpenter, R. von Glasow, J. C. Gómez Martín, G. McFiggans, and R. W. Saunders. Atmospheric chemistry of iodine. *Chemical Reviews*, 112(3):1773–1804, 2012.

[186] T. Sherwen, M. J. Evans, L. J. Carpenter, S. J. Andrews, R. T. Lidster, B. Dix, T. K. Koenig, R. Sinreich, I. Ortega, R. Volkamer, A. Saiz-Lopez, C. Prados-Roman, A. S. Mahajan, and C. Ordóñez. Iodine's impact on

tropospheric oxidants: a global model study in GEOS-Chem. *Atmos. Chem. Phys.*, 16(2):1161–1186, 2016.

[187] R. Vogt, R. Sander, R. von Glasow, and P. J. Crutzen. Iodine chemistry and its role in halogen activation and ozone loss in the marine boundary layer: A model study. *Journal of Atmospheric Chemistry*, 32(3):375–395, 1999.

[188] G. P. Ayers, S. A. Penkett, R. W. Gillett, B. Bandy, I. E. Galbally, C. P. Meyer, C. M. Elsworth, S. T. Bentley, and B. W. Forgan. Evidence for photochemical control of ozone concentrations in unpolluted marine air. *Nature*, 360(6403):446–449, 1992.

[189] G. P. Ayers and I. E. Galbally. A preliminary investigation of a boundary layer-free troposphere entrainment velocity at Cape Grim. *Baseline 92*, 1995.

[190] D. J. Jacob, E. G. Heikes, S.-M. Fan, J. A. Logan, D. L. Mauzerall, J. D. Bradshaw, H. B. Singh, G. L. Gregory, R. W. Talbot, D. R. Blake, and G. W. Sachse. Origin of ozone and NO_x in the tropical troposphere: A photochemical analysis of aircraft observations over the South Atlantic basin. 101(D19):24235–24250, 1996.

[191] S. T. Andersen, L. J. Carpenter, B. S. Nelson, L. Neves, K. A. Read, C. Reed, M. Ward, M. J. Rowlinson, and J. D. Lee. Long-term NO_x measurements in the remote marine tropical troposphere. *Atmos. Meas. Tech.*, 14(4):3071–3085, 2021.

[192] K. A. Read, J. D. Lee, A. C. Lewis, S. J. Moller, L. Mendes, and L. J. Carpenter. Intra-annual cycles of NMVOC in the tropical marine boundary layer and their use for interpreting seasonal variability in CO. *Journal of Geophysical Research: Atmospheres*, 114(D21), 2009.

[193] R. Steinbrecher. System and performance audit for non methane volatile organic compounds: Global GAW station – Cape Verde atmospheric observatory Calhau, Cape Verde. Report, 2019.

[194] C. Zellweger, M. Steinbacher, and B. Buchmann. Evaluation of new laser spectrometer techniques for in-situ carbon monoxide measurements. *AMT*, 5(10):2555–2567, October 2012.

[195] C. Zellweger, L. Emmenegger, M. Firdaus, J. Hatakka, M. Heimann, E. Kozlova, T. G. Spain, M. Steinbacher, M. V. van der Schoot, and B. Buchmann. Assessment of recent advances in measurement techniques for atmospheric carbon dioxide and methane observations. *AMT*, 9(9):4737–4757, September 2016.

[196] J. P. Pinto, J. Dibb, B. H. Lee, B. Rappenglück, E. C. Wood, M. Levy, R.-Y. Zhang, B. Lefer, X.-R. Ren, J. Stutz, C. Tsai, L. Ackermann, J. Golovko, S. C. Herndon, M. Oakes, Q.-Y. Meng, J. W. Munger, M. Zahniser, and J. Zheng. Intercomparison of field measurements of nitrous acid (HONO) during the SHARP campaign. *Journal of Geophysical Research: Atmospheres*, 119(9):5583–5601, 2014.

[197] T. E. Kleindienst. Recent developments in the chemistry and biology of peroxyacetyl nitrate. *Research on Chemical Intermediates*, 20(3):335–384, 1994.

[198] I. Bridier, F. Caralp, H. Loirat, R. Lesclaux, B. Veyret, K. H. Becker, A. Reimer, and F. Zabel. Kinetic and theoretical studies of the reactions $CH_3C(O)O_2 + NO_2 + m \rightleftharpoons CH_3C(O)O_2NO_2 + m$ between 248 and 393 K and between 30 and 760 torr. *J. Phys. Chem.*, 95(9):3594–3600, May 1991.

[199] L. K. Whalley, A. C. Lewis, J. B. McQuaid, R. M. Purvis, J. D. Lee, K. Stemmler, C. Zellweger, and P. Ridgeon. Two high-speed, portable

GC systems designed for the measurement of non-methane hydrocarbons and PAN: Results from the Jungfraujoch high altitude observatory. *Journal of Environmental Monitoring*, 6(3):234–241, 2004.

[200] B. S. Nelson, G. J. Stewart, W. S. Drysdale, M. J. Newland, A. R. Vaughan, R. E. Dunmore, P. M. Edwards, A. C. Lewis, J. F. Hamilton, W. J. Acton, C. N. Hewitt, L. R. Crilley, M. S. Alam, Ü. A. Şahin, D. C. S. Beddows, W. J. Bloss, E. Slater, L. K. Whalley, D. E. Heard, J. M. Cash, B. Langford, E. Nemitz, R. Sommariva, S. Cox, Shivani, R. Gadi, B. R. Gurjar, J. R. Hopkins, A. R. Rickard, and J. D. Lee. In situ ozone production is highly sensitive to volatile organic compounds in delhi, india. *Atmospheric Chemistry and Physics*, 21(17):13609–13630, 2021.

[201] M. E. Jenkin, J. C. Young, and A. R. Rickard. The MCM v3.3.1 degradation scheme for isoprene. *Atmos. Chem. Phys.*, 15(20):11433–11459, 2015.

[202] R. Sommariva, S. Cox, C. Martin, K. Borońska, J. Young, P. K. Jimack, M. J. Pilling, V. N. Matthaios, B. S. Nelson, M. J. Newland, M. Panagi, W. J. Bloss, P. S. Monks, and A. R. Rickard. AtChem (version 1), an open-source box model for the Master Chemical Mechanism. *Geosci. Model Dev.*, 13(1):169–183, 2020.

[203] T. D. Fairlie, D. J. Jacob, J. E. Dibb, B. Alexander, M. A. Avery, A. van Donkelaar, and L. Zhang. Impact of mineral dust on nitrate, sulfate, and ozone in transpacific Asian pollution plumes. *Atmos. Chem. Phys.*, 10(8):3999–4012, 2010.

[204] X. Wang, D. J. Jacob, W. Downs, S. Zhai, L. Zhu, V. Shah, C. D. Holmes, T. Sherwen, B. Alexander, M. J. Evans, S. D. Eastham, J. A. Neuman, P. R. Veres, T. K. Koenig, R. Volkamer, L. G. Huey, T. J. Bannan, C. J. Percival, B. H. Lee, and J. A. Thornton. Global tropospheric halogen

(Cl, Br, I) chemistry and its impact on oxidants. *Atmos. Chem. Phys.*, 21(18):13973–13996, 2021.

[205] S. Vaughan, T. Ingham, L. K. Whalley, D. Stone, M. J. Evans, K. A. Read, J. D. Lee, S. J. Moller, L. J. Carpenter, A. C. Lewis, Z. L. Fleming, and D. E. Heard. Seasonal observations of oh and HO_2 in the remote tropical marine boundary layer. *Atmos. Chem. Phys.*, 12(4):2149–2172, 2012.

[206] M. D. A. Hernández, J. Burkert, L. Reichert, D. Stöbener, J. Meyer-Arnek, J. P. Burrows, R. R. Dickerson, and B. G. Doddridge. Marine boundary layer peroxy radical chemistry during the AEROSOLS99 campaign: Measurements and analysis. *Journal of Geophysical Research: Atmospheres*, 106(D18):20833–20846, 2001.

[207] J. Burkert, M.-D. Andrés-Hernández, D. Stöbener, J. P. Burrows, M. Weissenmayer, and A. Kraus. Peroxy radical and related trace gas measurements in the boundary layer above the Atlantic Ocean. *Journal of Geophysical Research: Atmospheres*, 106(D6):5457–5477, 2001.

[208] L. J. Carpenter, K. C. Clemitshaw, R. A. Burgess, S. A. Penkett, J. N. Cape, and G. G. McFadyen. Investigation and evaluation of the NO_x/O_3 photochemical steady state. *Atmospheric Environment*, 32(19):3353–3365, 1998.

[209] D. A. Hauglustaine, S. Madronich, B. A. Ridley, S. J. Flocke, C. A. Cantrell, F. L. Eisele, R. E. Shetter, D. J. Tanner, P. Ginoux, and E. L. Atlas. Photochemistry and budget of ozone during the Mauna Loa observatory photochemistry experiment (MLOPEX 2). *Journal of Geophysical Research: Atmospheres*, 104(D23):30275–30307, 1999.

[210] R. Atkinson, D. L. Baulch, R. A. Cox, J. N. Crowley, R. F. Hampson, R. G. Hynes, M. E. Jenkin, M. J. Rossi, J. Troe, and IUPAC Sub-

committee. Evaluated kinetic and photochemical data for atmospheric chemistry: Volume ii - gas phase reactions of organic species. *ACP*, 6(11):3625–4055, September 2006.

[211] K. C. Clemitshaw, L. J. Carpenter, S. A. Penkett, and M. E. Jenkin. A calibrated peroxy radical chemical amplifier for ground-based tropospheric measurements. *Journal of Geophysical Research: Atmospheres*, 102(D21):25405–25416, 1997.

[212] G. M. Handisides, C. Plass-Dülmer, S. Gilge, H. Bingemer, and H. Berresheim. Hohenpeissenberg photochemical experiment (HOPE 2000): Measurements and photostationary state calculations of OH and peroxy radicals. *Atmos. Chem. Phys.*, 3(5):1565–1588, 2003.

[213] C. A. Cantrell, R. E. Shetter, T. M. Gilpin, and J. G. Calvert. Peroxy radicals measured during Mauna Loa observatory photochemistry experiment 2: The data and first analysis. *Journal of Geophysical Research: Atmospheres*, 101(D9):14643–14652, 1996.

[214] B. A. Ridley, S. Madronich, R. B. Chatfield, J. G. Walega, R. E. Shetter, M. A. Carroll, and D. D. Montzka. Measurements and model simulations of the photostationary state during the Mauna Loa observatory photochemistry experiment: Implications for radical concentrations and ozone production and loss rates. *Journal of Geophysical Research: Atmospheres*, 97(D10):10375–10388, 1992.

[215] S. Sillman. The relation between ozone, NO_x and hydrocarbons in urban and polluted rural environments. *Atmospheric Environment*, 33(12):1821–1845, 1999.

[216] J. E. Dyson, G. A. Boustead, L. T. Fleming, M. Blitz, D. Stone, S. R. Arnold, L. K. Whalley, and D. E. Heard. Production of HONO from

NO_2 uptake on illuminated TiO_2 aerosol particles and following the illumination of mixed TiO_2/ammonium nitrate particles. *Atmos. Chem. Phys.*, 21(7):5755–5775, 2021.

[217] Y. Dupart, L. Fine, B. D'Anna, and C. George. Heterogeneous uptake of NO_2 on Arizona test dust under UV-A irradiation: An aerosol flow tube study. *Aeolian Research*, 15:45–51, 2014.

[218] R. J. Gustafsson, A. Orlov, P. T. Griffiths, R. A. Cox, and R. M. Lambert. Reduction of NO_2 to nitrous acid on illuminated titanium dioxide aerosol surfaces: implications for photocatalysis and atmospheric chemistry. *Chemical Communications*, (37):3936–3938, 2006.

[219] A. M. Baergen and D. J. Donaldson. Photochemical renoxification of nitric acid on real urban grime. *Environmental Science & Technology*, 47(2):815–820, 2013.

[220] J. Du and L. Zhu. Quantification of the absorption cross sections of surface-adsorbed nitric acid in the 335–365nm region by Brewster angle cavity ring-down spectroscopy. *Chemical Physics Letters*, 511(4):213–218, 2011.

[221] N. K. Scharko, A. E. Berke, and J. D. Raff. Release of nitrous acid and nitrogen dioxide from nitrate photolysis in acidic aqueous solutions. *Environmental Science & Technology*, 48(20):11991–12001, 2014.

[222] C. Ye, H. Gao, N. Zhang, and X. Zhou. Photolysis of nitric acid and nitrate on natural and artificial surfaces. *Environmental Science & Technology*, 50(7):3530–3536, 2016.

[223] C. Ye, N. Zhang, H. Gao, and X. Zhou. Photolysis of particulate nitrate as a source of HONO and NO_x. *Environmental Science & Technology*, 51(12):6849–6856, 2017.

[224] X. Zhou, H. Gao, Y. He, G. Huang, S. B. Bertman, K. Civerolo, and J. Schwab. Nitric acid photolysis on surfaces in low-NO_x environments: Significant atmospheric implications. *Geophysical Research Letters*, 30(23), 2003.

[225] C. Zhu, B. Xiang, L. T. Chu, and L. Zhu. 308 nm photolysis of nitric acid in the gas phase, on aluminum surfaces, and on ice films. *The Journal of Physical Chemistry A*, 114(7):2561–2568, 2010.

[226] P. S. Romer, P. J. Wooldridge, J. D. Crounse, M. J. Kim, P. O. Wennberg, J. E. Dibb, E. Scheuer, D. R. Blake, S. Meinardi, A. L. Brosius, A. B. Thames, D. O. Miller, W. H. Brune, S. R. Hall, T. B. Ryerson, and R. C. Cohen. Constraints on aerosol nitrate photolysis as a potential source of HONO and NO_x. *Environmental Science & Technology*, 52(23):13738–13746, 2018.

[227] P. Kasibhatla, T. Sherwen, M. J. Evans, L. J. Carpenter, C. Reed, B. Alexander, Q. Chen, M. P. Sulprizio, J. D. Lee, K. A. Read, W. Bloss, L. R. Crilley, W. C. Keene, A. A. P. Pszenny, and A. Hodzic. Global impact of nitrate photolysis in sea-salt aerosol on NO_x, OH, and O_3 in the marine boundary layer. *Atmospheric Chemistry and Physics*, 18(15):11185–11203, 2018.

[228] Q. Shi, Y. Tao, J. E. Krechmer, C. L. Heald, J. G. Murphy, J. H. Kroll, and Q. Ye. Laboratory investigation of renoxification from the photolysis of inorganic particulate nitrate. *Environmental Science & Technology*, 55(2):854–861, 2021.

[229] C. Ye, N. Zhang, H. Gao, and X. Zhou. Matrix effect on surface-catalyzed photolysis of nitric acid. *Scientific Reports*, 9(1):4351, 2019.

[230] S. Laufs and J. Kleffmann. Investigations on HONO formation from photolysis of adsorbed HNO_3 on quartz glass surfaces. *Phys. Chem. Chem. Phys.*, 18(14):9616–9625, 2016.

[231] K. B. Benedict and C. Anastasio. Quantum yields of nitrite (NO_2–) from the photolysis of nitrate (NO_3–) in ice at 313 nm. *The Journal of Physical Chemistry A*, 121(44):8474–8483, 2017.

[232] L. Chu and C. Anastasio. Quantum yields of hydroxyl radical and nitrogen dioxide from the photolysis of nitrate on ice. *The Journal of Physical Chemistry A*, 107(45):9594–9602, 2003.

[233] M. Gen, Z. Liang, R. Zhang, B. Rosette Go Mabato, and C. K. Chan. Particulate nitrate photolysis in the atmosphere. *Environmental Science: Atmospheres*, 2022.

[234] S. R. Handley, D. Clifford, and D. J. Donaldson. Photochemical loss of nitric acid on organic films: a possible recycling mechanism for NO_x. *Environmental Science & Technology*, 41(11):3898–3903, 2007.

[235] N. Nishino, S. A. Hollingsworth, A. C. Stern, M. Roeselová, D. J. Tobias, and B. J. Finlayson-Pitts. Interactions of gaseous HNO_3 and water with individual and mixed alkyl self-assembled monolayers at room temperature. *Physical Chemistry Chemical Physics*, 16(6):2358–2367, 2014.

[236] N. K. Richards and B. J. Finlayson-Pitts. Production of gas phase NO_2 and halogens from the photochemical oxidation of aqueous mixtures of sea salt and nitrate ions at room temperature. *Environmental Science & Technology*, 46(19):10447–10454, 2012.

[237] L. M. Wingen, A. C. Moskun, S. N. Johnson, J. L. Thomas, M. Roeselová, D. J. Tobias, M. T. Kleinman, and B. J. Finlayson-Pitts. Enhanced surface photochemistry in chloride–nitrate ion mixtures. *Physical Chemistry Chemical Physics*, 10(37):5668–5677, 2008.

[238] C. Zhu, B. Xiang, L. Zhu, and R. Cole. Determination of absorption cross sections of surface-adsorbed HNO_3 in the 290–330nm region by Brewster angle cavity ring-down spectroscopy. *Chemical Physics Letters*, 458(4):373–377, 2008.

[239] C. A. Keller, K. E. Knowland, B. N. Duncan, J. Liu, D. C. Anderson, S. Das, R. A. Lucchesi, E. W. Lundgren, J. M. Nicely, E. Nielsen, L. E. Ott, E. Saunders, S. A. Strode, P. A. Wales, D.J. Jacob, and S. Pawson. Description of the NASA GEOS composition forecast modeling system GEOS-CF v1.0. *Journal of Advances in Modeling Earth Systems*, 13(4):e2020MS002413, 2021.

[240] J. Heland, J. Kleffmann, R. Kurtenbach, and P.r Wiesen. A new instrument to measure gaseous nitrous acid (HONO) in the atmosphere. *Environmental Science & Technology*, 35(15):3207–3212, 2001.

[241] J. Kleffmann and P. Wiesen. Technical note: Quantification of interferences of wet chemical HONO lopap measurements under simulated polar conditions. *Atmos. Chem. Phys.*, 8(22):6813–6822, 2008.

[242] C. Reed, C. A. Brumby, L. R. Crilley, L. J. Kramer, W. J. Bloss, P. W. Seakins, J. D. Lee, and L. J. Carpenter. HONO measurement by differential photolysis. *Atmos. Meas. Tech.*, 9(6):2483–2495, 2016.

[243] D. R. Glowacki, A. Goddard, K. Hemavibool, T. L. Malkin, R. Commane, F. Anderson, W. J. Bloss, D. E. Heard, T. Ingham, M. J. Pilling, and P. W. Seakins. Design of and initial results from a Highly Instrumented Reactor for Atmospheric Chemistry (HIRAC). *Atmos. Chem. Phys.*, 7(20):5371–5390, 2007.

[244] G. A. Boustead. *Measurement of nitrous acid production from aerosol surfaces using Photo-Fragmentation Laser-Induced Fluorescence.* Thesis, 2019.

[245] M. O. ANDREAE, W. ELBERT, R. GABRIEL, D. W. JOHNSON, S. OSBORNE, and R. WOOD. Soluble ion chemistry of the atmospheric aerosol and SO_2 concentrations over the eastern North Atlantic during ACE-2. *Tellus B*, 52(4):1066–1087, 2000.

[246] P. Formenti, W. Elbert, W. Maenhaut, J. Haywood, and M. O. Andreae. Chemical composition of mineral dust aerosol during the Saharan dust experiment (SHADE) airborne campaign in the Cape Verde region, september 2000. *Journal of Geophysical Research: Atmospheres*, 108(D18), 2003.

[247] R. Chance, T. D. Jickells, and A. R. Baker. Atmospheric trace metal concentrations, solubility and deposition fluxes in remote marine air over the south-east Atlantic. *Marine Chemistry*, 177:45–56, 2015.

[248] M. O. ANDREAE. Soot carbon and excess fine potassium: Long-range transport of combustion-derived aerosols. *Science*, 220(4602):1148–1151, 1983.

[249] A. R. Baker, T. D. Jickells, K. F. Biswas, K. Weston, and M. French. Nutrients in atmospheric aerosol particles along the Atlantic Meridional Transect. *Deep Sea Research Part II: Topical Studies in Oceanography*, 53(14):1706–1719, 2006.

[250] S. E. Bauer, D. Koch, N. Unger, S. M. Metzger, D. T. Shindell, and D. G. Streets. Nitrate aerosols today and in 2030: a global simulation including aerosols and tropospheric ozone. *Atmos. Chem. Phys.*, 7(19):5043–5059, 2007.

[251] W. Stumm and J. J. Morgan. *Aquatic Chemistry*. John Wiley, New York, 1996.

[252] H. C. Price, K. J. Baustian, J. B. McQuaid, A. Blyth, K. N. Bower, T. Choularton, R. J. Cotton, Z. Cui, P. R. Field, M. Gallagher,

R. Hawker, A. Merrington, A. Miltenberger, R. R. Neely III, S. T. Parker, P. D. Rosenberg, J. W. Taylor, J. Trembath, J. Vergara-Temprado, T. F. Whale, T. W. Wilson, G. Young, and B. J. Murray. Atmospheric ice-nucleating particles in the dusty tropical Atlantic. *Journal of Geophysical Research: Atmospheres*, 123(4):2175–2193, 2018.

[253] A. Sanchez-Marroquin, D. H. P. Hedges, M. Hiscock, S. T. Parker, P. D. Rosenberg, J. Trembath, R. Walshaw, I. T. Burke, J. B. McQuaid, and B. J. Murray. Characterisation of the filter inlet system on the FAAM BAe-146 research aircraft and its use for size-resolved aerosol composition measurements. *Atmos. Meas. Tech.*, 12(11):5741–5763, 2019.

[254] H. Bian and M. J. Prather. Fast-J2: Accurate simulation of stratospheric photolysis in global chemical models. *Journal of Atmospheric Chemistry*, 41(3):281–296, 2002.

[255] J. Mao, D. J. Jacob, M. J. Evans, J. R. Olson, X. Ren, W. H. Brune, J. M. St Clair, J. D. Crounse, K. M. Spencer, M. R. Beaver, P. O. Wennberg, M. J. Cubison, J. L. Jimenez, A. Fried, P. Weibring, J. G. Walega, S. R. Hall, A. J. Weinheimer, R. C. Cohen, G. Chen, J. H. Crawford, C. McNaughton, A. D. Clarke, L. Jaeglé, J. A. Fisher, R. M. Yantosca, P. Le Sager, and C. Carouge. Chemistry of hydrogen oxide radicals (HO_x) in the Arctic troposphere in spring. *Atmos. Chem. Phys.*, 10(13):5823–5838, 2010.

[256] K. R. Travis, C. L. Heald, H. M. Allen, E. C. Apel, S. R. Arnold, D. R. Blake, W. H. Brune, X. Chen, R. Commane, J. D. Crounse, B. C. Daube, G. S. Diskin, J. W. Elkins, M. J. Evans, S. R. Hall, E. J. Hintsa, R. S. Hornbrook, P. S. Kasibhatla, M. J. Kim, G. Luo, K. McKain, D. B. Millet, F. L. Moore, J. Peischl, T. B. Ryerson, T. Sherwen, A. B. Thames, K. Ullmann, X. Wang, P. O. Wennberg, G. M. Wolfe, and F. Yu. Con-

straining remote oxidation capacity with ATom observations. *Atmos. Chem. Phys.*, 20(13):7753–7781, 2020.

[257] R. R Draxler and G. D. Hess. Description of the HYSPLIT4 modeling system. 1997.

[258] J. D. Lee, F. A. Squires, T. Sherwen, S. E. Wilde, S. J. Cliff, L. J. Carpenter, J. R. Hopkins, S. J. Bauguitte, C. Reed, P. Barker, G. Allen, T. J. Bannan, E. Matthews, A. Mehra, C. Percival, D. E. Heard, L. K. Whalley, G. V. Ronnie, S. Seldon, T. Ingham, C. A. Keller, K. E. Knowland, E. G. Nisbet, and S. Andrews. Ozone production and precursor emission from wildfires in Africa. *Environmental Science: Atmospheres*, 2021.

[259] D. L. Savoie, J. M. Prospero, and E. S. Saltzman. Non-sea-salt sulfate and nitrate in trade wind aerosols at Barbados: Evidence for long-range transport. *Journal of Geophysical Research: Atmospheres*, 94(D4):5069–5080, 1989.

[260] B. Mason. *Principles of geochemistry.* Wiley, New York, 3 edition, 1966.

[261] R. Schlitzer, R. F. Anderson, E. M. Dodas, M. Lohan, W. Geibert, A. Tagliabue, A. Bowie, C. Jeandel, M. T. Maldonado, W. M. Landing, D. Cockwell, C. Abadie, W. Abouchami, E. P. Achterberg, A. Agather, A. Aguliar-Islas, H. M. van Aken, M. Andersen, C. Archer, M. Auro, H. J. de Baar, O. Baars, A. R. Baker, K. Bakker, C. Basak, M. Baskaran, N. R. Bates, D. Bauch, P. van Beek, M. K. Behrens, E. Black, K. Bluhm, L. Bopp, H. Bouman, K. Bowman, J. Bown, P. Boyd, M. Boye, E. A. Boyle, P. Branellec, L. Bridgestock, G. Brissebrat, T. Browning, K. W. Bruland, H.-J. Brumsack, M. Brzezinski, C. S. Buck, K. N. Buck, K. Buesseler, A. Bull, E. Butler, P. Cai, P. C. Mor, D. Cardinal, C. Carlson, G. Carrasco, N. Casacuberta, K. L. Casciotti, M. Castrillejo, E. Chamizo, R. Chance, M. A. Charette, J. E. Chaves, H. Cheng,

F. Chever, M. Christl, T. M. Church, I. Closset, A. Colman, T. M. Conway, D. Cossa, P. Croot, J. T. Cullen, G. A. Cutter, C. Daniels, F. Dehairs, F. Deng, H. T. Dieu, B. Duggan, G. Dulaquais, C. Dumousseaud, Y. Echegoyen-Sanz, R. L. Edwards, M. Ellwood, E. Fahrbach, J. N. Fitzsimmons, A. Russell Flegal, M. Q. Fleisher, T. van de Flierdt, M. Frank, J. Friedrich, F. Fripiat, H. Fröllje, S. J. G. Galer, T. Gamo, R. S. Ganeshram, J. Garcia-Orellana, E. Garcia-Solsona, M. Gault-Ringold, E. George, et al. The geotraces intermediate data product 2017. *Chemical Geology*, 493:210–223, 2018.

[262] R. M. Harrison and A.-M. N. Kitto. Evidence for a surface source of atmospheric nitrous acid. *Atmospheric Environment*, 28(6):1089–1094, 1994.

[263] R. M. Harrison, J. D. Peak, and G. M. Collins. Tropospheric cycle of nitrous acid. *Journal of Geophysical Research: Atmospheres*, 101(D9):14429–14439, 1996.

[264] J. Stutz, B. Alicke, and A. Neftel. Nitrous acid formation in the urban atmosphere: Gradient measurements of NO_2 and HONO over grass in Milan, Italy. *Journal of Geophysical Research: Atmospheres*, 107(D22):LOP 5–1–LOP 5–15, 2002.

[265] I. Trebs, L. L. Lara, L. M. M. Zeri, L. V. Gatti, P. Artaxo, R. Dlugi, J. Slanina, M. O. Andreae, and F. X. Meixner. Dry and wet deposition of inorganic nitrogen compounds to a tropical pasture site (Rondônia, Brazil). *Atmos. Chem. Phys.*, 6(2):447–469, 2006.

[266] J. W Deardorff. Convective velocity and temperature scales for the unstable planetary boundary layer and for Rayleigh convection. *J. atmos. Sci*, 27(8):1211–1213, 1970.

[267] J. Kleffmann. Daytime sources of nitrous acid (HONO) in the atmospheric boundary layer. *ChemPhysChem*, 8(8):1137–1144, 2007.

[268] V. Michoud, A. Colomb, A. Borbon, K. Miet, M. Beekmann, M. Camredon, B. Aumont, S. Perrier, P. Zapf, G. Siour, W. Ait-Helal, C. Afif, A. Kukui, M. Furger, J. C. Dupont, M. Haeffelin, and J. F. Doussin. Study of the unknown HONO daytime source at a European suburban site during the MEGAPOLI summer and winter field campaigns. *Atmos. Chem. Phys.*, 14(6):2805–2822, 2014.

[269] F. Spataro and A. Ianniello. Sources of atmospheric nitrous acid: State of the science, current research needs, and future prospects. *Journal of the Air & Waste Management Association*, 64(11):1232–1250, 2014.

[270] M. Li, H. Su, G. Li, N. Ma, U. Pöschl, and Y. Cheng. Relative importance of gas uptake on aerosol and ground surfaces characterized by equivalent uptake coefficients. *Atmos. Chem. Phys.*, 19(16):10981–11011, 2019.

[271] C. Ye, D. E. Heard, and L. K. Whalley. Evaluation of novel routes for NO_x formation in remote regions. *Environmental Science & Technology*, 51(13):7442–7449, 2017.

[272] S. L. Mora Garcia, S. Pandit, J. G. Navea, and V. H. Grassian. Nitrous acid (HONO) formation from the irradiation of aqueous nitrate solutions in the presence of marine chromophoric dissolved organic matter: Comparison to other organic photosensitizers. *ACS Earth and Space Chemistry*, 5(11):3056–3064, 2021.

[273] M. Ndour, P. Conchon, B. D'Anna, O. Ka, and C. George. Photochemistry of mineral dust surface as a potential atmospheric renoxification process. *Geophysical Research Letters*, 36(5), 2009.

[274] D. I. Reeser, N.-O. A. Kwamena, and D. J. Donaldson. Effect of organic coatings on gas-phase nitrogen dioxide production from aqueous nitrate

photolysis. *The Journal of Physical Chemistry C*, 117(43):22260–22267, 2013.

[275] Evelyn J. Freney, Scot T. Martin, and Peter R. Buseck. Deliquescence and efflorescence of potassium salts relevant to biomass-burning aerosol particles. *null*, 43(8):799–807, July 2009.

[276] K. J. Angle, D. R. Crocker, R. M. C. Simpson, K. J. Mayer, L. A. Garofalo, A. N. Moore, S. L. Mora Garcia, V. W. Or, S. Srinivasan, M. Farhan, J. S. Sauer, C. Lee, M. A. Pothier, D. K. Farmer, T. R. Martz, T. H. Bertram, C. D. Cappa, K. A. Prather, and V. H. Grassian. Acidity across the interface from the ocean surface to sea spray aerosol. *Proceedings of the National Academy of Sciences*, 118(2):e2018397118, 2021.

[277] B. Nozière and D. R. Hanson. Speciated monitoring of gas-phase organic peroxy radicals by chemical ionization mass spectrometry: Cross-reactions between CH_3O_2, $CH_3(CO)O_2$, $(CH_3)_3CO_2$, and c$-C_6H_{11}O_2$. *The Journal of Physical Chemistry A*, 121(44):8453–8464, 2017.

[278] L. Onel, A. Brennan, P. W. Seakins, L. Whalley, and D. E. Heard. A new method for atmospheric detection of the CH_3O_2 radical. *Atmos. Meas. Tech.*, 10(10):3985–4000, 2017.

[279] M. Lao, L. R. Crilley, L. Salehpoor, T. C. Furlani, I. Bourgeois, J. A. Neuman, A. W. Rollins, P. R. Veres, R. A. Washenfelder, C. C. Womack, C. J. Young, and T. C. VandenBoer. A portable, robust, stable, and tunable calibration source for gas-phase nitrous acid (hono). *Atmospheric Measurement Techniques*, 13(11):5873–5890, 2020.

[280] A. Stohl, C. Forster, S. Eckhardt, N. Spichtinger, H. Huntrieser, J. Heland, H. Schlager, S. Wilhelm, F. Arnold, and O. Cooper. A backward modeling study of intercontinental pollution transport using air-

craft measurements. *Journal of Geophysical Research: Atmospheres*, 108(D12), 2003.

[281] D. H. P. Vogelezang and A. A. M. Holtslag. Evaluation and model impacts of alternative boundary-layer height formulations. *Boundary-Layer Meteorology*, 81(3):245–269, 1996.

[282] K. A. Emanuel and M. Živković Rothman. Development and evaluation of a convection scheme for use in climate models. *Journal of the Atmospheric Sciences*, 56(11):1766–1782, 1999.

[283] C. Forster, A. Stohl, and P. Seibert. Parameterization of convective transport in a lagrangian particle dispersion model and its evaluation. *Journal of Applied Meteorology and Climatology*, 46(4):403–422, 2007.

[284] C. Forster, U. Wandinger, G. Wotawa, P. James, I. Mattis, D. Althausen, P. Simmonds, S. O'Doherty, S. G. Jennings, C. Kleefeld, J. Schneider, T. Trickl, S. Kreipl, H. Jäger, and A. Stohl. Transport of boreal forest fire emissions from Canada to Europe. *Journal of Geophysical Research: Atmospheres*, 106(D19):22887–22906, 2001.

[285] A. Stohl and T. Trickl. A textbook example of long-range transport: Simultaneous observation of ozone maxima of stratospheric and North American origin in the free troposphere over Europe. *Journal of Geophysical Research: Atmospheres*, 104(D23):30445–30462, 1999.

[286] A. Gressent, B. Sauvage, E. Defer, H. W. Pätz, K. Thomas, R. Holle, J.-P. Cammas, P. Nédélec, D. Boulanger, V. Thouret, and A. Volz-Thomas. Lightning NO_x influence on large-scale NOy and O_3 plumes observed over the northern mid-latitudes. *Tellus B: Chemical and Physical Meteorology*, 66(1):25544, 2014.

[287] B. Sauvage, A. Fontaine, S. Eckhardt, A. Auby, D. Boulanger, H. Petetin, R. Paugam, G. Athier, J. M. Cousin, S. Darras, P. Nédélec, A. Stohl,

S. Turquety, J.-P. Cammas, and V. Thouret. Source attribution using FLEXPART and carbon monoxide emission inventories: SOFT-IO version 1.0. *Atmospheric Chemistry and Physics Discussions*, pages 1–48, 2017.

[288] B. Bohn, D. E. Heard, N. Mihalopoulos, C. Plass-Dülmer, R. Schmitt, and L. K. Whalley. Characterisation and improvement of $j\mathrm{O}(^1\mathrm{D})$ filter radiometers. *AMT*, 9(7):3455–3466, July 2016.

[289] J. B. Burkholder, S. P. Sander, J. Abbatt, J. R. Barker, C. Cappa, J. D. Crounse, T. S. Dibble, R. E. Huie, C. E. Kolb, M. J. Kurylo, V. L. Orkin, C. J. Percival, D. M. Wilmouth, and P. H. Wine. Chemical kinetics and photochemical data for use in atmospheric studies, evaluation no. 19, JPL publication 19-5. Report, 2019.

[290] R. Atkinson, D. L. Baulch, R. A. Cox, J. N. Crowley, R. F. Hampson, R. G. Hynes, M. E. Jenkin, M. J. Rossi, and J. Troe. Evaluated kinetic and photochemical data for atmospheric chemistry: Volume iii - gas phase reactions of inorganic halogens. *ACP*, 7(4):981–1191, February 2007.

[291] V. Riffault, Y. Bedjanian, and G. Poulet. Kinetic and mechanistic study of the reactions of OH with IBr and HOI. *Journal of Photochemistry and Photobiology A: Chemistry*, 176(1):155–161, 2005.

[292] J. C. Gómez Martín, P. Spietz, and J. P. Burrows. Kinetic and mechanistic studies of the $\mathrm{I_2/O_3}$ photochemistry. *J. Phys. Chem. A*, 111(2):306–320, January 2007.

[293] J. J. Orlando and G. S. Tyndall. Rate coefficients for the thermal decomposition of $\mathrm{BrONO_2}$ and the heat of formation of $\mathrm{BrONO_2}$. *J. Phys. Chem.*, 100(50):19398–19405, January 1996.

[294] P. D. Rosenberg, A. R. Dean, P. I. Williams, J. R. Dorsey, A. Minikin, M. A. Pickering, and A. Petzold. Particle sizing calibration with refractive index correction for light scattering optical particle counters and impacts upon PCASP and CDP data collected during the Fennec campaign. *Atmos. Meas. Tech.*, 5(5):1147–1163, 2012.

[295] M. Hess, P. Koepke, and I. Schult. Optical properties of aerosols and clouds: The software package OPAC. *Bulletin of the American Meteorological Society*, 79(5):831–844, 1998.

[296] last accesed: June 4th 2021.

[297] C. L. Ryder, F. Marenco, J. K. Brooke, V. Estelles, R. Cotton, P. Formenti, J. B. McQuaid, H. C. Price, D. Liu, P. Ausset, P. D. Rosenberg, J. W. Taylor, T. Choularton, K. Bower, H. Coe, M. Gallagher, J. Crosier, G. Lloyd, E. J. Highwood, and B. J. Murray. Coarse-mode mineral dust size distributions, composition and optical properties from AER-D aircraft measurements over the tropical eastern Atlantic. *Atmos. Chem. Phys.*, 18(23):17225–17257, 2018.

[298] B. Weinzierl, D. Sauer, M. Esselborn, A. Petzold, A. Veira, M. Rose, S. Mund, M. Wirth, A. Ansmann, M. Tesche, S. Gross, and V. Freudenthaler. Microphysical and optical properties of dust and tropical biomass burning aerosol layers in the Cape Verde region—an overview of the airborne in situ and lidar measurements during SAMUM-2. *Tellus B: Chemical and Physical Meteorology*, 63(4):589–618, 2011.

[299] C. L. Ryder, E. J. Highwood, A. Walser, P. Seibert, A. Philipp, and B. Weinzierl. Coarse and giant particles are ubiquitous in Saharan dust export regions and are radiatively significant over the Sahara. *Atmos. Chem. Phys.*, 19(24):15353–15376, 2019.

[300] K. Kandler, K. Lieke, N. Benker, C. Emmel, M. Küpper, D. Müller-Ebert, M. Ebert, D. Scheuvens, A. Schladitz, L. Schütz, and S. Weinbruch. Electron microscopy of particles collected at Praia, Cape Verde, during the Saharan mineral dust experiment: particle chemistry, shape, mixing state and complex refractive index. *Tellus B: Chemical and Physical Meteorology*, 63(4):475–496, 2011.

[301] T. Müller, A. Schladitz, K. Kandler, and A. Wiedensohler. Spectral particle absorption coefficients, single scattering albedos and imaginary parts of refractive indices from ground based in situ measurements at Cape Verde island during SAMUM-2. *Tellus B: Chemical and Physical Meteorology*, 63(4):573–588, 2011.

[302] B. T. Johnson, S. R. Osborne, J. M. Haywood, and M. A. J. Harrison. Aircraft measurements of biomass burning aerosol over West Africa during DABEX. *Journal of Geophysical Research: Atmospheres*, 113(D23), 2008.

[303] K. Lieke, K. Kandler, D. Scheuvens, C. Emmel, C. Von Glahn, A. Petzold, B. Weinzierl, A. Veira, M. Ebert, S. Weinbruch, and L. Schütz. Particle chemical properties in the vertical column based on aircraft observations in the vicinity of Cape Verde islands. *Tellus B: Chemical and Physical Meteorology*, 63(4):497–511, 2011.

[304] S. Lance, C. A. Brock, D. Rogers, and J. A. Gordon. Water droplet calibration of the cloud droplet probe (CDP) and in-flight performance in liquid, ice and mixed-phase clouds during ARCPAC. *Atmos. Meas. Tech.*, 3(6):1683–1706, 2010.

[305] W. C. Hinds. *Aerosol Technology: Properties, Behavior, and Measurement of Airborne Particles*. Wiley, 2nd edition, 1999.